New concepts for enantioselective crystallisation

Dissertation

zur Erlangung des akademischen Grades

Doktoringenieur
(Dr.-Ing.)

von: Dipl.-Ing. Henning Kaemmerer
geb. am: 11. August 1979
in: Ibbenbüren

genehmigt durch die Fakultät für Verfahrens- und Systemtechnik
der Otto-von-Guericke-Universität Magdeburg

Gutachter: Prof. Dr. h.c. Dr.-Ing. Andreas Seidel-Morgenstern
Prof. Dr. Simon Black
asst. Prof. Dr.-Ing. Joop ter Horst

eingereicht am: 4. September 2011
Promotionskolloquium am: 11. November 2011

Preface

The thesis in hand originated from research I performed at the Max Planck Institute for Dynamics of Complex Technical Systems (MPI) in Magdeburg, Germany.

First and foremost, I am deeply thankful to Prof. Seidel-Morgenstern, who set the framework for the interesting and challenging research topic and for his patient und persistent guidance throughout the course of my research. The granted trust in the progress of this work and his endurance in solving challenges and encouraging optimism with respect to emerging ideas motivated me a lot. The support in presenting scientific results at national and international conferences and by a series of meetings within a European collaboration is appreciated much.

I would like to express my sincere gratitude to apl. Prof. Heike Lorenz for introducing the field of chiral crystallisation to me and for getting in contact with the scientific and industrial crystallisation community. I am very grateful for the sound support in both, experimental and theoretical crystallisation issues. Many fruitful discussions have strengthened this work and also the joy within.

Further thanks I owe to hon. Prof. Simon Black (AstraZeneca) and asst. Prof. Dr. ir. J. H. ter Horst (Delft University of Technology) for reviewing this thesis and acting as referees.

The financial support by AstraZeneca is gratefully acknowledged. I would like to thank Dr. Martin Hedberg and Dr. Matthew J. Jones for the fruitful collaboration and the numerous pleasant and productive calls, mails and meetings we had within INTENANT and after.

I am indebted to the lab technicians Jacqueline Kaufmann and Luise Borchert, who assisted me in analytics and made the lab work more convenient through their persistent jovial attitude. Neither the simulation studies nor the pilot-scale experimental work would have been possible without the comprehensive assistance by the people of the IT department, the mechanical workshop and the process engineers, respectively. Thank you, too.

Further, I am more than pleased for the opportunity I had, to supervise diligent and gifted students. Me and in parts also this thesis, have benefited much from their co-work. Halime Adem, Jogesh Bhintade, Elena Horosanskaia, Jens Rabitzsch, Oscar Braniella Rodríguez, Peter Schulze and Elvira Vorster, I thank you a lot and wish you all the best for the future.

Within my time at the MPI, I appreciated much the interest, the support and motivating discussions with doctoral fellows and post-docs of the group of Physical and Chemical Foundations of Process Engineering and others, who valued my time in Magdeburg even more. Among many others, the ‘Mensa group’ and the ‘Kicker connection’ must be named here.

Finally, I am truly grateful for the continous support and encouragement by my beloved family and my girlfriend Annette, who endured the entire spectrum of moods I brought home from work.

Aschaffenburg, 04.09.2011 Henning Kaemmerer

Kurzreferat

Die potentiell großen Diskrepanzen in der physiologischen Wirkung von Molekülpaaren, welche sich lediglich durch ihre Spiegelbildlichkeit unterscheiden, sind spätestens seit der Vermarktung des Moleküles Thalidomid (Contergan®, Grünenthal/Germany) allgemein bekannt geworden. Ausgehend von einer Forderung der Amerikanischen Food and Drug Administration (FDA) hat in chemischen, pharmazeutischen als auch in biotechnologischen Branchen ein sogenannter 'chiral switch' stattgefunden. Ziel ist die ausschliessliche Formulierung von Produkten, welche nur das gewünschte Enantiomer, das aktive Spiegelbild, enthalten. Aufgrund der weitgehenden Ähnlichkeit der Moleküle, erweist sich diese Forderung nach wie vor als sehr aufwendig und bedarf in der Regel des aufwendigen Screenings geeigneter Methoden für jedes neue Molekül. In der vorliegenden Arbeit wurden neuartige, leistungsfähige chirale Aufreinigungsverfahren entwickelt, welche methodisch verallgemeinbar sind und einen einfacheren Zugang zu enantiomerenreinen Produkten gewährleisten können.

Die dreigliedrige Arbeit beschäftigt sich im ersten Teil mit der systematischen Analyse von komplexen Flüssig-/Fest- und Fest-/Feststoffphasengleichgewichten, dessen Verständnis die Grundlage für chirale kristallisationsbasierte Trennungen ist. Hierzu wurde exemplarisch das System der chiralen Äpfelsäure, welches partielle Mischbarkeit in der Festphase aufweist, in mehreren Lösungsmitteln untersucht. Die experimentell aufwendige Analyse der Vermessung von Konoden wurde begleitet mit zeitaufgelösten Röntgenstrukturanalysen der korrespondierenden Festphasen. Die so gewonnenen kinetischen Daten und thermodynamischen Gleichgewichtsinformationen ermöglichten die Abschätzung des Erfolges von kristallisationsbasierten Trennungen für dieses und konzeptionell ähnliche Stoffsysteme.

Im zweiten Teil der Arbeit wurden für eine größere Anzahl chiraler Stoffsysteme sowohl korrelative als auch rein prädiktive thermodynamische Vorhersagemodelle angepasst und genutzt, um ausgehend von einem Minimum an experimentellen Daten, relevante Kenngrößen von Phasengleichgewichten für das Design chiraler Trennungen zu erhalten. Es zeigte sich, dass das vorhandene Potential oftmals die sichere Abschätzung und Auslegung von chiralen Trennprozessen ermöglicht. Das entwickelte short-cut und ein detaillierteres Model bieten die Möglichkeit der gezielten Variation einer charateristischen thermodynamischen Größe und die Grundlage für einen neuen, effektiveren Kristallisationsprozess. Letzterer wurde im folgenden Teil der Arbeit an verschiedenen Stoffsystemen evaluiert.

Das sich anschliessende Kapitel widmet sich der synergetischen Kopplung zweier chiraler Trennverfahren. Dabei wurden ausgewählte Verschaltungen von kontinuierlicher Gegenstromchromatographie und selektiver Kristallisation für zwei Stoffsysteme zunächst im Labormassstab und später im Pilotmassstab theoretisch und experimentell evaluiert. Die Optimierung der Kopplungen ergab signifikante Produktivitätsverbesserungen gegenüber den Einzelverfahren. Es konnte gezeigt werden, dass die Verschaltung eines im zweiten Teil der Arbeit neu entwickelten 2-Schritt-Kristallisationsprozesses mit einem chromatographischen Teilschritt und interner Rezyklierung in einer zusätzlich deutlich gesteigerten Produktivität resultiert. Diese Prozessvariante erwies sich als robuster und leistungsfähiger im Vergleich zu Kopplungsprozessen, welche den Stand der Technik repräsentieren.

Abstract

The large discrepancies in the physiological impact of a pair of molecules, that can be discriminated by its mirror symmetry only, are widely known not only after the commercialisation of the molecule Thalidomide (Contergan®, Grünenthal/Germany). Initiated by a claim by the American Food and Drug Administration (FDA) a so-called 'chiral switch' took place in the chemical, pharmaceutical and biotechnological branches. It aims on the exclusive formulation of products, which contain only the desired enantiomer, the active mirror image. Due to the very similar nature of the molecules, the claim remains very demanding and requires usually an extensive screening of suitable methods for each new molecule. Within the thesis in hand new powerful chiral purification methods were developed, which allow a certain degree of generalisation und the simplified access to single enantiomers.

Within the first part of the tripartite thesis, a systematic analysis of complex liquid/solid and solid/solid phase equilibria was performed, whose understanding provides the foundation for chiral separations. Therefore, the system of the chiral malic acid, which exhibits partial solid solutions, was investigated exemplarily in different solvents. The experimental determination of tie lines was accompanied by time-resolved X-ray powder determination of the corresponding solid phases. The obtained data on the prevailing phase equilibria allowed estimating the degree of success of crystallisation-based separations of this and conceptionally similar systems.

The second part of the thesis is concerned with the extension and application of both, correlative and entirely predictive thermodynamic models for a number of chiral systems in order to obtain relevant key properties of phase equilibria necessary for the design of chiral separations. Significant potential was found, which often allowed the estimation and design of chiral separation processes based on rather limited experimental data. The developed short-cut model and a more detailed model allowed tailoring a characteristic thermodynamic property, which was considered the key element for a new and more effective crystallisation process. The latter was validated using different chiral systems in the following part of the thesis.

The last part compares synergetic couplings of chiral separation processes. Hereby, selected combinations of continuous multi-column chromatography and selective crystallisation were evaluated for two chiral systems on a theoretical and experimental basis and both, on lab-scale and on a pilot-plant-scale. Optimisation of selected coupled processes revealed significant increases in productivities compared to the individual separation processes. It was shown, that the combination of a newly developed 2-step crystallisation process and a chromatographic pre-enrichment step with internal recycling of fractions leads to additional improvements in productivities. This process variation outperforms other coupled processes state-of-the-art in terms of robustness and productivity.

Contents

List of symbols

Symbols, that are relevant within a single paragraph only, are explained at the corresponding section and are not listed here.

Latin symbols		
A_{ij}	Margules model interaction parameter	[J mol^{-1}]
A_i	area of molecular cavity of component *i*	[Å^2]
C	number of components	[-]
c_p	heat capacity	[J mol^{-1} K^{-1}]
c_{ii}	cohesive energy density	[MPa]
c_{hb}	cutoff value for hydrogen bonding	[e Å^2]
D_{ax}	apparent axial dispersion coefficient	[m^2 s^{-1} kg^{-1}]
d_{mn}	distance between segment *m* and *n*	[Å]
E	total energy	[J]
F	phase ratio	[-]
f_{pol}	polarisability factor	[-]
G	Gibbs energy	[J mol^{-1}]
G_{ij}	model interaction parameter	[J mol^{-1}]
H	enthalpy	[J mol^{-1}]
H	Hamiltonian operator	[J]
$\hbar$	reduced Planck constant, 1.054571628 10^{-34}	[J s^{-1}]
H_i	Henry coefficient of component *i*	[arbitrary]
I_{ij}	binary interaction parameter	[-]
k	Boltzmann constant, 1.380 6504 10^{-23}	[J K^{-1}]
k_i'	capacity factor	[-]
L	lengths	[m]
M	molecular mass	[g mol^{-1}]
n	molar amount	[mol]
p	pressure	[Pa]
$p_i(\sigma)$	probability function of component *i* with respect to σ	[-]
q_i	normalised molecular volume of component *i*, 79.53	[Å^2]
q_i	specific adsorption of component *i*	[g dm^{-3}]
R	ideal gas constant, 8.3174	[J mol^{-1} K^{-1}]
R_{ij}	resolution	[-]
r_i	normalised molecular volume, 66.99	[Å^3]
r_{av}	effective radius of a surface element	[Å]
r_n	radius of surface segment *n*	[Å]
S	entropy	[J mol^{-1} K^{-1}]
T	temperature	[K]
t	time	[s]
U	internal energy	[J mol^{-1}]
u	linear velocity	[m s^{-1}]
V	volume	[m^3]
w	width of a Gaussian distribution	[arbitrary]
w	weight fraction	[-]
x_i	molar fraction of component *i* in the liquid phase	[-]
z_i	molar fraction of component *i* in the solid phase	[-]
z	lattice coordination number	[-]

Abbreviations	
BM	bootstrap method
COSMO	conductor-like-screening-model
DSC	differential scanning calorimetry
DFT	density functional theory
FIM	Fisher information matrix
HETP	height equivalent to a theoretical plate
MSZW	metastable zone width
NRTL	non-random two liquid (model)
NTP	number of transport plates
P-HO	primary, homogeneous
P-HE	primary, heterogeneous
RS	realistic solvation/real solvents
SAC	segment activity coefficient
Sec	secondary
SLE	solid/liquid equilibria
SMB	simulated moving bed
XRPD	X-ray powder diffraction (analysis)

Greek symbols		
$\mathcal{A}$	affinity	[J mol^{-1}]
α	activity	[-]
α_r	solubility ratio	[-]
a_{eff}	effective surface area	[Å^2]
ν	stoichiometric coefficient	[-]
φ	thermodynamic phase	[-]
ζ	reaction progress variable	[-]
δ_i	Hildebrand solubility parameter	[MPa$^{0.5}$]
υ	variance of possible thermodynamic phases	[-]
$v_{j/i}$	liquid volume	[m^3,dm^3,cm^3,…]
μ	chemical potential	[J mol^{-1}]
$\mu_{m,i}$	1st absolute moment	[s]
$\sigma^2_{m,i}$	2nd central moment	[s]
σ_m	surface charge density of element *m*	[e Å^2]
f	fugacity	[Pa]
τ_{ji}	energy parameter, interactions between components *i* and *j*	[J mol^{-1}]
χ	number of thermodynamic states	[-]
Θ_i	model parameter for component *i*	[arbitrary]
θ	diffraction angle	[degree]
λ_{ij}	interaction parameter	[J mol^{-1}]
γ_t	surface tension	[J m^{-2}]
γ	activity coefficient	[-]
$\Gamma_{i/S}(\sigma_m)$	segment activity coefficient for solute segment *m* in solution	[-]
ψ	wavefunction	[length$^{-dN/2}$ N: number of particles; d: dimensionality of space]

Superscripts	
I,II	index of the thermodynamic state
0	reference or standard state
*	saturated/ initial value
cav	cavity formation
cc	correction
classical	classical coupled process
disp	dispersive
E	excess quantity
el	electrostatic
eu	eutectic (composition)
f	fusion/melting
id	ideal
initial	initial property
is	ideal solvation
l	liquid
max	maximum
min	minimum
PE	preferential enrichment
s	solid
sol	solvation
res	restoring
SG	Stavermann-Guggenheim
t	transition
tv	virtual transition
vdw	van-der-Waals

Subscripts	
0	reference or standard property
I,II	polymorphic modification
A,B,i	components
c	column
crit	critical
int	internal
R	retention
(R)	(related to the) (R)-enantiomer
(R,S)	(related to the) racemic compound
(S)	(related to the) (S)-enantiomer
Sol	solvent
S	solution
s	mixture property
sur	surface
tot	total
tp	triple point
v	volume

1 Introduction

1.1 Motivation and scientific background

Unit operations for the separation of molecules similar in kind are a major field in process engineering. Despite great developments in a multitude of disciplines, new challenges remain to emerge and the quality and reliability of engineering tools define the pace in the advancement of applied chemical processes. Effective and efficient separations are of particular interest for tons-scale applications to get a hold on both, investment and running costs as well as for high-value products, where complex purification steps become necessary. For the latter the early access to pure product samples on the one hand and processes with high yields on the other are of vital interest.

Optical isomers are one prominent class of substances, for which short time-to-market demands and elevated purity constraints coincide. The number of chiral compounds used in agrochemicals, flavours, fragrances and pharmaceuticals has been growing rapidly over the last years and analogously the demand for optically pure products. The specific rise in value for the target enantiomer upon chiral separation from its antipode is significant for many cases.

The Nobel price award in 2001 was devoted to studies by William S. Knowles and Ryoji Noyori *for their work on chirally catalysed hydrogenation reactions* and further to the work by K. Barry Sharpless *for his work on chirally catalysed oxidation reactions* [1]. It highlights the need and the complexity for the probably most elegant technique to produce single enantiomers. Up to now the development of enantioselective synthesis routes for active pharmaceutical ingredients remains demanding and can outweigh the economical advantages of optically pure enantiomers. Intensive research on the advancement of physical separation methods has led in parallel to efficient alternatives to asymmetric synthesis. Selective crystallisation processes for diastereoisomers can be considered as state-of-the-art, whereas crystallisation processes for the isolation of single enantiomers are less frequently found in the industrial and pharmaceutical environment. Thermodynamically dominated crystallisation techniques comprise the inherent limitation that single enantiomers can be obtained from asymmetric mixtures only. The necessary magnitude of asymmetry for chiral separation is substance specific and often impedes efficient crystallisations. In summary, robust low-cost chiral separation techniques with a large degree of generality are missing.

This thesis will aim to develop new concepts for chiral separations, that are widely applicable. One major topic will be the accelerated model-based assessment of chiral systems on the bases of limited or even no available thermodynamic data. The amount and kind of information necessary for successful chiral separation will be evaluated. Further, the thesis will utilise the developed thermodynamic models in order to tailor solid/liquid equilibria (SLE) such, that new separation schemes emerge. The schemes will be evaluated for different operating modes. Hereby, the combination of innovative chiral crystallisations with continuous multi-column chromatography will be compared in terms of performance and robustness to approaches state-of-the-art. Theoretical considerations will be corroborated by experimental studies.

1.2 Conceptual approach

The knowledge of specific solid/solid and solid/liquid phase equilibria is an essential pre-requirement for the design of any crystallisation process. The interactions in both phases together define the domains, in which selective crystallisations of target compounds can take place. Systems of enantiomers in solution exhibit ternary solid/liquid equilibria (SLE), that share important characteristics. The work in hand is divided into 6 chapters. The first two chapters will provide an overview of the relevant fundamental context to the characterisation of crystalline phases, the estimation of solid/liquid equilibria and methodologies state-of-the-art for chiral separations. Chapters III and IV will comprise individual studies on coherent aspects of selective crystallisations of enantiomers. The subsequent chapter V rests on the outcome of foregoing chapters and will proceed with the application and validation of coupled separation schemes. A summary will be given by the concluding chapter.

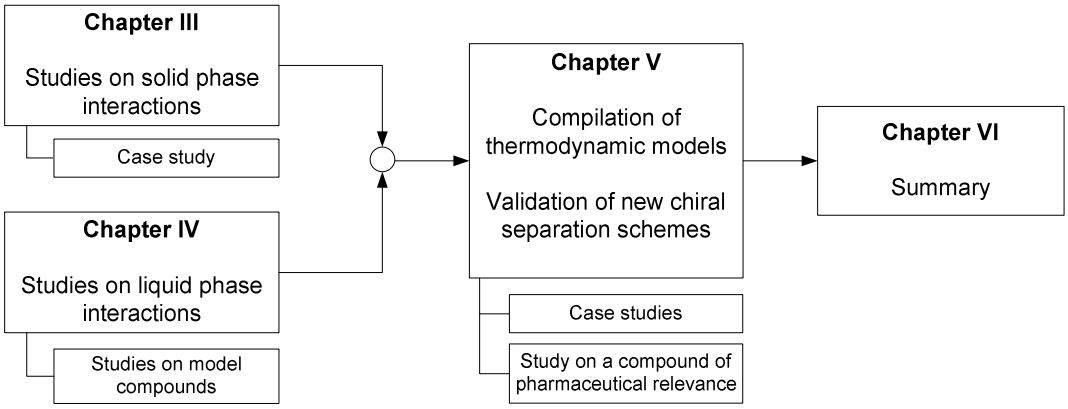

Figure 1.1 *Interlink of chapters.*

The first goal of the thesis in hand will be the identification and validation of methodologies for the accelerated estimation of phase diagrams of chiral compounds in the melt and in solution. Corresponding comprehensive binary, ternary and quaternary phase equilibria will be derived for selected chiral system on the basis of own experimental studies and literature values. Hereby, the composition of the so-called 'eutectic composition' will gain particular interest.

The merit of predictive thermodynamic models for solid phase descriptions is rather limited in comparison to models for liquid phase interactions. This is unfortunate, since the correct representation of SLE is directly connected to the prevailing crystalline phase present in solution. For this reason, particular emphasis will be given on the experimental investigation of the solid phases of all compounds considered. The role of more complex solid phases on the corresponding SLE will be investigated exemplarily for the chiral system of malic acid/acetone. A model for its description will be proposed and the impact of the specific solid phase on chiral separation will be investigated. Chapter 3 will aim to exemplify strategies how to overcome ambiguous phase behaviour through thorough studies on a system, which shows polymorphism and the formation of partial solid solutions.

The second contribution to the SLE of a chiral system are interactions in the liquid phase, which will be studied on the basis of a larger number of selected chiral systems and will be summarised in chapter 4. A correlative g^E-model will be applied and modified to allow the estimation of ternary and quaternary SLE on the basis of limited binary data. Further, an *a priori*

concept for the prediction of activity coefficients in the liquid phase will be evaluated and combined with the g^E-model to allow the estimation of ternary solubility data without recourse to experimental measurements. The applied method will make use of databases for the identification of (anti-) solvent candidates to achieve the most promising SLE for chiral separations.
In summary, solid phase interactions will be derived entirely from experiments in combination with correlative models, while liquid phase interactions will be estimated both through correlative and estimation models.

The second objective of this thesis will be the development and evaluation of new modes of chiral crystallisation-based separations. A summary of the conducted studies and results will be given in chapter 5. The investigated comprehensive SLE data of the previous chapter 4 will allow the identification of key parameters that pose large influences on the composition of the eutectic composition of chiral systems in solution. On this basis a new chiral separation process will be developed, that will allow to bridge the gap from poorly enriched asymmetric mixtures to optically pure products by a 2-step crystallisation process. Changes to the eutectic composition through well chosen temperatures and selected solvents will allow the purification of slightly asymmetric mixtures. The use of thermodynamic models for the corresponding SLE will pave the way for the design of separation processes. The new processes will be validated on an experimental basis firstly on model systems. Theoretical mass balances for proposed crystallisation schemes will be compared to practical results. Further, cyclic operation modes will be evaluated in practise.
The chiral separation of a racemic mixture of the active pharmaceutical ingredient Bicalutamide will be conducted on a pilot-plant–scale by a hybrid process consisting of a pre-enrichment step using continuous counter-current chromatography followed by the new 2-step selective crystallisation process. Prior to the separation, the optimal interface in terms of highest productivity between the two processes will be identified by a dynamic model and will allow the identification of advantageous operating modes of this particular process combination.

In summary, the work will aim to provide new crystallisation-based methodologies for the accelerated and rather generic access to single enantiomers originating from racemic mixtures. Differently detailed thermodynamic models will allow the rapid assessment of separation tasks and simplify the choice for the corresponding most promising separation technique. The concept will be illustrated for both model substances and compounds of pharmaceutical relevance by means of lab-scale and pilot plant-scale validation experiments.

All studies presented in this thesis were conducted under supervision of Prof. Andreas Seidel-Morgenstern in his group of Physical and Chemical Foundations of Process Engineering at the Max Planck Institute for Dynamics of Complex Technical Systems in Magdeburg. Individual tasks of pharmaceutical relevance were supported by and embedded in a bilateral collaboration with AstraZeneca. Selected conceptual studies and validation work on the pharmaceutical compound Bicalutamide were integrated in the collaborative project ‘INTENANT’ under the umbrella of the European framework program 7.

For the three fields of investigation, solid phase-, fluid phase analysis and chiral separation, selected chiral systems will be studied with different objectives. Table 1.1 summarises the systems and assigns the conducted investigations to corresponding chapters to clarify the objective of the corresponding studies.

Table 1.1 *Investigated chiral systems classified according to the investigated aspects.*

Type	Compound/solvent	Analysis		Chiral separation technique	Chapter
		Solid phase	Fluid phase		
considered as model compounds	3-Chloromandelic acid • water • 2-propanol	-	modelling	-	4.2.4
	Undisclosed system, denoted *UND* • ethyl acetate	-	modelling	-	4.2.2
	Mandelic acid • water • (S)-ethyl lactate • (2R, 3R)-diethyl tartrate	-	modelling	-	4.2.2
	Methionine • water	-	modelling	crystallisation	4.2.2 4.3 4.4.4 5.1.3.2
	Propranolol·HCL • water • methanol	-	modelling	- -	4.2.2
	Threonine • water	modelling	modelling	-	4.1.1
	Tröger's Base • ethanol	-	modelling	-	4.2.2
compounds of pharmaceutical relevance	N-methylephidrine • (S)-ethyl lactate • (2R, 3R)-diethyl tartrate	-	modelling	-	4.1.1
	Bicalutamide • methanol • toluene • water	analysis	measurement, modelling, solvent screening	crystallisation, chromatography, coupled mode, scale-up	4.2.4 4.4.2 5.2.2
	Proline • chloroform • dimethylsulfoxid • ethanol • methanol	analysis	measurement, modelling, solvent screening	crystallisation	4.2.3 5.1.2
	Serine • water • methanol • ethanol	analysis	measurement, modelling, solvent screening	crystallisation, chromatography, coupled mode	4.2.3 5.1.2 5.2.1.1 5.2.1
	Malic Acid • acetone	analysis, modelling	measurement, modelling	crystallisation	3

2 Theoretical foundations

The fundamental context necessary to understand the separation and screening techniques presented in the later chapters will be provided in the following. A characteristic property of a group of compounds – chirality - and its significance for human life and consequently valuable products will be highlighted. The role of chiral crystalline phases and the equilibria with and within liquid phases will be explained in appropriate depth. The introduction of relevant correlative and *a priori* models for the description and prediction of solid/liquid equilibria will be given followed by an outline of crystallisation-based separation techniques discriminating among chiral species.
Further, a brief outline of techniques and theories for the separation of chiral compounds by means of continuous multi-column preparative chromatography is given.

2.1 Systems of enantiomers

When Pasteur recognised in 1847, that an identical substance can appear in more than a single crystalline form and that these forms, dissolved separately, exhibit different properties, the phenomenon of *chirality* was described for the first time [2]. His discovery, that the two forms can interact differently with living organisms paved the way for a new discipline: stereo-chemistry.

2.1.1 Chirality

The concept of *Chirality*[1] is explained best by the geometric property that is responsible for the non-identity of an object with its mirror image. A hand, a snail shell or a key are examples, which lack inverse symmetry elements, that is, a centre, a plane and an improper axis of symmetry. A bar or a ball is considered as *achiral*, since at least one inverse symmetry element and therefore superimposable mirror images exist.
In chemistry, chirality is predominantly caused by the presence of an asymmetric carbon atom-a *chiral centre*-although exceptions are known. Chiral compounds can be divided into *constitutional (structural) isomers* and s*tereoisomers.* They latter are also called *spatial isomers* and are identical in atomic constitution and bonding, but differ in the three-dimensional arrangement of the atoms. Stereoisomerism comprises also geometric (cis/trans) isomers and *diastereoisomers*. The latter belong to a class of isomers with more than one chiral centre that are not mirror images of one another. According to the number of chiral centres *n* within the molecular structure, 2^n stereoisomers are possible. Diastereoisomers and geometric isomers are both, chemically distinct and pharmacologically different and are generally readily separated

[1] greek: χειρ (cheir), hand

without chiral techniques. In contrast, pairs of stereoisomers, whose individual isomers are mirror-images, have essentially identical physical (except for optical rotatory) and chemical properties (except in a chiral environment). The isomers, belonging to this class, are also called *enantiomers* or *optical isomers.*

Figure 2.1 compiles exemplarily the relationship between diastereoisomers and enantiomers of the amino acid Threonin*e*. Pairs of isomers with identical substituents on the same side of the chiral centres hold the prefix *threo*, while isomers with substituents opposing each other are *erythro*-compounds. The latter is called *meso*, if the isomers coincide as *e. g*. for (2S,3R)- and (2R,3S)-tartaric acid. *Erythro*-Threonine is usually substituted by *allo*-Threonine. Two pairs of the 4 Threonine isomers exhibit mirror symmetry with each other, while all other pairs are not enantiomers.

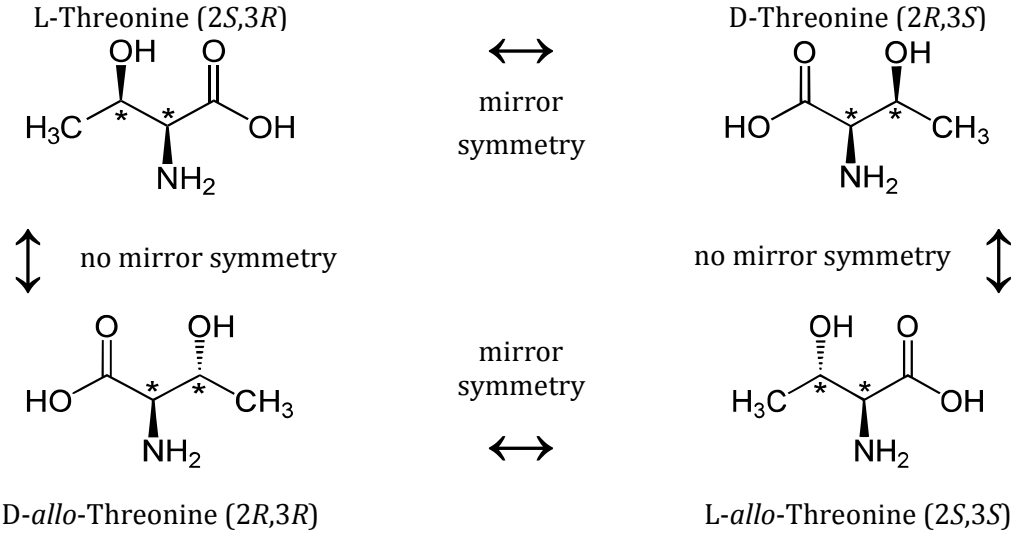

Figure 2.1 *Fischer projections of the 4 stereoisomers of Threonine. Chiral centres are denoted by asterisks. Symmetric and non-symmetric relations of the isomers are indicated by arrows.*

Basically three classifications for enantiomers are equally often found in the scientific literature. The enantiomer, which turns the plane of a beam of polarised light in positive direction upon passing through a sample containing this enantiomer, is denoted *(+)* and the antipode *(-)*. The classical projection method by Fischer allows a classification according to L- (lat. laevus "left") and D- (lat. dexter "right") enantiomers [3]. The letters are frequently set to small caps. Finally, the IUPAC recommends the use of *CIP conventions* (by Cahn, Ingold and Prelog [4, 5]), which classifies the enantiomers by the letters *(R)*- for "right" (lat. rectus) and *(S)*- for "left" (lat. sinister) respectively, according to the direction of chemical groups of increasing priority at the chiral centres. The latter classification will be used throughout this thesis.

Equimolar mixtures of two enantiomers are called a *racemate* or a *racemic mixture* of enantiomers. The expression must not be mixed up with *racemic compounds*, as will be explained in the following. The term most frequently used for a separation of a racemate is *resolution*. In case of incomplete separations the term *partially resolved racemate* is used.

2.1.2 Production of single enantiomers

The number of sold molecules with one or more chiral centres is huge and continuously rising [6-8]. A survey from 2004 lists 9 out of the top 10 selling drugs to contain chiral active ingredients [9]. In 2008 it was 8 and in 2009 still 7 entries in the list were chiral [10]. The majority of the chiral drugs within the 80 top-selling drugs in 2008 contained at least one single chiral centre. The existence of chirality does not necessarily imply enantiopure products, but the American Food and Drug Administration (FDA) arrogated in 1992 with large success the so-called 'chiral switch', the development of new drugs composed of single enantiomers, or alternatively, the proof of harmlessness of the antagonist, which can become elaborate [11]. Already Pasteur followed correctly, that biological systems exhibit a distinct ability to discriminate between two forms of the same substance. Different scenarios are known, that motivate the production of single enantiomers:

- both enantiomers are effective, but one enantiomer diminishes the pharmaceutical effect of the other (Esomeprazol , Nexium®, list entry n°2);
- while one enantiomer exhibits a desired physiological effect, the antagonist acts toxic (Thalidomide, Contergan®);
- while one enantiomer exhibits a desired physiological effect, the antagonist is ineffective (Bicalutamide, Casodex®).

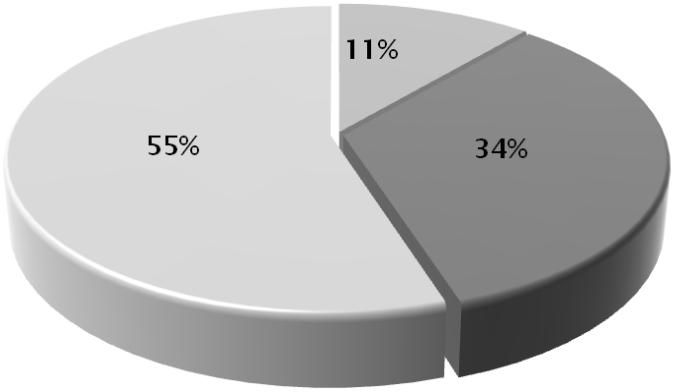

Figure 2.2 *Fraction of chiral (55%) and non-chiral drugs (34%) in 2008 (11% are macromolecules and entries of unknown chirality').*

Single enantiomers are nowadays of particular importance in the production of pharmaceuticals, agrochemicals and also cosmetics [12]. The relevance of single enantiomers in the pharmaceutical industry was recently summarised by Francotte *et al.* [13]. Numerous approaches are known for the production of single enantiomers (Figure 2.3). The most elegant way to enantiopure substances is the asymmetric synthesis. The key developments within this field of research (Noble price in chemistry W. S. Knowles, R. Noyori and K. B. Sharpless in 2001 [1]) utilise specialised catalysts. However, it is unlikely that generic approaches will be available soon, that will allow for the direct synthesis of single enantiomers for every compound. This is partly due to the manifold and diverse nature of pharmaceutical compounds. Secondly, already available asymmetric synthesis are often not competitive and symmetric classical synthesis outperform these, provided that subsequent efficient physical separation methods are available.

Another option, which is often considered, starts at the so-called 'chiral pool'. The phrase comprises cheap fragments or 'building blocks' of molecules, that show already the desired chirality. These molecules are used as initial compounds for further synthesis steps. The hope is here, that the present and wanted isomerism is preserved throughout upcoming synthesis steps.

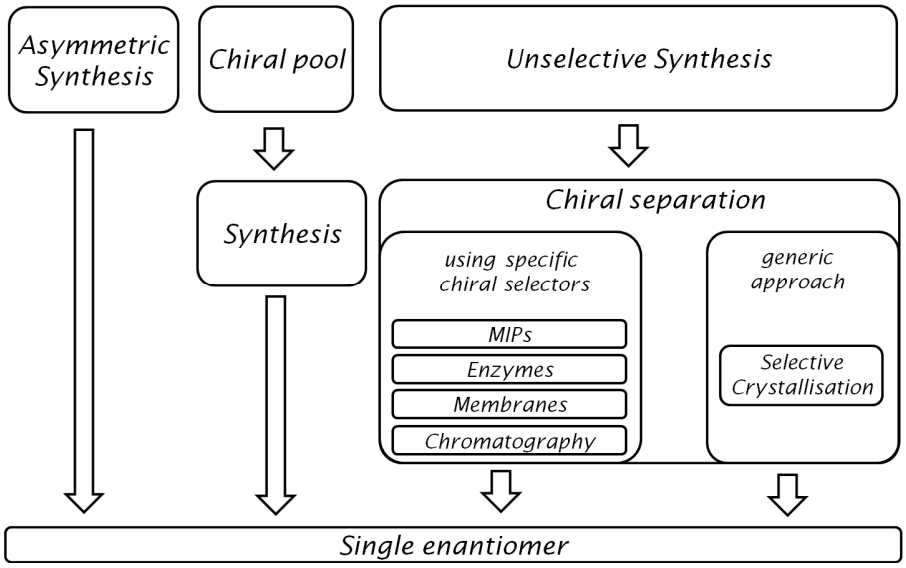

Figure 2.3 *Some sources of single enantiomers*

Finally, there is a large field of classical synthesis, where either racemic or slightly asymmetric mixtures of the desired compounds are produced. This approach entails the subsequent separation of mixtures by specific separation methods. The latter can be dived into a group of methods, where specific chiral selectors are used (often in immobilised form) and into the group of crystallisation-based methods, where the crystals itself exhibits the required chiral-specificity. The demand for the chiral selectivity originates from the physical properties of a pair of enantiomers, which are identical. Thus, the choice for separation methods is often limited for a specific compound. Several techniques have proven to allow the separation of mixtures. Besides the most frequently applied techniques of chiral chromatography and diastereomeric salt resolution, other methods as enzyme catalysed reactions, molecular imprinted polymers (MIP), chiral membranes and specific crystallisation techniques as Ostwald grinding and preferential crystallisation [14, 15] are studied more intensively. However, the applicability of Ostwald grinding remains limited to the minority of chiral systems, the so-called 'conglomerate-forming systems', and the determination of kinetic and thermodynamic data required to setup effective preferential crystallisation processes is rather demanding. Further, generalisation is possible within limits only and more generic tools appear to be largely missing.

2.2 Characteristic phase equilibria of chiral systems

2.2.1 System classification according to solid phases

Crystalline racemates

It is convenient to assign racemates according to the crystal lattice formed to one of three main groups. The crystalline racemate can form a mechanical mixture of crystals of the two pure

enantiomers next to each other. Such *conglomerates* are estimated to be present in the case of less than 10 % of all known systems of enantiomers [16]. A characteristic property of conglomerates is the lower melting point compared to the pure enantiomer. For achiral systems, like diastereoisomers and others it is very common to crystallise as conglomerates. A prominent example from everyday life in the winter season is the system water/NaCl. Already small quantities of salt lower the melting point in the mixture and prevent recrystallisation to a certain extend.

The majority of racemates crystallises as *racemic compounds* in which both enantiomers are situated in crystals of well ordered arrangements. The homogenous solid phase features largely different properties compared to crystals of the pure enantiomer. E*. g.* the heats and temperatures of fusion of racemates and therefore their solubility can deviate largely from the single enantiomer, depending on the stability of the racemic compound.

Less than 1 % of chiral racemates is known to form the third type of crystals, the so called *pseudoracemates* or *solid solutions* [16]. Within these crystals both enantiomers are coexisting in an unordered manner; the term *solid solutions* comprises also mixtures of non-equimolar proportion of the enantiomers. Hereby changes in thermodynamic properties can be positive, negative and negligible compared to the single enantiomer.

Polymorphs and solvates

"…every compound has different polymorphic forms and that, in general, the number of forms known for a given compound is proportional to the time and money spent in research on the compound", is an often cited phrase originally provocatively written by Walter McCrone in 1965 [17]. He defined *polymorphism* as the ability of a substance to exist as two or more crystalline phases, that have different arrangements and/or conformations of the molecules in the crystal lattice [18]. The probably most widely known example of polymorphism is the element carbon, which can exist in the form of graphite (hexagonal), diamond (cubic) or as fullerenes (C_{60} and C_{70}). The identification and description of modifications in the solid phase can be rather demanding. A previously uncovered conformational isomer of the active pharmaceutical ingredient (API) *Ritonavir*, which was not therapeutically effective, entered production lines and halted production processes at Abbott Laboratories in 1998 [19]. Pharmaceutical compounds are increasingly well studied with particular focus on polymorphism due to the current patent situation. Many drugs receive regulatory approval for only a single crystal form or polymorph. *Atorvastatin calcium* was the world-best selling medicine in 2009. Consequently more than 70 polymorphic forms and solvates are patented [20]. In addition, API are often chiral and polymorphism can appear separately for the racemic compound and the pure enantiomer.

The formation of *solvates* implies the inclusion of foreign solvent molecules into the crystal lattice. While this phenomenon is certainly solvent dependent and can be controlled more easily, often solvates with water form *hydrates* and hereby the ambient humidity can be sufficient to induce solvate formation to a crystalline sample.

Different polymorphs and solvates exhibit significantly different physicochemical properties, owing to differences in crystal packing or surface. Examples include the heat and temperature of fusion and therefore solubility, dissolution rate and stability [21]. Thus, the formation of additional *metastable* phases can act both, beneficial and adverse to the formulation of a product.

Solid phase stability

A first phase analysis is often made on the basis of *Gibb's phase rule*. For a system involving C components and φ phases, the degree of freedom of the system υ is limited by $\upsilon = C - \varphi + 2$. The assumption of constant pressure for condensed systems leads further to $\upsilon = C - \varphi + 1$ [16]. Under these conditions, a system of C=1 component can possess φ=2 different crystalline phases simultaneously only at a single temperature, since then it is *invariant* with $\upsilon = 0$. The stability of a polymorphic phase is limited to a certain thermodynamic state. Hereby, it is generally discriminated among *Enantiotropic* and *Monotropic* systems. Figure 2.4 considers the temperature influence for two modifications I and II of a molecular crystal at constant pressure, with I being the more stable phase at 0 K. The ordinate represents qualitatively Gibbs energy and Enthalpy, which are related by Eq. (2.1) and coincide for negligible temperatures.

$$G(p,T) = H - T \cdot S \tag{2.1}$$

Enantiotropic systems are characterised by a transition temperature T^t below the melting temperature T_i^f of the higher melting phase. A dimorphic enantiotropic system is split by T^t into a low temperature domain in which phase I exhibits superior thermodynamic stability (lower Gibbs energy) with respect to phase II. Exceeding the temperature threshold T^t and disregarding kinetic limitations, phase II will form and prevail with lower Gibbs energy. It undergoes solid-liquid transformation (melting) and is substituted by the liquid phase through a further rise in temperature. The phase transformations are reflected in the corresponding enthalpies. The change in Gibbs energy at the transition temperature is usually zero, since both solid phases coexist in equilibrium. The thermodynamic properties as the solubilities in any solvent and the vapour pressure of both forms are identical at this temperature. Taking into account that the variation in entropy is positive upon heating, the resulting change in enthalpy ΔH^t according to Eq. (2.1) must be positive also and the solid phase transformation is endothermic [22]. Additionally, the latent energy representing the heat of fusion ΔH_I^f of phase I and ΔH_{II}^f of phase II can be derived from Figure 2.4a.

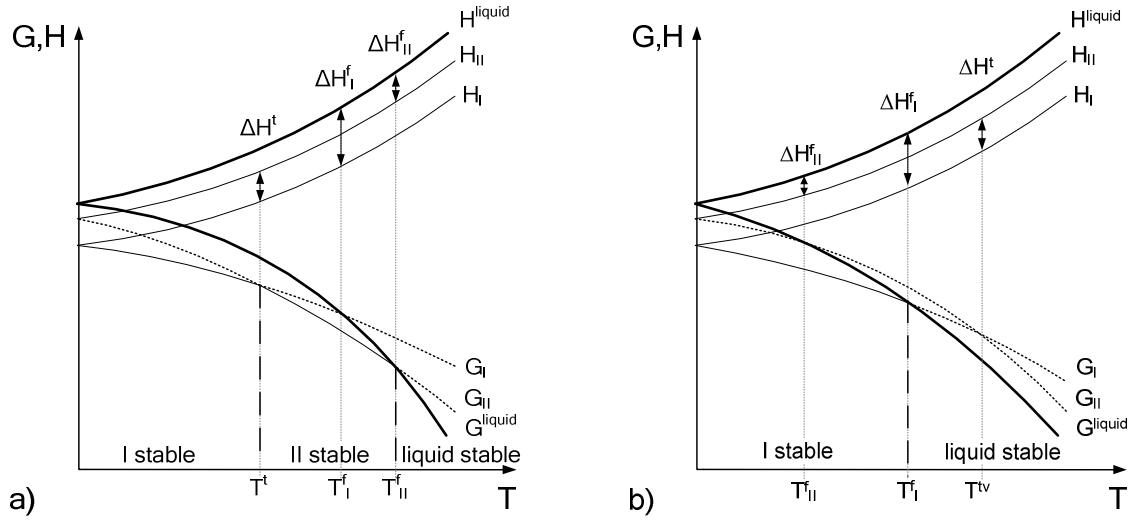

Figure 2.4 *Schematic representation of two dimorphic systems. Within the enantiotropic system in a) phase I is stable below the transition temperature T^t. Phase II becomes the stable phase above this temperature up to the melting temperature of this phase. The dimorphic monotropic system in b) reveals a stable phase I up to the melting temperature of this phase. The Gibbs energy of phase II does not intersect with the Gibbs energy of phase I in the range corresponding to the solid state.*

Monotropic systems do not undergo a solid/solid phase transformation through temperature changes due to thermodynamic reasons. Transformations are virtually possible, but can not pose thermodynamically stable phases (T^{tv}, Figure 2.4b). The fact, that those systems become monotropic systems above a virtual T^{tv}, unfolds the problem of a realistic identification of the type of systems. It is generally possible that a system possesses a T^{t} below measureable melting points, accordingly the phases are enantiotrophically related around this temperature and monotrophically related at ambient temperature [18].
The proper identification of the relation of solid phases and their transformations is crucial for the description of the SLE and for further process design.

2.2.2 Melting point phase diagrams

A measureable thermodynamic property of crystalline compounds is the temperature T^{f}_{i} at which fusion takes place. It can be determined for a large number of compounds directly through calorimetric measurements and provides fundamental information on the underlying SLE of enantiomers.
Roozeboom published a comprehensive work in 1899 aiming to classify binary mixtures on the basis of measureable properties of fusion [23]. Among the multitude of possible SLE, three fundamental types are most prominent for enantiomers (Figure 2.5). The arrangement of the liquidus, solidus and solvus lines determines the phase boundaries and the domains in which different phase equilibria exist.
In the simplest case, only pure crystals of the (R)- and the (S)-enantiomer are found in the solid phase. The increasing slope of the liquidus line towards the centre of the diagram at $T^{f,eu}$ and $x^{eu}_{(S)}$ is defined solely by the properties of the crystals (Figure 2.5a).
The most frequently found binary phase diagram (compare chapter 2.1.2) is governed by the formation of a crystalline racemic compound. The resulting additional liquidus line peaks at the

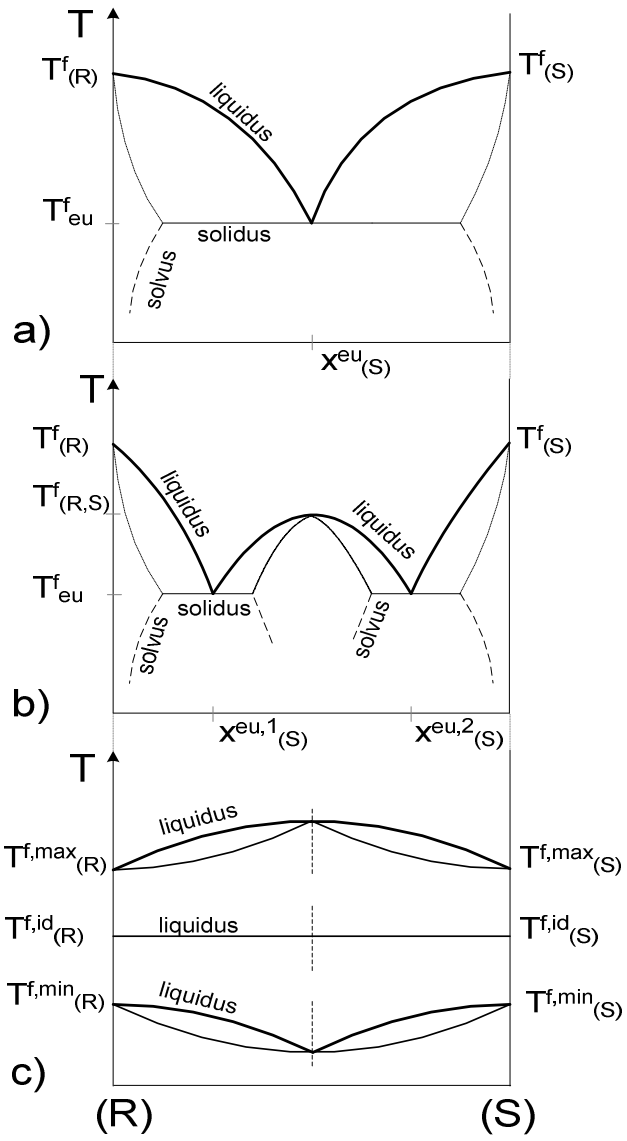

Figure 2.5 *Melting point phase diagrams for a) conglomerate type, b) compound-forming type and c) solid solution type of chiral systems.*

dystectic melting point at $T^{f}_{(R,S)}$ where the (reversible) dissociation of the racemic compound into the two constituent enantiomers takes place (Figure 2.5b). The liquidus line of the racemic compound intersects the liquidus lines of the pure enantiomers twice at $x^{eu,1/2}_{(S)}$ and $T^{f,eu}$. Another important property, that can be derived through the determination of melting point phase diagrams, is denoted by the dashed lines in Figure 2.5a/b. The lines define fractions, for which the above mentioned solid phases do not crystallise in pure form, but exhibit partial miscibility with other molecules. Hereby, limited amounts of the counter enantiomer are incorporated into the crystal lattice of a single enantiomer and/or the crystal lattice of the racemic compound looses its 1:1 restriction and incorporates a single enantiomer in excess. If the solid phase is fully miscible, solid solutions form over the whole range of compositions and the liquidus line yields a straight line as exemplified at $T^{f,id}_{(R)}$ and $T^{f,id}_{(S)}$, respectively, in Figure 2.5c. Phase boundaries can be attributed directly to the solid phases present and for ideal systems also their slope can be derived accurately from the heat and temperature of fusion. In reality, the curvatures of the liquidus and solidus lines are influenced by specific interactions among the constituents in the melt and in the solid phase and their courses can deviate significantly from the courses according to the assumption of ideal solutions. Two additional liquidus lines through $T^{f,\max}_{(R)}$ and $T^{f,\min}_{(R)}$, respectively, are given by Figure 2.5c with possible negative and positive deviations from the ideal case. In practice, a cross-check, whether experimental melting points coincide with ideal liquidus lines, is an appropriate method to evaluate the complexity of a given system [16].

A reliable and accurate experimental method for the determination of melting points and heats of fusion is given by differential scanning calorimetry (DSC) devices. This technique allows to apply temperature profiles to solid samples and to track changes in the differential heat flow *dq/dT* with respect to a reference. Figure 2.6 illustrates typical heat flow profiles obtained from subsequent heating of four solid samples i)-iv) with different ratios of enantiomers.

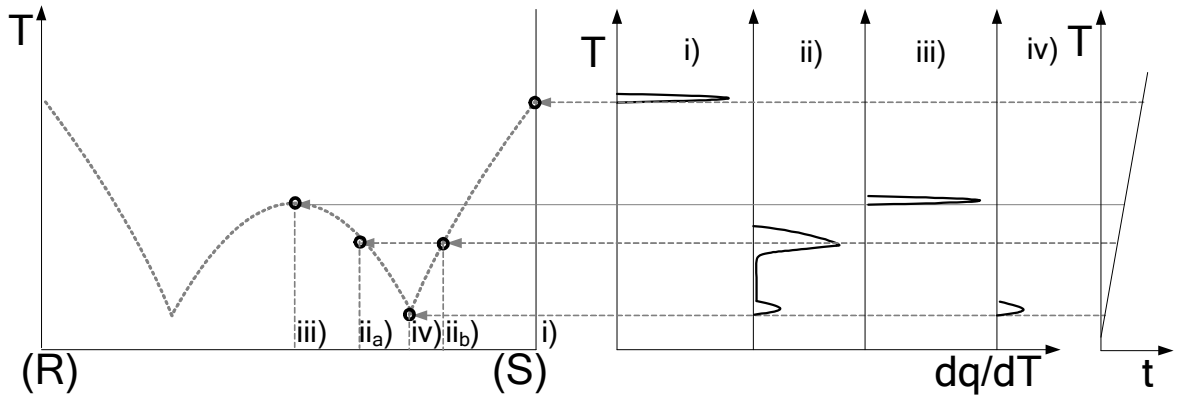

Figure 2.6 *Derivation of liquidus curves from the interpretation of heat flow curves of discrete DSC measurements. Beginning with a sample of the pure (S)-enantiomer (i)) a single sharp melting peak indicating the (high) fusion temperature of the enantiomer is recorded. From initial compositions, where upon melting solution equilibria between a pure component and a mixture are passed through (e. g. ii$_a$),ii$_b$)), a narrow and a broad peak can be measured. These endothermic events can be assigned points on the liquidus line.*

The temperature and shape of the peaks provides information on the (here endothermic) phase transformations, which can be interpreted to estimate the melting point phase diagram. Further the heat of fusion of the pure enantiomer i) and the racemic compound iii) can be obtained as a function of the areas covered by the melting peaks.

General care must be taken in the interpretation of results, since the curves can be ambiguous (Figure 2.6, compositions $ii_{a/b}$)) and it is possible that identical melting point curves originate from completely different solid phases.
A specific advantage of DSC measurements, besides the identification of solid/liquid transformations, is that solid/solid transformations (*i. e.* between polymorphic modifications) can be quantitatively described. Also metastable phases and related transformations can be determined in principle.

2.2.3 Solubility diagrams

The general ability of a chiral substance to dissolve in a solvent is a crucial property not only for most separation processes, but also for the formulation of products and the intake and dosing of pharmaceutically active compounds. It can vary significantly for different solid phase modifications of the same compound as discussed *e. g.* for the case of Ritonavir [19]. Four solubility curves for the same molecule are plotted in Figure 2.7. Metastable phases, denoted *II*, often melt at a lower temperature, which in turn corresponds to higher solubilities. If a racemate forms a racemic compound, its solubility can deviate in positive or negative direction from the solubility of the single enantiomer. In contrast, a racemate will always exhibit higher solubility in conglomerate-forming systems. The situation can become more complex, if the solubility curves of two modifications do not run in parallel as in Figure 2.7 (monotrophically related) but intersect at a certain temperature (enantiotrophically related). Thus, even for ideal solutions the determination and representation of SLE can be a difficult task.

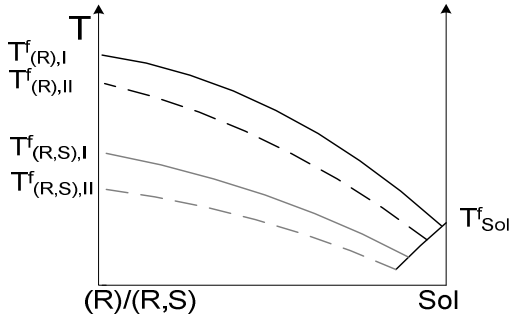

Figure 2.7 *Schematic solubility curves for two modifications I/II of a single enantiomer and two modifications I/II of a racemic compound of an identical substance in the same single solvent*

Realistic solubility

For the description of real systems, interactions in the liquid phase can cause changes in solubility curves and must be taken into account. While both enantiomers (R) and (S) have identical physical properties and therefore solubilities, the simultaneous presence of both enantiomers in solution can alter the solubility curve of a single enantiomer. This can be explained best by a plot of a ternary phase diagram involving a pair of enantiomers and a single solvent. It is convenient to explain at first the derivation of this type of diagram for ideal systems. Therefore the already introduced binary subsystems i) for the (R)-enantiomer and ii) for the (S)-enantiomer in an arbitrary solvent (Sol) as well as the binary phase diagram of the melt of enantiomers iii) are sketched in a linked form in Figure 2.8. The subsystems i) and ii) are in fact identical in the case of enantiomers. The composition of solutions in i) and ii) at three independent temperatures $T_{1\text{-}3}$ can be transferred onto the outer boundaries of the ternary (shaded) phase diagram. The solubility lines of both enantiomers originate here and intersect in the middle of the diagram with the dashed 'eutectic line', which can be derived from the

intersection of the liquidus lines in subsystem iii) [24]. The solubility of a single enantiomer is not influenced by the presence of the other in ideal solutions and thus, the overall solubility increases linearly by addition of the counter enantiomer until its value doubles itself for a racemate in solution. This ideal case is described by the 'double-solubility-rule' formulated by Meyerhoffer [16, 25, 26]. Accordingly, all solubility isotherms appear parallel to the sides of the triangle of the ternary phase diagram.

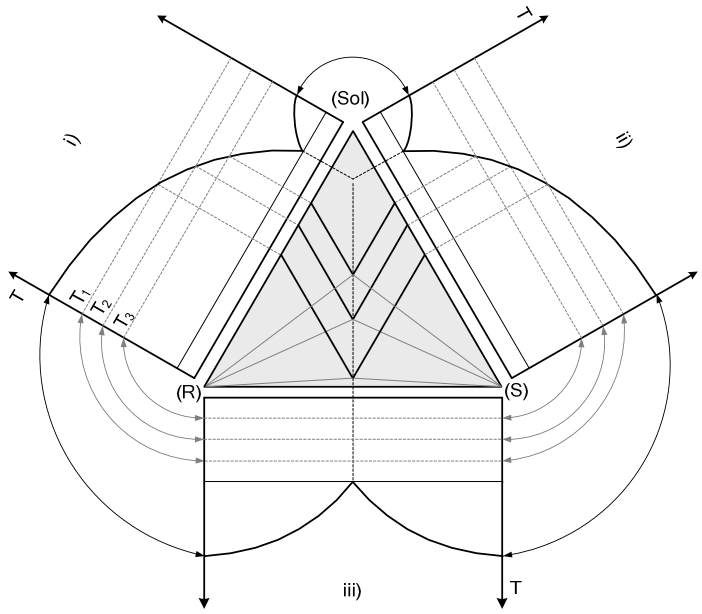

Figure 2.8 *Compilation of a ternary phase diagram of a simple conglomerate-forming system from three binary subsystems. Ideal solubility isotherms are drawn for three temperatures.*

A typical deviation from ideal solubility is exemplified by Figure 2.9. The dashed lines in the subsystems i) and ii) respectively, are altered with respect to the ideal (solid line) solubility. Consequently, the dissolved fraction of an enantiomer at the same temperature T_1 is diminished at the binary solubility curve and the origin of the ternary solubility isotherm at the outer side of the ternary phase diagram is shifted upwards.

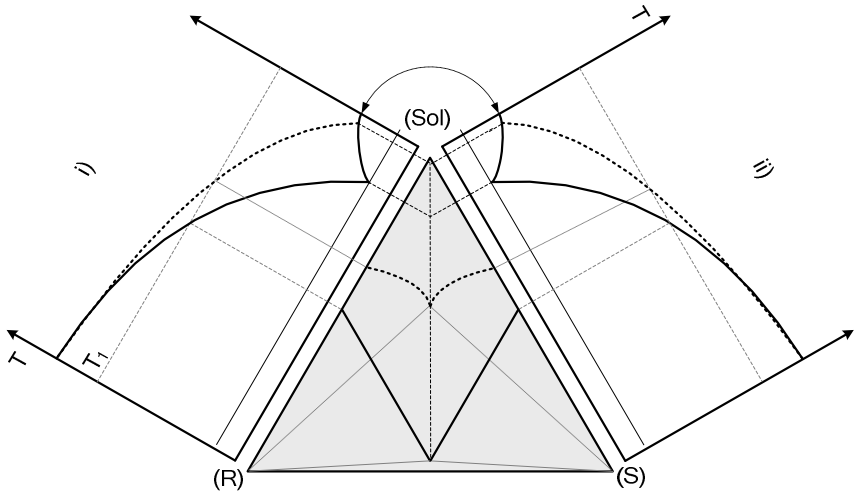

Figure 2.9 *Non-ideal solubilities of the (R)- and the (S)-enantiomer in the corresponding binary subsystems and the impact of non-ideality on ternary solubility isotherms.*

It is worth to emphasise, that the deviation from ideal solution in both subsystems i) and ii) is assumed identical and possible non-ideal heterochiral interactions (compare subsystem iii)) are not considered in this figure. However, ternary solubility isotherms deviate now from a straight line and the 'double solubility rule' fails in this case. Thus, an exact description of ternary solubility isotherms can not be derived directly from the binary subsystems, but requires either experimental determined ternary data or suitable theoretical models with predictive capabilities.

Solubility phase diagrams involving compound formation

Analogously to the conglomerate-forming systems, ternary phase diagram involving compound formation can be derived from binary subsystems. Hereby, the second subsystem ii) for a second enantiomer in solution is substituted by the binary solubility diagram of the racemic compound in solution (Figure 2.10a).

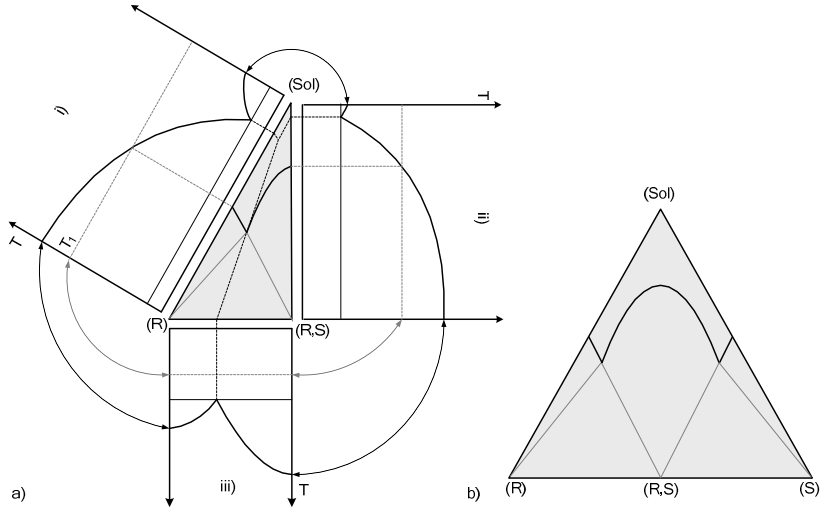

Figure 2.10 *Ternary phase diagram of a compound-forming system and the corresponding binary subsystems.*

The compiled figure yields one half of the mirror-symmetrical ternary phase diagram. The shape of the whole solubility isotherm and four corresponding and important tie lines are given by Figure 2.10b. They separate 6 different mono-, bi- and triphasic domains, whose spatial arrangement is relevant for the design of separation processes.

Solubility phase diagrams involving more than one solvent

The introduced graphical representations of chiral phase equilibria may here appear still slightly peculiar; however, important conclusions with respect to chiral separations can be drawn directly from those figures. If binary mixtures of solvents need to be considered, a graphical modification can be achieved in a way straightforward as given by Figure 2.11. A second solvent or antisolvent (Sol_2) contributes exemplarily to a given SLE. As in all figures above, the fractions of the constituents sum up to unity in the pyramidal quaternary representation a). A variation of this diagram in b) is often simpler to understand. Hereby, the axis representing the second solvent is placed rectangular above the plane of the ternary phase diagram of enantiomers in the first solvent. Its scale can be adjusted independently from the three others. The quaternary phase equilibria considered in this work are illustrated by the type given in Figure 2.11b).

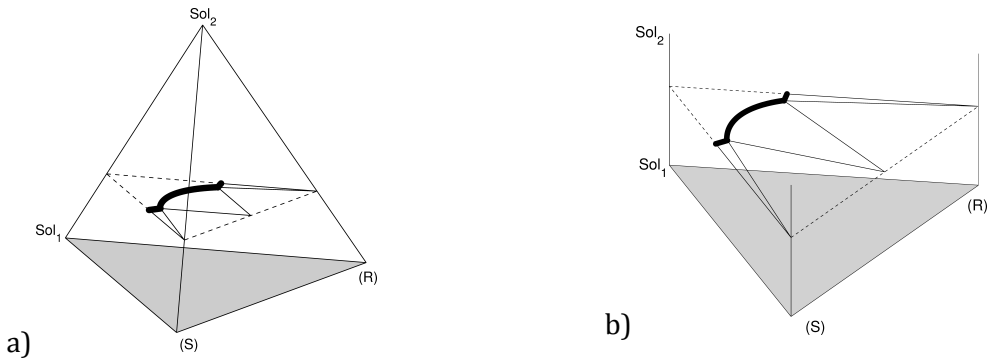

Figure 2.11 *Methods for the graphical representation of quaternary phase equilibria.*

For multicomponent mixtures exceeding four components, it is suitable to keep the ratio of (at least) two constituents constant and place this fixed composition in a 'corner' of one of the diagrams above in order to simplify the graphical interpretation of SLE.
Often, the operating range for a cooling crystallisation spans over a wide temperature range or a second solvent is added in significant amounts for antisolvent crystallisations. Consequently, the experimental determination of a multitude of data points for an adequate description of the relevant SLE can become time-intensive and theoretical models with predictive capabilities are in high demand. A suitable model for the rapid description of ideal SLE and more comprehensive approaches will be explained in the following.

2.3 Thermodynamic description of solid/liquid equilibria

Thermodynamic equilibrium
The description of homogeneous and coexisting heterogenous phases demands for the outmost cases the fulfilment of fundamental criteria of thermodynamic equilibria. Herein, a pure component or a mixture is considered to be enclosed in a system, which has reached its specific minimum in energy. By definition, thermodynamic equilibrium is obtained, if the internal energy, denoted by *U*, can not be lowered upon changes in the natural variables. This applies to a single phase to coexisting phases of the same state of matter and to SLE. The equilibrium state implies equal temperatures T^{χ}, equal pressures p^{χ} and identical chemical potentials μ_i^{χ} of all components *i* in all phases χ .

$$T^{I} = T^{II} = \ldots = T^{\chi} \tag{2.2}$$

$$p^{I} = p^{II} = \ldots = p^{\chi} \tag{2.3}$$

$$\mu_i^{I} = \mu_i^{II} = \ldots = \mu_i^{\chi} \tag{2.4}$$

The binary melt of enantiomers and the SLE of enantiomers in a single solvent or in a solvent mixture are considered as the most relevant phase equilibria involving enantiomers. The following brief descriptions introduce the main types.

Solubility of simple compounds

The mathematical derivation of solubility from fundamental thermodynamics requires introducing several formal quantities. The fugacity[2] f_i describes isothermal changes of every single component *i* at every state of matter. It is related to the chemical potential by Eq. (2.5) using the same reference state, denoted *0,* with respect to temperature. The relation between fugacity and chemical potential is of conceptual aid in performing the translation from thermodynamic to physical (measureable) variables.

$$\Delta\mu_i = \mu_i - \mu_i^0 = RT \cdot \ln \frac{f_i}{f_i^0} \tag{2.5}$$

The term *thermodynamic equilibrium* implies for SLE, that besides identical temperatures, pressures and chemical potentials in all phases, another property, the fugacity of the pure (solid) solute *i* equals the fugacity of the solute in solution [27].

$$f_i^s = f_i^l \tag{2.6}$$

Another representation of the Gibbs energy *G,* besides Eq. (2.1), utilises the internal energy *U*.

$$G(T, p) = U + p \cdot V - T \cdot S \tag{2.7}$$

$$U = T \cdot S - p \cdot V + \sum_i \mu_i n_i \tag{2.8}$$

Consideration of the definition of *U* and combination of Eq. (2.7) and Eq. (2.8) yields Eq. (2.9). It is convenient to related the Gibbs energy to *e. g.* molar quantities and to work with the specific Gibbs energy g_i as will be demonstrated for the thermodynamic cycle in the following. Differences in the Gibbs energy between two thermodynamic states are denoted herein a delta symbol Δ (Eq. (2.10)).

$$G(T, p) = \sum_i \mu_i n_i \tag{2.9}$$

$$\frac{\Delta G_i}{n_i} = \Delta g_i = \Delta\mu_i \tag{2.10}$$

In thermodynamics it is often avoided (or impossible) to derive an absolute value for the reference state μ_i^0. Instead, the reference state is chosen such, that either its quantity drops from the equation or the difference among two states is obtained. Here, the direct description of the solute in solution is substituted by a three step thermodynamic cycle in Figure 2.12. The reference state is defined by the pure, subcooled solid at temperature *T* under its own saturation pressure (a)). The solute is heated from the temperature *T,* that represents ambient or solution temperature level, up to its triple point temperature (b)). The latent heat to effect fusion is added and the solute melts (c)). Afterwards the melt is cooled down again to the solution temperature without a change in the state of matter (d)).

Lewis called the ratio of the actual fugacity and the fugacity of the reference state the *activity*, designated by α [28]. The *activity* defines how 'active' a certain fraction x_i in solution is relative to its standard state. Multiplication of x_i^l by an activity coefficient for the liquid phase

[2] lat.: fugare, fleetness

$\gamma_i^l = \gamma_i^l(T, x_i^l)$ yields α_i. Consequently, the real fugacity of a dissolved component can be related to its standard state by Eq. (2.11). Here, the solubility of the solvent in the solute is assumed negligible.

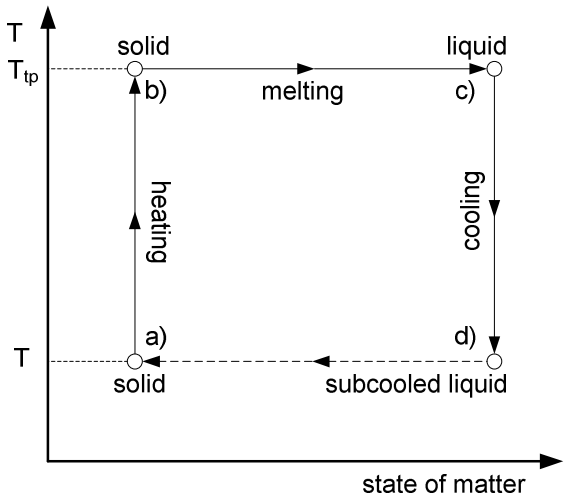

Figure 2.12 *Thermodynamic cycle a)→b) expressing the dissolution of a solute by passing through two states of matter and two temperature domains*.

$$f_i^s = \gamma_i^l x_i^l f_i^{l,0} = \alpha_i f_i^{l,0} \tag{2.11}$$

It becomes visible, that the fugacities depend on the properties of the solute only and are independent on the solvent used.

Combining the Eqs. (2.1), (2.5) and (2.10) allows a quantitative description of the thermodynamic pathway a)→b)→c)→d) within Figure 2.12 through changes in Gibbs energy, which can be expressed by the corresponding measureable variations in enthalpy and entropy according to the Eq. (2.12). The index *i* is omitted in the following for simplicity.

$$\underset{a)\to d)}{\Delta g} = RT \cdot \ln \frac{f^s}{f^{0,l}} = \underset{a)\to d)}{\Delta h} - T \underset{a)\to d)}{\Delta s} \tag{2.12}$$

Changes in enthalpy can be determined from the heat of fusion at the triple point temperature $\Delta h^{f,T_{tp}}$ and the difference in the heat capacities Δc_p between the solid and the liquid state of matter, respectively. In practise, the difference is often constant for a larger temperature range [16]. The change in entropy can be derived analogously, using the heat of fusion at the triple point.

$$\underset{a)\to d)}{\Delta h} = \Delta h^{f,T_{tp}} + \int_{T_{tp}}^{T} \Delta c_p \, dT \tag{2.13}$$

$$\underset{a)\to d)}{\Delta s} = \Delta s^{f,T_{tp}} + \int_{T_{tp}}^{T} \frac{\Delta c_p}{T} \, dT \tag{2.14}$$

$$\Delta s^{f,T_{tp}} = \frac{\Delta h^{f,T_{tp}}}{T^{tp}} \tag{2.15}$$

With reference to Eq. (2.1) and Eq. (2.12), the three terms above can be summarised into Eq. (2.16) and yield an expression for the fugacity and therefore solubility of a solute on the basis of measureable caloric properties, *i. e.* the heat and temperature of fusion.

$$\ln\frac{f^{0,l}}{f^{s}} = \ln\left(\frac{1}{x^{l}\gamma^{l}}\right) = \frac{\Delta h^{f,T_{tp}}}{RT_{tp}}\left(\frac{T_{tp}}{T}-1\right) - \frac{\Delta c_p}{R}\left(\frac{T_{tp}}{T}-1\right) + \frac{\Delta c_p}{R}\ln\frac{T_{tp}}{T} \tag{2.16}$$

Several simplifying assumptions are usually considered. The triple point temperature is often replaced by the melting temperature. The heat of fusion is also taken at this temperature. The first term on the right-hand side is the dominant one and the remaining two terms possess opposite signs and tend to cancel out each other. They drop off completely, if experimental measurements are made close to the triple point, which is possible. Thus, often only the first term is considered. Other assumptions in the derivation of the equation imply constant or negligible effects through pressure changes. Of course, no solid/solid transformations are allowed to occur in the considered temperature range. In its most simple representation, for $\gamma^{l} = 1$, the equation can be written as follows.

$$\ln\left(x^{l}\right) = \frac{\Delta h^{f}}{R}\left(\frac{1}{T^{f}}-\frac{1}{T}\right) \tag{2.17}$$

If applied for SLE estimations Eq. (2.17) is called the equation by 'Schröder and van-Laar', while its general form bears resemblance to the equations by van't Hoff and Clausius-Clapeyron. Those equations relate changes in temperature to changes in the equilibrium constant using the standard enthalpy change or relate the saturation pressure to the saturation temperature using the enthalpy of phase change, respectively. The expressions by Schröder and van-Laar and Clausius-Clapeyron both, manage to link intensive quantities to extensive quantities, which is often in demand in thermodynamic applications. Further, they have in common, that they are entirely based on pure component properties, which simplifies their use, but often implies limitations in accuracy in practical applications.

The Apelblatt equation is one example for an alternative estimation of solubilities by a (semi-) empirical expression [29, 30]. It shares similarities with the (extended) Antoine equation for the description of vapour/liquid equilibria.

$$\ln\left(x^{l}\right) = a + \frac{b}{T} + c\cdot\ln\left(T\right) \tag{2.18}$$

The analogies to Eq. (2.16) are evident; the three terms with caloric values are replaced by free variables, to be found through correlation to experimental data. Since no activities are considered, all deviations from ideal solubility are lumped into the three variables, which hold no physical relevance. Of course, extrapolations of SLE data to other temperatures and concentrations is not admissible, if non-ideal SLE behaviour cannot be excluded.

Solubility of dissociating compounds

As announced in the very first section, most chiral systems form a compound in the solid phase, which dissociates fully upon dissolution. The corresponding balance can be described by a

simple schema as given in Eq. (2.19) and analogously by the chemical potentials of the constituents in Eq. (2.20).

$$(R,S)^s \leftrightarrow (R)^l + (S)^l \qquad (2.19) \qquad \sum_i \mu_i \nu_i = \nu_{(S)}\mu^l_{(S)} + \nu_{(R)}\mu^l_{(R)} - \nu_{(R,S)}\mu^s_{(R,S)} \qquad (2.20)$$

Prigogine and Defay [31] considered the physical dissociation of the solid compound, denoted *(R,S)*, into the enantiomers (R),(S) in the liquid phase as a chemical reaction. The extent of dissociation is represented here by the progress variable ζ and the stoichiometric coefficients ν_i give the amount of consumed or produced molecules relative to their overall amounts n_i.

$$\nu_i = \frac{dn_i}{d\zeta} \qquad (2.21)$$

The total differential of the Gibbs energy depends on the quantities *T*, *p* and n_i.

$$dG = \left(\frac{\partial G}{\partial T}\right)_{p,n} dT + \left(\frac{\partial G}{\partial p}\right)_{T,n} dp + \sum_i \left(\frac{\partial G}{\partial n_i}\right)_{T,p,n_j} dn_i = -SdT + Vdp + \sum_i \mu_i dn_i \qquad (2.22)$$

Analogously, this total differential can be derived by substitution of n_i by the progress variable ζ as in Eq. (2.23).

$$dG = \left(\frac{\partial G}{\partial T}\right)_{p,n} dT + \left(\frac{\partial G}{\partial p}\right)_{T,n} dp + \left(\frac{\partial G}{\partial \zeta}\right)_{T,p,n_j} d\zeta \qquad (2.23)$$

For conditions of constant temperature and pressure, the total differential of the partial derivative of the Gibbs energy with respect to the progress variable can be derived. The expression is numerically identical to the total differential of the so-called affinity *A*, which was originally used for the description of reactions by Prigogine and Defay [31]. It is beneficial to utilise this quantity instead of extensive quantities, whenever a link between a set of stoichiometric chemical reactions and the underlying thermodynamics is needed. Thus, for a single reaction, the affinity *A* is defined as the negative partial derivative of the Gibbs energy with respect to the progress variable ζ at conditions of constant pressure and temperature.

$$\left(\frac{\partial G}{\partial \zeta}\right)_{T,p} = \sum_i \mu_i \nu_i = -\mathrm{A} \qquad (2.24) \qquad \left(\frac{\partial^2 G}{\partial \zeta^2}\right)_{T,p} = \sum_i \nu_i \frac{\partial \mu_i}{\partial \zeta} = -\left(\frac{\partial \mathrm{A}}{\partial \zeta}\right)_{T,p} \qquad (2.25)$$

$$d\left(\frac{\partial G}{\partial \zeta}\right)_{T,p} = -\left(\frac{\partial G}{\partial T}\right)_{p,n} dT + \left(\frac{\partial G}{\partial p}\right)_{T,n} dp + \left(\frac{\partial^2 G}{\partial \zeta^2}\right)_{T,p} d\zeta = d(-\mathrm{A}) \qquad (2.26)$$

The affinity becomes zero in thermodynamic equilibrium and here the chemical potential of the solid racemic compound equals the sum of the chemical potentials of the enantiomers in the liquid phase. The stoichiometric coefficients ν_i for each enantiomer and the racemic compound are usually set to unity, since the racemic compound is considered to consist of equimolar amounts of the two enantiomers. Very few examples, given in the literature, prove that other stoichiometric coefficients can become principally reasonable, too. Tabora *et al.* identified a 1:3

compound of (R)- and (S)-3-hydroxy-4-(2,4,5-trifluorophenyl) butanoic acid and yielded good results with adjusted stoichiometric coefficients [32]. However, specific crystal lattices must exist, that allow besides the formation of a racemic compound at least a second crystal lattice, with another ratio of enantiomers. Such cases were rarely observed.

The fraction of one enantiomer, *e. g.* the (R)-enantiomer, can be chosen as a suitable progress variable $\zeta = x^l_{(R)}$ for the description of dissociation according to Eq. (2.20). Consequently, the second derivative of the Gibbs energy with respect to the quantity $x^l_{(R)}$ provides Eq. (2.27).

$$\left(\frac{\partial^2 G}{\partial\left(x^l_{(R)}\right)^2}\right)_{T,p} = \nu_{(S)}\frac{\partial\mu^l_{(S)}}{\partial x^l_{(R)}} + \nu_{(R)}\frac{\partial\mu^l_{(R)}}{\partial x^l_{(R)}} \tag{2.27}$$

The chemical potential of the stoichiometric compound has dropped off from the summation, leaving two partial derivatives. Now, a Gibbs-Duhem equation for binary systems (Eq. (2.28)) can be used to remove another partial derivative and Eq. (2.29) is obtained. Insertion into Eq. (2.26) and assumption of negligible pressure differences provides Eq. (2.30).

$$x^l_{(s)}\frac{\partial\mu^l_{(S)}}{\partial x^l_{(R)}} + x^l_{(R)}\frac{\partial\mu^l_{(R)}}{\partial x^l_{(R)}} = 0 \tag{2.28}$$

$$\left(\frac{\partial^2 G}{\partial\left(x^l_{(R)}\right)^2}\right)_{T,p} = -\nu_{(S)}\left(\frac{x^l_{(R)}}{x^l_{(S)}} - \frac{\nu_{(R)}}{\nu_{(S)}}\right)\frac{\partial\mu^l_{(R)}}{\partial x^l_{(R)}} \tag{2.29}$$

$$0 = -\left(\frac{\partial G}{\partial T}\right)_{p,n} dT + \underbrace{\left(\frac{\partial G}{\partial p}\right)_{T,n} dp}_{=0} - \nu_{(S)}\left(\frac{x^l_{(R)}}{x^l_{(S)}} - \frac{\nu_{(R)}}{\nu_{(S)}}\right)\frac{\partial\mu^l_{(R)}}{\partial x^l_{(R)}} dx^l_{(R)} \tag{2.30}$$

The Gibbs-Helmholtz equation as given by Eq. (2.33) relates changes to the G/T ratio to the enthalpy of dissociation h_{diss}. Provided, the latter is only weakly affected by temperature, Eq. (2.32) applies. Rearragement using the quotient rule leads to a term, which can be used in conjuction with Eq. (2.30). The term for the change in Gibbs energy ΔG equals zero, since thermodynamic equilibrium is given und the compound dissociation is reversible.

$$\left(\frac{\partial\left(\frac{G}{T}\right)_p}{\partial T}\right)_p = -\frac{h_{diss}}{T^2} \tag{2.31}$$

$$\left(\frac{\partial\left(\frac{\Delta G}{T}\right)_p}{\partial T}\right)_p = -\frac{\Delta h_{diss}}{T^2} = \frac{T\left(\frac{\partial\Delta G}{\partial T}\right)_p - \Delta G}{T^2} \tag{2.32}$$

Thus, Eq. (2.30) can be rewritten as Eq. (2.33).

$$\left(\frac{dT}{dx^l_{(R)}}\right)_p = -\frac{T}{\Delta h_{diss}}\nu_{(S)}\left(\frac{x^l_{(R)}}{x^l_{(S)}} - \frac{\nu_{(R)}}{\nu_{(S)}}\right)\frac{\partial\mu^l_{(R)}}{\partial x^l_{(R)}} \tag{2.33}$$

For identical ratios of the constituents (R),(S) and identical stoichiometric coefficients, the term in brackets on the right-hand side becomes zero and thus, the differential expression on the left-hand side equals zero, too. The composition shows an extremum (only maxima are physically possible) in solubility. This complies with the melting point maxima of racemic compounds (dystectic type) as introduced in section 0. If more than one stoichiometric compound exists, several local extrema may be present. The equation allows estimating the whole shape of the

liquidus curve for a pair of enantiomers in the melt, if a correlation for the differential change in the chemical potential with respect to the composition is available. Reformulation of Eqs. (2.11) and (2.15) provides the general form of the chemical potential in Eq. (2.34).

$$\mu^{l}_{(R)} = \mu^{l,0}_{(R)}(T, p) + RT \cdot \ln(x^{l}_{(R)}) + RT \cdot \ln(\gamma^{l}_{(R)}) \tag{2.34}$$

Provided, the third term on the right-hand side is negligible (*e. g.* ideal melt), the following expression of the partial derivative with respect to the composition can be applied (Eq. (2.35)) and Eq. (2.36) follows.

$$\frac{\partial \mu^{l}_{(R)}}{\partial x^{l}_{(R)}} = \frac{RT}{x^{l}_{(R)}} \tag{2.35}$$

$$\frac{\Delta h_{diss}}{RT^2} dT = \left(\frac{v_{(R)}}{x^{l}_{(R)}} - \frac{v_{(S)}}{1 - x^{l}_{(R)}} \right) dx^{l}_{(R)} \tag{2.36}$$

The deviation of the actual heat of dissociation h_{diss} from its ideal quantity is formally related to the activity coefficients of the constituents according to Eq. (2.37). Substitution of the heat of dissociation by the heat of fusion of the stoichiometric compound $\Delta h^{f}_{(R,S)}$, though common practice in numerous publications, is formally correct only at constant temperature or for negligible deviations of the activity coefficients from unity of the enantiomer in the melt. In summary, pronounced differences between h_{diss} and $\Delta h^{f}_{(R,S)}$ should only be present *i)* for explicitly non-ideal systems and *ii)* far away from the melting point of the compound at relative low solution temperatures.

$$\Delta h_{diss} = \Delta h^{id}_{diss} - RT \sum_i v_i \left(\frac{\partial \ln \gamma_i}{\partial T} \right)_{p,\zeta} \tag{2.37}$$

By assumption of an ideal ($\gamma^{l}_{(R)} = 1$) binary system ($x^{l}_{(S)} = 1 - x^{l}_{(R)}$), the simplified Eq. (2.36) is obtained. The lower integration limits are the composition of the stoichiometric compound (for a racemic compound applies $x^{s}_{(R,S)} = 0.5$) and its melting point $T^{f}_{(R,S)}$. The upper limits are the composition and temperature of interest. The formation of a racemic compound implies $v_{(R)} = v_{(S)} = 1$.

$$-\frac{\Delta h^{f}_{(R,S)}}{R} \left(\frac{1}{T} - \frac{1}{T^{f}_{(R,S)}} \right) = \left[v_{(R)} \ln(x^{l}) + v_{(S)} \ln(1 - x^{l}) \right] \Big|_{x^{s}_{(R,S)}}^{x^{l}} = \ln(x^{l})(1 - x^{l}) - \ln(0.25) \tag{2.38}$$

$$\frac{\Delta h^{f}_{(R,S)}}{R} \left(\frac{1}{T^{f}_{(R,S)}} - \frac{1}{T} \right) = \ln 4 (x^{l})(1 - x^{l}) \tag{2.39}$$

The obtained simplified expression of Eq. (2.39) is frequently cited in the literature and yields good results for a number of systems [16, 31, 33, 34]. Other systems with pronounced non-ideal behaviour, *i. e.* with dominating repulsive or cohesive forces in the mixture, are expected to deviate from the predicted curves of Eq. (2.39). The formation of hydrogen bonds between (R)- and (S)-enantiomers strengthens cohesive forces and lessens the repulsive forces between homochiral molecules. Consequently, activity coefficients of Eq. (2.34) become smaller than unity. The resulting lowered melting temperature is comparable to a lowered partial vapour

pressure of a mixture of molecules and is denoted accordingly a negative deviation from Raoult's law, which is known from the description of VLE. On the contrary, minor chances in the melting temperature close to the racemic compound account for a positive deviation from Raoult's law [31]. Figure 2.13 exemplifies two deviating liquidus lines and their intersection with the liquidus lines of the single enantiomers (Eq. (2.17)). Further, the corresponding changes in the eutectic compositions $X^{eu,pos}$ and $X^{eu,neg}$ and in the temperatures T^{pos} and T^{neg} are given.

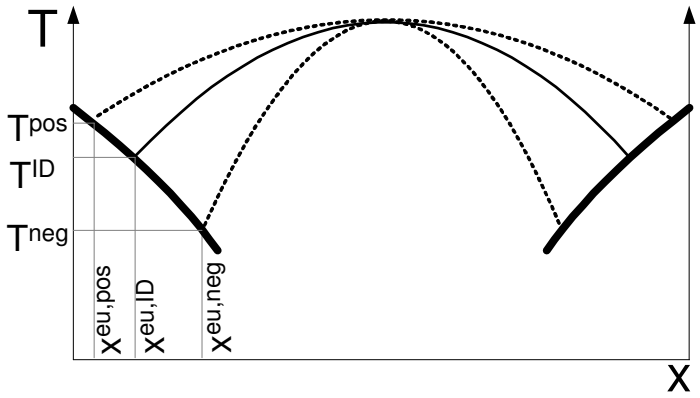

Figure 2.13 *Liquidus curves of a compound-forming system representing ideal behaviour (ID), negative (neg) and positive deviations (pos) from Raoult's law [31]. The bold lines denote liquidus lines according to Eq. (2.12) by Schröder and van-Laar. The compositions $x^{eu,i}$ indicate different eutectic compositions due to the deviation from ideality.*

2.3.1 Estimating the eutectic composition

While the eutectic composition of a conglomerate-forming system of enantiomers is set fixed to the mirror axis of a binary phase diagram, the eutectic compositions of compound-forming systems varies as a substance specific property. It is determined by the intersection of the two branches of the liquidus curves of the single enantiomer and the dissociating stoichiometric compound (Figure 2.13). Its composition holds a large importance in crystallisation-based chiral separations, as will be shown in section 2.4.1.2. For this reason, it is worth investigating this specific composition in more detail.

Considering a model compound, which is physically stable upon melting, the heat and temperature of fusion needed to apply Eqs. (2.17) and (2.39) can be obtained. Further, the solubility isotherms for the single enantiomer and the stoichiometric compound and therefore the eutectic compositions in the ideal melt can be derived. In principle, it is not required to plot the whole phase diagram in order to derive the eutectic composition in solution. Wang *et al.* [35] and Klussmann *et al.* [36] presented two shortcut methods, which can be transferred one in another. Hereby, the ratio α_r of the solubilities of the stoichiometric compound $x^l_{(R,S)}$ and the single enantiomer $x^l_{(R)}$ is used to express the eutectic composition x^{eu} in solution. It is assumed that $x^l_{(R,S)}$ equals the sum of the solubilities of the enantiomers at the stoichiometric composition of the compound.

$$\alpha_r = \left(\frac{x^l_{(R,S)}}{x^l_{(R)}} \right) \qquad (2.40)$$

$$x^{eu} = \frac{1}{1 + \frac{(\alpha_r)^2}{4}} \qquad (2.41)$$

The limiting case of $\alpha_r = 2$ yields $x^{eu} = 0.5$ and matches ideal conglomerates. Klussmann *et al.* listed a number of compounds for which the ratio of solubilities resulted in fair agreement with respect to measured eutectic compositions. Hereby, variations in the ratio of a single compound were obtained from different solvents and at different temperatures. Thus, a first estimation of the eutectic composition in solution, without recourse to solubility measurements can be made on the basis of the Eqs. (2.17) and (2.39). For a racemic compound the molar fraction of one enantiomer equals the fraction of the other in solution and the solubility of the compound can be expressed by Eq. (2.42). By integration of this expression and introducing Eq. (2.17) into Eq. (2.41), the eutectic composition of ideal systems can be predicted avoiding any measurements in solution.

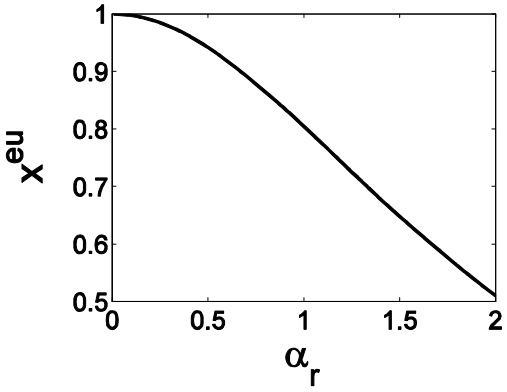

Figure 2.14 *Eutectic composition in relation to the solubility ratio of the racemic compound and the single enantiomer for ideal systems.*

$$x_{(R)}^{l} = \sqrt{0.25 \cdot \exp\left[\frac{\Delta h_{(R,S)}^{f}}{R}\left(\frac{1}{T_{(R,S)}^{f}} - \frac{1}{T}\right)\right]} \tag{2.42}$$

$$x^{eu} = \frac{1}{1 + \frac{\left(\frac{2 \cdot \sqrt{0.25 \cdot \exp\left[\frac{\Delta h_{(R,S)}^{f}}{R}\left(\frac{1}{T_{(R,S)}^{f}} - \frac{1}{T}\right)\right]}}{\exp\left[\frac{\Delta h_{(R)}^{f}}{R}\left(\frac{1}{T_{(R)}^{f}} - \frac{1}{T}\right)\right]}\right)^{2}}{4}} \tag{2.43}$$

In using Eq. (2.41), it must be kept in mind, that the simple formula is restricted to ideal solubilities. Very non-ideal solubility ratios far above two have been observed. The system of Propranolol·HCl/water is such an example [37].

2.3.2 Theoretical approaches to non-ideal SLE

Although used throughout the last chapter, the terms *ideal* and *non-ideal* have not been defined up to know. The official definition is given here to make good for. A component is denoted ideal according to the *International Union of Pure and Applied Chemistry* (IUPAC) if its activity equals its molar fraction in a mixture. If this applies for all constituents, the composition is called *ideal mixture* or *ideal solution* [38]. It is thermodynamically equivalent to a solution, for which the *enthalpy of mixing* $\Delta h_{solution}^{mix}$ is zero. An analogy becomes evident by comparison of the differential form of Eq. (2.17) and an expression for solubility using the *van'T Hoff enthalpy of solution* $\Delta h_{solution}^{vH}$ [39]. It can be accounted for non-idealities in solution either on the left-hand or on the right-hand side of the expressions. The equations coincide, if the activity coefficients become unity.

$$\frac{d\ln(\gamma^l x^l)}{dT} = \frac{\Delta h^f}{RT^2} \quad (2.44) \qquad \frac{d\ln(x^l)}{dT} = \frac{\Delta h^{vH}_{solution}}{RT^2} \quad (2.45)$$

$$\Delta h^{mix}_{solution} = RT \cdot \ln(\gamma^l) \quad (2.46) \qquad \Delta h^{vH}_{solution} = (\Delta h^f + \Delta h^{mix}_{solution}) \frac{\partial \ln(x^l)}{\partial \ln(\gamma^l x^l)} \quad (2.47)$$

In general, it is more convenient to work with Eq. (2.44) since expressions of partial derivatives are readily available for a number of activity coefficient models as will be shown in the next paragraph.

A large enthalpy of mixing indicates a solution far from being ideal. Pronounced intermolecular forces are usually considered to be the reason for non-ideal solutions. The forces can be assigned to four main groups of increasing order of strength:

- van der Waals (dispersive) forces,
- forces due to dipole-dipole interactions,
- forces due to hydrogen bond formation and
- ionic forces.

Thermodynamic models account either separately for each physical force or the contributions by all forces are merged into lumped parameters.

In thermodynamic terms, deviations from ideality are usually captured by introducing excess functions. The excess Gibbs energy is defined by

$$G^E \equiv G_{(actual\ solution\ at\ T,p,x)} - G_{(ideal\ solution\ at\ T,p,x)}. \quad (2.48)$$

The partial derivatives of extensive excess functions are analogous to those of the total excess functions. Thus, the activity coefficient of an arbitrary constituent in a mixture can be assigned to the partial derivative of the excess Gibbs energy (compare Eqs. (2.21) and (2.24)).

$$\left(\frac{\partial G^E}{\partial n_i}\right)_{T,p,n_j} = g_i^E = \mu_i - \mu_i^{id} \quad (2.49)$$

$$\mu_i - \mu_i^{id} = \mu_i^{l,0}(T,p) + RT \cdot \ln(x_i^l) + RT \cdot \ln(\gamma_i^l) - [\mu_i^{l,0}(T,p) + RT \cdot \ln(x_i^l)] \quad (2.50)$$

Figure 2.15 attempts to outline briefly the virtually vast field of models and expressions available for describing the excess Gibbs energy of solutions. More comprehensive reviews on these and other SLE models can be found by [27, 40-46].

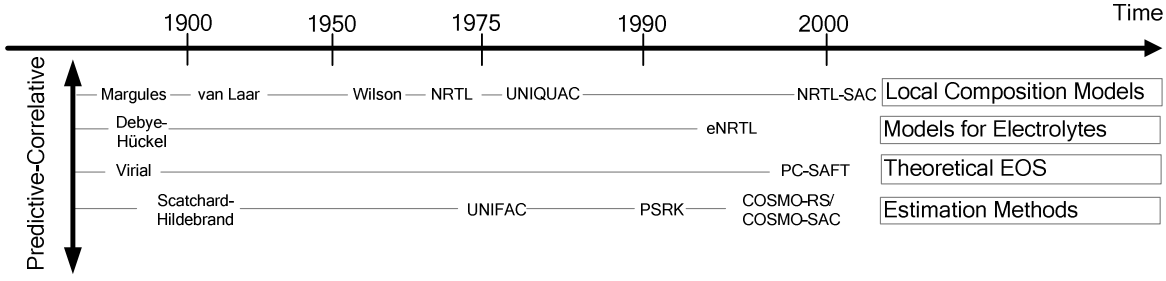

Figure 2.15 *Overview of one century of the development of models for the application in process developments* [41].

2.3.2.1 Local composition models

The first group of so called *local composition models* is named after local compositions that are used in the description of deviation from ideality. The simplest model by *Margules* is based on a single empirical constant A_{ij} for a binary mixture, which is neither temperature nor composition dependent. It represents the behaviour of mixtures of molecules, similar in size, shape and chemical nature in a good manner [27]. A series expansion of the equation by Margules is known as the *Redlich-Kistler expansion* and allows modelling of larger complexity in solution. The expansion of the same equation through a power series by *Wohl* added for the first time a rough physical significance to the formulation. The first parameter in Wohl's equation is related to the effective volumes q_i of molecules in the mixture and the parameter a_{ij} attempts to characterise intermolecular interactions. Truncation of the power series after the first term yields the often cited equation by *van Laar*. Depending on the kind of solution the physical significance of the two parameters can turn (again) into purely empirical for polar systems. The concept of models like the *Wilson* model, the *non-random two liquid (NRTL)* model and the *universal quasi-chemical (UNIQUAC)* model rests on the *theory of corresponding states* [27, 47]. The key idea is to express the configurational properties of two different fluids in reduced form, such that they coincide on a generalised plot using non-dimensional coordinates. It is asserted that the properties of any mixture of two liquids are situated on a common function within the same plot. According to the theory, a hypothetical pure fluid exits with the same configurational properties as those in the mixture, at the same temperature and pressure. The achievement of thermodynamic models is essentially to relate the pairwise interactions within the hypothetical fluid to known pairwise interactions and the composition. One option is to use reduced variables. In the case of a pure fluid, the reducing parameters are constants, which characterise molecular size and intermolecular forces in the pure fluid. For a mixture the reducing parameters are composition-dependent because they characterise average molecular size and average intermolecular forces in the mixture. The approach is not limited to a single hypothetical fluid, the non-random two liquid model and the UNIQUAC model are prominent examples. However, theories based on several fluids come along with a significantly higher mathematical complexity and the increased model flexibility does not guarantee automatically a better representation of experimental data.

While the general concept of local compositions is the same, the model by Wilson *et al.* [48], the non-random two liquid model by Renon *et al.* [49] and the UNIQUAC model [27] can be discriminated according to the thermodynamic assumptions applied in their derivations.
Flory and Huggins set the molecular size to be decisive for a solution of molecules, which are chemically similar (*athermal solution*). Accordingly, mixtures of molecules of similar liquid volume $v_{j/i}$ are ideal. The same applies for the Wilson model, but here in addition, intermolecular forces come into play. A stronger cohesive force between dissimilar molecules 1→2 compared to the 1→1 case is reflected in a larger interaction parameter $|\lambda_{12}| > |\lambda_{11}|$. This definition is not precise. Care must be taken if pronounced hydrogen bonds exist for the 1→1 case and if the second component is nonpolar. Then, the mixture yields $|\lambda_{12}| < |\lambda_{11}|$ and $|\lambda_{22}| < |\lambda_{11}|$ and the relation of $|\lambda_{12}|$ and $|\lambda_{22}|$ would remain undefined. It is an advantage of the Wilson model, that it can be extended easily to multicomponent mixtures and is not restricted to binary mixtures as *e. g.* Margules. Renon *et al.* introduced a third, the so-called non-random parameter into the NRTL model, which is formally equivalent to the reciprocal of the coordination number

in the *quasi-chemical theory* by Guggenheim [49]. The theory is a simplification to the *lattice theory* suggested by the same inventor. The lattice theory assigns every molecule in a mixture a distinct and discrete position (similar to a lattice) and the energy needed to interchange its place is used as the argument to describe the (excess) enthalpy of mixing. Hereby, the *interchange energy* is a function of the potential energy of all possible molecular pairs in solution. Their numerical values can, in principle, be obtained from potential functions. The lattice theory assumes no preference in the choice of neighbours, *i. e.* a mixture where all possible arrangements of the molecules on the lattice are equally probable. The quasi-chemical theory asserts, that for different pair potentials, segregation of molecular pairs 1→2, 1→1 or 2→2 must occur, invoking an altered order (the nonrandomness) of the solution. The theory is not rigorous, but uses a simplification named the *quasichemical approximation* for the implementation into models [50]. It could be shown that the difference to models for fully randomly distributed molecules becomes large only for very non-ideal mixtures and in areas close to phase separation [27]. In summary, the NRTL model requires two interaction parameters G_{ji} and G_{ij} and a well chosen randomness parameter α_{ij}. Also this model does not take into account differences in the molecular sizes, which renders the model unfavourable for *e. g.* polymer solutions.

The Wilson, the UNIQUAC, the NRTL and many other models split molar excess Gibbs energy (Eq. (2.49)) into contributions by a combinatorial term and a residual term. The first is an entropic term quantifying the deviation from ideal solubility as a result of differences in molecular shape. The latter is an enthalpic correction caused by the change in interacting forces between different molecules upon mixing.

$$g^E \equiv g^{combinatorial} - g^{residual} . \tag{2.51}$$

The UNIQUAC model is a combination of the Wilson equation and Guggenheim's lattice theory. Guggenheim formulated a term for the combinatorial entropy of mixing, which accounts explicitly for the size and shape of molecules. Thus, the UNIQUAC model contains two adjustable energy parameters τ_{ij} / τ_{ji}, again the lattice coordination number z and in addition two substance specific physical parameters, reflecting the normalised molecular size (by r_i) and the normalised molecules surface area q_i of molecules in the mixture. The latter values are defined according to the lattice model as 66.99 Å^3 and 79.53 Å^2, respectively [51, 52]. It was found that experimental data of systems containing water or lower alcohols were better represented for $q_i \neq q_i'$, though, this deviates from the original formulation of $q_i = q_i'$. While substance specific data can be found tabulated for the most solvents, these parameters are usually not available for solutes and need to be estimated by a functional group approach as *e. g.* UNIFAC (s. chapter 2.3.2.4) [53].

Table 2.1: Overview of selected local composition models for the description of activity coefficients

Model	Expressions for		Parameters
	g^E/RT	$\ln(\gamma_i)$	
1-constant Margules	$\frac{A}{RT}\cdot x_i \cdot x_j$ (1)	$\frac{1}{2}\frac{1}{RT}\sum_{i=1}^{c}\sum_{j=1}^{c}(A_{ik}+A_{jk}-A_{ij})x_i x_j$ (2)	$A_{ij}=A_{ji}$ (3) $A_{ii}=0$ (4)
van Laar	$\frac{2a_{ij}x_i x_j q_i q_j}{x_i q_i + x_j q_j}$ (5)	$\frac{A}{\left(1+\frac{A}{B}\frac{x_i}{x_j}\right)^2}$ (6)	$A=2q_i a_{ij}$ (7) $B=2q_j a_{ij}$ (8)
Wilson	$-\sum_{i=1}^{c} x_i \ln\left(\sum_{j=1}^{c} x_j \Lambda_{ij}\right)$ (9)	$1-\ln\left(\sum_{j=1}^{c} x_j \Lambda_{ij}\right)-\sum_{j=1}^{c}\frac{x_j \Lambda_{ji}}{\sum_{k=1}^{c} x_k \Lambda_{jk}}$ (10)	$\Lambda_{ij}=\frac{v_j}{v_i}\exp\left[-\frac{\lambda_{ij}-\lambda_{ii}}{RT}\right]$ (11) $\Lambda_{ji}=\frac{v_i}{v_j}\exp\left[-\frac{\lambda_{ij}-\lambda_{jj}}{RT}\right]$ (12)
NRTL	$\sum_{i=1}^{c} x_i \frac{\sum_{j=1}^{c} x_j G_{ji}\tau_{ji}}{\sum_{j=1}^{c} x_j G_{ji}}$ (13)	$\frac{\sum_{j=1}^{C}\tau_{ji}G_{ji}x_j}{\sum_{j=1}^{c} G_{ji}x_j} + \sum_{j=1}^{c}\frac{x_j G_{ij}}{\sum_{k=1}^{c} x_k G_{kj}}\left(\tau_{ij}-\frac{\sum_{k=1}^{c} x_k \tau_{kj} G_{kj}}{\sum_{k=1}^{c} x_k G_{kj}}\right)$ (14)	$\tau_{ji}=\frac{g_{ji}-g_{ii}}{RT}$ (15) $G_{ij}=\exp(-\alpha_{ij}\tau_{ij})$ (16) $\tau_{ij}=\frac{g_{ij}-g_{ii}}{RT}$ (17) $G_{ji}=\exp(-\alpha_{ij}\tau_{jj})$ (18)
UNIQUAC	$\underbrace{\sum_{i=1}^{m} x_i \ln\left(\frac{\phi_i^*}{x_i}\right)+\frac{z}{2}q_i\sum_{i=1}^{m} q_i x_i \ln\left(\frac{\theta_i}{\phi_i^*}\right)}_{combinatorial}$ (19)	$\underbrace{\ln\left(\frac{\phi_i^*}{x_i}\right)+\frac{z}{2}q_i\ln\left(\frac{\theta_i}{\phi_i^*}\right)+l_i-\frac{\phi_i^*}{x_i}\sum_{j}^{m} x_j l_j}_{combinatorial}$ (20)	$\phi_i^*=\frac{r_i x_i}{\sum_{j=1}^{m} r_j x_j}$ (21) $\theta_i=\frac{q_i x_i}{\sum_{j=1}^{m} q_j x_j}$ (22)
	$\underbrace{-\sum_{i=1}^{m} q_i' x_i \ln\left(\sum_{j}^{m}\theta_j'\tau_{ji}\right)}_{residual}$ (23)	$\underbrace{-q_i'+\ln\left(\sum_{j}^{m}\theta_j'\tau_{ji}\right)+q_i'-q_i'\sum_{j}^{m}\frac{\theta_j'\tau_{ij}}{\sum_{k}^{m}\theta_k'\tau_{kj}}}_{residual}$ (24)	$\theta_i'=\frac{q_i' x_i}{\sum_{j}^{m} q_j' x_j}$ (25) $\tau_{ij}=\exp\left(\frac{\alpha_{ij}}{T}\right)$ (26) $\tau_{ji}=\exp\left(\frac{\alpha_{ji}}{T}\right)$ (27) $l_j=\frac{z}{2}(r_j-q_i)-(r_j-1)$ (28)

A second combinatorial term, which is often used in thermodynamic models, was derived by Flory and Huggins. Chen *et al.* used the term in their formulation of a NRTL model for polymers and split the excess Gibbs energy accordingly into a combinatorial and a residual term [54]. Further development of the approach resulted in the *non-random two liquid segment activity coefficient model* (NRTL-SAC) [55, 56]. The model attempts to map solvent and solute molecules into predefined functional groups based on chemical structure. Hereby, the effective surface interaction of the molecules is described by hydrophobic, polar and hydrophilic segments. The ratio of the three conceptual segments can be characteristic for a certain molecule and is usually derived for a solute from solubility measurements in a test set of solvents with pronounced hydrophobicity, hydrophilicity or polarity. Databases on segment parameters for the most common solvents in the pharmaceutical environment are available [55], the analogue database for solutes is far from being comprehensive. The obtained segment parameters for a solute can allow the prediction of solubilities in mixtures of solvents.

2.3.2.2 Solutions containing electrolytes

Besides neutral molecular species also ionic and charged species can be present in solution and may alter or even dominate the shape of SLE. Debye and Hückel proposed the most relevant theoretical approach for long-range ion-ion interactions in 1924. Chen *et al.* [57] implemented the theory into the *electrolyte NRTL* model (eNRTL). More recently, an estimation model was extended also by a Debye-Hückel term (eCOSMO-SAC) by the same author [58]. The separate treatment of ions and molecular species is more precise in physical terms and allows more accurate predictions, *e. g.* for ionic liquids [59]. Since the effort for model parameterisation is rather high, one is advised to assess the degree and relevance of dissociation of a strong acid (or base) or the fraction of salts in solution before switching to electrolyte models.

2.3.2.3 Theoretical equations of state

Another group of models, whose origin was (initially) entirely theoretical, are the equations of state (EOS). Within the *virial equation* the compressibility factor is given by as a power series and the reciprocal molar volume. The equation constants hold a clear physical significance and link pressure, temperature and molar volume. Since for many liquids the value of $(\partial p/\partial T)_v$ is a function of the molar volume only [46], the expression can represent non-ideal liquids. Furthermore, it can be simply extended to multicomponent mixtures and provides the fugacities and therefore activity coefficients of the constituents of the mixture. Virial coefficients can be derived through regression to experimental data. In addition, the second virial coefficient can be acquired through potential functions like *Hard-Sphere, Lennard-Jones* or many others [27]. The derivation of the third and following coefficients requires sound theoretical assumptions. A rapid development of different EOS for polar compounds, close to and above the critical point of substances and for various other applications of interest was observed in the last century. Recent EOS like the *perturbed chain-statistical associating fluid theory* (PC-SAFT) are not anymore fully theoretical, but have been fitted in parts to reference data and yield excellent agreements for a number of complex systems [60]. The model parameters possess physical significance. The PC-SAFT EOS is parameterised using three parameters (five, in case of associating compounds) and pure component properties, like vapour pressures. Parameters for the most common solvents can be found tabulated. However, prior to the prediction of multicomponent mixture properties, reasonable values for the binary interaction parameter of each binary mixture need to be identified by means of experimental data. The formation of solid stoichiometric compounds can be modelled with such EOS [61, 62].

2.3.2.4 Estimation methods for SLE

The last group of theoretical approaches to SLE to be introduced here comprises *estimation methods*, whose nature is more predictive rather than correlative. The difference in the actual Gibbs energy and the ideal Gibbs energy of a solution is denoted by the Gibbs energy of mixing. The energy term comprises the enthalpy of mixing and the contribution of the entropy of mixing. As described earlier, the first term vanishes for ideal solutions. Solutions, for which the second

term becomes zero at negligible volume change upon mixing are called a *regular solution* according to Hildebrand.

$$\Delta g^{mix} = \Delta h^{mix} - T \cdot \Delta s^{mix} \tag{2.52}$$

Solubility parameters by Hildebrand and Hansen

Hildebrand and Scatchard related independently the internal energy of mixing Δu_v^{mix} to the activity coefficient of a solute in solution [63]. Δu_v^{mix} reflects the energy of complete vaporisation, that is, the energy change upon isothermal vaporisation of a saturated liquid to the ideal-gas state (Eq. (2.55)). The model was developed on the basis of van Laar's theory and the van der Waals EOS. Here, the assumption of a regular solution with $g^E = u^E$ applied. A comprehensive derivation of the model is given by [27, 64]. The key quantity *cohesive energy density* c_{ii} reflects intermolecular forces. The obtained activity coefficients are always larger than unity, since no other forces are considered. Usually, the binary parameter I_{ij} is neglected. Despite its limitations, the model gives still good results for a number of non-polar solutions.

$$RT \cdot \ln \gamma_i = \upsilon_i \phi_j^2 [(\delta_i - \delta_j)^2 + 2 I_{ij} \delta_i \delta_j] \tag{2.53}$$

$$c_{ij} = \sqrt{c_{ii} c_{jj}} \cdot (1 - I_{ij}) \tag{2.54}$$

$$\delta_i = \sqrt{c_{ii}} = \sqrt{\frac{\Delta h_v^{vaporization} - RT}{V_{m,i}}} = \sqrt{\frac{\Delta u_v^{mix}}{V_{m,i}}} \tag{2.55}$$

$$\phi_i = \frac{x_i V_{m,i}}{x_i V_{m,} + x_j V_{m,j}} \tag{2.56}$$

The regular solution equation can be extended to multicomponent mixtures and yields predictions for mixture properties. The required molar liquid volumes and the heat of vaporisation can be obtained from databases for a large number of compounds. Hansen proposed additive extensions to the model to allow predictions for polar and hydrogen bonding systems also. The database of Hansen solubility parameters comprises currently more than 10.000 entities [65].

UNIFAC/PSRK

Similar in kind but different in the method is the *universal functional activity coefficient* (UNIFAC) model. Herein the Guggenheim equation is used to estimate the combinatorial contribution to the excess Gibbs energy. The remaining residual term is derived through specific contributions based on the molecular structure of the molecules in the mixture. The approach exhibits similarities to the NRTL-SAC model, but utilises a much larger set of predefined functional groups. The UNIFAC model attempts to break down the huge number of possible binary interactions into a limited number of interactions among these functional groups, that can still be handled. The simplification entails several deficiencies. The mutual effect of neighbouring groups and the information on the relative position of functional groups (isomerism can not be treated) is lost. Predictions can only be made on the basis of a complete set of functional groups in the database for all constituents of a mixture. This is particularly problematic for molecules in the size of 200-600 g/mol, which are typical *e. g.* in the pharmaceutical industry [57].

The *Predictive Soave-Redlich-Kwong* (PSRK) model was initially developed for the estimation of properties of substances close to and of mixtures partly above their critical state. These properties could not be derived from the UNIFAC model. The PSRK model uses an EOS, such as

the Soave-Redlich-Kwong approach and a suitable mixing rule. Parameters for the mixing rule can be derived through UNIFAC.

Molecular estimation models

A number of models attempt estimating characteristic mixture properties entirely from molecular structures without depending on experimental data or reference to databases. While the view on thermodynamics was macroscopic for the models above, the following considers the microscopic level and focuses on particles at the (sub-) atomic level. Due to the rather different theoretical backgrounds a rapid classification will be given below. Much more comprehensive information is found *e. g.* by [45, 66, 67].

The Schrödinger equation uses the wavefunction to determine the exact locus of any particle (electron, nuclei) between x and x+Δx at a time t. The wavefunction $\psi(r,t)$ is in general a complex valued quantity and a function of the Cartesian position coordinates x,y,z (in the vector r) and time. It links the total energy *E* of a system and the so–called Hamiltonian operator *H*, also referred as Hamiltonian.

$$H\psi(r,t) = E\psi(r,t) \tag{2.57}$$

The Hamiltonian consists of an operator for the kinetic energy and an operator representing the potential energy *U* with $\hbar$ being the reduced Planck constant and *m* being the mass of the particle. Both operators depend on the three Cartesian coordinates.

$$H\psi(r,t) = \left(-\frac{\hbar^2}{8\pi^2 m}\nabla^2 + U(r,t) \right)\psi(r,t) = j\frac{\hbar^2}{2\pi}\frac{\partial\psi(r,t)}{\partial t} \quad \text{with} \tag{2.58}$$

$$\nabla^2 = \left(\frac{\partial^2}{\partial x^2} + \frac{\partial^2}{\partial y^2} + \frac{\partial^2}{\partial z^2} \right) \tag{2.59}$$

The equations (2.58) and (2.59) represent only a single particle (electron, nuclei). It becomes evident, that the complexity of the Schrödinger equation increases largely with the number of electrons of a system and computations for typical molecules in engineering tasks cannot by be treated by far up to now. The major problem lies in the formulation of the wavefunction. The exact formulation is difficult to find, since every particle interacts mutually with the remaining particle ensemble. The Born-Oppenheimer-Approximation decouples the movement of atom cores and electrons and allows the exact solution of the electronic Schrödinger equation for just two particles [68, 69].

For more complex systems *ab initio* methods like the Hartree-Fock-approximation (HF) or, numerically less demanding but less rigorous, semi-empirical methods like MNDO, AM1 or PM3 can be applied [67]. *Ab initio* methods do not require information other than fundamental constants and the charges of relevant atom cores. Semi-empirical methods contain parameters, that are fitted to experimental data. The methods are numerically faster since only valence electrons are considered and their basis sets are restricted to a limited number of functions and hence, the theoretical background for the estimation of molecular orbitals is less profound. The HF-approximation neglects the Coulomb electron correlation leading to a total electron energy, which is always higher than the one obtained from the Schrödinger equation. The density

functional theory (DFT) takes the electron correlation explicitly into account and provides more accurate results [67, 69-71]. Computational methods based on DFT are widely used tools for geometry optimisations and electron density descriptions. Accurate estimations for molecules of 40 and more atoms on standard computers are feasible in a day and less. However, DFT computations yield predominantly results for isolated molecules in vacuum; intermolecular forces do not exist here. The latter are present (and important) in the condensed systems of interest in this work. Since DFT is in addition not suitable to derive accurately dispersive forces, a detour needs to be made to get a hold on quantitative solution behaviour.

Continuum solvation model COSMO

In 1995 a theory quantifying solvent/solute interactions based on quantum chemistry calculations was introduced by Klamt *et al.* [70]. The so-called *COnductor-like Screening MOdel for Real Solvents* (COSMO-RS) consists of two separate parts originating from the disciplines of theoretical physics and statistical thermodynamics. The COSMO part is a *Continuum solvation* model. These models are simplifications to the formal representation of the electrostatic potential energy and can lead directly to macroscopic thermodynamic properties, notably changes in the Gibbs energy of solvation as a consequence of electrostatic interactions and changes in the van der Waals Gibbs energy [66]. Continuum solvation models account for the effects, that are experienced by a molecule, *e. g.* a solute, being transferred from an ideal gas state into a liquid solvent. The solute is presumably surrounded by solvent molecules only, similar to an infinitely diluted solution. The reference state after solvation can be used to derive the chemical potential in solution. Within the concept of continuum approaches the atomic structure of the solvent is neglected and the electrostatic properties are replaced by those of the dielectric continuum. The polarisation of the medium and the back polarisation of the solute, whose geometry is represented by a model specific cavity, is a measure of the electrostatic interaction between the solute and its surroundings. The COSMO model places a molecule into an infinitely extended electrical conductor ($\varepsilon = \infty$) and simplifies hereby the derivation of so-called screening charges. The electric field arising from the nuclei and the electrons of the solute molecule is screened by the polarisation of the continuum. Within the COSMO approach the resulting electrostatic potential is zero for every point on the surface of the cavity in the conductor, because the special conductor screens the charges perfectly and all charges are balanced. The obtained histogram of charges σ, the so-called 'surface charge density distribution', is characteristic for every molecule, or more precisely, for every conformation of a molecule. Thus, in contrast to the UNIFAC model, the specific information is not linked to functional groups but it is extracted from the whole molecule. It could be expected, that a description of solutes by the COSMO model contains a higher degree of information on *e. g.* the

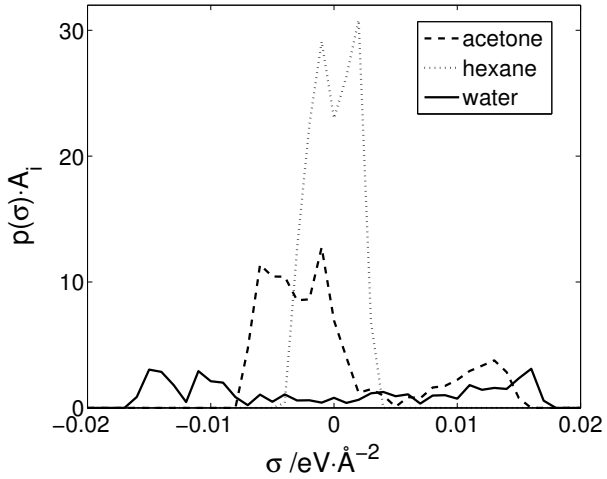

Figure 2.16 *Characteristic charge histograms for some molecules (COSMO-SAC model).*

spatial arrangement of atoms, that can be used further. However, this is apparently not the case, since it is possible to derive identical charge histograms also through group contribution methods as shown by Mu and Gmehling *et al.* [72, 73]. Only compounds containing sulphur resulted in different charge histograms. Thus, it can be possible to avoid the time consuming quantum mechanical computation of charge histograms, provided that all functional groups of a compound of interest can be well represented through group contributions methods. However, information on isomerism are lost also in this model, *i. e.* a pair of enantiomers shows identical charge histograms.

Implementations of COSMO are found in a number of modules of commercial software packages like *Gaussian, MOPAC, TURBOMOLE, DMol3, ADF* and also in the open-source software *GAMESS*. The most comprehensive product *COSMOtherm* is developed and distributed by the *COSMOlogic* GmbH & Co. KG. The charge histograms of every package varies due to slightly different COSMO implementations, specific parameterisations, basis sets and the functionals used. Apparently, the differences are not large [74]. However, a coupling of the algorithm for the statistical thermodynamics with a certain COSMO software is important for consistent model parameterisation using experimental data. The applied algorithm in this thesis was parameterised on the basis of charge histograms generated through the *DMol3* package [75, 76].

COSMO-RS/ COSMO-SAC

Charge histograms can be used to derive activity coefficients of solutes in solutions. The procedure is to the greatest extend the same in the COSMO-'Real-Solvent' and in the later re-implementation, the COSMO-'Segment Activity Coefficient' model.

According to implicit continuum solvation theories, the solvation Gibbs energy ΔG^{sol} of transferring a molecule stepwise from an ideal gas state through a state in an ideal conductor to a solvated state can be written as the sum of the contributions of the long-range electrostatic Gibbs energy ΔG^{el} and the van der Waals Gibbs energy ΔG^{vdw}. The latter can be expressed through the cavity formation Gibbs energy ΔG^{cav}, which is needed to create a cavity in a liquid upon insertion of a solute molecule and the short-range dispersion Gibbs energy ΔG^{disp}, which results from the interactions between the actual charges on the molecular surface. Other terms for the Gibbs energies of vibration, rotation and the internal structure of the molecule are considered to be negligible, since their change resulting from the transfer of the molecule from vacuum into a real solvent is small [77].

$$\Delta G^{sol} = \Delta G^{el} + \underbrace{\Delta G^{cav} + \Delta G^{disp}}_{\Delta G^{vdw}} \qquad (2.60)$$

$$\Delta G^{el} = \Delta G^{is} + \Delta G^{cc} + \Delta G^{res} \qquad (2.61)$$

Wang *et al.* have shown that the contribution of the dispersion interaction term ΔG^{disp} to the activity coefficients is small and can also be neglected. In the recent COSMO-SAC models ΔG^{cav} is generally expressed by the Stavermann-Guggenheim term. The electrostatic Gibbs energy ΔG^{el} itself consists of the contributions of the difference in ideal solvation charge ΔG^{is} (ideal gas state – ideal conductor state), a model specific correction term ΔG^{cc} and the restoring Gibbs energy term ΔG^{res}, which accounts for the change from the corrected screening state (ideal conductor) to the real liquid state. The first two terms cancel out within the calculations, while the restoring Gibbs energy term ΔG^{res} remains. It is the main contribution to the derivation of

activity coefficients. The Gibbs energy of solvation ΔG^{sol} reflects the difference of a solute molecule at a fixed position in an ideal gas with respect to a fixed position in a solution.

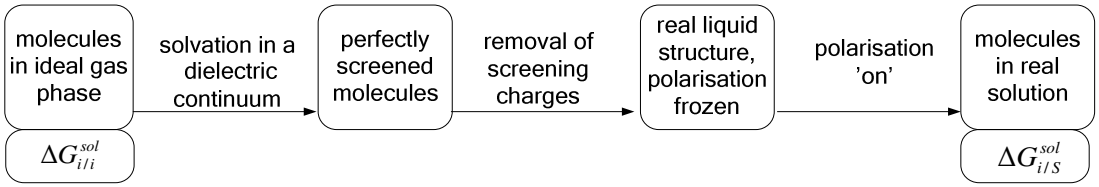

Figure 2.17 *Pathway to the Gibbs energy of solvation from ideal screening charges.*

The activity of the solute *i* in solution *S* can be described by the change in Gibbs energy through solvation $\Delta\Delta G^{sol}$ and the Gibbs energy required to span the molecular cavity. The second term $\ln(\gamma_{i/S}^{SG})$ equals the combinatorial Stavermann-Guggenheim term as applied also in *e. g.* the UNIQUAC model (Eq. (20) of Table 2.1).

$$\ln(\gamma_{i/S}) = \frac{\Delta G_{i/S}^{Sol} - \Delta G_{i/i}^{Sol}}{RT} + \ln(\gamma_{i/S}^{SG}) \tag{2.62}$$

A more detailed description of the (refined) COSMO-SAC model can be found in Sandler, Lin, Wang, Mullins and also Banerjee [75, 77-80].

2.3.3 Estimating the heat and temperature of fusion

Though, it is a rather challenging task to derive accurate activity coefficients from estimation methods, a predictive SLE model would still demand the knowledge of the latent heat of fusion Δh^f and the temperature of fusion T^f of the solutes considered. Solubilities are in general very sensitive to the value of the heat and temperature of fusion of solutes since they are related by exponential functions (Eqs. (2.17) and (2.39)). Unfortunately, the heat of fusion is not known for a larger class of substances that undergo decomposition during melting as *e. g.* many amino acids do. Estimation methods on the basis of group contributions and molecular descriptors can provide rough estimates, but their accuracy is usually very limited with mean errors of up to 20 % [81, 82]. Thus, it might be advantageous to refine those values during SLE model parameterisations [37, 83].

An additional hurdle relevant for enantioseparation is the possible formation of racemic compounds, solvates or partial solid solutions. The obtained heat and temperature of fusion often differ significantly from the values of the single enantiomer. Since property estimation procedures are based on the molecular structure only, rather than on the (different) crystalline phases, no predictions regarding discrimination between the racemic compound, solvates and the single enantiomer is possible.

2.4 Separation of mixtures of single enantiomers

Numerous physical, chemical and enzymatic methods for the separation of mixtures of enantiomers are available form the literature. Two physical methods, that are mostly generic, will be described in the following paragraphs in brief. Further, compilations of these two methods aiming to enhance the overall productivity will be introduced.

2.4.1 Selective crystallisation of enantiomers

The purification of enantiomers and the chiral separation of mixtures of diastereoisomers by crystallisation can be considered as state-of-the-art in the chemical and pharmaceutical industry. Comparatively simple processes and low investment as well as operating costs can yield single enantiomers with high purities and desired particle formulations. The thermodynamic properties, that should be known for successful separations and the physical limitations of characteristic phase diagrams will be discussed.

2.4.1.1 Nucleation and crystal growth

Phase transitions follow directed driving forces. The formation of crystals from a saturated solution is made possible through *e. g.* cooling, solvent removal or antisolvent addition. The driving force can be expressed in terms of supersaturation *S* or the change in Gibbs energy as the difference in the chemical potentials of a saturated (denoted an asterix) and a solution of other (higher) concentration.

$$\mu = \mu^0 + RT \cdot \ln\alpha \qquad (2.63)$$

$$\mu^* = \mu^0 + RT \cdot \ln\alpha^* \qquad (2.64)$$

$$\frac{\mu - \mu^*}{RT} = \ln\left(\frac{\alpha}{\alpha^*}\right) = \ln(S) \qquad (2.65)$$

$$\Delta G = -RT\,ln\,(S) \qquad (2.66)$$

Large *S* values do not necessarily cause crystallisation events. The birth of nuclei, clusters of solute molecules, requires additional energy, since a new surface is generated and may even grow. The process of nucleation of crystals is more complex compared to the formation of *e. g.* stable droplets from supersaturated vapour, since the constituent molecules of a single nucleus have to become orientated into a fixed lattice [84].

Figure 2.18a) depicts the tradeoff between the Gibbs energy ΔG_s needed to increase the surface and the volumetric energy gain ΔG_v from the generation of a new volume. The new volume consists typically of a cluster of *n* molecules with numbers between very few and a couple of thousands molecules. A maximum in ΔG is found, which represents the critical nuclei size, that needs to be exceeded to allow crystals to grow further. The shape and height of the maxima is substance specific and depends largely on the modification of the crystalline phase.

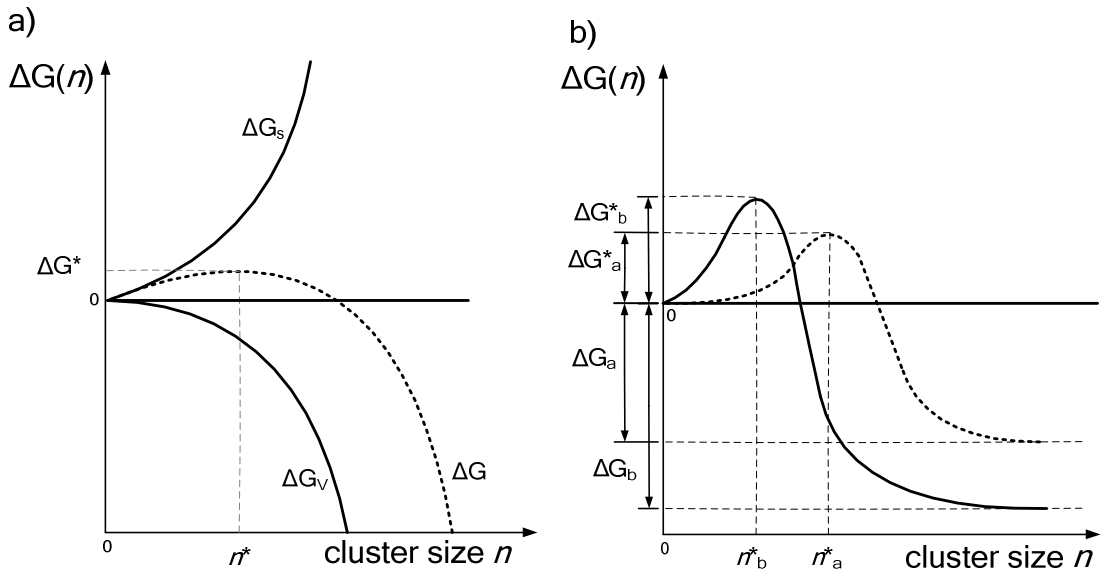

Figure 2.18a)/b) *Relations of cluster size and Gibbs energy. a) Contributions by surface and volume formation, b) Changes in Gibbs energy upon crystal formation for a polymorphic system.*

The change in Gibbs energy ΔG_v due to the formation of a single cluster of n molecules can be expressed by Eq. (2.67). The chemical potential is not a molar quantity in this equation, but relates to the cluster only.

$$\Delta G_v = -n\ \Delta\mu_{clus} = -k\ T\ n\ \ln\ S \tag{2.67}$$

The second contribution ΔG_s is related according to the classical nucleation theory by the surface tension γ_t and the surface area of the new cluster A. The latter can be defined by a shape factor c representing the cluster's form [85] and by the specific volume of the cluster v_{clus}. Provided, the cluster appears cubic c equals six, for spherical clusters as assumed here $c=(36\ \pi)^{1/3}$ applies. The cluster size can be substituted by an equivalent cluster radius as shown by several authors [85, 86].

$$\Delta G(n) = \Delta G_v + \Delta G_s = -n\ \Delta\mu_{clus} + \gamma_t\ A(n) = -n\ \Delta\mu_{clus} + \gamma_t\ c\ \left(v_{clus} n\right)^{2/3} \tag{2.68}$$

The 1st derivative of ΔG with respect to the nucleus size yields the critical Gibbs energy and the critical size of a single spherical cluster (Eqs. (2.70)/(2.71)).

$$\frac{d}{dn}\Delta G = 0 = -k\ T\ \ln\ S + \frac{\frac{2}{3}\gamma_t\ c\ v_{clus}^{\ 2/3}}{n^{1/3}} \tag{2.69}$$

$$n^* = \left(\frac{2\gamma_t\ c\ v_{clus}^{\ 2/3}}{3k\ T\ \ln\ S}\right)^3 = \frac{8\gamma_t^3 c^3 v_{clus}^2}{27k^3 T^3\ \ln^3 S} \tag{2.70}$$

$$\Delta G^* = \frac{4\gamma_t^3 c^3 v_{clus}^2}{27k^2 T^2\ \ln^2 S} \tag{2.71}$$

Figure 2.18b) illustrates differences in the change of the Gibbs energy for a system, that crystallises as two polymorphs. Both, the total changes in energy upon crystallisation $\Delta G_{a/b}$ as well as the critical Gibbs energies $\Delta G^*_{a/b}$ are shown. In general, a higher thermodynamic stability,

expressed by a larger ΔG, will result in a higher solubility [86]. Thus, a metastable phase experiences a lower driving force at the same supersaturation, compared to the stable modification. This contradicts the common observation, that metastable phases tend to crystallise first from a supersaturated solution. The phenomenon can be explained through a comparison of Eqs. (2.70) and (2.71). It allows to relate the critical Gibbs energy to supersaturation in Eqs (2.72).

$$\frac{\Delta G^*}{k\,T} = \frac{1}{2} n^* \, ln \;\; S \tag{2.72}$$

It is found, that the barrier to exceed the critical nucleus size and to allow crystal growth is as high as half of the chemical potential of the supersaturated solution, which is significant.Thus, the higher possible supersaturation of the stable modification prior to a nucleation event implies a smaller size of critical nuclei but also a higher critical Gibbs energy, that needs to be overcome. This entirely thermodynamic relation is known as the 'Ostwald's rule of stages'. Due to the larger number of exceptions from this rule, also kinetic-thermodynamic derivations were proposed, which had also limited success proving the complex nature of nucleation [84]. For this reason, rather simple theoretical approaches are more frequently used. The rate of nucleation *J*, expressed by the number of nuclei formed per unit time and per unit volume is hereby assumed to follow an Arrhenius reaction rate term with *A* being an fitting parameter.

$$J = A \;\; exp(-\Delta G^* / k\,T) \tag{2.73}$$

Classification of nucleation

The description above refers to primary homogeneous nucleation only, though there are a number of different nucleation events known. As a matter of fact, the classical nucleation theory fails in most cases of industrial crystallisers, most likely due to the dominance of heterogeneous nucleation processes [84, 85].

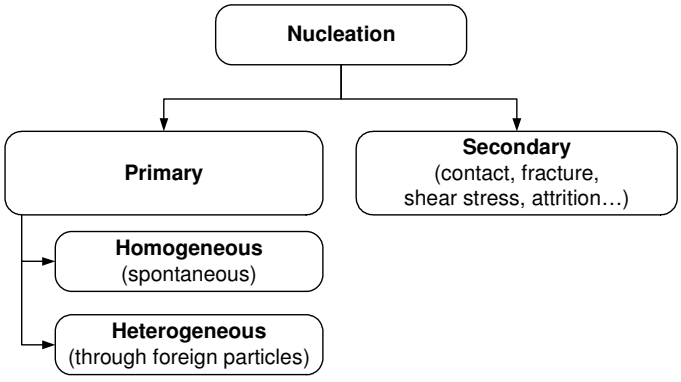

Figure 2.19 *Speciation of nucleation according to driving forces.*

Often, it is attempted to lump several phenomena in apparent model constants. It can be beneficial to relate empirical relationships to the maximal supersaturation (so called metastable zone widths, see below) using fitted nucleation rate constants *k* and *apparent order*s *n* of nucleation.

$$J = k_n \Delta c_n^{\max} \tag{2.74}$$

Secondary nucleation can be caused by the joint effect of a number of factors. It is *e. g.* observed at high shear velocities through intensive agitation in crystallisers, where attrition and breakage of crystals cannot be avoided.

Metastable zone widths

The term 'metastable zone width' (MSZW) describes according to Nyvlt [87] the maximal supersaturation, that can be achieved before nucleation events take place. The quantity is important for the design of both, thermodynamically and kinetically controlled crystallisation processes. This width can be obtained through repeated subcooling of saturated solutions. The temperature, at which the first detectable crystals appear ('cloud point') is recorded, the solute is dissolved again by heating and subsequent cooling runs are carried out with varied cooling rates, varied initial concentrations or varied saturation temperatures. By extrapolation of the corresponding data points, a virtual subcooling temperature at a negligible small cooling rate can be estimated (Figure 2.20). It represents the MSZW within crystallisation should not occur for a given initial condition.

The MSZW depends largely on the experimental conditions and the nucleation mechanism as depicted in Figure 2.21.

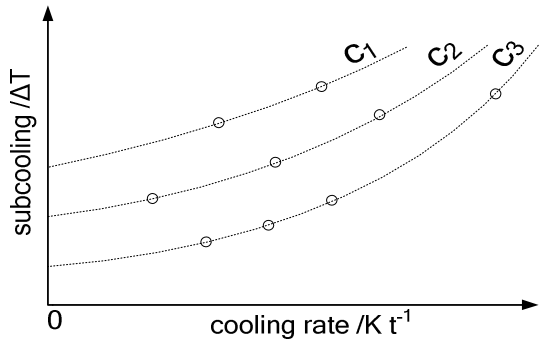

Figure 2.20 *Extrapolation procedure for three different initial concentrations c_i used to estimate the maximal possible subcooling.*

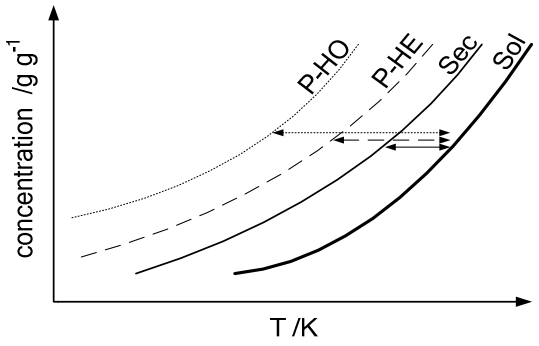

Figure 2.21 *Solubility curve (Sol) and theoretical subcooling ranges from identical initial conditions (concentration, temperature) for*

- *primary homogeneous (P-HO),*
- *primary heterogeneous (P-HE) and*
- *secondary (Sec) nucleation.*

Crystal growth

Besides nucleation, crystal growth is the main process for the depletion of supersaturation. The growth kinetics of different crystals sites and their ratios are responsible for crystal habits and morphology. In case of crystal growth, disturbances as *e. g.* mother liquor inclusion, limit the product purity to be achieved. The control of crystal growth is of particular interest in the final product formulation (crystals size distribution, habitus, crystal stability) and in subsequent downstream processes to guarantee wash-ability and filter-ability. The field of crystal growth was considered only briefly in the course of this thesis with its restricted focus on crystallisation thermodynamics. Product formulation was not subject of the investigations.

Both nucleation and crystal growth of single enantiomers are inherently linked to the presence of the antipode, *i. e.* the counter enantiomer. Already traces can lead to specific blocking of

growth sites of the desired enantiomer [88]. Also, the MSZW is generally influenced significantly by the antipode for systems of enantiomers in solution [89-91]. Estimation, measurement and correlation of those mainly kinetic effects are rather demanding. These data were determined in this work for selected cases and process design.

2.4.1.2 Selective crystallisation strategies based on phase diagrams

The measurement and thermodynamic description of SLE usually provides sound information on the relevant phase diagrams for chiral systems in solution. These can be exploited subsequently for the design of separation processes. Hereby, a larger fraction of the antipode in solution has a directing effect on the thermodynamic domain, in which the target enantiomer is situated and can either force or hinder selective crystallisation. The following descriptions are predominantly, but not entirely, based on equilibrium thermodynamics. In principle, three cases of selective crystallisation strategies can be deduced directly from the information on thermodynamic equilibria.

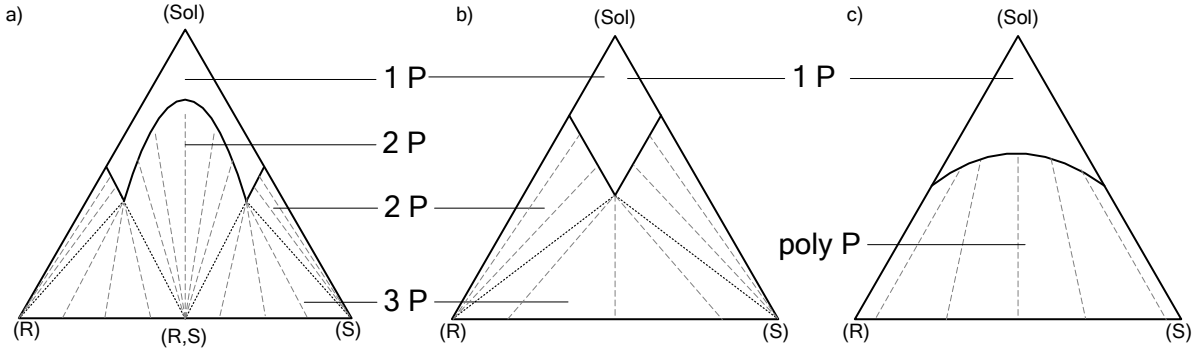

Figure 2.22 *Undersaturated solution (1 P), biphasic domains (2 P), triphasic domains (3 P) and polyphasic domains (poly p) and the corresponding tie lines within a compound-forming system a), a system exhibiting a conglomerate b) and a system with complete miscibility in the solid phase c).*

Provided, that the (R)-enantiomer is the target component, an asymmetric initial mixture must be situated in the outer left biphasic domain in Figure 2.22a) in order to crystallise solely the target enantiomer from solution. The same applies also to the conglomerate-forming system as of Figure 2.22b), but not to a solid solutions system depicted in subfigure c), since no biphasic domain is present here. Instead, a polyphasic domain consisting of all ratios of the enantiomers in the solid phase in equilibrium with corresponding ratios of the enantiomers in the liquid phase is found. Within the inner biphasic domain of compound-forming systems, the racemic compound can be crystallised only.

The tie lines of the triphasic domains link mixtures of either the racemic compound and the single enantiomer or mixtures of both enantiomers with the liquid phase of eutectic composition. This domain can be used for the enrichment of slightly asymmetric mixtures further up to the eutectic composition, provided that the latter is higher than the initial composition [16, 92, 93]. The slope of the tie lines of systems with full miscibility in the solid phase allow no direct equilibration with a phase containing the pure product, but is decisive for enantiomeric enrichment by crystallisation. Its knowledge requires usually laborious experimental measurements. It is generally possible to design a multi-stage-crystallisation

process by simultaneous enrichment of a product stream in one direction and stripping of the target enantiomer in another counter-current stream. However, it is possible, that numerous stages are necessary [94]. Those separations are out of the scope of this thesis.

Figure 2.23 summarises the possible product purities, that can be obtained starting with initial solutions of different purity. The figure does not consider kinetically controlled crystallisations. The final purity to be obtained through crystallisation processes is related to the initial composition of the feed mixture. Initial solutions exhibiting a purity below the eutectic composition, but above 50 % can be enriched up to a purity, which equals the eutectic composition. An initial solution, that exceeds already this value, can be purified up to a 100 % pure enantiomer. Since the eutectic composition is a substance specific property, the ease of purification may by high in case of low eutectic compositions. Here, only slightly asymmetric initial solutions are required in order exceed the corresponding eutectic composition and to gain pure product. High eutectic compositions between *e. g.* 80-100 % demand highly asymmetric initial solutions, which often causes selective crystallisation to fail.

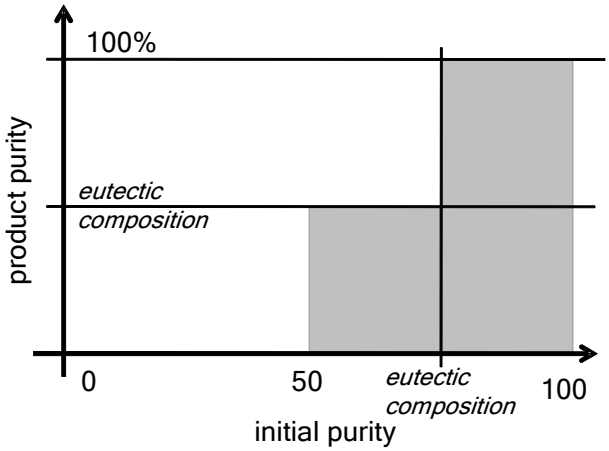

Figure 2.23 *Product purities to be obtained from different initial purities through thermodynamic dominated crystallisations. Boxes indicate feasible relations. Initial composition below the eutectic composition can be purified up to the eutectic composition, initial composition above this value can be purified up to 100 %.*

This work aims to overcome this limitation such that, also only slightly enriched solutions far below the eutectic composition can be purified up to the pure enantiomer.

All described processes end up in condition of thermodynamic equilibrium, which are described by the corresponding phase diagram. Thus, it is not a hurdle if the transient process trajectories are unknown. On the contrary, the kind of driving force to be applied can be chosen freely, which bears a degree of freedom in process design. In addition, seeding with a slurry or with dry crystals of the product, although possible, is not required to obtain the pure product. This renders this class of processes to be rather robust. The process design and its outcome is derived directly from mass balances.

Preferential crystallisation

Another field of selective crystallisation exploits the so-called 'entrainment effect' [16, 95-98]. Hereby, crystallisation is initialised by the addition of crystalline seeds of either the target enantiomer in order to crystallise this species 'preferentially' or by seeds of another species in order to remove the latter from solution and purify the mother liquor. These kinetic crystallisations yield process trajectories, which are not in thermodynamic equilibrium and can

make crystallisation-based processes possible even within domains of phase diagrams with unfavourable thermodynamics. In fortunate cases and if the entrainment trajectories cross phase boundaries, process yields above the thermodynamically possible yields were observed [99]. However, the process success depends largely on the existence of an exploitable entrainment effect and on the controllability of the nucleation event of the unwanted species, that has to be prevented in any case [100]. Preferential crystallisation is not applicable to systems as given by Figure 2.22 c), since no distinct product phases exist, that could grow preferentially.

Solubility phase diagrams involving metastable phases, solvates and partial solid solutions

The three cases given by Figure 2.22 illustrate only a simplified image of real systems. Often, several modifications of the solid phases are found, leading to significant differences in the shape of the corresponding phase diagrams. A number of the most prominent examples is given by Figure 2.24.

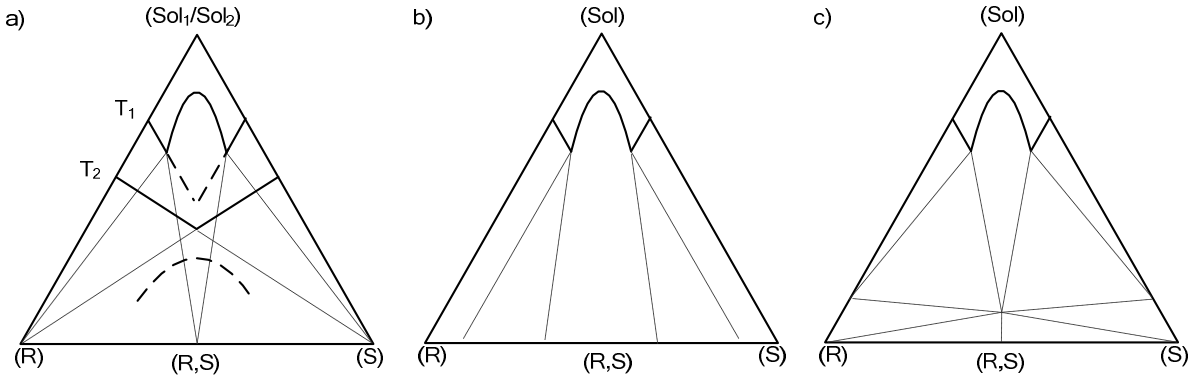

Figure 2.24 *Illustrations of resulting shapes of phase diagrams upon changes in the solid phases:*
a) Solvent and/or temperature changes-entire change in the type of phase diagram;
b) Formations of partial solid solutions of terminal type and a type involving the racemic compound;
c) Solvate formation involving the single enantiomer and the racemic compound.

As discussed in section 2.1.2, the stability of a certain solid phase may be restricted to a specific temperature (range) and solvent.

Figure 2.24 a) aims to illustrate such an example with a particularly large impact on selective crystallisation processes. The transformation of a compound-forming to a conglomerate-forming system is very beneficial for separation purposes. Examples of systems of enantiomers involving metastable phases are known from the literature [101-103].

The limited inclusion of molecules of the antipode into the crystal lattice of the single target enantiomer (terminal partial solid solutions) or of the racemic compound widens the biphasic domains as in Figure 2.24b). Thermodynamic equilibration of solutions in the outer biphasic domain yields crystals composed of both enantiomers and therefore lowered purity. Equilibration of a supersatured solution within the inner biphasic domain results in crystals of the racemic compound, which do not necessarily exhibit a 1:1 ratio. This generally undesired property in selective crystallisation processes is frequently cited in the literature [104-106].

Solvates and hydrates incorporate distinct amounts of solvent molecules into their crystal lattice. The consequences on the shape of phase diagrams can be large, especially, if both species,

the racemic compound and the enantiomer, form a solvate upon changes to the solvent composition or the process conditions.
Evaluation of the introduced changes to phase diagrams and assessment with respect to enantioseparation is one task within this thesis.

2.4.2 Chiral chromatography

Within the last years chiral chromatography has gained increasing attention as a powerful method in the purification of mixtures of enantiomers. This can be attributed to two key factors: Rapid progress in the development of effective and efficient stationary phases and innovations in the modes of operation of batchwise and continuous chromatography in general. Chromatography remains an expensive unit operation, but the choice for competitive alternatives is limited. Due to the broad field of available stationary phases, nowadays almost every separation problem can be solved (with different productivities, of course), which makes chromatographic techniques more and more generically applicable.

2.4.2.1 Fundamental relations

Both, in analytical and preparative chromatography a number of specific terms and relations are frequently used, whose meanings are of fundamental relevance in chromatographic separations. While most definitions will be explained in the view of batch-wise chromatography, they are also helpful in understanding modern concepts of continuous multi-column chromatography.

Chromatographic separation concepts are based on the unequal distribution of molecules (solutes) different in kind between a fluid phase (eluent) and a stationary phase (the adsorbent). It is usually discriminated among physisorption and chemisorption as the two main binding forces, that can lead to adsorption of a solute onto the adsorbent's surface. Chromatographic separations require a reversible binding. Therefore, stationary phases are chosen such, that only physisorption takes place.
In chiral chromatographic separations usually binary mixtures of solute molecules (*e. g.* a pair of enantiomers) are dissolved in a suitable solvent. This feed mixture is injected into an eluent stream and passes through a column, which is filled with a specific enantioselective packing material. The stationary phase can consists of a solid support made of porous (spherical) silica particles, that is functionalised by derivatised amylose-, cellulose- or antibiotic molecules containing numerous stereocentres. It is assumed, that a pair of enantiomers adsorbs equally onto the solid (nonchiral) support, but the interplay with the chiral part of the adsorbent is different in strength and so the adsorption. In efficient separations both enantiomers escape (elute) from the column one after the other with a clear gap in time. UV-detectors at the column outlet are used to record the so-called *chromatogram*, which contains the substance (-mixture)-specific *elution-profiles*. For chiral separations in addition polarimeter devices are frequently used, since a pair of enantiomers and therefore the order of elution can not be distinguished from UV-absorption signals.

Assessing chromatographic separations-performance and productivity factors

A chromatogram obtained from the injections of three different components is given in Figure 2.25. The adsorption of each individual component onto the stationary phase is proportional to the specific retention times $t_{R,i}$ for small injection amounts. Virtually every chromatographic device produces a specific additional retention time t_0 due to the volumes of connecting tubings, pump heads and the detector cell. The time t_0 is obtained from the injection of a non-retained substance. Since the retention time depends also on the geometry of the column and the flow rate, a normalised value, the *capacity factor* k_i', is introduced [107-109].

$$k_i' = \frac{t_{R,i} - t_0}{t_0} \tag{2.75}$$

The ratio of the individual capacity factors of two components determines the selectivity α for a binary separation. By convention, the numerator contains the less adsorbed component. Consequently, the selectivity is always greater than unity.

$$\alpha_{ij} = \frac{k_j'}{k_i'} = \frac{t_{R,j} - t_0}{t_{R,i} - t_0} \tag{2.76}$$

Besides highest selectivity, also elevated throughput is essential for efficient preparative chromatographic applications. This is achieved through large injection volumes and/or highly concentrated injections in batch chromatography. Peaks in the elution profile encounter broadening due to mass transfer limitations and fluid-dynamic non-idealities (axial dispersion). Further increase in the column loading leads to distorted and asymmetric peaks, whose shapes are depending on the substance specific adsorption behaviour [108].

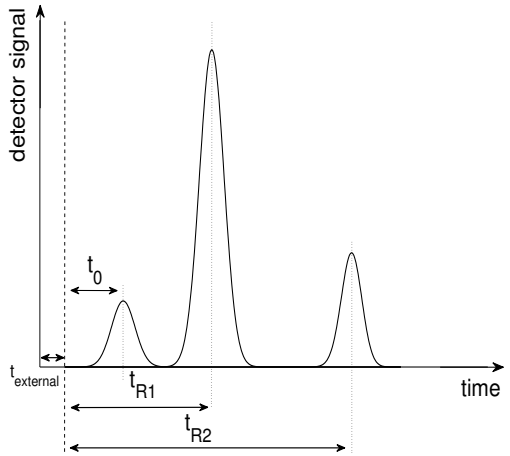

Figure 2.25 *Chromatogram of discrete analytical injections of two substances leading to symmetric peaks.*

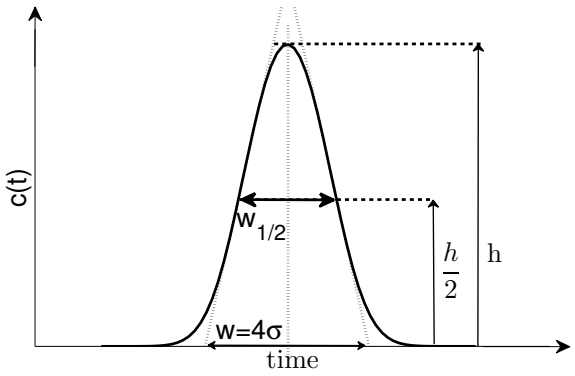

Figure 2.26 *Estimation of column efficiency from peak shapes.*

The efficiency of a chromatographic column can be assessed by the number of apparent theoretical equilibration plates (NTP), similar to distillation processes. The plate number as well as the corresponding height of an equivalent theoretical plate (HETP) lumps together all effects responsible for peak broadening. For perfectly symmetric peaks from high efficiency columns, the width of the Gaussian distribution *w* can be used to estimate the number of transport plates.

A more robust method is based on the width $w_{1/2}$ at half-height of the peak. The NTP is specific for any component *i* and denoted NTP_i within the following.

$$NTP_i = 16\left(\frac{t_{R,i}}{w_i}\right)^2 \quad (2.77) \qquad NTP_i = 5.54\left(\frac{t_{R,i}}{w_{1/2,i}}\right)^2 \quad (2.78)$$

For heavily distorted peaks, the concept of moments is more reliable. Hereby, the *1st* absolute moment $\mu_{m,i}$ equals the retention time and the normalised *2nd* central moment $\sigma^2_{m,i}$ determines the squared variance [107].

$$\mu_{m,i} = \frac{\int_0^\infty c_i(t)\ t\ dt}{\int_0^\infty c_i(t)\ dt} = t_{R,i} \quad (2.79) \qquad \sigma^2_{m,i} = \frac{\int_0^\infty (t-\mu_i)^2\ c_i(t)\ dt}{\int_0^\infty c_i(t)\ dt} \quad (2.80)$$

The number of plates is given by the quotient of the squared retention time over the squared variance.

$$NTP_i = \frac{\mu_i^2}{\sigma_i^2} \quad (2.81)$$

Its value is related linearly to the flow rate. The contribution of axial dispersion can be attributed to Eddy-diffusion and to molecular diffusion. The latter follows also a function involving the flow rate. Summation of the three terms leads to the well known equation by van-Deemter [110].

$$HETP_i = \frac{L_c}{N_i} = A_i + \frac{B_i}{u} + C_i u \quad (2.82)$$

The function runs through a minimum, for which the highest column separation efficiency can be assumed. The highest productivity is usually found at much higher flow rates as a compromise between separation efficiency and throughput.

Another performance factor to be named for completeness is the *resolution* R_{ij} of separating *i* and *j.* It relates the peak distances to the peak widths [109]. The number of components to be separated is denoted by N_c.

$$R_{ij} = \frac{t_{R,j} - t_{R,i}}{4\ \sigma_{ji}} \qquad (i,j = 1,\ldots, N_c) \quad (2.83)$$

$$\sigma_{ji} = \tfrac{1}{2}\left(\sigma_i + \sigma_j\right) \qquad (i,j = 1,\ldots, N_c) \quad (2.84)$$

The productivity of a chromatographic separation is usually defined by the amount of product per unit time and per amount (volume) of stationary phase.

2.4.2.2 Equilibrium thermodynamics

Theoretical descriptive models for chromatographic processes require the quantitative description of the adsorption of solutes onto the stationary phase. Pressure effects are usually neglected in liquid chromatography and adsorption is determined assuming isothermal conditions.
The simplest expression for adsorption follows a linear approach by introducing a Henry constant H_i. The constant represents the slope, that links the loading q_i of a component i onto the stationary phase with the concentration c_i of the same component in the fluid phase. The ratio of Henry constants of two components equals the introduced separation factor α_{ij}.

$$q_i = H_i c_i \qquad (i= 1,..., N_c) \tag{2.85}$$

Numerous models for adsorption isotherms are available, whose physical foundations range from entirely empirical to rather sound. The Bi-Langmuir type of adsorption isotherms is one suitable model for the description of chiral-specific adsorption. It reflects the possibility of non-chiral adsorption onto the support layer and the adsorption on a second site featuring chiral discrimination. The modelling of adsorption was conducted exclusively with the Bi-Langmuir model within this thesis. Since two different binding sites are considered, two constants q_{s1} and q_{s2} are used to describe the corresponding saturation conditions. The first site describes the non-chiral site. Consequently, adsorption onto this site is assumed to be of equal strength for a pair of enantiomers. Further, two constants b_1 and b_2 need to be estimated in order to describe the site- and concentration-specific adsorption.

$$q_i = q_{S1,i} \frac{b_{1,i} c_i}{1 + b_{1,i} c_i} + q_{S2,i} \frac{b_{2,i} c_i}{1 + b_{2,i} c_i} \qquad (i= 1,..., N_c) \tag{2.86}$$

The competitive behaviour of two enantiomers with respect to adsorption sites on the stationary phase can be expressed under certain assumptions by multi-component isotherms.

$$q_i = q_{S1,i} \frac{b_{1,i} c_i}{1 + \sum_j^C b_{1,j} c_j} + q_{S2,i} \frac{b_{2,i} c_i}{1 + \sum_j^C b_{2,j} c_j} \qquad (i= 1,..., N_c) \tag{2.87}$$

2.4.2.3 Modelling of single column chromatography

The migration velocity of a component through a column with a volume V_c depends on the void fraction, that is not occupied by the packing material V_{int} and the volume of the porous particles, that is accessible to the mobile phase V_{pore}. Obviously, the total porosity ε has a large impact on the outcome of theoretical descriptions of chromatography and needs to be known prior to the use of models.

$$\varepsilon = \frac{V_{\text{int}} + V_{pore}}{V_c} \tag{2.88}$$

It is often more convenient to use the *phase ratio F* as the ratio of the volumes of the solid and the liquid phase.

$$F = \frac{1-\varepsilon}{\varepsilon} \tag{2.89}$$

Non-retained components migrate with an interstitial velocity u through a column (with Q being the volumetric flow and A_c being the cross-sectional area of the column). Thus, the retention time t_0 can be expressed by the interstitial velocity u and the column lengths L_c.

$$u = \frac{Q}{\varepsilon A_c} \tag{2.90}$$

$$t_0 = \frac{\varepsilon A_c L_c}{Q} = \frac{L_c}{u} \tag{2.91}$$

The migration velocity for an adsorbed component depends largely on the corresponding adsorption isotherm. Mass balances around a column and consideration of linear adsorption leads to the following expression for the retention time.

$$t_R = t_0 (1 + FH) \tag{2.92}$$

For nonlinear isotherms and high concentrations, the curvature of the adsorption isotherm needs to be taken into account and comprehensive models are of demand.

In general, it can be discriminated among four classes of models for the theoretical representation of chromatographic columns. Model complexity increases beginning from

a) ideal models (no dispersion, no mass transfer limitations),
b) the consideration of a single band-broadening effect (Thomas model, equilibrium-dispersive model, transport model) towards
c) lumped rate models with an independent description of either mass transfer or kinetic limitations and axial dispersion (transport-dispersive model, reactive-dispersive model).
d) General rate models describe mass transfer in the most detailed manner.

Analogously, the computational effort for the model solution increases in the same direction since the availability of analytical solutions is scarce. For the equilibrium-dispersive model considering linear adsorption isotherms analytical solutions are available, but not for nonlinear isotherms. Comprehensive reviews on chromatographic models and their specific application areas can be found [107, 111].

Within this thesis the equilibrium-dispersive model was used due to its comparatively fast numerical solution and motivating results from the literature [112-114]. Continuous models balance differential slices within the axial dimension of a column with respect to every individual component *i*. The differential mass balances comprise the solute movement through convective flow and lump all effects leading to axial dispersion into an apparent coefficient D_{ax}. The differential mass balance for a single component reads as follows.

$$\frac{\partial c}{\partial t} = D_{ax} \frac{\partial^2 c}{\partial z^2} - F \frac{\partial q}{\partial t} - u \frac{\partial c}{\partial z} \tag{2.93}$$

Provided D_{ax} can be neglected due to *e. g.* highly efficient columns, the first term on the right hand side cancels out and the equation can be further simplified by considering Eq. (2.94).

$$\frac{\partial q}{\partial t} = \frac{\partial q}{\partial c}\frac{\partial c}{\partial t} \qquad (2.94)$$

$$\frac{\partial c}{\partial t} + \frac{u}{1 + F\dfrac{dq}{dc}}\frac{\partial c}{\partial z} = 0 \qquad (2.95)$$

The migration velocity u_c of the component at a concentration level c is described by an expression for its propagation through the column, the so-called *wavefunction*.

$$u_c(c) = \frac{u}{1 + F\left.\dfrac{dq}{dc}\right|_c} . \qquad (2.96)$$

For this simplified case the expression for the retention time for a certain concentration c bears similarities with the expression for linear adsorption.

$$t_R(c) = t_0 \left(1 + F\left.\frac{dq}{dc}\right|_c\right) \qquad (2.97)$$

2.4.2.4 Determination of adsorption behaviour

Proper design of chiral chromatographic separation processes relies strongly on the availability and quality of fundamental information on the competitive adsorption behaviour of mixtures of enantiomers. Due to the complex nature of the interactions between solutes and chiral stationary phases, experimental studies are essential in most cases. Experiments should allow the correlation of models for the quantitative description of processes.

The Henry coefficients are obtained best, regardless of the model applied, from analytical injections. Any additional parameter for nonlinear adsorption isotherms requires the measurement of the entire corresponding adsorption isotherm to allow its estimation.
Usually, the most comprehensive information can be derived from dynamic measurements. Four characteristic techniques, namely *frontal analysis*, *elution by a characteristic point*, *perturbation method* and *peak-fitting* are frequently found. They vary in the experimental effort and amount of substance required, the influence of kinetics on the measurement and the theoretical background (model availability) [111, 115]. Adsorption isotherms in this thesis were solely derived through *peak fitting*.

2.4.2.5 Design of continuous multi-column chromatography

Besides the rapid development of new stationary phases, the modes of operation are most relevant for chromatographic process efficiency. Preparative separations are conducted, whenever possible, in continuous mode. An attractive (semi-) continuous mode is the so-called 'steady state recycling' (SSR). Here, the feed mixture is injected batchwise onto a HPLC column and the leaving fractions are cut such, that pure fractions are harvested and removed from the

system, whilst fractions, which contain mixtures of *e. g.* the target and also the unwanted counter-enantiomer are fed back to the inlet of the column. These impure fractions are injected again together with fresh feed in a cyclic mode. Compared to a classical batchwise HPLC operation, much higher productivities can be obtained [116-118]. However, the operation of such a system is demanding since the cut times need to be determined very accurately. A major advantage is the intensified usage of the (expensive) stationary phase material.

Another more frequently found continuous operation mode is based on a serially connected setup of columns comprising two inlet ports for feed and eluent and two outlet ports for *extract* and *raffinate*. The feed, *e. g.* a solution containing a racemic mixture of an (R)- and (S)-enantiomer, is pumped continuously into the column setup. In the simplest case, the setup consists of four so-called *separation zones* with *e. g.* two columns each (Figure 2.27). The feed enters between zone II and zone III and is pumped in clockwise direction through the columns towards zone IV. Provided, the (S)-enantiomer is retained less by the stationary phase, it will migrate faster through the columns and will reach the *raffinate* port faster. The mode of operation to be introduced here is called *simulated moving bed chromatography* (SMB) due to a simulated movement of the stationary phase in counter-current direction with respect to the mobile phase. The important counter-current movement is realised by discrete changes of the in- and outlets of the system. Thus, after a defined periode, the feed mixture will be fed into the system one position further up in clockwise direction (into the former zone III). The same applies to the position of removal of the raffinate. The discrete simultaneous port switching event causes a simulated movement of the stationary phase in counter-clockwise direction and the (R)-enantiomer, migrating slowlier through the columns, approaches the *extract* port, where it is collected continuously.

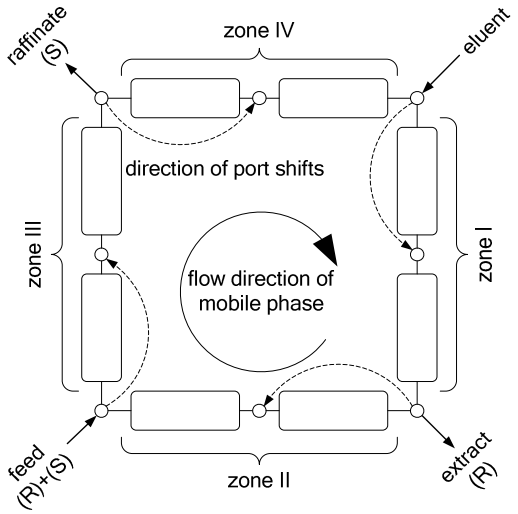

Figure 2.27 *Illustrative setup and description of flow directions and in- and outlet port shifts of a simulated moving bed process.*

The continuous removal of a raffinate fraction containing the pure (S)-enantiomer and an extract fraction with the (R)-enantiomer requires the rigorous control of the switching time and the internal flows through the columns. The assignment of columns to zones is hereby of conceptual aid. Each zone can consist of different numbers of columns and needs to fulfil different tasks. The different internal flow rates within the zones II and III are chosen such, that the binary feed

mixture separates. Well defined internal flow rates within zones I and IV and a corresponding eluent flow rate result in the complete regeneration of the mobile phase in zone IV and regeneration of the stationary phase in zone I, respectively.
The development of SMB techniques has made significant progress over the last years and the classical processes has been modified and adapted successfully for numerous separation tasks [108, 119, 120]. Analogue to SSR techniques, an intensified usaged of the stationary phase takes place, leading to higher separation productivities compared to classical batch chromatograpy. Further, the specific solvent consumption is reduced, if a *closed loop* (Figure 2.27, outlet of zone IV is connected to the inlet of zone I) process can be realised [120]. Comprehensive work on the theoretical description and optimisation of SMB processes has supported the general acceptance of SMB techniques, such that a number of SMB plants of industrial-scale for *e. g.* pharmaceutical and biotechnological applications were realised.

The conducted experimental work and theoretical modelling within this thesis is based on continuous multi-column chiral chromatographic separation techniques and *classical* SMB modes of operation. It is possible, that other than the conducted continuous separation modes and also certain batchwise operating modes can achieve higher productivities. However, the obtained trends should remain the same and a generalisation of the findings with care should be possible.

SMB techniques allow the continues processing of a binary feed mixture of enantiomers. The classical SMB setup comprises four identical zones *i=I...IV* arranged in a closed loop. The time between discrete port shifts t^{shift} is defined by the column volume and the virtual solid phase flow $\dot{V}^S$

$$t^{shift} = (1-\varepsilon)\frac{V_c}{\dot{V}^S} \tag{2.98}$$

Mass balances around a single zone need to take into account the amount of solute, that is shifted backwards upon each discrete port shift. Thus, the simulated zone flow rate $\dot{V}_i^{SMB}$ deviates from the ideal flow rate $\dot{V}_i$ according to the following equation. V_{tot} denotes the additional volume from tubings, pumps and valves and n_s denotes the number of columns.

$$\dot{V}_i^{SMB} = \dot{V}_i + \frac{\varepsilon\, V_c}{t^{shift}} + \frac{V_{tot}}{n_s\, t^{shift}} \tag{2.99}$$

It is advantageous to consider dimensionless flow rates m_i in each zone *i* by normalisation of the zone flow rates $\dot{V}_i^{SMB}$.

$$m_i = \frac{\dot{V}_i^{SMB}\, t^{shift}}{(1-\varepsilon)\, V_{column}} - \frac{1}{F} - \frac{V_{tot}}{n_s\, (1-\varepsilon)\, V_{column}} \tag{2.100}$$

Provided, very efficient columns (high NTP) are available and the system considered can be described by linear isotherms (nonlinear within limits), the so-called ‘triangle theory’ provides valuable information on the most promising choice of m_i-values for a given separation problem

[121, 122]. However, *e. g.* in case of very few theoretical stages, parameter estimation procedures using numerical solvers are needed. In principle, the SMB process has five degrees of freedom by the four external flow rates (feed, eluent, raffinate, extract) and the time between port shifts. Typical constraints in the optimisation problem are the maximal flow rates within the columns limited by the maximal allowed pressure drop, the packing stability and/or the pumps used. The purities at the extract and the raffinate port and (more strictly) the full regeneration of zone I and IV are further constraints. The objective function can be defined by the productivity of a single or both components. Typical mathematical solvers for constrained and non-linear problems can be used to estimate promising operating points. Therefore, more comprehensive process models are needed (compare chapter 2.4.2.3), which are capable of reflecting the dynamics of the SMB process.

Typically, semi-stationary concentration profiles over all zones are obtained after a few tens of shifts after the process start-up. From Figure 2.28 the internal spatial distribution of a binary mixture is given. Dotted lines represent the concentration profile at the beginning of a *tact* (in between two shifts), solid lines illustrate the same profiles right before the port shifting at the end of the tact. Both curves migrate towards zone IV and will be moved back at the port shift event. For the case given, the profile of component a) is always superimposed by component b) at the extract port, while pure component b) can be removed at the raffinate port.

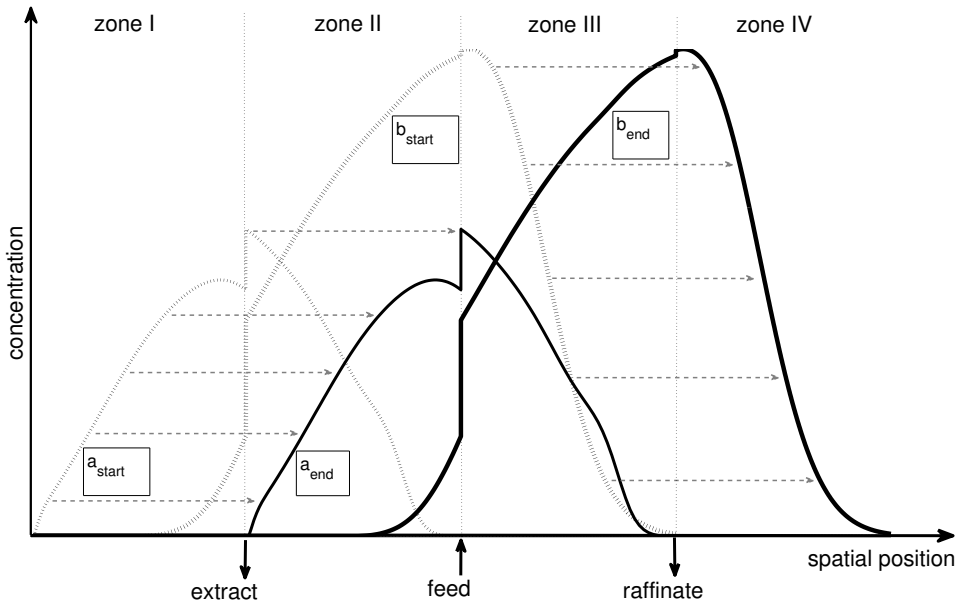

Figure 2.28 *Spatially distributed quasi-stationary concentration profiles (dashed lines: stronger adsorbed component a), solid lines: less adsorbed component b); left profile: start of tact; corresponding right profile lines: end of tact).*

The concentration at both outlets is not constant over the duration of the tact, but is an increasing function at the raffinate port and decreases at the extract port (compare terminal concentrations in Figure 2.28). Periodic shifting of ports causes 'reset events' in the column profiles. Thus, the outlet concentrations within a *tact* (in between two shifts) are a function of time. These profiles appear as a series of subsequent 'saw-teeth'. The purified amount of *e. g.* (S)-enantiomer at the raffinate port within a given period of time is obtained from integration and summation of the 'saw-teeths' for all tacts within the given period.

2.4.3 Coupling of single processes

A common figure can be drawn for the majority of physical separation methods: the overall productivity decreases with increasing purity requirements. This applies to distillation as well as to membrane separation processes. In principle, product purity is likely to drop for selective crystallisation processes also, if the establishment of thermodynamic equilibria is dominated by kinetic effects through *e. g.* too high driving forces. However, the comparatively simple constructional design of crystallisers without chiral specific internals allows a cheap scale-up. This motivates the investigation of couplings of unit operations involving selective crystallisation. Further, crystallisation is the process of choice for product formulations in pharmaceuticals. In ideal cases chiral separation and product formulation can go hand in hand saving additional time.
The process combination of continuous chromatography and selective crystallisation was investigated already in depth by a number of authors. Lowering the purity constraints on the chromatographic separation step resulted in much higher productivities [123-129]. If the eutectic composition of a chiral system is exceeded by a chromatographic enrichment, the single enantiomer can be crystallised. Provided rapid crystallisation kinetics can be exploited, a eutectic composition close to 50 % and a pronounced gain in productivity of the pre-enrichment step at low purity constraints are available, hybrid processes can outperform chromatographic processes [125, 126, 128]. If the crystallisation operation is significantly faster compared to the pre-enrichment step, the design of the chromatographic separation step at low purity requirements is the limiting property to the overall productivity.

All introduced hybrid processes are limited by the underlying SLE and the substance specific pre-enrichment, that is needed to be provided by the first enrichment step. Within this thesis a crystallisation process will be introduced, that requires no substance specific pre-enrichment. Instead, every asymmetry originating from a pre-enrichment step can be processed in the subsequent crystallisation step. The additional degree of freedom will alter the objective function of pre-enrichment processes and lead to different figures of the coupled process productivity. Subsequently, new process parameters need to be identified aiming to approach the process optimum.
The newly designed hybrid processes will be evaluated and compared in terms of productivity enhancement and process stability.

3 Study of solid phases in the Malic acid system

Provided that the phase equilibria relevant for chiral separation can be deduced from interactions in the solid and in the fluid phase, the former exhibits the predominant role. This chapter introduces experimental techniques for the quantitative determination and description of more complex solid phase interactions derived from investigations of (chiral-) specific interactions in the system of Malic acid in acetone and water. Solid/solid and solid/liquid equilibria were analysed with particular focus on crystallisation-based chiral separation.

3.1 Analysis of partial solid solutions

The natural character of crystals to exhibit a very strict and predetermined structure is the key property to separate multi-component mixtures and to obtain highly purified drugs. The incorporation of foreign molecules into the crystals lattice of the desired product is generally considered as a defective property in the development and formulation of high-value products and cause changes to the separation strategies to become necessary [104]. A possible hint for a formation of mixed crystals is given if resolution by crystallisation does not yield the expected theoretical purity, as it was deduced prior to crystallisation from estimates of the related phase diagrams. Reasons for unexpected crystallisation pathways, beside kinetic limitations, can be found in thermodynamic uncertainties regarding the formation and interaction of phases. Recent examples are given in the literature [24, 104-106, 130-133]. Partial solid solutions are, according to their name, limited with respect to miscibility in the solid state. The crystal lattice of those compounds can only be distorted up to a certain extent by incorporation of foreign but similar molecules. This behaviour must be reflected by the shape of the related phase diagram.
The chiral Malic acid (2-hydroxy-1,4-butanedicarboxylic acid) is an example for a compound-forming system with pronounced partial solid solutions.

Figure 3.1 *Molecular structures of (S)- and (R)-Malic acid.*

Various authors reported up to three intermediate compounds and polymorphism of the racemic compound [134, 135]. In addition the existence of an "anomalous racemate" at the enantiomeric ratio of 2:1 was claimed [136]. A comprehensive approach to describe the behaviour

of this system by Kuhnert-Brandstätter and Friedl [134] furnishes proof of dimorphism of the racemic compound and partial miscibility both for the enantiomers and the racemic compound. Nevertheless, inconsistencies within the literature remain among others due to the very limited experimental verification work, which has been undertaken for this system up to now.
The motivation for the study described in this chapter was threefold. Firstly, a comprehensive investigation of the chiral Malic acid systems was intended aiming to overcome the remarkable diversity of phase interpretations present in the literature for this system. Secondly, it was also intended to provide a guideline towards a more rapid access to solid/solid and solid/liquid phase equilibria of systems exhibiting solid solutions. Further, an attempt was made to evaluate the possibility of enantioselective crystallisation for a system exhibiting large miscibility in the solid state and a eutectic composition of > 96 % optical purity [134].
In a first step the binary melting point phase diagram was determined and analysed in order to elucidate the multiplicity of phases. Systematic solubility measurements of Malic acid in acetone provided a basis for the determination of the ternary phase diagram. Intensive usage of solid phase analysis by XRPD accompanied by ATR FT-IR measurements have become necessary to define the regions of existence of the two polymorphic forms of the racemic compound and to enable the allocation of mixed crystals to these forms. Time resolved results of the latter techniques were analysed in addition to track changes to the solid phases. The orientation of the tie lines in the ternary phase diagram allowed the assignment of characteristic areas to corresponding phases.
In a second step it was evaluated whether the formation of partial solid solutions in this system can be kinetically altered in a desired manner with respect to chiral resolution from solution. Thus, the question was raised whether the first crystal formed is already of mixed type (as it will be in thermodynamic equilibrium). To study this problem the development of the solid phase was analysed after primary nucleation and during crystal growth. Finally, considerations regarding the molecular structure of Malic acid suggest an explanation of the formation of the corresponding particular solid solutions. Consequences for chiral separation of the Malic acid enantiomers are drawn and discussed.

3.1.1 Experimental section

Solid phase analysis
The binary melting point phase diagram of Malic acid was determined by a combination of analyses of DSC melting curves and measurements of XRPD patterns.
Different mixtures of (R,S)- and (S)-Malic acid were investigated with compositions over the whole relevant range. Substance mixtures were weighed to the determined composition with errors <0.1 wt%. A sufficient amount of deionised water respectively acetone as solvent was added (typically 5 mL) and the sample was gently stirred until complete dissolution occurred.
The solid samples were dried in an oven at 323 K at vacuum and subsequently crushed and ground in a mortar. This procedure is claimed to be the most promising way to achieve the required homogeneous composition of molecularly dispersed solids [104]. The prepared samples were split for DSC (DSC 131, SETARAM, France; closed aluminium crucibles, ~12 mg substance, 1 K/min, 20 mL/min helium purge gas flow) and XRPD (X`Pert Pro Diffractometer (PANalytical

GmbH, Germany; X`Celerator detector, CuK-α radiation, 2θ range of 3-40°, step size of 0.017°, counting time of 50 s or 100 s per step) analysis respectively.
The melting temperatures of the pure substances were taken from extrapolated DSC-onset temperatures within the heat flux/ temperature plane. Peak values were used to determine the liquidus line in case of mixtures. Passing the solidus line caused melting peaks, which disappeared for compositions exhibiting < 74 wt% of the (S)-enantiomer. The melting temperature was correlated by extrapolation of the appropriate onset temperature.
Thermogravimetrical measurements of the racemic compound aiming to evaluate possible thermal degradation of Malic acid during the melting were conducted by use of a SETARAM TG- DSC 111 device. The applied heating rate was set to 1 K/min and the temperature range investigated was between 298 K and 473 K.
Due to the plurality of phases in addition an ATR FT-IR Nicolet 6700 device (Thermo, GB, DTGS, scans: 32, res.:4 cm^{-1}) was used to discriminate between polymorphic forms and between solid solutions.

Determination of the ternary SLE

Solubility data of Malic acid in acetone were available from previous studies [137] in the temperatures range of 293 K to 308 K. Additional data for elevated temperatures (up to 313 K) were determined in this work. Sealed flasks of 5 mL were used with a large excess of solid phase and the content was agitated by a magnetic stirrer. Above the liquid phase only very little vapour phase was present. All flasks were tempered in a water bath over at least 48 h to ensure, that the phase compositions got sufficiently close to thermodynamic equilibrium.
Subsequently, the liquid phase was withdrawn quickly with a syringe and fed directly through a 0.45 µm filter into a tempered density meter (Mettler-Toledo, DE40). By means of a calibration function, the saturation concentrations for the given temperature were obtained. Tie lines and hence borders of miscibility were determined from 15 different compositions at 298 K. The first five compositions were repeated once.
Some samples were prepared in such a way, that their initial compositions were located clearly within the 2-phase area, while other samples were located within the 3-phase region of the ternary solubility phase diagram. The experimental procedure was based on the method for solubility measurements, except that both phases were analysed and the time for the samples to reach equilibrium had been extended to 10 days in order to ensure equilibration also of solid/solid-phase transitions.
After the density measurement the liquid phase samples were dried by solvent evaporation at vacuum, dissolved in the applied HPLC eluent and analysed by chiral HPLC. The solid phase was filtered simultaneously and washed with n-Heptane. The dried material was dissolved in the eluent and analysed also by chiral HPLC. For this purpose a HP 1100 HPLC system (Hewlett-Packard, Germany) equipped with an analytical chiral column (Phenomenex, Chirex 3126, V_{eluent}=0.5 mL/min, 5 mM $CuSO_4$ at pH 3.2 (acetic acid), v_{inj}=2 µL, T=293 K, 254 nm) was used and the enantiomeric ratios of solid and liquid samples were determined. A change of the solvent of the samples became necessary since traces of acetone did cause unfavourable peak shifts.
By analyses of both phases the accuracy and reliability of the measurement can be verified by use of mass balance calculations. This cross-check is necessary, since the analysis of the solid phase can suffer from the problem of adherent mother liquor.

Crystallisation from solution

All crystallisation experiments have been conducted in an automated system (autoMATE, HEL, UK) equipped with standard probes for turbidity and temperature. The solvent volume was 200 mL of acetone except for additional measurements of the metastable zone width (MSZW) (20 mL). The MSZW of the (S)-enantiomer and the racemic compound were determined prior to crystallisation experiments by means of the polythermal method by Nyvlt *et al*. [87].

Primary nucleation was induced by cooling. A saturated solution (60 wt% of the (S)-enantiomer) was reduced by evaporation prior to the cooling ramp to facilitate crystallisation at elevated temperatures. Saturated solutions of acetone at 318 K have been supersaturated up to 122 % by evaporation of the solvent. Subsequent cooling with 1 K/h down to 293 K led to nucleation at temperatures between 315 K and 298 K (increase in turbidity). Samples of the liquid as well as the solid phase were withdrawn and analysed by chiral HPLC and XRPD periodically from that time.

A slurry of saturated solution of acetone with a defined excess of solid (R,S)-Malic acid (stable polymorph) was used for seeding experiments. Crystallisation was initiated from solutions with different supersaturations $S(c/c_{sat})$=1.12-1.27 and with different seed loads (2.0-14.2 mL seed slurry/ 0.4-2.9 g undissolved seeds). The solution was initially enantiomerically enriched (80 wt% (S)-enantiomer). Again, samples of the solid and liquid phase were withdrawn periodically after seeding and analysed by chiral HPLC and XRPD.

A slurry of (S)-enantiomer/ acetone was further used for preferential crystallisation experiments. 5 mL of seed slurry (2.5 g undissolved seeds) were used for seeding of two enantiomerically enriched solutions (85 wt%/ 92 wt% (S)-enantiomer, 200 mL each) of the same supersaturation. Solid and liquid phases were analysed periodically after seeding.

3.2 Discussion of results

3.2.1 Derivation of phase diagrams

Solid phase identification by XRPD

All solid phase samples were analysed by a high precision XRPD device. NaCl (<1 wt%) was used as an internal standard to assure that shifts in the patterns are clearly recognised. For most of the samples Malic acid did not crystallise completely and few amorphous material was present additionally. Some measurements were affected by the distinct preferred orientation of the crystals (*e. g.* Figure 3.2, f)). Therefore the quality of the obtained patterns varied significantly.

Six specific XRPD patterns of crystallisations of different Malic acid mixtures from acetone are shown in Figure 3.2. The racemic compound was crystallised herein from water additionally. The patterns represent all recognised phases of the Malic acid system. It can be differentiated amongst the patterns of the (S)-enantiomer and the stable racemic compound by the existence of the main reflection at ~20° respectively ~24° 2θ. The solid particles of the racemic compound, crystallised from water, show much less crystallinity. This phase has a lower melting temperature, consistent with the metastable racemic compound. This β-form can be identified also by XRPD by the shift of the reflection at 20.1° (stable α-form) towards 20.4° 2θ. The shift of the reflection accompanies the findings from ATR FT-IR measurements in the next section.

The powder pattern of an (R,S)-Malic acid sample (crystallised from water) was recorded once directly after evaporation of the solvent and again after 17 hours. Any mechanical stress on the sample has been avoided (no grinding) to prevent the metastable form transforming into the stable analogue. Therefore the prepared solution was put directly on the sample carrier for drying. The same treatment was done on an (R,S)-sample from acetone for comparison purposes. It was found that the sample from water changed its structure overnight towards the pattern known from the stable form, while the sample from acetone was already the stable modification and remained unchanged.

The XRPD patterns of *mixed crystals* (denoted *MC* in the following) exhibiting concentrations of lower than 70 wt% (S)-enantiomer showed a typical shift of the main reflection of the (R,S)-crystal at ~20° 2θ towards smaller angles. This shift was in accordance with changes of the lattice due to incorporation of the enantiomer in excess. This aspect is discussed in the following section. Up to a fraction of 85 wt% (S)-enantiomer no XRPD patterns of the pure (S)-enantiomer were found. This is surprising since from DSC measurements the area of miscibility was considered to be smaller than 74 wt% (S)-enantiomer (see next but one section). Instead, a fourth pattern was found. The pattern c) of Figure 3.2 represents a sample of 77 wt% (related to dry matter) of the (S)-enantiomer and shows explicit differences with respect to the patterns of the stable racemic compound and the enantiomer. Two new reflections at 23.3° and 24.1° 2θ were observed, while the specific reflection of the metastable β-form at 20.4° remained constant. This allows an interpretation, that involves more than one stoichiometric compound. Andersson *et al.* [136] claimed that an 'anomalous racemate' exists in the Malic acid system exhibiting an enantiomeric ratio of 2:1. Thus, the question was raised whether this pattern represents a *mixed crystal* involving the *metastable* racemic compound (*MCM*, case A) or whether this is a non-racemic compound (compound II) exhibiting a (hidden) dystectic or peritectic point (case B). The solid phases for both possible cases are summarised in Table 3.1.

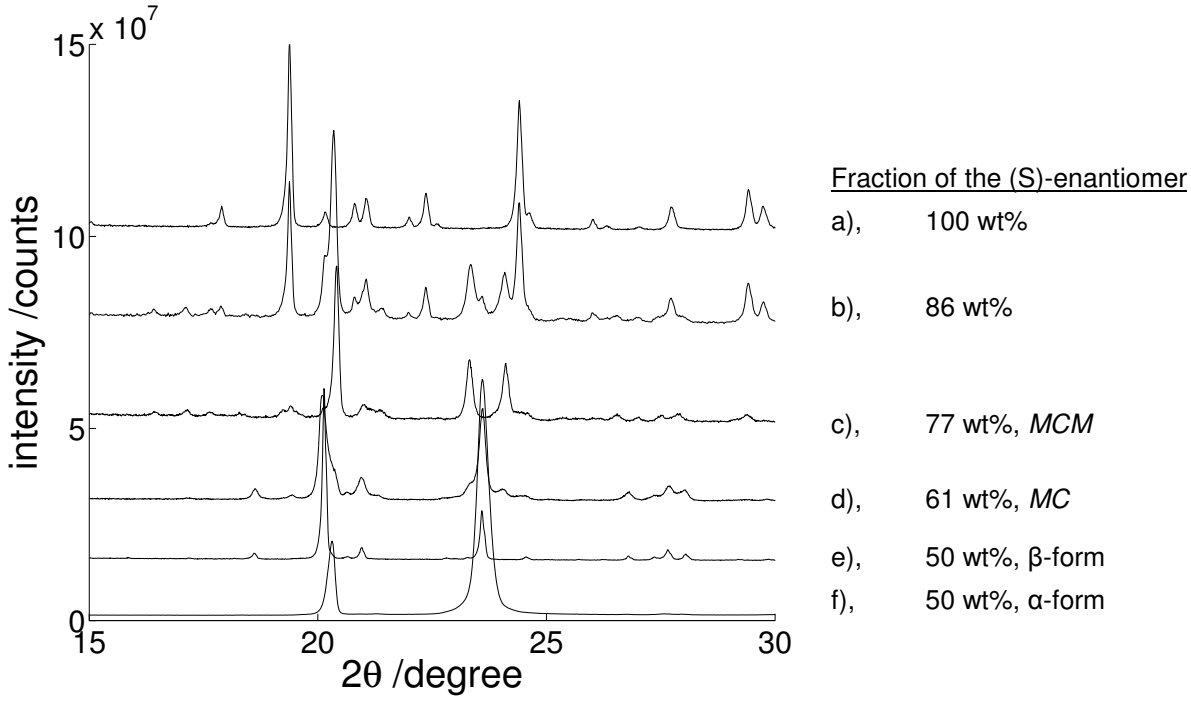

Figure 3.2 *XRPD patterns of the enantiomer a), the two polymorphs of the racemic compound e)/f) and two different mixed crystals d)/ c) and a mixture b).*

The pattern b) represents a sample of the solid phase of 86 wt% (S)-enantiomer. Superposition of the patterns of phases of the pure enantiomer and *MCM* is visible. Considering the case B the composition of the new compound is clearly below 86 wt%, probably close to 80 wt% of the (S)-enantiomer. In contrast to *MC*, no shifts of a certain reflection of this pattern due to changes of the composition of partial solid solutions have been determined.

Table 3.1 *Summary of observed solid phases. Common phases are denoted by full dots, open dots compare two possible interpretations.*

case A (Kaemmerer *et al.* [90])	case B (Andersson *et al.* [136])
• (S)-enantiomer • stable racemic compound (α-form) • metastable racemic compound (β-form) • mixed crystals involving the stable α-form (*MC*)	
○ mixed crystals involving the metastable β-form (*MCM*)	○ existence of a 2:1 stoichiometric compound II

Solid phase identification by ATR FT-IR

Solid phase samples were investigated by ATR FT-IR in order to obtain a better insight into the phase variations by use of an orthogonal measurement technique. Some spectra of solid phase samples from the measurement of tie lines are drawn together with the (S)-enantiomer and the two forms of the racemic compound in Figure 3.3 and Figure 3.4. It can be seen from both figures that the spectra of the stable racemic compound (α-form), the (S)-enantiomer and the metastable racemic compound (β-form) differ significantly in the range of 500-1000 cm^{-1} and in the range of 3200-3600 cm^{-1}. For the latter variations in the oscillation of the hydroxyl group due to differences in the intermolecular bonds appear to be likely.

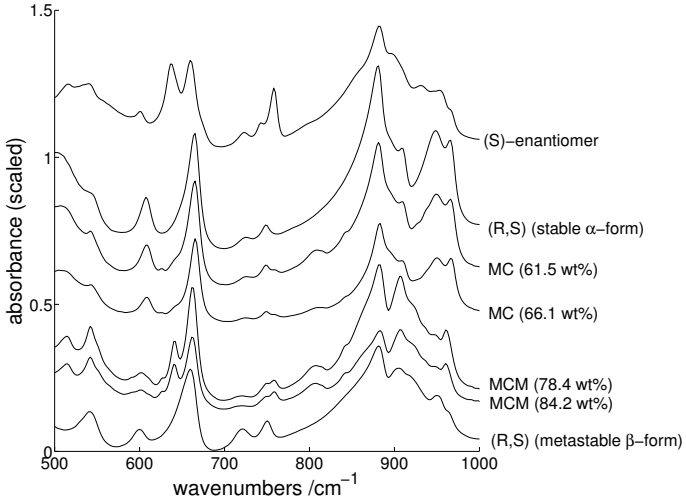

Figure 3.3 *FT-IR spectra of the five recognised solid phases in the fingerprint region. MC is very similar to the stable racemic compound, while MCM clearly resembles the metastable compound between 800 and 1000 cm-1.*

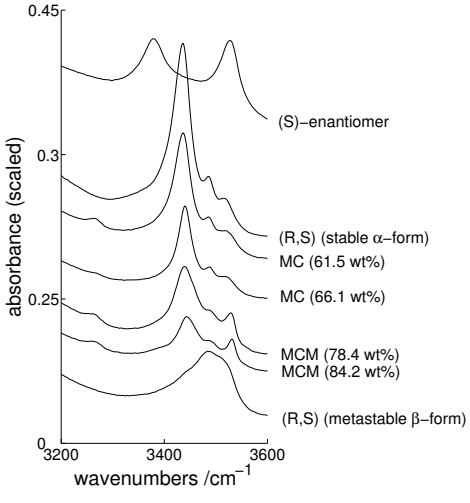

Figure 3.4 *FT-IR spectra at higher wavenumbers. The spectrum of the metastable racemic compound MCM appears completely different.*

The series increases by the amount of the (S)-enantiomer. The spectrum of the α-form of the racemic compound is very similar in comparison with the spectra from samples of 61.5 wt% and 66.1 wt% (S)-enantiomer. By contrast the spectra of samples composed of 78.4 wt% and 84.1 wt% (S)-enantiomer agree with bands of the β-form in the range of 800-1000 cm^{-1}, in

particular at 920 cm^{-1}. The samples show the band of the (S)-enantiomer at 650 cm^{-1} additionally.

Interpretation of DSC results

In the TG-DSC analysis up to a temperature of 408 K (<< 1 wt%.) only minor thermal degradation of Malic acid was observed. Thus, results of the DSC should be hardly influenced from that side and the measured enthalpy and temperature of fusion can be considered as accurate. Accelerated substance degradation occurs above the melting temperature. Unfortunately, liquid Malic acid did not recrystallise upon cooling. Therefore an often conducted procedure (mechanical mixing of enantiomers→ heating and melting→ cooling at different rates and recrystallisation→ slowly heating), which can indicate the formation of metastable phases, was not feasible.

DSC measurements of the pure (S)-enantiomer and the (R,S)-Malic acid showed melting temperatures of 376 K and 401 K and specific melting enthalpies of 197 J/g and 249 J/g respectively. These values are in good agreement with data obtained by Ceolin *et al.* [135]: 376 K, 402 K and 200 J/g, 250 J/g.

Figure 3.5 exemplifies measurements obtained from physical mixtures of the enantiomers between 50 wt% and 76.5 wt% of the (S)-enantiomer. The heat flow curves show a stepwise disappearance of the eutectic melting peak with decreasing fraction of (S)-Malic acid in the mixture. This observation is a hint for the existence of mixed crystals in the region. Instead of melting of the single enantiomer, continuous melting of the racemic compound together with the incorporated enantiomer occurs up to the liquidus line.

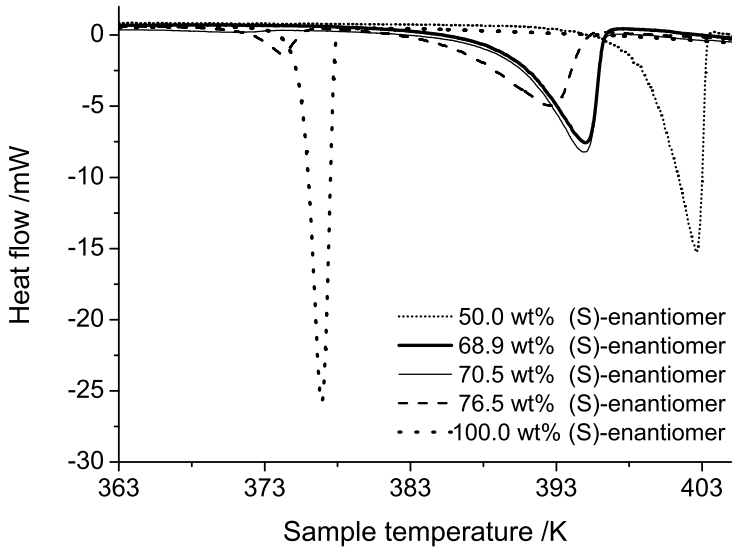

Figure 3.5 *DSC curves of physical mixtures of Malic acid enantiomers in the vicinity of the limit of solid solutions. The eutectic melting peak disappears between 70.5-68.9 wt%. The melting curves of the pure enantiomer and the racemic compound are shown additionally.*

A composition with 68.9 wt% (S)-enantiomer features no peak for the eutectic line, while samples with a slightly higher fraction of the (S)-enantiomer show deviations from a straight baseline. Mixtures of higher excess of the (S)-enantiomer led to a typical melting curve with one peak representing the eutectic temperature and the second peak indicating the temperature at the liquidus line for this

composition. Thus, boundaries of the partial solid solutions at elevated temperatures can be identified by DSC measurements. From literature a lower melting β-form of the racemic compound is known [134, 135]. While Ceolin found the β-form preferably after crystallisation from acetone and the α-form from water, here the complementary case was observed; the α-form was mainly obtained from acetone. The measured thermodynamic properties of this lower melting form ($T^{f}_{(R,S)} = 395 \quad K$, $\Delta h^{f}_{(R,S)} = 225 \quad J/g$) furnished proof that the same phase was considered (Ceolin *et al.* [135]: $T^{f}_{(R,S)} = 396 \quad K$, $\Delta h^{f}_{(R,S)} = 225 \quad J/g$).

It was found that the rate of supersaturation generation induced by solvent removal through evaporation has major effects on the formation of a particular polymorphic form. Fast evaporation of the solvent favoured the formation of the β-form for both used solvents. Nevertheless, the metastable form was obtained from acetone by fast solvent removal at vacuum only, while this form crystallised from water from much lower evaporation rates also. Subsequently the generation of the stable α-form from water was obtained from very low evaporation rates only.

Kuhnert-Brandstätter and Friedl [134] investigated the Malic acid system in order to explain certain discontinuities of the liquidus line and found the β-form finally. They claimed the interception of the regions of existence of the two polymorphs to cause a discontinuous liquidus line. This implies that the polymorphic forms are of enantiotropic type and a transition temperature was suggested to be close to 393 K. Unfortunately, no experimental work was undertaken in this regard. Thus, a larger sample of the β-form was kept clearly below this transition temperature for three weeks at ambient temperature. Fractions of the sample were taken for regular DSC measurements. After two weeks a fraction of the remaining sample was put to an oven and kept at 353 K to enhance the kinetics of solid phase transitions. The temperature was still 40 K below the supposed transition temperature. Figure 3.6 shows the heat flow curves obtained from the DSC measurements. The initial sample at t=0 days melted at 395 K.

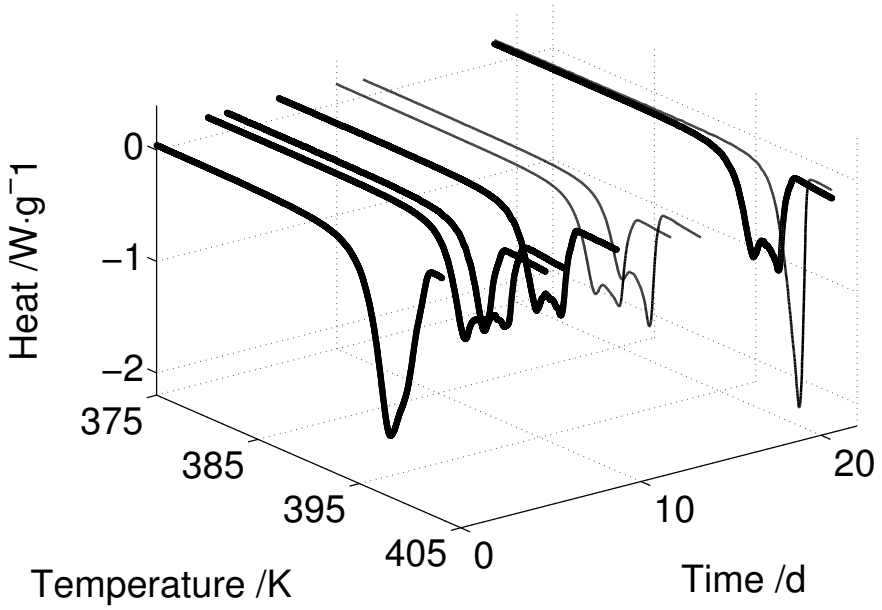

Figure 3.6 *Time resolved DSC heat flow curves of an identical sample of the metastable racemic compound (β-form) over three weeks. A second melting peak appears, indicating the transformation of the metastable towards the stable modification of the racemic compound (bold lines indicate storage of the sample at ambient temperature, while thin lines represent annealing of the sample at 353 K).*

A peak shoulder having its origin in the higher melting form is present here already. During two weeks a solid phase transition towards the higher melting phase was visible. The transition was accelerated by higher temperatures; after three weeks the stable higher melting phase was present only. Thus, the observed β-form was a monotropic modification of the stable α-form. The relationship of the two modifications is in agreement with the *heat of fusion rule* [22]. The form melting at higher temperatures has the larger heat of fusion ($\Delta h^{f}_{(R,S)}$).

Figure 3.7 summarises the results obtained from DSC measurements as well as the conducted phase analyses. Triangles on the right half represent DSC peaks (liquidus line) and onset values of eutectic melting peaks. The initial slope of the solvus line can be derived from the decaying temperature of the 'eutectic' melting peaks close to the area of solid solutions. Lines, which are drawn through, represent curves calculated by equations of Schröder and van-Laar (2.17) and Prigogine-Defay (2.39). Both equations were applied in their simplified form without the minor contribution of the two heat capacity terms which tend to compensate mutually [16]. The eutectic composition of the stable system was calculated to 96.7 wt%. The experimental valued (Figure 3.7) was found to differ only slightly from the calculated intersection of the two liquidus lines. The small gap between the eutectic point and the pure enantiomers did not allow reasonable statements regarding partial miscibility in this narrow region.

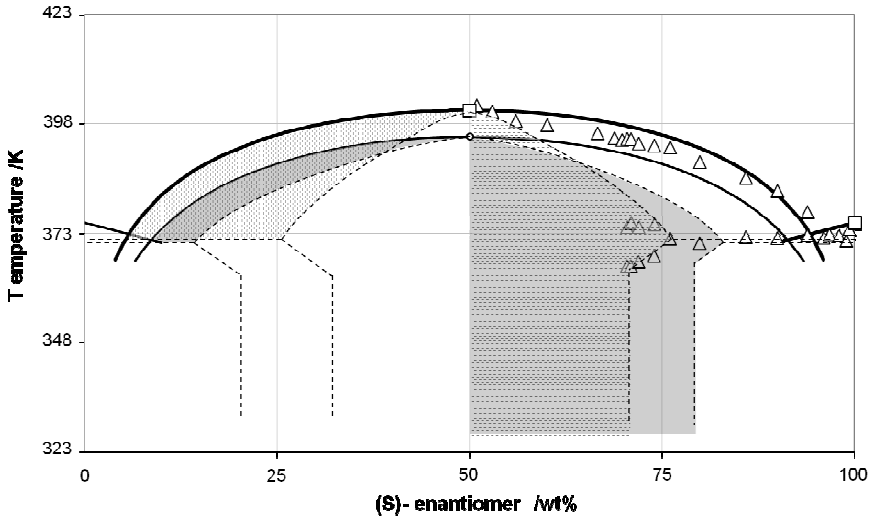

Figure 3.7 *Binary melting phase diagram of Malic acid. The two modifications of the racemic compound and the corresponding two different liquidus lines are shown. The differently shaded areas in the right half of the figure stand for the areas of mixed crystals of the stable (MC) and the metastable racemic compound (MCM), respectively. The same colours in the left section (0-50 wt% (S)-enantiomer) represent the areas between the liquidus and the solidus line of MC and MCM (triangles: measurements; bold lines: calculated curves; dotted lines: assumed phase boundaries drawn to guide the eye).*

The upper liquidus line represents the stable α-form, the thinner lower line indicates the metastable β-form. No intersection of the two lines is visible due to polymorphism of monotropic type as stated above. The heat and temperature of fusion of the three phases were used for the description of the liquidus lines as described. It is assumed that the measurement values of the mixtures (Figure 3.7, triangles) must not be assigned to the metastable phase. This could be easily assumed, since the two liquidus lines seem to confine the area of the values. XRPD measurements confirmed, that the stable form was present prior to the DSC measurements. It should be noted that for systems, which exhibit monotropic behaviour, any

heating simplifies the transition of the metastable phase towards the stable phase [138]. Thus, it is possible that the phase transition can take place already before or during melting of the metastable phase.
The dashed lines in Figure 3.7 define, in addition, assumed phase areas. The hatched region in the left half of the figure (25-50 wt% of the (S)-enantiomer) indicates the existence of mixed crystals of the stable racemic compound (*MC*) and the enantiomer in excess, while the (underlying) gray region represents the limits of the equivalent region for mixed crystals of the metastable racemic compound (*MCM*). It should be noted that the eutectic melting occurs at slightly lower temperatures in the case of the metastable form and the width of the area of solid solution is extended (15-85 wt% of the (S)-enantiomer). The latter is exemplified in the right half of the figure (gray area: region of existence of mixed crystals involving the metastable form (*MCM*); hatched region: stable form- *MC*).

At this point both, the interpretation given by Figure 3.7 and the proposed 2:1 compound by Andersson *et al.* [136], are possible options. The latter, case B, is shown in Figure 3.8 for completeness. Here, the liquidus line of an additional compound II is drawn, leading to a peritectic point at the intersection with the liquidus line of the racemic compound (bold lines). The (underlying) gray region represents again the limits of the region of partial solid solutions. Small deviations regarding the eutectic composition can be explained easily by this figure. Tabora *et al.* have shown [32], that the correct intersection of the liquidus lines should be described by use of the thermodynamic properties of the additional compound II.

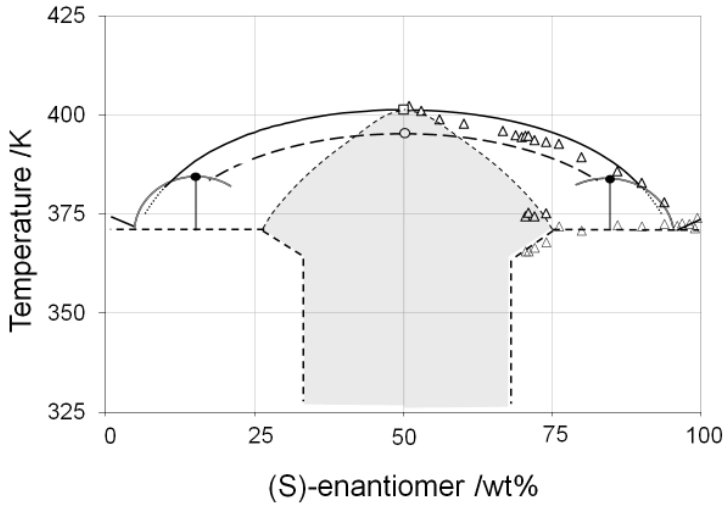

Figure 3.8 *Another interpretation of the binary phase diagram showing a second compound. The interpretation is confirmed by the measured melting points and the XRPD pattern of MCM, while tie lines determined in the next section proved this option to be impossible (triangles: observed melting peaks; open dot: determined melting point of the metastable racemic compound).*

The presence of the additional phase cannot be derived from DSC or XRPD measurements alone. The results obtained here illustrate the need for a combination of different measurements techniques. Tie line measurements are necessary to clarify which phase interpretation is correct and which is wrong.

S/L-equilibria and tie lines of the Malic acid/acetone system

The ternary phase diagram was estimated on the basis of solubility isotherm measurements at five temperatures (Figure 3.9a: 293 K, 298 K, 303 K, 308 K, 313 K) and again with the knowledge of the slopes of certain tie lines (Figure 3.9b). All measurements were restricted to the half of the (S)-enantiomer, since both sides of the phase diagram must appear in symmetric manner. Full squares in Figure 3.9b indicate the initial composition of the tie line measurements at 298 K. Open signs link the resulting compositions of the liquid with the solid phase.

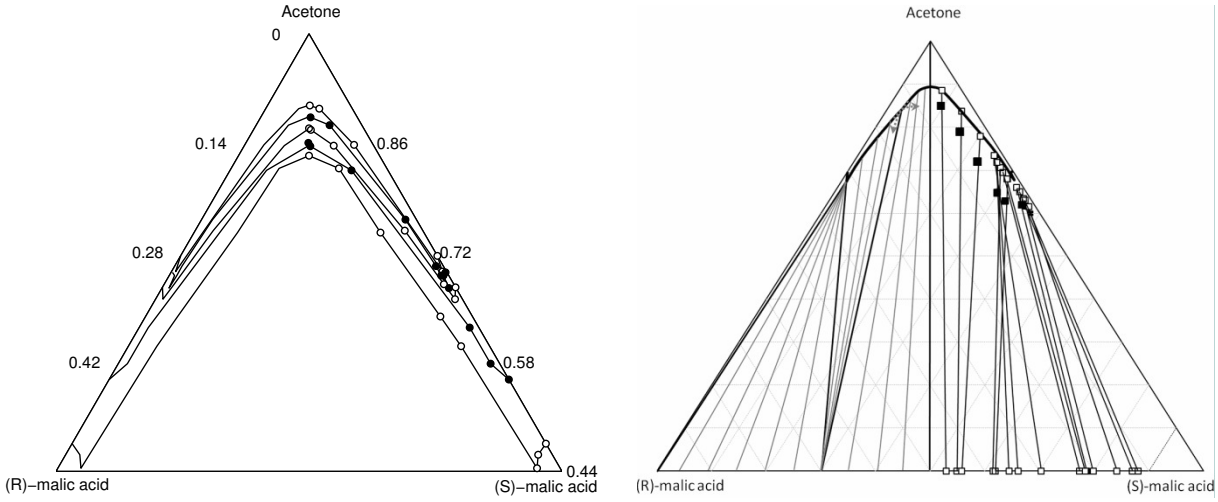

Figure 3.9a/b *Determined phase equilibria of the solubility isotherms in the Malic acid/acetone system at 293, 298, 303, 308 and 313 K. Solubility increases with temperature. Full dots (initial composition) and open dots (composition of the solid and liquid phase after equilibration) denoted results of measurements, lines are guide to the eye. The eutectic composition shifts slightly towards lower optical purity with increasing temperature. The right half plane of b) shows the determined tie lines at 298 K. The left half plane allows the direct comparison with the slopes of tie lines in a system exhibiting a hidden peritectic.*

For completeness, the possible tie lines for a dystectic or peritectic point of a second compound as discussed above were sketched in the left half plane. Its existence can be ruled out from Figure 3.9b, since reasonable agreement of the tie lines in the left (existence of compound II) and right half plane (measurements) of Figure 3.9b is not given. Thus, a partial solid solution involving the metastable racemic compound (*MCM*) must exist and indeed the determined tie lines fit well to the interpretation introduced in Figure 3.10. The ternary phase diagram involving the stable and the metastable modification of the racemic compound are shown in a decoupled manner in Figure 3.10b.

The eutectic composition of the stable compound identified by equilibriation experiments was identified to be slightly higher (98.5 wt%) in comparison to DSC results (96.7 wt%). This may be due to the large difference in temperature between the melt and the solution. As a consequence the outer 2-phase region, denoted as *D*, is very limited in size and the inner 2-phase region dominates the phase diagram. The latter area is even extended, since a large area of partial solubility needs to be considered (capital letters A/ B in Figure 3.10a/b).

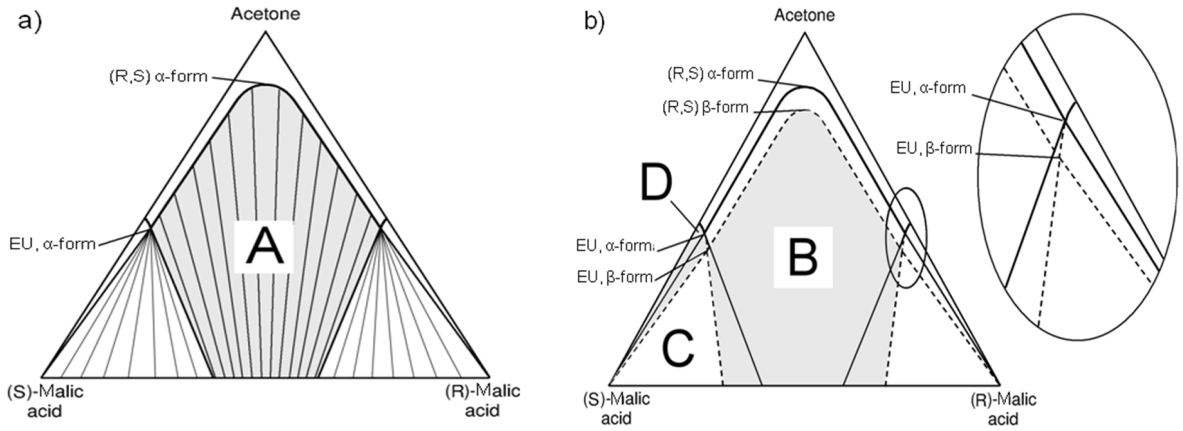

Figure 3.10a/b *Description of phases in the ternary phase diagram. (R,S) α-/β-form: stable/metastable racemic compound; EU, α-/β-form: point of eutectic composition in the system involving the stable/metastable racemic compound; A in a): 2-phase area of MC and saturated solution; B in b): 2-phase area of MCM and saturated solution; C in b): 3-phase area of the enantiomer, MCM and the saturated solution of eutectic composition (EU, β-form); D in b): 2-phase area of the enantiomer and the saturated solution; C and the difference of B and A together yield the second 3-phase region, which is made up of MC, the enantiomer and the saturated solution of eutectic composition (EU, α-form).*

The tie lines given can be assigned to four different regions according to the capital letters *A*-*D*:

A: MC: Incorporation of the (S)-enantiomer into crystals of the stable racemic compound. No other solid phase was found from XRPD and ATR FT-IR measurements for these samples. The measured solid phases close to the racemic compound do not exhibit a ratio of 1:1 but up to 70 wt% of the (S)-enantiomer according to the tie lines and results of DSC measurements. Therefore the intersection with the baseline is shifted from the centre of the diagram (at 0 wt% acetone) towards the side of the (S)-enantiomer. The mass balances of these tie lines are fulfilled regarding the two enantiomers in the liquid and the solid phase. It is assumed from the conducted measurements, that the limit of the partial solid solution of the stable racemic compound is not shifted by temperature.

B: MCM: The second region contains tie lines with solid phase compositions in the range of 15-~85 wt% (S)-enantiomer. The amount of the metastable phase increases continuously whilst the solid phase composition approaches the side of the enantiomers. Solid phase samples exhibited XRPD patterns of MCM, incorporation of the (S)-enantiomer into the lattice of the metastable racemic compound took place. Since the performed DSC measurements are based on the stable racemic compound only, it can be followed that incorporation of the (S)-enantiomer into the lattice of the metastable compound occurs at even larger extent. Nevertheless (very weak) reflections of the (S)-enantiomer could be determined. Additionally, patterns of MC were found. It is presumed that this was due to incomplete washing of the crystals.

C: The third region (3-phase region: metastable racemic compound/ (S)-enantiomer/ saturated solution) is defined by an increase in solubility and large differences in the XRPD patterns. The patterns of the metastable racemic compound are accompanied by intensive reflections of the (S)-enantiomer patterns.

D: Region D is the domain of the pure enantiomer and the saturated solution. Due to the narrow region of existence no experiments have been performed here. The metastable racemic compound becomes the prevailing crystalline phase at higher enantiomeric excess. Thus, the curves of the isotherms cannot be assigned completely to the stable form of Malic acid crystals. Region *B* spans over large parts of the region *A*, but the metastable compound is not stable in this area. It was found from some solid phase samples, that the eutectic composition was shifted to lower enantiomeric excess whilst higher solubility was determined. It is evident, that the composition of the eutectic point depends on the prevailing phase and so does the phase boundary between regions *D* and *C*.

3.2.2 Modelling of solid/solid interactions

Deviations of experimental data in Figure 3.7 from the calculated lines are due to the non-ideal behaviour of the substances in the melt and in the solid phase. The approach by Prigogine and Defay (Eq. (2.39)) is inadequate for this system between 25-75 % (S)-enantiomer, since the equation is limited to cases, in which miscibility in the solid phase does not exist and activity coefficient are therefore unity. Thus, the application of Eq. (2.39) is thermodynamically consistent only at the outer regions. Correlation of the measured data and the NRTL model (Eqs. (13)-(18) of Table 2.1) leads to the curve of the liquidus line in Figure 3.11. The area between 25-75 % (S)-enantiomer was estimated by the model, too. Larger deviation between the model correlation and experiments were found mainly in the latter section; these can be attributed to the non-idealities in the melt and the discussed model insufficiencies. There are a few approaches for solid phase compounds of different compositions in the recent literature (Tabora *et al.* [32, 139]), but partial solid solutions have not been modelled in more detail so far. A consistent approach, that accounts for the miscibility of enantiomers in the solid phase by use of a simple activity coefficient model is proposed below. It is related to a model by Slaughter *et al.* [140].

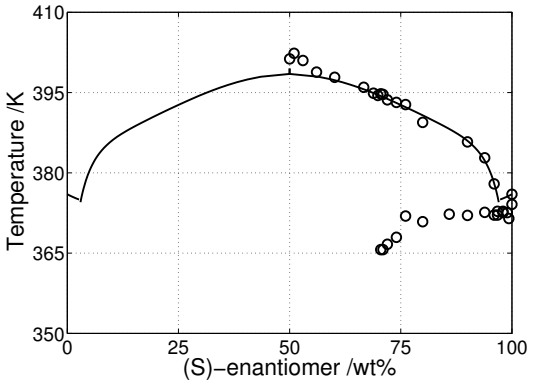

Figure 3.11 *Liquidus line as obtained from the approach by Prigogine and Defay and the NRTL model.*

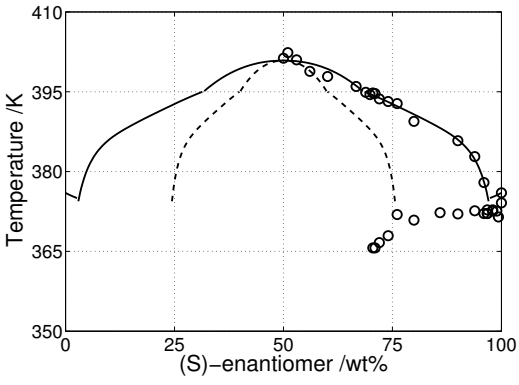

Figure 3.12 *Liquidus line as obtained from an approach considering non-ideal mixing in the solid state. Dashed lines represent the computed corresponding solidus line.*

The relation of the species in the solid phase and in the liquid phase can be expressed by a general chemical reaction equilibrium. The reaction equilibrium constant K is hereby described by the Gibbs free energy of reaction ΔG and a prefactor A.

$$K = \prod_{i=1}^{c} \left(z_i \gamma_i^s \right)^{\nu_i} \qquad (3.1)$$

$$K = A \cdot \exp\left(-\frac{\Delta G}{RT} \right) \qquad (3.2)$$

Eq. (3.3) can be derived for the given binary system of the enantiomers (S) and (R), with z_i being the fractions in the solid phase and γ_i^s being the corresponding activity coefficients.

$$A \cdot \exp\left(-\frac{\Delta G}{RT} \right) = \frac{z_{(S)} \gamma_{(S)}^s z_{(R)} \gamma_{(R)}^s}{x_{(S)} \gamma_{(S)} x_{(R)} \gamma_{(R)}} \qquad (3.3)$$

The interactions in the solid phase are considered to be rather complex. It is not clear, whether any model, that has been developed in the frame of fluid phase interactions is capable of reflecting non-ideal solid phase behaviour. For this reason as a rather simple approach the 1-constant Margules equation (Table 2.1, Eqs. (1)-(4)) was chosen and evaluated, being aware of its physical limitations. In order to estimate the three parameters A, ΔG and A_{ij} (Eq. (3.2); Table 2.1, Eq. (3)) a relation of the composition of the liquid and the solid phase needs to be assumed. At the racemic composition the liquid and the solid phase composition coincide, while at the eutectic composition of the liquid phase, the composition of the solid phase is the limit of the solid solution, *i. e.* 75% (see chapter 3.2.1). The simplest function is given by a linear interpolation in between these boundaries. In summary, the activity coefficients for the liquid phase were applied as derived for Figure 3.11 and the 1-constant Margules equation and Eq. (3.3) was fitted again against the determined liquidus curve data.

Table 3.2 *Optimised parameters for the representation of partial solid solutions of Malic acid.*

Relation for x_i/z_i	$f(x_{(S)})=0.54348x_{(S)}+0.22826$	
NRTL	α	9.1625e-2
	Δg_{12}	2.7241e4 kJ mol^{-1}
	Δg_{21}	-1.5609e4 kJ mol^{-1}
1-constant Margules	A_{12}	3.0592e2 kJ mol^{-1}
Reaction equilibrium constant K	A	3.7351e4
	ΔG	-3.7333e4 kJ mol^{-1}

The obtained parameters are given by Table 3.2 and the resulting liquidus line is shown in Figure 3.12. The agreement of the prediction with experimental values has improved clearly, moreover the proposed functional relation of the liquidus and the solidus lines appears to be feasible. Thus, the Malic acid system provides one example, for which interactions in the solid phase are very relevant for the course of the liquidus line. The simple model introduced here, provides one approach, that accounts explicitly for non-idealities in the (partial) solid solution.

3.2.3 Considerations regarding the molecular structure

Three crystal structures of Malic acid are known– the enantiomer and two polymorphs of the racemic compound [135]. In addition two regions of partial solid solutions of compositions in the range 30-70 wt% and 15-85 wt% (S)-enantiomer are found. Within this chapter the three known crystal structures are investigated for a structural understanding of this behaviour.
In all three structures, the carboxylic acids form hydrogen-bonded dimers, which are then linked into chains. This is a common motif for linear dicarboxylic acids *e. g.* terephthalic acid [141-143] and adipic acid [144] in solution and also in the crystalline phase. There are various bonding options, both intra- and intermolecular, for the hydroxyl hydrogen atom.
The XRPD patterns, the unit cell parameters and the atom configuration of the three crystal structures have been used as taken from the Cambridge Crystallographic Data Centre [145] (CCDC). Unfortunately, not all hydrogen positions are available from the database.

There is one conformation in the structure of the stable racemic compound (Z'=1, Figure 3.13). The carboxylic acid groups are not co-planar but twisted. The chains contain alternating (R) and (S) molecules linked 'head to head' and 'tail to tail'. The carboxylic acid groups are linked by intermolecular hydrogen bonds.

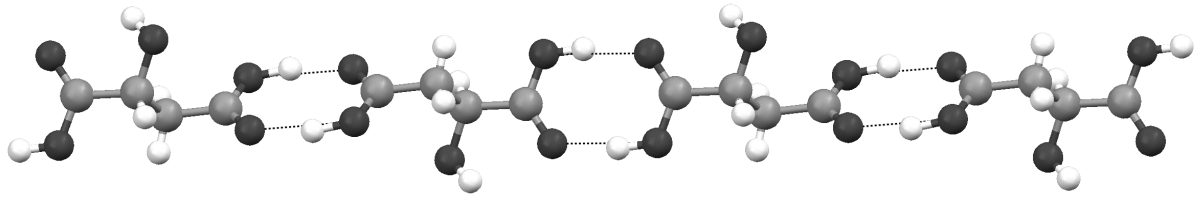

Figure 3.13 *Molecular structure of the dicarboxylic acid chain of the stable (R,S)-Malic acid (α-form) (heterochiral (R)-(S)-(R)-(S); 'head-head', 'tail-tail').*

There is further one conformation in the structure of the metastable racemic compound (Z'=1). This conformation is very similar to the conformation in the stable racemic compound (Figure 3.14). The chains contain alternating (R) and (S) molecules linked 'head to tail'. Intermolecular hydrogen bonds are denoted only, since the positions of hydrogen atoms of the carboxylic acid groups and the hydroxyl groups of this compound are not listed in the CCDC database.

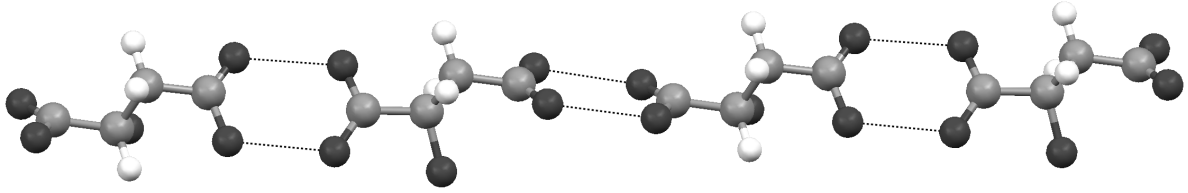

Figure 3.14 *Molecular structure of the dicarboxylic acid chain of metastable (R,S)-Malic acid (β-form) (heterochiral (R)-(S)-(R)-(S): 'head-tail').*

The chains of the (S)-enantiomer contain two crystallographically independent molecules (Z'=2) that alternate. The conformations of these two molecules are significantly different. One conformation is very similar to that observed in the racemic compounds. The other differs significantly in the relative orientation of the two carboxyl groups, which are much more nearly co-planar. This allows the hydroxyl hydrogen to form an intramolecular hydrogen bond with an

oxygen atom of the carboxylic group, as shown in Figure 3.15. The linkages between molecules in the chain are alternately 'head to head' and 'tail to tail'.

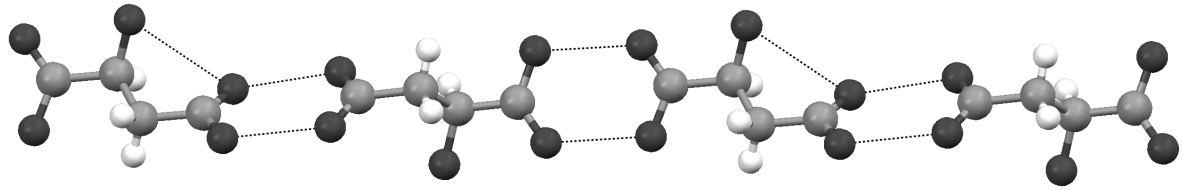

Figure 3.15 *Molecular structure of the dicarboxylic acid chain of (S)-Malic acid (homochiral (S)-(S)-(S)-(S); head-head; tail-tail).*

The strongest intermolecular bonds in all three structures are the hydrogen bonds holding the chains together. These chains can form with either enantiomer or with both in equal proportions, i. e. they are not themselves chirally specific. This is consistent with the ability to form solid solutions.

However the observations are more subtle. Two kinds of partial solid solutions are observed, and only from the racemic compounds (s. chapter 3.2.1). There is no evidence for solid solution formation in the enantiomer structure. Moreover from experimental findings only the stable racemic compound structures were found to accommodate non-stoichiometric R:S ratios in the range of 30-70 wt% (S)-enantiomer.

The presence of two significantly different molecular conformations in the (S)-enantiomer structure prompted an investigation into the relative energies of these two conformations. A geometry optimisation method was applied on a chain of (S)-enantiomers of both conformations in order to identify the preferred conformation. The bond type has been adjusted manually and missing hydrogen atoms were added by use of the commercial software package Materials Studio 4.3 (Accelrys, USA). The DMol3 module was used for geometry optimisation. Hereby the type of the exchange-correlation potential was the Perdew-Burke functional (PB) and the local correlation was replaced by the gradient-corrected potential by Vosko-Wilk-Nusair (GGA-VWN). The basis for the number and type of atomic orbitals was DNP, version 4.0.0. Further the COSMO solvation scheme with parameters for the solvent acetone was applied. The calculations indicate that the energetically preferred molecular conformation (Figure 3.16) is similar to the conformation in the racemate structures.

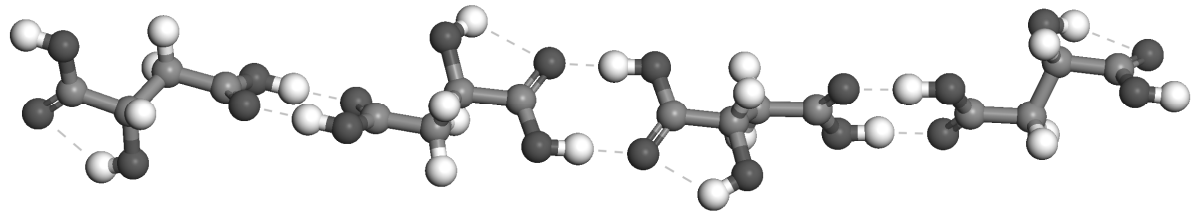

Figure 3.16 *Structure of the (S)-enantiomer chain after DFT geometry optimisation.*

When the single enantiomer crystallises, a second, less energetically favourable conformation is present. It may be that this second conformation is necessary to create chains with a crystallographic repeat that can pack in a crystal structure. This would be consistent with the lower stability (lower melting point and melting enthalpy) of the (S)-enantiomer crystals.

The structure of the stable racemic compound contains 'head to head' dimers of (R) and (S) molecules. Homochiral 'head to head' dimers are found in the enantiomer structure. It is

plausible that these could be incorporated into chains in the structure of the stable racemic compound. However the hydrogen bonding between the chains would be disrupted. Moreover, complete substitution of one enantiomer by the other does not appear possible. It is tempting to suggest that the structure of the stable racemic compound can accommodate an (R,S)-(S)-(S)-(R,S) sequence, but not an (R,S)-(S)-(S)-(S)-(R,S) sequence. This would be consistent with a restricted stoichiometry of a solid solution of 66 wt%.

The formation of partial solid solutions involving the metastable racemic compound cannot be explained from considerations on the molecular structure alone. The formation of chains consisting of metastable-(R,S)-(S) are hindered and presumably energetically unfavorable. Accordingly the changes to the crystal lattice should be larger. In fact, the recorded XRPD patterns vary substantially upon formation of the partial solid solution involving the metastable racemic compound. More detailed molecular modeling activities to investigate the solid state might help in future to figure out, which structure should be expected here.

3.2.4 Chiral separation in case of occurrence of mixed crystals

The initial and the final composition of a crystallisation process are determined by the thermodynamics, while the linking trajectory between the latter points is influenced by the crystallisation kinetics. It was further investigated in this work whether the solid phase undergoes a certain development of the crystal lattice composition during supersaturation depletion. Prior to these experiments, the metastable zone width (MSZW) was determined. Some results can be seen in Figure 3.17.

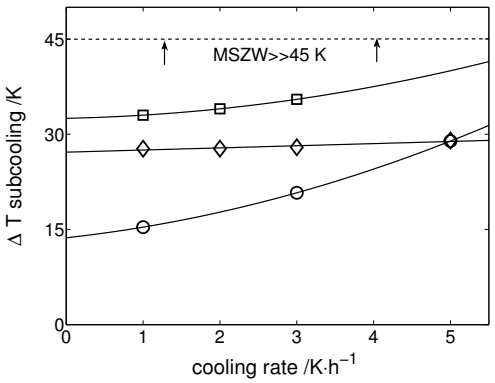

Figure 3.17 *Results of the metastable zone width measurements of Malic acid in acetone ($T_{saturation}$=318 K). The MSZW differ significantly for the (S)-enantiomer (circles) and (R,S)-Malic acid (diamonds). Squares denote a solution of 60 % (S)-enantiomer. A solution of eutectic composition did not crystallise upon subcooling below 45 K (dashed line). Lines are guide to the eye.*

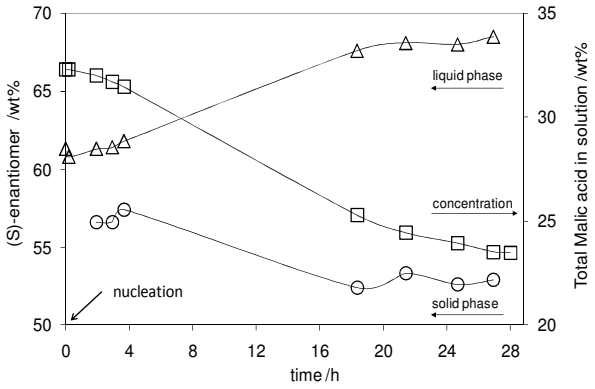

Figure 3.18 *Concentration and composition trajectories after primary nucleation of an asymmetric mixture (60%) of enantiomers of Malic acid. The first crystals of MC show large incorporation of the enantiomer in excess. The (S)-enantiomer was released after 20 h and the MC crystals equilibrated.*

The MSZW of the racemic compound depends largely on the applied cooling rate while the MSZW of the (S)-enantiomer remains constant close to 30 K. The largest MSZW (> 45 K) was obtained for a solution of eutectic composition. Nucleation experiments have been conducted at rather low enantiomeric enrichment of 60 wt% (S)-enantiomer for this reason. The first crystals

obtained by primary nucleation upon cooling crystallisation showed larger incorporation of the (S)-enantiomer than deduced from the tie line equilibration measurements (Figure 3.18).
The enantiomeric excess in the solid phase decreased during supersaturation depletion and pointed towards the equilibrium value. The enantiomeric enrichment in the liquid phase due to the formation of the described crystals and the subsequent release of the (S)-enantiomer from these crystals can be seen in Figure 3.18.
Motivated by these findings, seeded crystallisation experiments have been conducted in order to investigate, whether the initial incorporation of the (S)-enantiomer in excess can be influenced.
Preferential crystallisation is a suitable chiral separation technique for this kind of compound-forming systems. The procedure was presented elsewhere in detail [105, 146] and was discussed briefly in section 2.4.1.2. In a first step a supersaturated solution is adjusted in such a way that the composition is located inside the 3-phase area of a ternary phase diagram. To this enantiomerically enriched solution in turns seed crystals of the enantiomer or the racemic compound will be provided in order to obtain periodically crystals of either the target enantiomer or to enrich the solution optically by crystallisation of the racemic compound.
Feed material for preferential crystallisation is often of eutectic composition after partial separation by *e. g.* chiral chromatography. Nevertheless, the single enantiomer can also be preferentially crystallised from a much less enriched solution, which is relevant and attractive for cases of elevated eutectic compositions (as considered here: 98.5 wt%). The feasibility to separate this system by preferential crystallisation is, however, limited according to the observations made during this study.

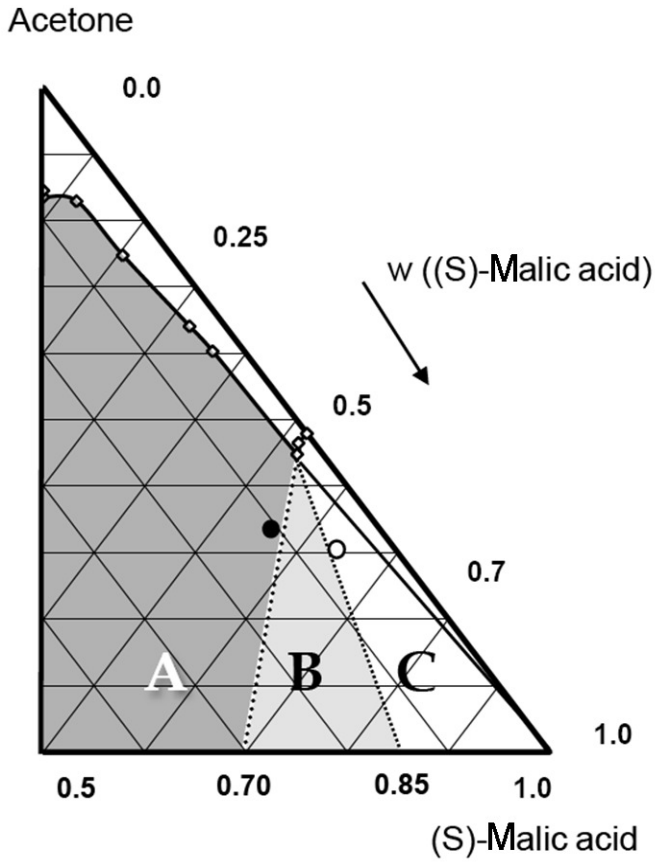

Figure 3.19 *Section of the ternary phase diagram (313 K) with three phase areas (regions A/B/C: Figure 3.10). Seeding with crystals of the (S)-enantiomer inside region A (full dot): dissolution of the seeds. Seeding within the (limited) 3-phase region C (empty dot): crystal growth.*

Firstly a slurry of the (S)-enantiomer was used as seeds and added to a supersaturated Malic acid/ acetone solution as described in the experimental section 3.1.1. The treatment of the seeds and the supersaturation of both points within the ternary phase diagram as shown in Figure 3.19 were the same. Repeated seeding within the gray area (A: full circle) resulted in dissolutions of the seed crystals, while seeding within the 3-phase area (C: open circle with composition >90 wt% (S)-enantiomer) caused initialisation of preferential crystallisation of the (S)-enantiomer. This rather higher initial enantiomeric excess in solution was necessary to enter the 3-phase region and to initiate crystal growth. In a second step seed crystals of the racemic compound (α-

form) were added to a supersaturated solution to force preferential crystallisation of the racemic compound. Upon crystal growth a large fraction of the (S)-enantiomer was incorporated in the solid phase. This effect was much more pronounced than expected. Sampling of the solid phase during crystallisation from an enantiomerically enriched solution exhibited a change of the optical enrichment within the MC crystals (Figure 3.20).

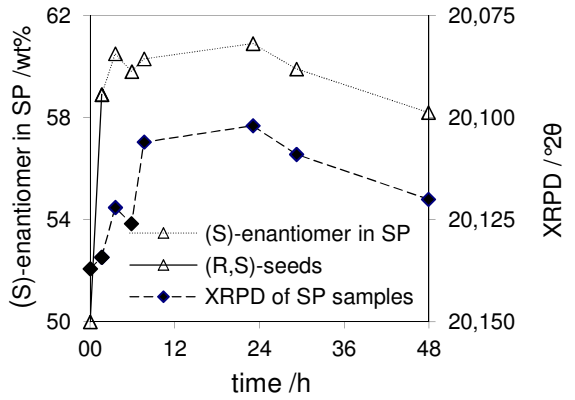

Figure 3.20 *Development of the solid phase (SP) lattice and composition after seeding with (R,S)-crystals (S=1.19; 6.75 mL seed slurry).*

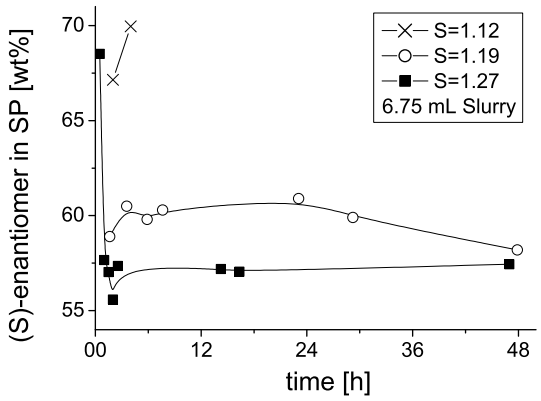

Figure 3.21 *Development of the composition of the solid phase (SP) with respect to the initial supersaturation.*

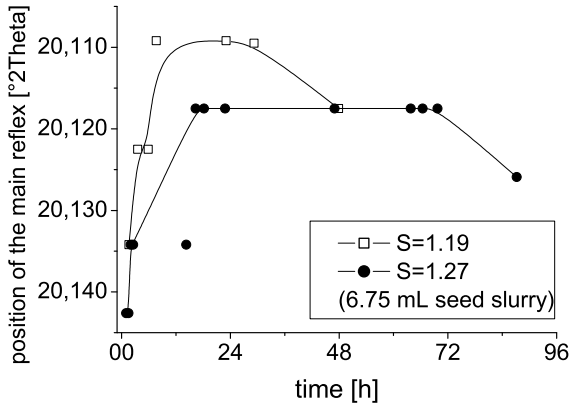

Figure 3.22 *Development of the position of the main reflex of the racemic compound with respect to the initial supersaturation.*

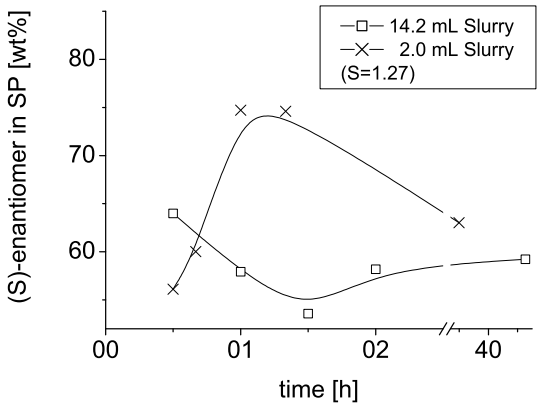

Figure 3.23 *Development of the composition of the solid phase (SP) with respect to the initial amount of seeds.*

The measured XRPD pattern of the stable racemic compound experienced only minor changes upon incorporation of the enantiomer in excess (Figure 3.2, patterns d) and e)). It was found that the change to the lattice is small but very specific. The larger the incorporation of the excess enantiomer and the consequent deviation from the equimolar ratio within the crystal, the larger was the shift of the main reflection at ~20.1° 2θ towards smaller angles. The change in the angle of the main reflection and the ratio of the enantiomers in the solid phase match up (Figure 3.20). Conducted TG-DSC experiments showed no evidence for substantial inclusion of mother liquor into the (R,S)-crystals. The direction exhibits a counter-trend with respect to the formation of the metastable phase (shift towards higher angles). This behaviour has been found for cooling as well as for seeding experiments. Further results of the seeding experiments with (R,S)-crystals

(α-form) and different initial conditions are shown by the following Figure 3.20 to Figure 3.23. The amount of the (S)-enantiomer within the solid phase increased always directly after seeding. Large differences were observed in the composition of the crystals by variation of the initial supersaturation (Figure 3.21 and Figure 3.22) at constant seed masses. The incorporation of the enantiomer in excess was especially large beginning with low supersaturations.Thermodynamic equilibrium was approached faster for larger driving forces. The formation of racemic crystals was not observed. The crystal lattice of the seeds was highly distorted if only a small seed amount was added. Incorporation of the enantiomer in excess was obviously kinetically favoured with respect to crystallisation of the racemic compound. For all cases an initial 'overshoot' of the 2θ value of the main reflection was detected, followed by a slow approach toward the 'equilibrium' 2θ value.
Any excess incorporation of the target enantiomer into crystals of the solid phase is especially unfavourable in terms of preferential crystallisation, because the mother liquor lacks the desired enantiomer. In principle the liquid phase should be enriched with the target enantiomer upon seeding with the racemic compound.

3.3 Summary

Within this chapter the binary phase diagram of Malic acid has been determined aiming to clarify the crystallisation behaviour for an example of a complex chiral system. The discontinuities of the liquidus line, which were proposed in literature as the result of an 'anomalous racemate' could be associated to the formation of partial solid solutions of the system. It was shown that the racemic compound crystallises in two different polymorphic forms. The lower melting metastable form obtained from water was not stable over time and was of monotropic type. Solvent mediation was of minor importance, since the metastable phase was obtained from water as well as from acetone at high solvent evaporation rates. The mechanism whether the metastable or the stable form was obtained from crystallisation, remaines still unclear.

It was observed, that in solution both the metastable and the stable racemic compound allowed the incorporation of non-stoichiometric quantities of the enantiomer in excess resulting in two phases (*MC* and *MCM*). This accounts for a stabilisation of the metastable racemic compound at large enantiomeric excesses in solution. While the disappearance of eutectic melting peaks for compositions ≤70 wt% of the enantiomer served as a good guide to estimate the limits of partial solubility of *MC* also in solution, a region of partial miscibility of *MCM* could not be identified. A simplified model was developed and applied for the quantitative description of the partial solid solution of *MC*.

The conclusions drawn from the results concerning the eutectic compositions and the extent of solid solutions are consistent with the data from solution studies. Five crystalline phases were obtained in total in crystallisation experiments from solution. The XRPD patterns of *MC* and *MCM* were consistent with two possible interpretations of the Malic acid system. Additional tie line measurements have become necessary to rule out the existence of a second intermediate compound of defined composition and proved that *MCM* is a second solid solution.

Investigations concerning the two regions of possible partially miscibility at the pure enantiomer sides of the melting phase diagram did neither confirm nor deny the existence of mixed crystals, since the regions were rather narrow.
Neither XRPD pattern nor FT-IR spectra or DSC measurements alone were found sufficient to clarify the co-existence of the different solid phases, that were found. The conducted additional elaborate experiments appear to be necessary to describe the regions of existence of all determined phases in a more quantitative manner.

The high eutectic composition (96-98.5 wt%) is not unfavourable for chiral resolution by crystallisation in general. Preferential crystallisation of the (S)-enantiomer was performed from solutions of smaller enantiomeric excess within this work. The major drawback was found in the formation of the large area of partial solid solutions of *MCM*, which was necessary to overcome by pre-enrichment of the mother liquor. Another difficulty in optical resolution of this system was recognised: enrichment of the mother liquor through crystallisation of the racemic compound was less successful, since large amounts of the target enantiomer were incorporated into the crystalline phase. All conducted crystallisation experiments yielded trajectories by which the thermodynamic equilibria were indeed approached. Experiments have shown that during the initial supersaturation depletion mixed crystals of even higher enantiomeric excess were formed. The lower the initial supersaturation and the seed mass, the slower equilibration took place and the higher the initial lattice distortion.

The study of the complex Malic acid system exemplified that extensive phase analysis can cause a multiplicity of possible consistent but also misleading phase interpretations. Important aspects of the formation of partial solid solutions of Malic acid were investigated. The findings contributed to the thermodynamic as well as to the kinetic understanding of the behaviour of such chiral system. The structured approach described here can serve as a guideline of how to determine the presence or absence and the extent of solid solutions and to assess the feasibility of chiral resolution for systems of enantiomers characterised by such complex phase behaviour.
A more comprehensive description of the conducted experimental work and conclusion drawn on the Malic acid system was published in the Journal of Crystal Growth and Design [90].

4 Solid/liquid equilibria in chiral systems

More than the absolute values for the solubility of an enantiomer in a given solvent, the shape of a corresponding solubility isotherm in the environment of a pair of enantiomers and one or more solvents is of interest for chiral separations. In particular the slopes of solubility isotherms and the eutectic composition are decisive for the ease and adaptability of known separation schemes for a specific solvent/substance system. While the measurement of binary systems can be done comparably fast and simple analytical techniques can be used (no demand for chiral specificity), the determination of thermodynamic data in the ternary or quaternary space is more cumbersome and chiral analysis techniques become necessary. Results on the model-based estimation of such data from binary systems considering different types of chiral systems and thermodynamic models are presented in the following. Within this chapter different models were evaluated, both on the basis of model compounds and further on compounds of pharmaceutical relevance. Hereby, an estimation model approach was combined with a correlative model to allow for predictions of chiral-specific interactions. Examples are given, how solvent systems can be tailored to simplify chiral separations by crystallisation.
The sources of thermodynamic data of the systems considered are referenced in the following sections. Individual data were obtained from the literature, sources of the research group of *Physical and Chemical Foundations of Process* Engineering' at the Max Planck Institute Magdeburg and, when missing, from own measurements.

4.1 Modelling conglomerate-forming systems

4.1.1 Investigated systems

Three chiral systems have been investigated exemplarily for this class of systems. The choice comprises an amino acid and an active pharmaceutical ingredient (API) in two different solvents. Emphasis was spent on their characteristic SLE properties and the theoretical description thereof.

Threonine/water
The amino acid Threonine is besides Asparagine the only proteinogenic amino acid, that does not form a racemic compound. Thermodynamic data on this compound is available from a number of publications [147, 148]. The molecular structure of the four stereoisomers was given already in Figure 2.1. This study is focussed on the pair of L-Threonine (2*S*,3*R*) and D-Threonine (2*R*,3*S*).
Commonly, amino acids decompose upon heating before melting occurs. This applies also to Threonine. Differential scanning calorimetry cannot be used to derive neither the heat of fusion nor the melting point and these important properties need to be estimated. The group

contribution method by Marrero *et al.* [149] reveals a melting point of 579.5 K and a latent heat of fusion of 38.4 kJ/mol for (2S,3R)-Threonine. Herein, the estimation was based on so-called second order groups. The average deviation of the estimation method is known to be smaller than 16 %. The obtained parameters can be used as suitable initial values and are supposed to vary within the given uncertainty during further optimisation procedures [83, 148]. In this case the parameters were kept as provided and have not been optimised further.

In Figure 4.1 the dependency on temperature of the solubilities of (2S,3R)-Threonine (full diamonds) and racemic Threonine (open dots) in water is illustrated. The solubility of the single enantiomer deviates largely from the ideal solubility (dashed line) as provided through Eq. (2.17) using the heat and temperature of fusion above.

The multicomponent NRTL model (s. Table 2.1, Eqs. (13)-(18)). with the expressions for two components in the case of a single enantiomer in solution (c=2) or three components in the case of a mixture of two enantiomers in solution (c=3) (i,j: constituents) was used to quantify non-ideal interactions in the solution. The three binary model parameters α_{13}, Δg_{13} and Δg_{31} ([1](2S,3R)-Threonine, [2](2R,3S)-Threonine, [3]water) were estimated by minimisation of the objective function *OF* and the gap between the composition depending solution temperatures at saturation and the temperatures of the experiments. The used Matlab (MathWorks, USA) routine utilised a Nelder-Mead optimiser.

$$OF = \min \sum_{k=1}^{N} T_{k,i}^{\exp}(x) - T_{k,i}^{calc}(\alpha_{ij}, g_{ij}, g_{ji}, x) \tag{4.1}$$

The parameter search was restricted to reasonable ranges. Temperature dependency of the activity coefficients was implemented in the NRTL model by the expressions provided in Table 2.1 (Eqs. (15) and (17)). Third and higher-order interaction terms of the NRTL model were neglected and consideration of the symmetry of the system allowed for a simplification of the model ($\Delta g_{13} = \Delta g_{23}, \Delta g_{31} = \Delta g_{32}, \alpha_{13} = \alpha_{23} = \alpha_{31} = \alpha_{32}$).

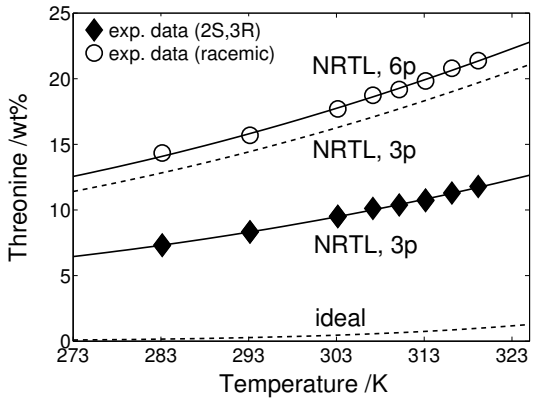

Figure 4.1 *Experimental solubility data of the single enantiomer and racemic Threonine in water [147]. Lines: NRTL model with different parameterisations (3-parameters and 6-parameters) [147] and ideal solubility (lower dashed line).*

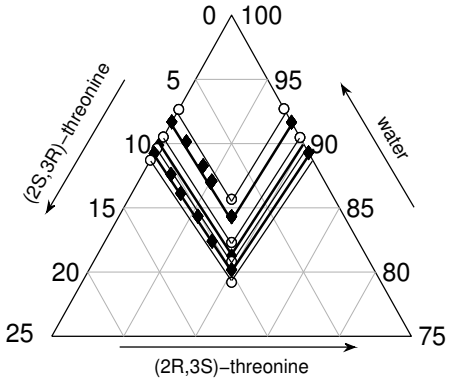

Figure 4.2 *Predicted ternary solubility isotherms compared to experimental data points from Sapoundjiev et al.[147] at T=283.15K, 293.15K, 303.15K, 307.15K, 310.15K, 313.15K and 316.15K.*

Firstly, only solute-solvent interactions were considered and heterochiral interactions among the enantiomers were neglected. This implies that the non-idealities among the solvent and each

enantiomer (1/2) were the same. Application of the NRTL model using the obtained parameters for the estimation of the solubility of racemic Threonine gave limited accuracy (dotted line). Apparently, the additional presence of the (2R,3S)-enantiomer causes pronounced heterochiral interactions, that need to be taken into account. Therefore, α_{13}, Δg_{13}, Δg_{31} were set fixed, while the objective function was used again in order to identify α_{12}, Δg_{12}, Δg_{21} [2](2R,3S)-enantiomer) by minimising the gap to the solubility data of racemic Threonine. The obtained 6-parameter model fits both the solubility of the single enantiomer and the solubility of the racemic mixture very well. The predicted solubility within the ternary phase diagram of both enantiomers in water reveals a good agreement with all available experimental data of Figure 4.2. It is remarkable, that the obtained solubility isotherms run almost in parallel to the sides of the phase diagram despite the observed pronounced non-ideality in solution. A trial confirmed, that also large changes to the (comparably uncertain) heat and temperature of fusion can not render the solubility ideal. It is tempting to suggest that the combination of the specific heat and temperature of fusion, the solute/solvent interactions and the (weaker) heterochiral interactions contribute to the almost linear solubility isotherms by coincidence. Consequently, the chemical potentials of the species in solution, *i. e.* the driving forces for crystallisation, which can be derived from the NRTL model, vary substantially from the ideal case (compare Eq. (2.34)).

The relation of the activity coefficients on temperature and on solution composition are reflected by Figure 4.4. Temperature dominates the changes in the activity coefficients for this system, while the activity coefficients appear to be almost composition-independent.

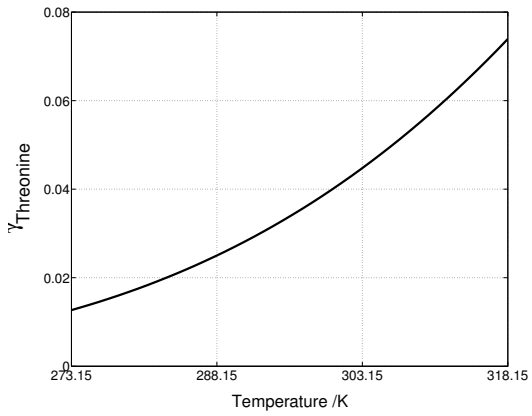

Figure 4.3 *Temperature dependency of the activity coefficients of (2S,3R)-Threonine in water at saturation*.

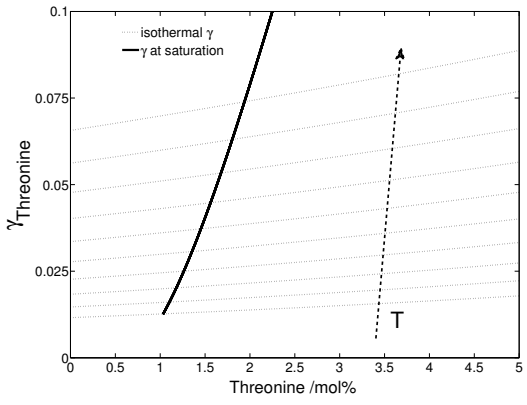

Figure 4.4 *Dependency of activity coefficients of the single enantiomer on the composition and on temperature for T=273.15, 278.15,…,318.15 for the undersaturated (left) and the saturated (right) region.*

The introduced methodology accelerates the access to the shape of specific solubility isotherms in the ternary phase diagram. The chemical potential of the solute in solution can be derived for every given composition within the range of the model parameterisation using the activity coefficient model. Further, the continuation of the solubility isotherms, *i. e.* the metastable solubility isotherms can be derived, which allows estimating the productivity of preferential crystallisation processes [150]. The parameterised model may be used for the prediction of properties outside the known temperature and composition plane, but validation experiments are still crucial. Model parameters are listed in the appendix in Table A.1.

N-methylephedrine/(S)-ethyl lactate and N-methylephedrine /(2R,3R)-diethyl tartrate

A typical strategy to induce asymmetry within a system of enantiomers is the application of chiral molecules. These can be found immobilised as chiral stationary phases in chromatographic columns and also in chiral membranes. Consequently, the use of suitable chiral solvents might cause chiral discrimination either in terms of thermodynamics or kinetics or both in *e. g.* crystallisation processes. A chiral-specific thermodynamic effect would lead to different solubilities of the enantiomers in the chiral solvent and therefore to an asymmetric ternary phase diagram.

Data from solubility measurements were available for enantiomeric compositions and temperatures ranging from 1:1 mixtures to the pure enantiomer and from (273 to 313) K for the API of N-methylephedrine (NME) in the two chiral solvents (S)-ethyl lactate and N-methylephedrine /(2R,3R)-diethyl tartrate within the research group. The molecular structures of the solutes and the two chiral solvents are given by Figure 4.5a)-d).

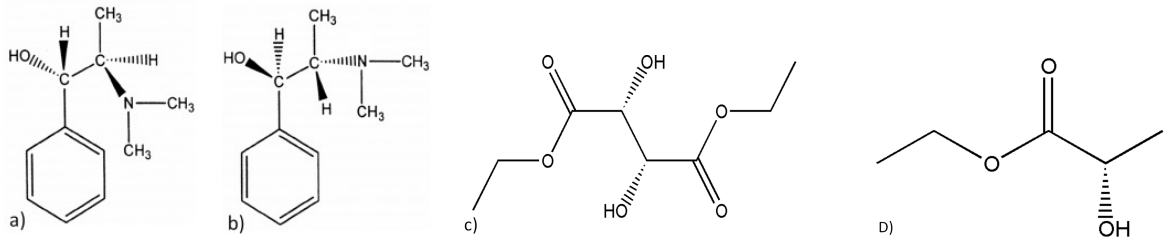

Figure 4.5a)-d) *Chemical structures of the solutes a) (1S, 2R)-(+)-N-methylephedrine and b) (1R,2S)-(-)-N-methylephedrine and the chiral solvents c) (2R, 3R)-diethyl tartrate) and d) (S)-ethyl lactate.*

The introduced NRTL model was parameterised separately by binary solubility data of a single enantiomer of one of the solvents and evaluated in the ternary space [150]. The conducted XRPD analysis revealed no additional or new phases (neither polymorphs nor solvates) differing from those of the pure enantiomers. The enthalpy of fusion and the melting temperature of the N-methylephedrine enantiomers were available from repeated differential scanning calorimetry experiments. The predicted ideal solubility curves of the N-methylephedrine species in both solvents revealed deviations from experimental data (Figure 4.6 and Figure 4.7).

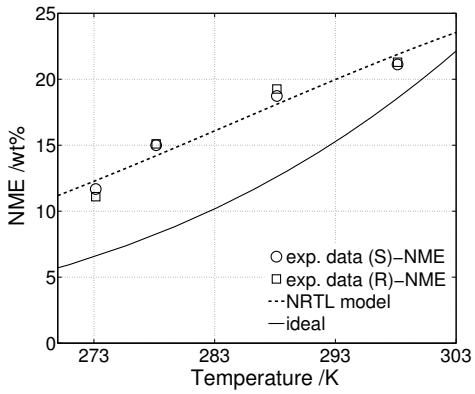

Figure 4.6 *Solubility of NME in (S)-ethyl lactate. Symbols, experimental data; lines, ideal and solubility according to the NRTL model.*

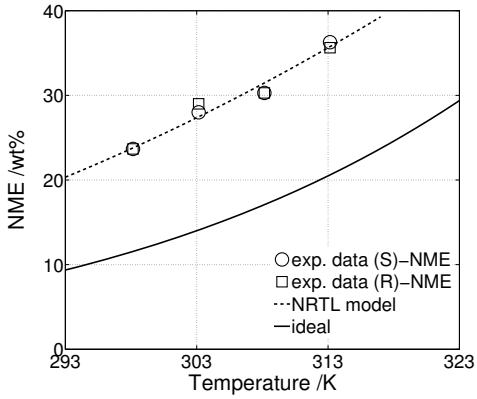

Figure 4.7 *Solubility of NME in (2R,3R)-diethyl tartrate. Symbols, experimental data; lines, ideal and solubility according to the NRTL model.*

Apparently, significant attractive forces exist between (S)-(-)-ethyl lactate/(2R, 3R)-(+)-diethyl tartrate and N-methylephedrine molecules. Interestingly, no chiral-specific interactions were found, the solubilities of both enantiomers were identical. This finding allowed for the same model simplification as in the case of Threonine/water $\left(\Delta g_{13}=\Delta g_{23}, \Delta g_{31}=\Delta g_{32}, \alpha_{13}=\alpha_{23}=\alpha_{31}=\alpha_{32}\right)$. The model correlation in the case of (S)-ethyl lactate is satisfying. However, only limited data were available. Again, a satisfying agreement was observed for the second solvent (2R,3R) diethyl tartrate.

Figure 4.8 and Figure 4.9 illustrate the resulting ternary solubility phase diagrams of the N-methylephedrine enantiomers in (S)-(-)-ethyl lactate and (2R, 3R)-(+)-diethyl tartrate. The diagrams show symmetrical mirror images with respect to the racemic axis, rather than asymmetry which is possible in chiral solvents. As known from the binary phase diagram of the chiral system, N-methylephedrine enantiomers do not form a racemic compound but rather a simple eutectic (conglomerate) system. The dashed solubility isotherms in the left figure are the prediction on the basis of the upper binary phase diagram.

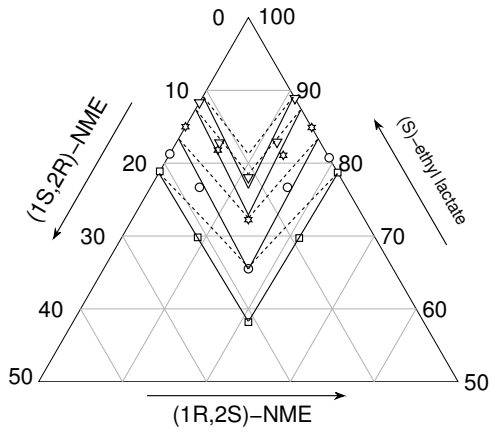

Figure 4.8 *Solubility of NME enantiomers in (S)-ethyl lactate. Symbols, experimental data at 273.15 K, 278.15 K, 288.15 K and 298.15 K [150]; lines, ideal (w/o heterochiral interactions, dashed) and solubility according to the NRTL model (solid).*

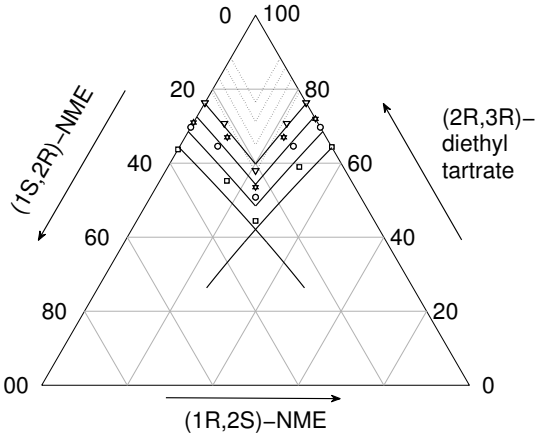

Figure 4.9 *Solubility of NME enantiomers in (2R,3R)-diethyl tartrate. Symbols, experimental data at 298.15 K, 303.15 K, 308.15 K* and *313.15 K [150]; lines, ideal (dashed) and solubility according to the NRTL model (solid).*

The solubilities of racemic mixtures are underestimated for all temperatures and the model agreement with solubilities of the single enantiomer is poor for some temperatures. The latter is a consequence of the less successful fitting of the binary phase diagram. The attempt to use solubility data of the racemic mixture to estimate the parameters $\alpha_{12,}\Delta g_{12}$ and Δg_{21} allowed a much better agreement as denoted by the solid lines. Surprisingly, no parameterisation of heterochiral interactions was necessary for the systems involving (2R,3R) diethyl tartrate. The difference in ideal solubility isotherms and isotherms according to the parameterised NRTL model are shown in Figure 4.9 by dashed and solid lines, respectively. A rather good agreement with experimental data is visible.

The temperature and composition dependency of the modelled activity coefficients is illustrated in Figure 4.10 and Figure 4.11. The γ-values are smaller in (2R,3R) diethyl tartrate, indicating a larger deviation from an ideal solution. The temperature effect is less pronounced in comparison to (S)-ethyl lactate. It is incongruous, that heterochiral interactions were found in only one of the two solvent systems, since these are considered as solvent-independent. A second fitting procedure omitting the solubility data points at the highest temperature in (S)-ethyl lactate,

which appear rather low yielded binary interaction parameters α_{12}, Δg_{12} and Δg_{21}, that improved also the accuracy within the ternary phase diagram of (2R,3R) diethyl tartrate. Thus, the introduced model is strongly sensitive with respect to the binary data and the number of available data points may be not sufficient for an unambiguous description. On the contrary, the accuracy of the ternary phase diagram is considered to be satisfying for process design.

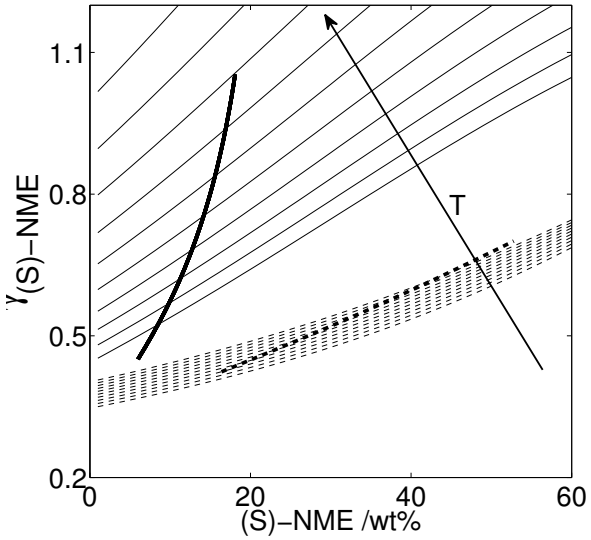

Figure 4.10 *Activity coefficients of (S)-NME in (S)-ethyl lactate (solid) and in (2R,3R)-diethyl tartrate (dashed). Bold lines indicate saturation conditions, thin lines to the left denote the undersaturated solid, thin lines to the right correspond to the supersaturated solution, respectively.*

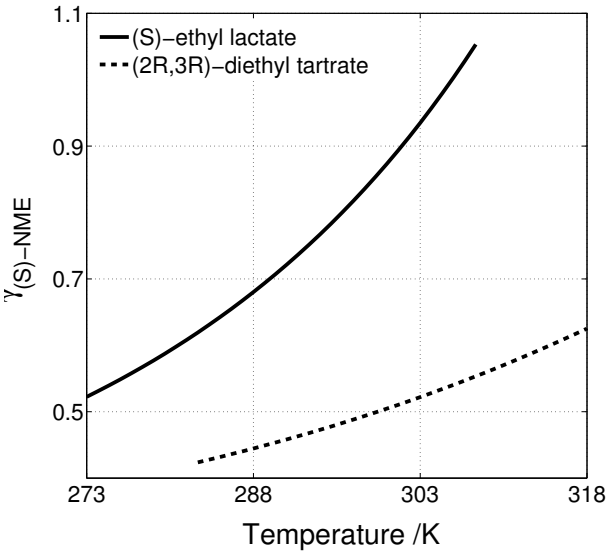

Figure 4.11 *Activity coefficients of the saturated binary system of NME in (S)-ethyl lactate (solid) and in (2R,3R)-diethyl tartrate (dashed) for comparison.*

The general shape of both ternary systems is rather similar, while the solubility isotherms are clearly steeper in (S)-(-)-ethyl lactate than in (2R,3R)-(+)-diethyl tartrate. This aspect is reflected in the ratio of the solubilities of the racemic mixture and the single enantiomer. It has been determined for (S)-ethyl lactate to be about 2 (1.95 at 273 K, 2.14 at 298 K) and for (2R, 3R)-diethyl tartrate to be significantly smaller (1.73 at 298 K, 1.49 at 313 K), revealing a clear deviation from ideal behaviour for this system (compare chapter 2.3.1). An ideal system always exhibits ratios equal to 2 according to the 'double solubility rule' by Meyerhoffer [26]. One has to be aware that this statement does hold only in one direction. Also non-ideal systems like N-methylephedrine in (S)-ethyl lactate can have ratios close to 2. The ratio means that the solubility of one enantiomer is not (strongly) affected by the other one. Ratios smaller 2 account for a decrease in solubility of one enantiomer in the presence of the other enantiomer. Accordingly, at large ratios, the solubility of one enantiomer increased significantly by the presence of the other enantiomer. It is known that the solubility ratios have a large influence on the possible productivity of preferential crystallisation strategies due to the change in the slope of the metastable solubility isotherms. This aspect will be discussed in chapter 5.1 in more detail.

The study of the ternary systems of N-methylephedrine in (S)-ethyl lactate and (2R, 3R)-diethyl tartrate revealed no asymmetry, allowing for a simplified model description. The parameterisation of the NRTL model with binary solubility data in (S)-ethyl lactate was possible with limited precision. Consequently, the predicted ternary phase diagram represented only partly the experimentally determined values. Therefore, interactions between the enantiomers

were considered and additional model parameters were introduced resulting in an improved agreement of experimental data and model prediction. In summary, the solid/liquid phase equilibria of N-methylephedrine enantiomers in (2R, 3R)-diethyl tartrate were predicted accurately on the basis of the model parameterisation using only binary solubility data. It is likely that more solubility data would provide a more congruent figure of the heterochiral interactions between N-methylephedrine enantiomers. For both solvents the magnitude of the solubility ratio was estimated correctly, while the general shapes of the bent solubility isotherms were not reflected well by the NRTL model prediction. It is concluded, that the use of the applied model offers reasonable improvements compared to the precision of predicted ideal solubilities, but the quality of the binary data basis remains decisive.
The estimated model parameters and the used heats and temperatures of fusion for the systems are listed in the appendix in Table A.2 and Table A.3 respectively.

4.1.2 Activity coefficients and the shape of solubility isotherms

Often, the simultaneous presence of homo- and heterochiral interactions masks the individual relations of specific activity coefficients in solvent/solute systems on the corresponding ternary systems. Low activity coefficients shift the fraction of the single enantiomer alongside the outer axis towards the edge of the pure enantiomer. Homochiral interactions can further affect changes to the slope of the whole solubility isotherm in the ternary phase diagram; this applies also in the absence of heterochiral interactions. Pronounced deviations from ideality lead to either very steep or flat solubility isotherms in the ternary phase diagram. This is illustrated by the examples given in Figure 4.12 and Figure 4.13.

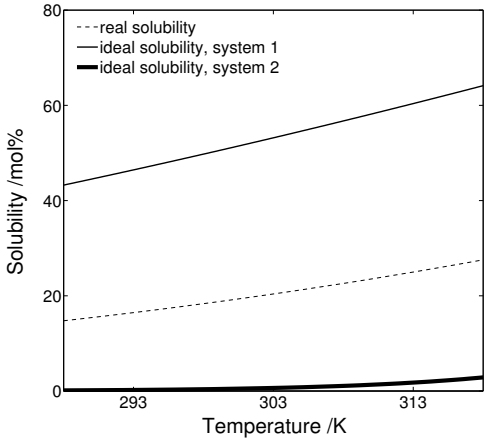

Figure 4.12 *Two cases of non-ideal solubilities. Low activity coefficients, system 1 (thin line); high activity coefficients, system 2 (bold line).*

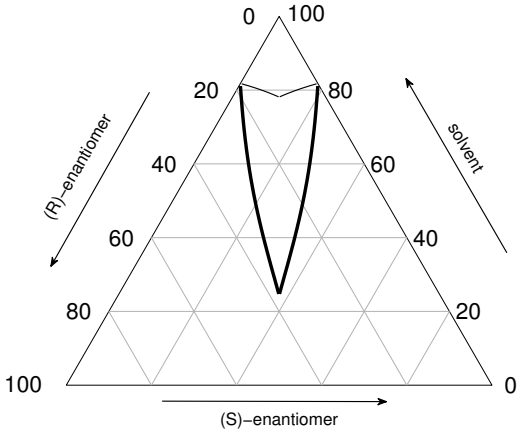

Figure 4.13 *Corresponding solubility isotherms in the ternary space. Low activity coefficients, system 1 (flat solubility isotherms, thin lines); high activity coefficients, system 2 (steep solubility isotherms, bold lines).*

Two theoretical systems are considered, that deviate strongly in negative and positive direction from ideal solubilities. The actual solubility is the same in both systems for the ease of comparison (dashed line). For modelling purposes the temperatures of fusion were assumed the same for both systems, while the heats of fusion differed by a factor of eight. System 1 (thin line) exhibits activity coefficients far below unity, its real solubilities are decreased in comparison to the ideal case. Parameterisation of a g^E-model and estimations in the ternary space result in flat

solubility isotherms (Figure 4.13, thin lines). An increase in solubility compared to the ideal case indicates activity coefficients above unity (Figure 4.12, bold line). The estimated solubility isotherms in the ternary space will exhibit a rather steep shape (Figure 4.13, bold lines). This might be unexpected from the point of view, that one enantiomer should not increase the solubility of another without heterochiral interactions in place. However, the presence of the second enantiomer affects the solute/solvent ratio and therefore the activity coefficients of all components in the mixture according to the applied g^E-model. In other words, the probability of interactions among *e. g.* the (S)-enantiomer and the solvent is altered upon introducing the (R)-enantiomer into a mixture, even if no heterochiral interactions between the (S)- and the (R)-enantiomer are encountered. It was found in the course of analysing the compounds in this thesis, that the shape of non-ideal solubility isotherms in the ternary space can be well approximated by this model approach. However, this applies only to systems in the absence of heterochiral interactions. The latter can superimpose the discussed general trends.

4.2 Modelling compound-forming systems

4.2.1 Investigated systems

The majority of known chiral systems reveal the formation of a compound in a distinct 1:1 composition. Very few exceptions are known [32]. A thermodynamic consistent model was developed and evaluated. It is introduced and explained for both model compounds, as Tröger's Base, Methionine, Mandelic acid, Serine, Proline, 3-Chloro-Mandelic acid and two compounds of pharmaceutical interest- Propranolol hydrochloride and Bicalutamide. Further, a precursor to compounds of commercial interest was studied in this context. Unfortunately, its name and structure has to remain undisclosed according to a pending patent between the MPI Magdeburg and an industrial collaboration partner. It will be denoted *UND* in the following.
The possibility to incorporate pronounced heterochiral interactions among a pair of enantiomers was investigated.

4.2.2 Heterochiral interactions in solution

Tröger's Base/ethanol
The isomerism of the enantiomers of Tröger's base emanates not from a chiral centre situated at a central carbon atom, but from two stereogenic nitrogen atoms, that are bridged.

a) b)

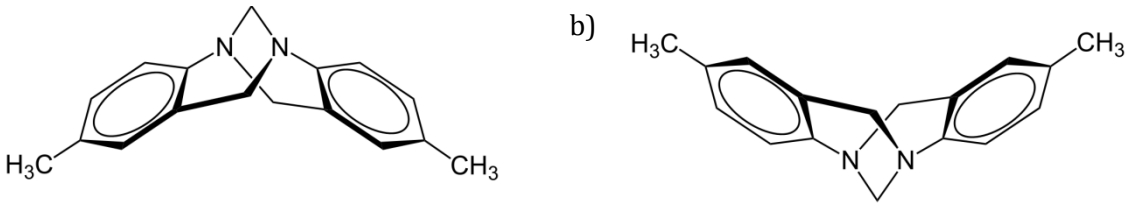

Figure 4.14 *Enantiomers of Tröger's base: (5S,11S)-(-)-enantiomer, a) ((S)-enantiomer for brevity); (5R,11R)-(+)-enantiomer, b).*

A thermodynamic model as well as the heats and temperatures of fusion and SLE data in ethanol were published by Worlitschek *et al.* [33]. In this study, the model was refined and extended and yielded, in contrast to the former approach, thermodynamic consistent model parameters. As in the Threonine/water system, pronounced non-ideal solubility in solution was observed from the single enantiomer and the racemic compound, respectively. Figure 4.17 illustrates the large differences with respect to the ideal solubilities. The NRTL model was parameterised by correlating the solubility of the (S)-enantiomer to Eq. (2.17) with the same objective function as in the case of Threonine (Eq. (4.1)). The same assumptions on symmetry applied. The correlation between the model and the (few) experimental data from Worlitschek *et al.* [33] was good.

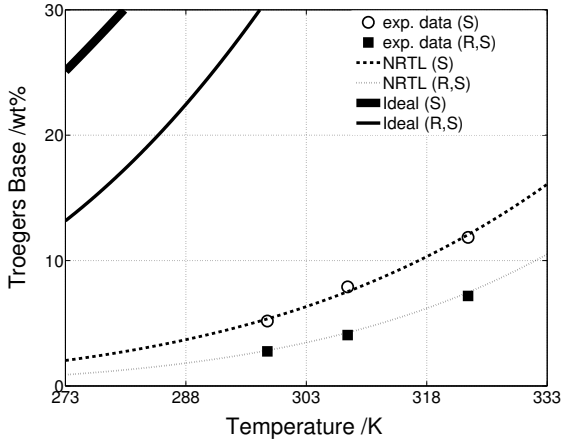

Figure 4.15 *Symbols denote the solubility of the single enantiomer and the racemic compound of Tröger's Base in ethanol as published by Worlitschek et al. [33]. Lines indicate ideal solubilities and the correlations by the NRTL model approach.*

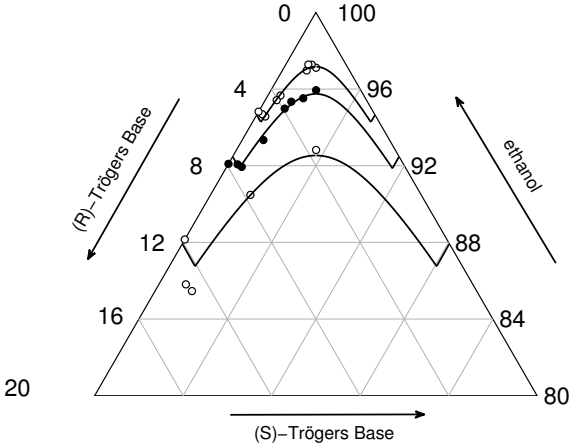

Figure 4.16 *Predicted ternary solubility isotherms compared to experimental data points (Worlitschek et al. [33]) at T=298.15K, 308.15K and 323.15K.*

The use of the parameterised activity coefficient model for the estimation of the non-ideal SLE of the racemic compound may save additional experimental work. The description of the approach requires to refer back to the thermodynamic derivation of the theory by Prigogine and Defay (Eq. (2.39)). Rearranging Eq. (2.33) reads

$$\frac{\Delta h_{diss}}{T}\frac{dT}{dx^l_{(R)}} = v_{(S)}\frac{\partial \mu^l_{(S)}}{\partial x^l_{(R)}} + v_{(R)}\frac{\partial \mu^l_{(R)}}{\partial x^l_{(R)}}. \tag{4.2}$$

The definition of the partial derivatives of the terms on the right hand side can be written according to Eq. (2.34) as follows.

$$\frac{\partial \mu^l_{(S)}}{\partial x^l_{(R)}} = \frac{\partial \mu^{l,0}_{(S)}}{\partial x^l_{(R)}} + \frac{RT\partial \ln x^l_{(S)}}{\partial x^l_{(R)}} + \frac{RT\partial \ln \gamma^l_{(S)}}{\partial x^l_{(R)}} \tag{4.3}$$

$$\frac{\partial \mu^l_{(R)}}{\partial x^l_{(R)}} = \frac{\partial \mu^{l,0}_{(R)}}{\partial x^l_{(R)}} + \frac{RT\partial \ln x^l_{(R)}}{\partial x^l_{(R)}} + \frac{RT\partial \ln \gamma^l_{(R)}}{\partial x^l_{(R)}} \tag{4.4}$$

The first term on the right hand side of both equations vanishes, while the remaining terms can be obtained through differentiation of a suitable g^E-model as given by Table 2.1. The solubility of a racemic compound can be derived from the ordinary differential Eq. (4.5), provided $\Delta h^f_{(R,S)}$ =

Δh_{diss} (compare chapter 2.3). The integration limits are the heat of fusion of the racemic compound and the temperature of the solution of interest. Accordingly, the activity coefficients need to be taken at the solution temperature and at the temperature of fusion.

$$\int_{T^f_{(R,S)}}^{T} \frac{\Delta h^f_{(R,S)}}{RT^2} dT = \int_{x^l_{(R)}=x^l_{(S)}=0.5}^{x^l_{(R)}} \frac{1}{1-x^l_{(Sol)}-x^l_{(R)}} + \frac{1}{x^l_{(R)}} + \frac{RT\partial \ln \gamma^l_{(S)}}{\partial x^l_{(R)}} + \frac{RT\partial \ln \gamma^l_{(R)}}{\partial x^l_{(R)}} dx^l_{(R)} \tag{4.5}$$

$$\frac{\Delta h^f_{(R,S)}}{R}\left(\frac{1}{T^f_{(R,S)}} - \frac{1}{T}\right) = \ln\left(\left(1-x^l_{(Sol)}-x^l_{(R)}\right)\ x^l_{(R)}\ \gamma^l_{(S)}\ \gamma^l_{(R)}\right)\Big|_{x^l_{(R)}=x^l_{(S)}=0.5}^{x^l_{(R)}} \tag{4.6}$$

The estimated solubilities of the figure above (Figure 4.15, dotted line) agree well with the experimental data. The enantiomers do not show evidence of heterochiral interactions, that would contribute to the SLE. Application of the 3-parameters NRTL model on three solubility isotherms in the ternary phase diagrams yields good agreement with experimental data. A change of about 4 % in the eutectic composition for a temperature difference of 25 K was found from the data by Worlitschek (Figure 4.17). Inserting the ratios of the solubilities of the racemic compound and the enantiomer into the shortcut model introduced in section 2.3.1, a similar trend is observed. The same decaying curve is derived form the shortcut model fed with the heats and temperatures of fusion. A plot of eutectic compositions from the NRTL model coincides with these results. The scatter of measurement data of the eutectic composition is not unusual, since its determination requires the isothermal solid/liquid separation and often a solvent change for chiral chromatographic analysis becomes necessary. These steps can lead to experimental errors. It is not determinable, whether the model deviations from experimental data must be attributed to the model or errors in the (small) experimental data basis. However, it was possible to derive the ternary phase diagram from three data points only. Its accuracy is believed to be sufficient for further process design. The characteristic shift of the eutectic composition was estimated on the basis of the heat and temperature of fusion only. For this system no influence of the solvent on the eutectic composition was found. The absence of heterochiral interactions, disallows to describe changes in the general shape of the ternary phase diagram in other solvents. Though, the absolute solubilities will change, it is expected that for the same temperature, the same eutectic composition is found. This is in agreement with the postulate by Wang *et al.* [35]. The estimated model parameters for the system of Tröger's Base in ethanol are listed in the appendix in Table A.4.

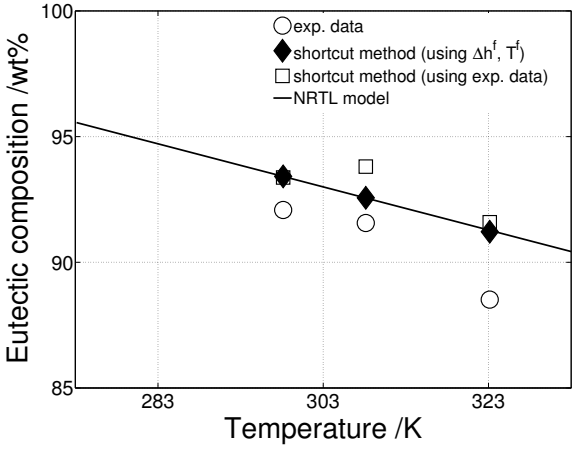

Figure 4.17 *Eutectic compositions of Tröger's base in ethanol- experimental data and model estimations*

Methionine/water

The system of the amino acid methionine (Figure 4.18) was studied with a particular view on the eutectic composition. Polenske *et al.* described a large change of this property between 273 K

and 333 K in water [89]. Methionine is not melt-stable and the heats and temperatures of fusion of the single enantiomer and the racemic compound need to be estimated. The introduced methodology by Marrero *et al.* [149] does not discriminate among the two solid species and thus, the obtained values for both species were considered as equal.

Within the NRTL parameter estimation procedure, the initially estimated heat and temperature of fusion for the enantiomer were allowed to vary within the method uncertainty (16 %). The values for the racemic compound were allowed to vary freely within a physical reasonable range. Although or even hence, the heats and temperatures of fusion are decisive for the description of SLE, numerous largely different values have been published [83, 151]. The few experiment-based data reveal, that (S)-Methionine does not melt below 549 K [152] or 581 K [153]. The upper values was taken into account, while fitting the three binary NRTL parameters together with the heats and temperatures of fusion to solubilities of the enantiomer and the racemic compound.

Figure 4.18 *(S)-enantiomer (a)) and (R)-enantiomer (b)) of Methionine (2-amino-4-(methylthio)butanoic acid).*

The binary solubility data by Polenske *et al.* [89] (Figure 4.19) exhibits pronounced differences with respect to the ideal solubilities (solid lines). The model-based solubility correlation involving solvent/solute interactions only agree well for the enantiomer (bold dashed line) and less good for the racemic compound (thin dashed line) indicating that heterochiral interactions are present. Incorporation of the solubilities of the racemic compound into the data set to be fitted and addition of three parameters for solute/solute interactions allowed a better agreement between model and experimental data (dotted line).

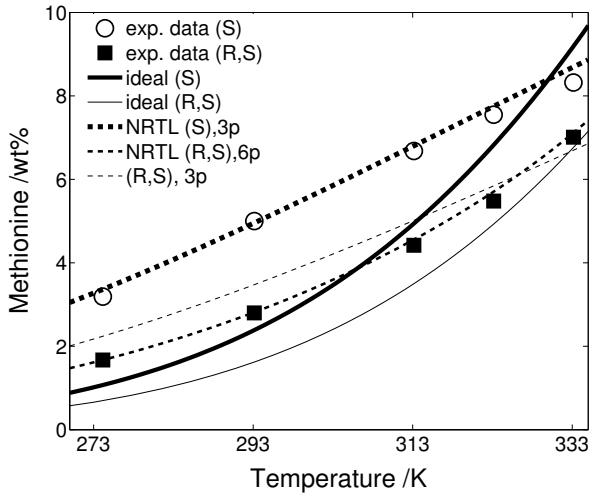

Figure 4.19 *Solubility data of the single enantiomer (open squares) and the racemic compound (open dots) in water from Polenske et al. [88] Curves by the NRTL model.*

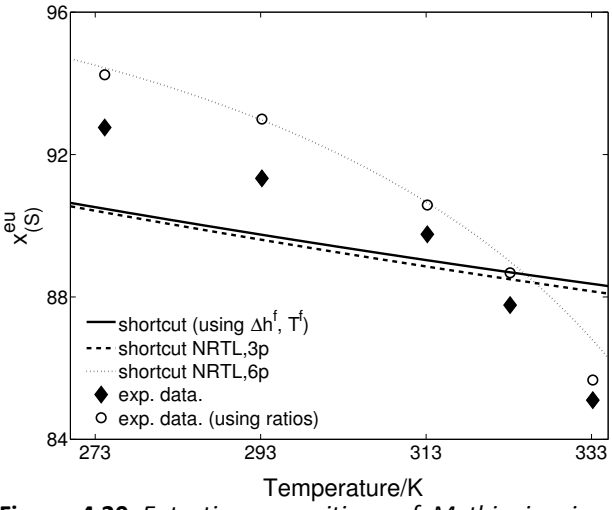

Figure 4.20 *Eutectic compositions of Methionine in water- experimental data and model estimations.*

Application of the shortcut model for eutectic compositions fails as illustrated by Figure 4.20. Both, consideration of the heat and temperature of fusion only and the non-ideality in solution (3-parameters NRTL model) yield straight lines, which cannot represent the experimentally determined $x_{(S)}^{eu}$-values. The additional consideration of heterochiral interactions (6-parameters NRTL model) led to a better agreement. Even though, the experimentally observed solubility ratios are well captured, the determined eutectic compositions by Polenske *et al.* are slightly lower for all temperatures (full symbols).

A plot of the ternary phase diagram on the basis of the 3-parameters NRTL model led to a fair agreement with ternary experimental data between 274.15-333.15 K in Figure 4.21a). Apparently, the identified combination of NRTL parameters and the heat and temperature of fusion is promising. The simple estimation of ternary SLE based on the solubility of the enantiomer as the only input might serve already as a good basis for process design. However, since specific emphasis was given to the eutectic composition in the ternary space, the obtained estimate lacks accuracy.

The addition of 3 parameters for heterochiral interactions yielded a better estimate for the eutectic composition, but the resulting estimate for the ternary space captured the solubility isotherms less good. It is likely, that the limitation to data of racemic composition is too restrictive for this system and cannot yield satisfying description of heterochiral interaction parameters. Thus, ternary data of selected solubility isotherms was used to identify a more suitable set of parameters for solute/solute interactions via a second fitting procedure. Figure 4.21b) illustrates the resulting ternary system of Methionine enantiomer in water. The description of the eutectic composition and the overall accuracy was improved. The estimate shows high accuracies up to 313.15 K. The correct shape of solubility isotherms above this value is still reflected, but the model tends to overestimate the solubility values of the enantiomer, while underestimating the values for the racemic compound.

All estimated model parameters and the heats and temperatures of fusion of this system are listed in the appendix in Table A.5 and Table A.6.

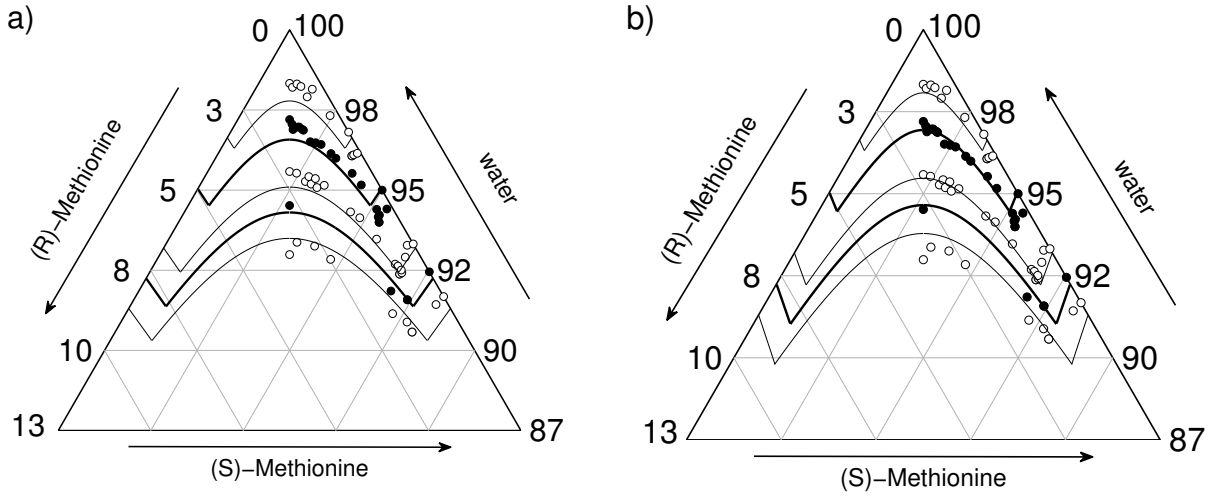

Figure 4.21 *Predicted ternary solubility isotherms based on the 3-parameters model (a)) and the 6-parameter model (b)), respectively. The estimates are compared to experimental data points at T=274.15 K, 293.5 K, 313.15 K, 323.15 K, 333.15 K from Polenske et al.* [88].

On the estimation of heterochiral interactions from the melt: undisclosed chiral system *UND*

This paragraph comprises studies of a pair of enantiomers, that were performed in the course of an- still ongoing- industrial collaboration with the MPI Magdeburg. Neither the common project nor the patent application have been finalised, thus the following data can be considered as foreground and the compound will not be named here.

The two enantiomers of the undisclosed compound *UND* form a racemic compound in the crystalline phase, when crystallised from ethyl acetate. Measurement of the heats and temperatures of fusion of the racemic compound and the (R)-*UND*-enantiomer by differential scanning calorimetry yielded 24.0 kJ/mol, 398.7 K and 14.4 kJ/mol, 370.8 K, respectively. Solubility data in ethyl acetate were available from internal studies in the research group. The binary system of the (R)-enantiomer in that solvent showed a deviation from ideal solution behaviour by a factor of two. Interestingly, the ideal solubility of the racemic compound agrees well with experimental data. The system was analysed with the introduced methodology in order to explain the apparently different activity coefficients of the single enantiomer and the racemic compound Firstly, the parameters α_{13}, Δg_{13} and Δg_{31} ([1](R)-*UND*, [2](S)-*UND*, [3]ethyl acetate) were estimated by correlating the NRTL model to solubility data of the single enantiomer. The agreement between model and experimental data was good for the enantiomer, while the estimated solubility of the racemic compound was far below the determined values in solution. It is possible, that heterochiral interactions between the single enantiomers increase the solubility of a mixture in solution. This does not apply to a homochiral mixture of the enantiomers, since the determined solubility is significantly lower compared to the ideal case. It is assumed that the two contributions compensate each other mutually at the racemic composition, giving rise to the (misleading) assumption, that the racemic compound behaves ideally. Introducing the parameters α_{12}, Δg_{12} and Δg_{21} allows a much better description of the two binary SLE. The latter parameters were found by correlating the NRTL model to the solubility data of the racemic compound (R,S). The obtained agreement with experimental data is illustrated by Figure 4.22. The estimated solubility of the single enantiomer remained, as expected, unchanged using this 6-parameters NRTL model.

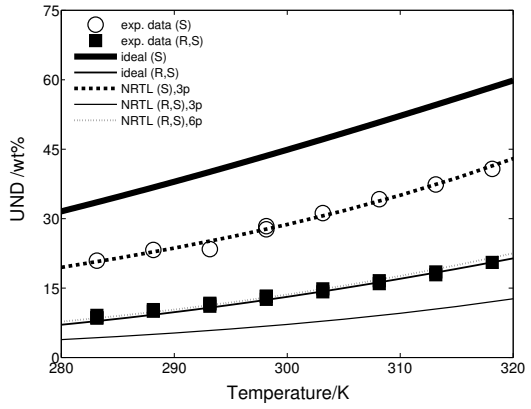

Figure 4.22 *Solubility of the single enantiomer and the racemic compound of UND in ethyl acetate- experimental data and model estimations.*

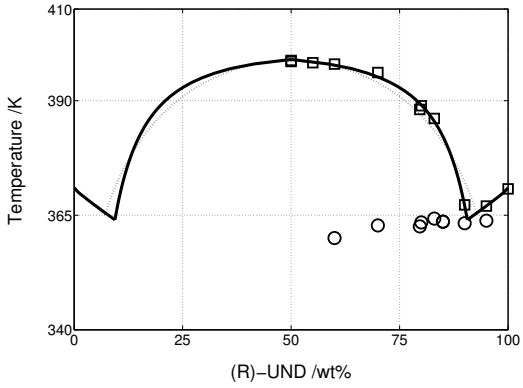

Figure 4.23 *Melting point phase diagram of mixtures of (R)- and (S)-UND exhibiting compound formation (dotted lines: ideal SLE; solid lines: NRTL model).*

In principle, binary heterochiral interactions should be reflected also by the melting point phase diagram. In the case of the *UND*-enantiomers only small deviations from the ideal liquidus curve were observed (Figure 4.23). However, the eutectic point deviates slightly towards a smaller value. It is tempting to quantify the binary interactions among the two enantiomers in the melting point phase diagram, since this can be derived quickly in comparison to solubility measurements. Only a few milligrams of substance are required. However, the estimation of the parameters α_{12}, Δg_{12}, Δg_{21} takes place at more than 40 K above the solution temperature. Often, the temperature dependency is decisive for activity coefficients as in the case of Threonine. Here, the parameterisation of the NRTL model using the data from the melt resulted in rather different model parameters. The plots of activity coefficients of the *UND*-enantiomer in the absence of ethyl acetate for different temperatures and compositions and the two parameter sets appear rather different (Figure 4.24/Figure 4.25). It should be noted, that the area corresponding to the melting point phase diagram gives similar results compared to the same area in the figure derived from the solution. It is likely that a set of NRTL model parameters exists, whose extrapolation agrees with Figure 4.24. Since no feasible methodology is known, it is believed that a parameter set obtained from DSC data cannot be transferred to gain detailed inside in solution behaviour. In addition, heterochiral interactions may be of different kind in the presence of the solvent and it seems to be advantageous to quantify heterochiral interactions directly from solution.

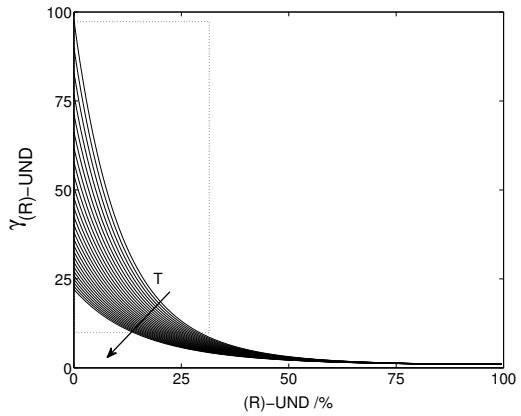

Figure 4.24 *Activity coefficients of mixtures of the (R)- and (S)-enantiomer according to the model parameterisation from solution (solvent free case, T=270, 275,…,400 K). The area used for parameter estimation is framed.*

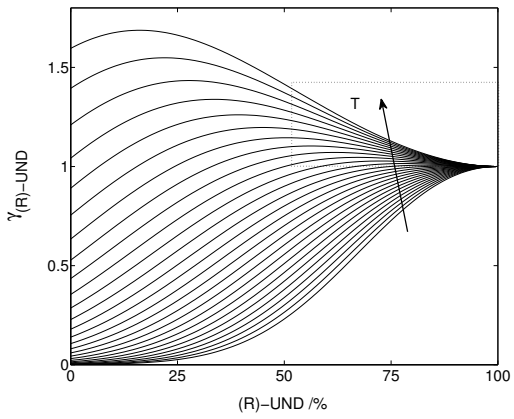

Figure 4.25 *For comparison: activity coefficients according to the model parameterisation from the melt (solvent free case, T=270, 275,…,400 K). Again, the area used for parameter estimation is framed.*

A characteristic property of the chiral ternary system of *UND*-enantiomers in ethyl acetate, the eutectic composition, shifts to lower values at higher temperatures from the shortcut method (Eq. (2.43)). The trend was not observed from experiments (full symbols, Figure 4.26). On the contrary, the ratios of the experimental solubilities of the racemate and the single enantiomer in conjunction with the shortcut method yielded decaying eutectic compositions (open symbols, Figure 4.26). While the combination of the 3-parameters NRTL model with the shortcut method provided almost constant eutectic compositions of about 98 wt%, the full 6-parameters NRTL model in combination with the shortcut model yielded the same decaying trend.

Direct measurement of the eutectic compositions from solution revealed a counter-trend- a slight increase with temperature was found here. Apparently the description by the simple

shortcut model is not accurate if heterochiral interactions are present. The 6-parameters NRTL model reflected the rather little increase in eutectic composition with good accuracy. Figure 4.26 summarises all results and illustrates the remarkable large differences in the predictions by the full NRTL model and the shortcut methods.

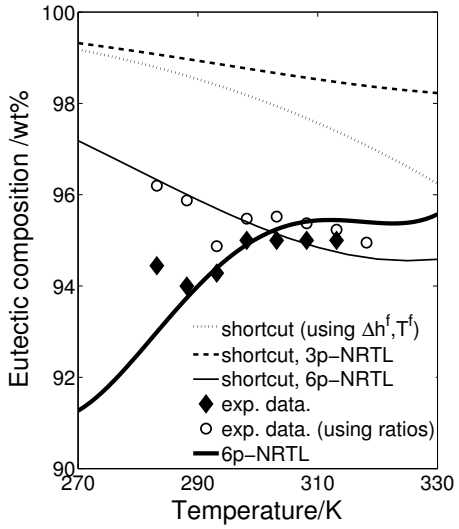

Figure 4.26 *Eutectic composition of UND-enantiomers in ethyl acetate from experiments and models.*

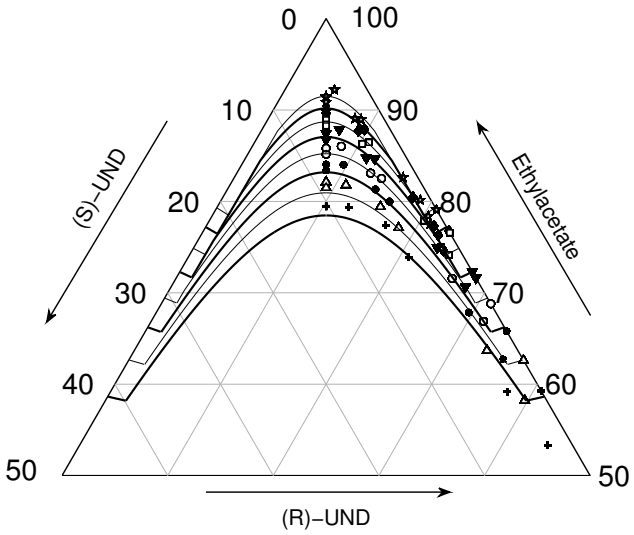

Figure 4.27 *Predicted ternary solubility isotherms for the system of (R)- and (S)-UND in ethylactete compared to experimental data points at T=283.15 K, 288.15 K, 293.15 K, 298.15 K, 303.15 K, 308.15 K and 313.15 K.*

The ternary phase diagram of the enantiomers in ethyl acetate is represented well by the NRTL prediction. There are significant differences in the solubility at the eutectic compositions at elevated temperatures. As discussed earlier, the compositions themselves were estimated accurately by the model. It is not clear, whether these deviations can be attributed to model insufficiencies or measurement uncertainties.

The system of *UND*-enantiomers poses a more complex system, however with less pronounced non-idealities with respect to the solvent. Heterochiral interactions among the enantiomers proved to have large influences on the overall SLE characteristics. More detailed modelling is necessary to capture correctly the temperature depending change in the eutectic composition. It is assumed that the eutectic composition in other solvents will deviate from this example, since the interplay of the solute/solvent non-idealities and the present heterochiral solute/solute interactions compensated each other here by coincidence. The introduced methodology may serve as a guideline to characterise similar systems more quickly.

The 2 sets of estimated model parameters for this system are listed in the appendix in Table A.7.

Inflection point of activity coefficients in solution: Mandelic acid/water

The system of mandelic acid enantiomers in water is well studied and comprehensive SLE data are available [88, 154, 155]. (Semi-) empirical solubility models have been proposed, but no parameterisation of any classical g^E-model was found. This might be due to the somewhat peculiar S-shaped solubility curve of both the racemic compound and the single enantiomer in water (Figure 4.29). Though, the physical cause was not investigated in detail, it was attempted to find a suitable thermodynamic description by the NRTL model. The proceeding might be permitted in the view of providing a quick assessment of the feasibility of chiral separations by crystallisation. However, the initial attempt to use a parameterised 3-parameters NRTL model to capture the solubility curve failed. The specific temperature-solubility relation demanded the addition of two parameters in order to describe the temperature-dependency of solute-solvent interactions in more detail. One approach frequently found uses a pair of parameters a_{ji}/a_{ij} and b_{ji}/b_{ij}.

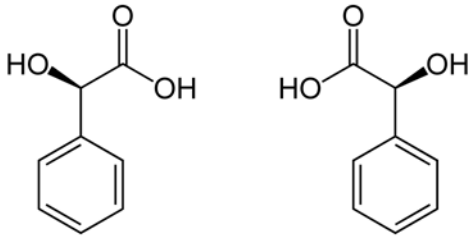

Figure 4.28 *(R)- and (S)-enantiomers of Mandelic acid.*

$$\Delta g_{ji} = g_{ji} - g_{ii} = a_{ji} + b_{ji}T \tag{4.7}$$

Figure 4.29 points up the large differences between experimental data and the ideal solubility curves of the racemic compound and the single enantiomer.

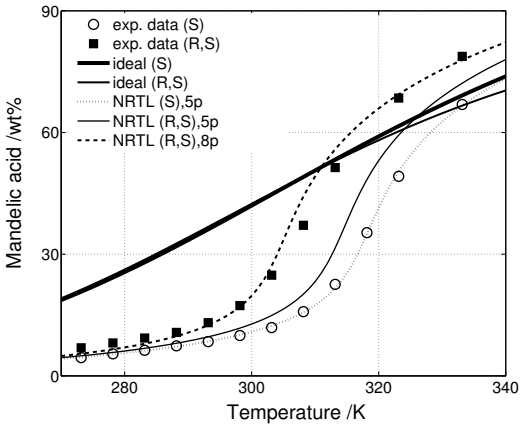

Figure 4.29 *Solubility of the single enantiomer and the racemic compound of Mandelic acid in water-experimental data [154] and model correlations.*

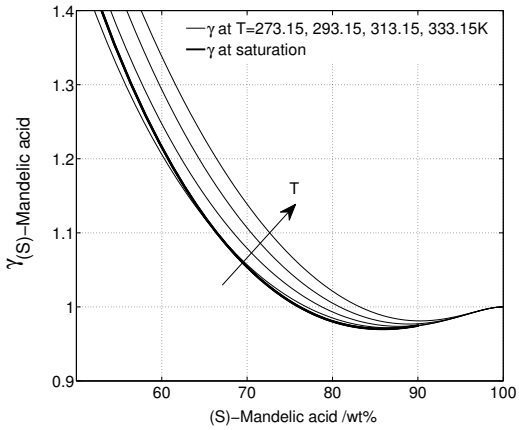

Figure 4.30 *Activity coefficients of (S)-Mandelic acid in water at saturation according to the model parameterisation.*

The obtained fit by the 5-parameters NRTL model represents the experimental data of the single enantiomer accurately (dotted line). Application of this model for the estimation of the real solubility of the racemic compound reveals an unsatisfactory agreement with the experimental data (thin solid line). Thus, it is assumed that the systems experiences variations to the SLE due to the presence of heterochiral interactions. Incorporation of these by addition of the parameters α_{12}, Δg_{12}, Δg_{21} for solute-solute interactions permitted a much better agreement with experimental data (dashed solid line). However, solubilities at temperatures in the middle region were slightly overestimated. The S-shaped solubility curve is reflected in the activity

coefficients of the NRTL model (Figure 4.30). An increase of γ-values is followed by a drop with increasing temperature. At 78 wt% the γ-value becomes smaller than unity.

The use of temperature dependent model parameters led to a difficult situation with respect to the lower boundaries of Eq. (4.6). The activities of the enantiomers at solvent free conditions need to be considered at the temperature of fusion of the racemic compound, which is far above solution temperature. For the previous examples a correct description of these interactions were performed successfully by the parameter estimation procedure. The additional temperature-dependent parameters did not allow to cover the large gap to the melting temperature. The activities of the enantiomers in the melt have therefore been set empirically to unity. This applied to the parameter estimation procedure as well as to the prediction of the ternary phase diagram. The latter represents the challenging phase behaviour of the enantiomers in solution quite well. The are two different shapes of the solubility isotherms for the single enantiomer corresponding to the inflection point of the activity coefficient curve. While the solubilities of the single enantiomer were predicted well throughout the whole temperature range, the prediction of the solubilities of the racemic compound suffered inaccuracies in the middle temperature range. This is a consequence of the fit of Figure 4.29.
The eutectic composition is predicted with limited accuracy by the proposed model as illustrated by Figure 4.31 and Figure 4.32 on the next page.

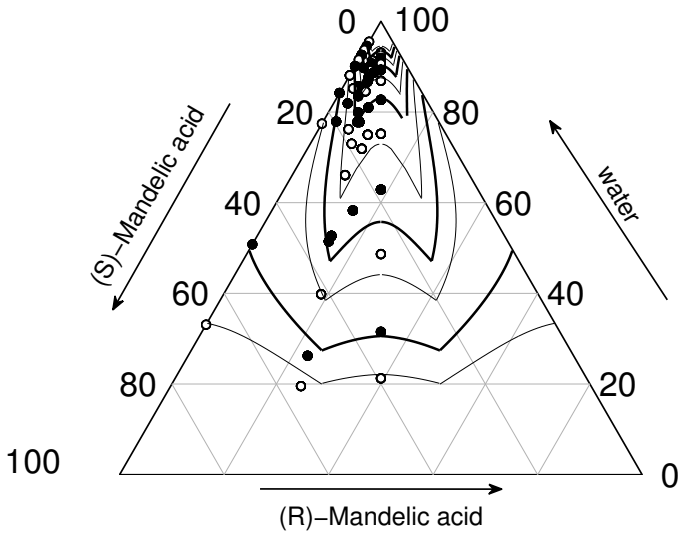

Figure 4.31 *Predicted ternary solubility isotherms by the NRTL model compared to experimental data points from Lorenz et al.[154] at T=273.15 K, 278.15 K,…, 333.15 K.*

The eutectic composition remains constant from the experiments, while a decaying slope is obtained from the shortcut method fed with the heats and temperatures of fusion and the full 8-parameters NRTL model. It should be noticed that the solubility ratios are higher than 3, which is outside the physical range of the shortcut model introduced in section 2.3.1. Application of the shortcut model using the experimental solubility ratios and the 8-parameters NRTL model provides a peculiar curve, which is not relevant in physical terms.

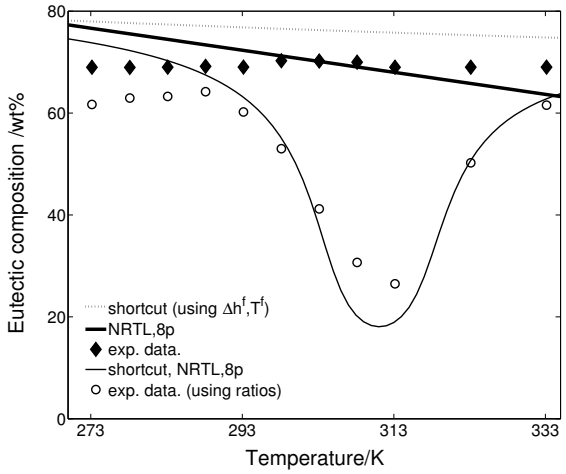

Figure 4.32 *Eutectic compositions of the enantiomers of Mandelic acid in water as given in the literature [154] (full symbols), derived from the shortcut model and the experimental ratios of the solubilities of the enantiomer and the racemic compound (open symbols) and from the NRTL model (lines).*

The NRTL model variation proposed above appears to be a suitable option to correlate also more complex solubility behaviour over a large temperature range. The model assumption of ideality in the melt did allow the prediction of the ternary phase diagram and the eutectic composition with superior accuracy compared to a simple shortcut model. The investigated system proved that the knowledge of the ratios of solubilities is not a sufficient criteria to estimate (changes in) the eutectic composition. Binary solubility data and a g^E-model together deemed to be a reliable basis for the estimation of characteristics of corresponding ternary SLE. All estimated model parameters for this system are listed in the appendix in Table A.8.

Solvent-independency of heterochiral interactions:
Mandelic acid/(S)-ethyl lactate and Mandelic acid/(2R, 3R)-diethyl tartrate

In analogy to the NME system, also the thermodynamics of Mandelic acid in chiral solvents were investigated. Solubility measurements have been available in the chiral solvents (S)-ethyl lactate and (2R, 3R)-diethyl tartrate (compare chapter 4.1.1) or a number of enantiomeric compositions between the racemic compound and the single enantiomer for temperatures between 273 K and 333 K [156]. All binary solubility data considered is summarised in Figure 4.33 and Figure 4.34. No additional or new phases were identified other than the racemic compound and the enantiomers from the crystal lattice analysis by XRPD. The effect of temperature on solubility was more pronounced in (2R, 3R)-diethyl tartrate for the temperature ranges considered. All solubility values exhibited a significant deviation from ideal solubility for both chiral solvents. This raised the question whether the gap is due to speciation of the acid or other pronounced binary interactions with the two solvents. The NRTL-model as applied here accounts successfully for the latter and model parameterisation was done with negligible deviations for the (S)-enantiomer.

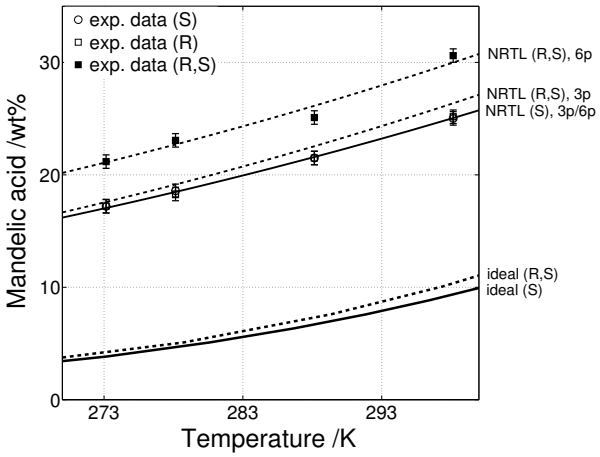

Figure 4.33 *Solubility of the single enantiomer and the racemic compound of Mandelic acid in (S)-ethyl lactate -experimental data and model estimations.*

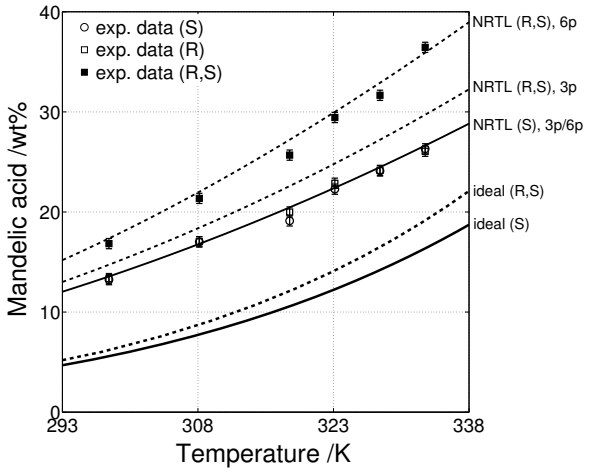

Figure 4.34 *Solubility of the single enantiomer and the racemic compound of Mandelic acid in (2R, 3R)-diethyl tartrate -experimental data and model estimations.*

The NRTL model predictions match the determined values quite closely. Since the solubilities for both enantiomers (S)- and (R)-Mandelic acid were the same, the NRTL model result was plotted only for the (S)-Mandelic acid. The rather large deviations from ideality in both chiral solvents is exemplified in Figure 4.36 by means of plotting the theoretical activity coefficients of the (S)-Mandelic acid as a function of temperature. While the values in (2R, 3R)-diethyl tartrate were already far from unity, the deviation from ideality in (S)-ethyl lactate is even more pronounced. In addition, the order of non-ideality in the two solvents is visible. A more comprehensive compilation of the activity coefficients according to the NRTL model also for under- and supersaturated solutions is given by Figure 4.35. The activity coefficients relevant for the determined solubility isotherms can be found on the thick lines and correspond to the values in Figure 4.36.

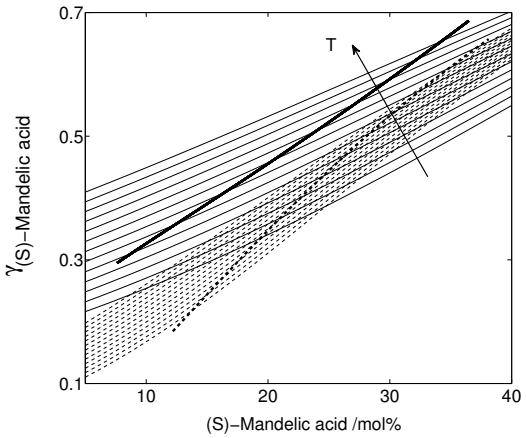

Figure 4.35 *Activity coefficients of (S)-Mandelic acid in (S)-ethyl acetate (solid) and in (2R, 3R)-diethyl tartrate (dashed). Solid lines represent saturation conditions.*

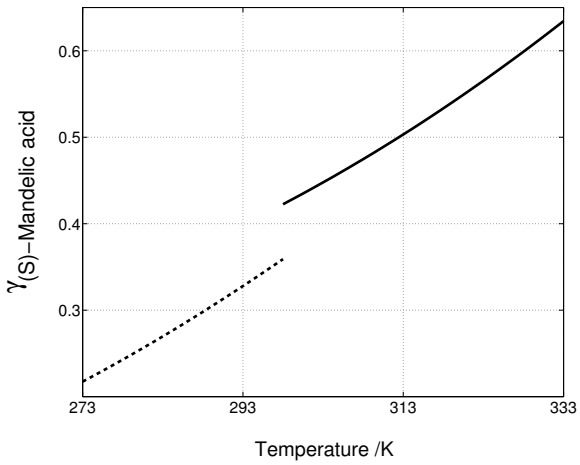

Figure 4.36 *Activity coefficients of saturated solutions of (S)-Mandelic acid in (S)-ethyl acetate (dashed) and in (2R, 3R)-diethyl tartrate (solid).*

The prediction of the solubilities of the racemic Mandelic acid based on the activity coefficients for the enantiomer was improved significantly in comparison to the large gap between ideal solubility and experimental values. Nevertheless, larger deviations remained. It was assumed that this was due to pronounced heterochiral interactions among the enantiomers, which were

not yet incorporated in the model and required a re-parameterisation of the model by introducing the parameters α_{12}, Δg_{12} and Δg_{21}. The already obtained parameters α_{13} , Δg_{13}, Δg_{31}, α_{23}, Δg_{23} and Δg_{32} were set fixed and the solubilities of the racemic compound were used to estimate suitable parameters to express the heterochiral solute-solute interactions. In principle, heterochiral interactions are solvent-independent properties. Thus, the interchange of the parameters α_{12}, Δg_{12} and Δg_{21} between different solvent systems should be possible. Figure 4.37 and Figure 4.38 compare the predicted ternary solubility phase diagrams and measurements of the Mandelic acid enantiomers in (S)-ethyl lactate and (2R, 3R)-diethyl tartrate, respectively. The solubility isotherms confirm the (unchanged) compound-forming character of the Mandelic acid system. The diagrams show symmetrical mirror images with respect to the racemic axis as observed in the case of NME in the same solvents. The predicted solubility isotherms were in good agreement with the measured solubility points in (S)-ethyl lactate in particular for lower temperatures. The determined solubility points in (2R, 3R)-diethyl tartrate are less well represented by the NRTL model prediction; the agreement is again better for lower temperatures. The solubilities in the region of the outer 2-phase region of the enantiomers are better captured than for the inner 2-phase region. The worst agreement is found for the solubilities at the eutectic compositions, while the eutectic compositions were fairly good derived by the model. The eutectic compositions remained unchanged with temperature at 69 % and 31 % (S)-enantiomer, respectively, in both solvents as it was also reported in earlier results for non-chiral solvents [157, 158].

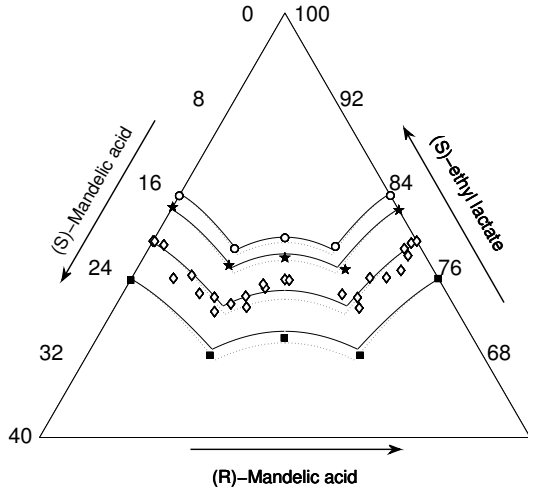

Figure 4.37 *Predicted ternary phase diagram of Mandelic acid enantiomers in (S)-ethyl lactate. Solid lines: predictions based on a parameterisation of heterochiral interactions in ethyl acetate; dotted lines: predictions based on parameterisation of heterochiral interactions in (2R, 3R)-diethyl tartrate.*

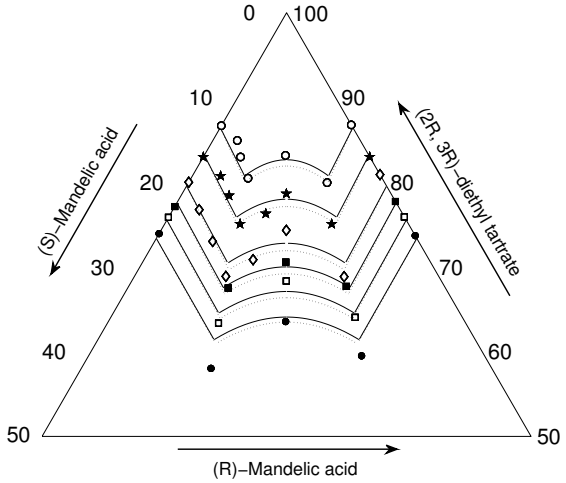

Figure 4.38 *Predicted ternary phase diagram of Mandelic acid enantiomers in (2R, 3R)-diethyl tartrate. Solid lines: predictions based on parameterisation of heterochiral interactions in (2R, 3R)-diethyl tartrate; dotted lines: predictions based on parameterisation of heterochiral interactions in (S)-ethyl lactate.*

An important aspect of the two figures concerns the rather good agreement upon interchanging the model parameters for the heterochiral interactions. It has been possible to parameterise these in one solvent and to apply them in another. Consequently, the ternary phase diagram of Mandelic might be predicted on the basis of few measurements of a single enantiomer in an arbitrary solvent. If those binary data can be derived through an estimation model, an entirely measurement-free estimation of unknown ternary phase diagrams might be possible.

Disregarding heterochiral interactions led in this case to significantly underestimated solubilities of the racemic compound in both solvents (compare Figure 4.33 and Figure 4.34) and erroneous predictions with respect to the eutectic compositions.
The presented thermodynamic modelling of the solubilities of Mandelic acid in two chiral solvents based on limited binary data yielded good results. As a matter of fact, even less data would have been sufficient, to allow for the estimation of the ternary phase diagrams. It is likely that the derived parameter sets can support the estimation of phase equilibria also in other solvents.
The estimated model parameters for this system are listed in the appendix in Table A.10.

Consequences of speciation in solution-limits of the presented approach: Propranolol hydrochloride/methanol, Propranolol hydrochloride/water

The pharmaceutical compound Propranolol has been one of the first beta blockers on the market and is nowadays among other available in form of Propranolol hydrochloride. The enantiomers of Propranolol·HCl form a racemic compound in the solid phase [159]. The melting point phase diagram and solubility data in at least two solvents is published [99]. Within all phase diagrams the eutectic composition is found very close to the mirror axis. Thus, it is likely that heterochiral interaction among the enantiomers do not contribute to the SLE. This is supported by the ideal melting point phase diagram [159]. On the contrary, the ternary phase diagrams in methanol and in water exhibit significant differences though, the eutectic composition remains constant. An attempt was made, to specify, whether the large differences in SLE can be explained on the basis of a g^E-model in this work.

Figure 4.39a)/b) *Molecular structures of the (R)- and the (S)-enantiomer of 1-(1-methylethylamino)-3-(1-naphthyloxy)-propanolol hydrochloride*

The heats and temperatures of fusion of the single enantiomer and the racemic compound provided in the literature deviate by up to 16% [99, 160]. Here, the heats and temperatures of fusion were optimised within this range of uncertainty together with the NRTL model parameters α_{13}, Δg_{13} and Δg_{31} by correlation with the solubility data of the single enantiomer. The obtained agreement with respect to the racemic compound confirms the absence of pronounced heterochiral interactions. The predicted ternary phase diagram in methanol exhibits slightly steeper solubility isotherms compared to the non-ideal case. It resamples the measurements at 293 K well. The eutectic composition decays from 59% at 273 K down to 55% at 313 K. The ternary SLE behaviour seems to be adequately described by the model.

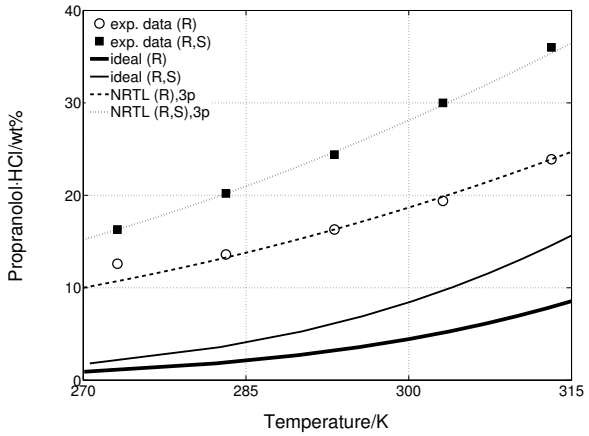

Figure 4.39 *Solubility of the single enantiomer and the racemic compound of Propranolol·HCl in methanol- experimental data and model estimations*

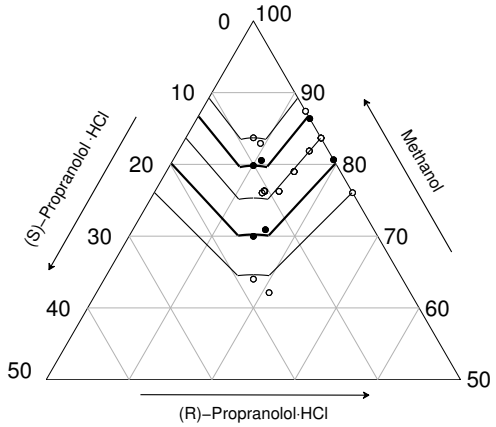

Figure 4.40 *Predicted ternary solubility isotherms and experimental data points of Propranolol·HCl in methanol at T=273.15 K, 283.15 K, 293.15 K, 303.15 K and 313.15 K.*

Application of the same model to the system of Propranolol·HCl/water allows to describe the binary solubility of a single enantiomer in solution. In water the solubility is strongly suppressed in comparison to the ideal solubility. Interestingly, this applies only to the single enantiomer. The solubility of the racemic compound appears to be more ideal. Thus, transfer of the model parameters to the estimation of the solubility of the racemic compound leads to significantly lower solubilities, that do not represent the experimental values at all. A clear differentiation between homochiral and heterochiral pairs of enantiomers in solution must exist. The speciation in solution deviates from the melt and from the methanol solution.

It is likely, that water molecules cause the chiral discrimination. A possible rational for the mechanism can be derived from the molecular structure. The Propranolol·HCl molecule consists of an unpolar section A and a section B (Figure 4.42), which contains more polar functional groups. Provided, that polar water molecules interact predominantly with section B, it is tempting to suggest, that this section is less good accessible to the solvent in a homochiral mixture. One explanation is given by the formation of AB-BA dimers in solution, that shield the B sections. Moreover, the dimer sequence must be chiral-specific. Considering the B sections, only (S)-(S) or (R)-(R) pairs are likely to form. The solubility of the racemic mixture is not suppressed, probably due to the accessible B section, since no dimer formation takes place. Since this behaviour is not observed from methanol, it is assumed that water molecules exhibit a coordinating role in dimer formation. The distinct coordination of molecules in solution contradicts with the basic assumptions of the NRTL model. Indeed, it was not possible to identify any set of model parameters for heterochiral interactions, that allowed for a proper estimation of the ternary solubility behaviour observed in water (Figure 4.41).

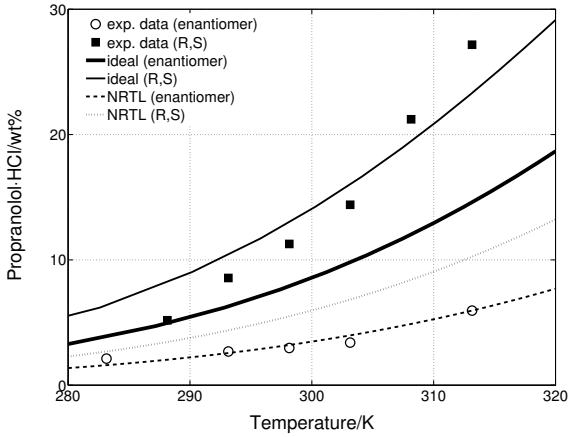

Figure 4.41 *Solubility of the single enantiomer and the racemic compound of Propranolol·HCl in water- experimental data and model estimations.*

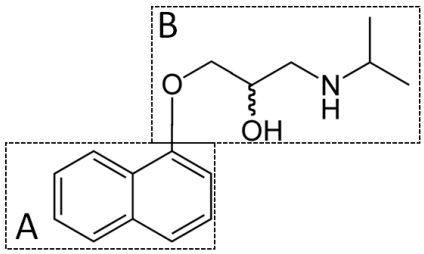

Figure 4.42 *Molecular structure of Propranolol·HCl divided into a polar section B and a less polar section A.*

In summary, modelling of the Propranolol·HCl systems yielded two results. Firstly, the compound belongs in general to the class of simple systems for which ternary solubility data can be derived on the basis of few binary solubility data. Secondly, the water system serves as one example, that shows up the limits of the g^E approach. The speciation in solution can be followed directly from a single binary measurement of the racemic mixture. It is obvious, that the systems requires either extensive ternary measurements or a theoretically much more sound approach or both in order to get a hold on the specific SLE in water.
The estimated model parameters and heats and temperatures of fusion for both systems are listed in the appendix in Table A.10 and Table A.11.

4.2.3 Solvate formation

Serine/water
The system of the amino acid Serine in water is known to feature a characteristic eutectic composition very close to 100%. Comprehensive solubility data for the racemic compound is available from Dalton *et al.* [161] and for the (S)-Serine by Ferreira *et al..* The ternary solubility data of a single solubility isotherm was published by Klussmann *et al.* [36]. Further, several solubility models considering either the racemic compound or the single enantiomer were parameterised by several authors [151, 162].

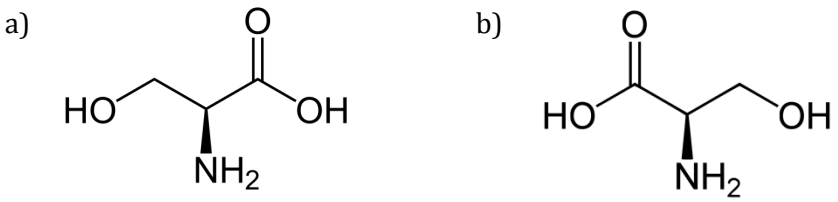

Figure 4.43 *Molecular structures of (S)- and (R)-Serine.*

This study aimed to introduce a first thermodynamic consistent model for the ternary phase equilibria of Serine in water. Additional solubility data were determined in the course of this work. The heat and temperature of fusion of the compound were not available, since it decomposes prior to the melting. The proposed values in the literature range from melting points of 375 K for the enantiomer [163] up to 776 K for the racemic compound [164] and highlight the difficulty in their proper estimation. It is known from a database [152] that decomposition of (S)-Serine occurs at 493 K and thus, the melting point was expected to be close by or above this value. The group contribution method by Marrero *et al.* yielded a melting point of 588.9 K and a heat of fusion of 33.273 kJ/mol for the single enantiomer. These values were used as initial

values and have been optimised during the parameterisation procedure. As described earlier, 16% variance was given as the model accuracy. The initial values for the racemic compound were taken as identical. Physical reasonable limits set the boundaries for the solver. The correlation of the solubilities of the single enantiomer with the NRTL model was generally possible. It is obvious, that the 3-parameters NRTL model together with the two heats and temperatures of fusion allow numerous possible parameter sets, that represent well the given solubility data. Surprisingly, it was not possible to describe the solubility of the racemic compound even after adjustment of its heat and temperature of fusion in addition. Apparently, heterochiral interactions are relevant. The attempt to fit simultaneously all parameters, 6 for the NRTL model and the 4 values for the heats and temperatures of fusion, to the solubility data of the single enantiomer and the racemic compound failed. No suitable set of parameters was found. XRPD analysis of the solid phase of the single enantiomer clarified the situation. A monohydrate of the serine enantiomer is known from the literature [165]. However, Luk *et al.* described its formation to occur only above 303 K. The conducted XRPD analysis did prove the existence of the monohydrate at any temperature within the investigated range.
In Figure 4.44 the patterns of the racemic compound (n°1), the anhydrous enantiomer (n°2) and patterns from the time-resolved analysis of a sample of the single enantiomer (n°3-6), crystallised from water at 283 K, are summarised.

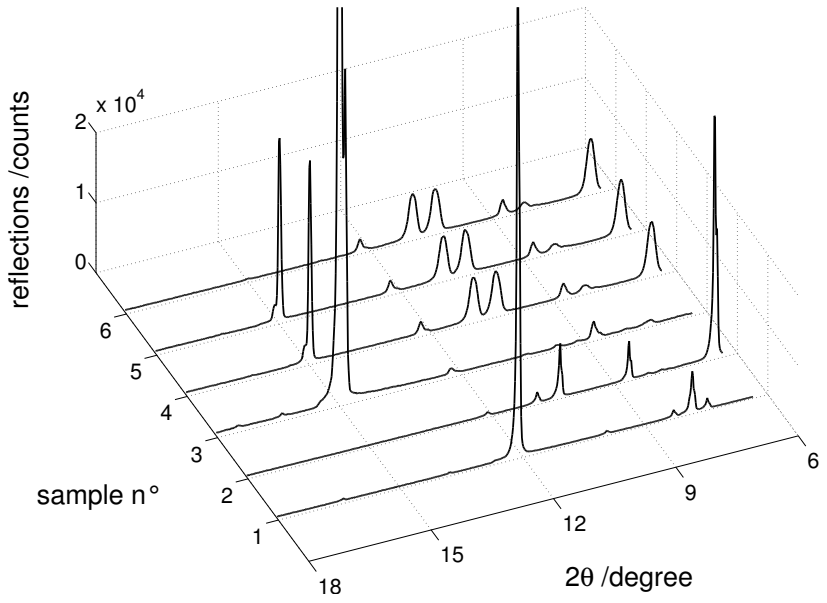

Figure 4.44 *Time-resolved evolution of the solid phase of (S)-Serine after recrystallisation from water. A hydrate-specific reflection at ~15° 2θ vanishes after time. Samples: n°1, (R,S)-reference; n°2, (S)-reference; n°3-6, identical sample at 20 min, 140 min, 200 min and 21 h.*

The result of the first XRPD analysis directly after recrystallisation showed distinct preferred orientation of the crystals at ~15° 2θ. The reflections indicates the presence of the monohydrate, which is stable for about 20 hours. The pattern of the latest analysis of the sample (n°6) were identical to the ones of the anhydrous sample n°2. The incorporation of water and also the 1:1 stoichiometry were supported by a conducted TG-DSC experiment. For the racemic compound no changes to the solid phase were observed.

The general shape of the phase diagram under consideration is illustrated in Figure 4.45.

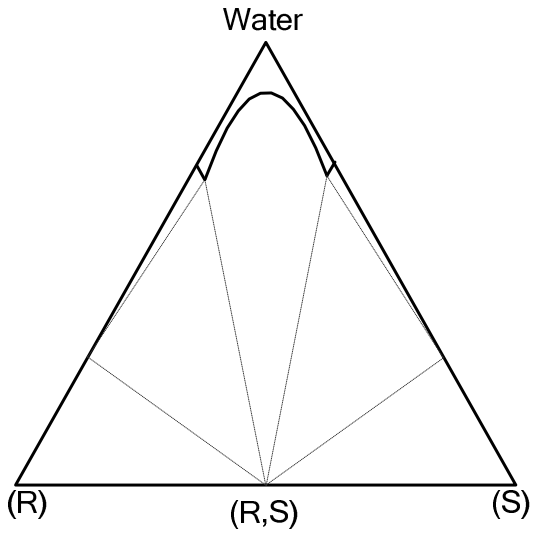

Figure 4.45 *Schematic representation of hydrate formation of the single enantiomer (compare chapter 2.4.1.2).*

Taking into account that the obtained solubility values should actually be assigned to the monohydrate of the enantiomer, a much better correlation of the NRTL model to the experimental data was possible. The solubility data of both species was reflect by minor adjustments of the heats and temperatures of fusion and use of the NRTL model with 3 parameters. No decision was made on whether heterochiral interactions were present or not due to the high model sensitivity with respect to changes to the heats and temperatures of fusion.

The outcome of the parameterisation procedure points up large discrepancies between the actual measurements and the ideal solubilities for both species. Despite the rich databases available, only own data were used for the model parameterisation (Figure 4.46, open symbols). Good agreement was found also for the literature values, except for some solubilities of the enantiomer at elevated temperatures from Luk *et al.* [165]. The accuracy of the prediction of the ternary phase diagram compared to literature values and own data was acceptable. The general shape of the solubility isotherms and the important eutectic composition was captured well. Own experimental data points in the domain of the racemic compound were less well represented, while data at the solubility isotherm at 298 K from Klussman *et al.* was predicted accurately. The eutectic composition was found slightly below 99% for all temperatures. From the experiments conducted, no dependency of the hydrate formation on temperature was found.

One possibility to adjust the formation of the monohydrate is given by use of aqueous methanol or ethanol solutions. The alcohols suppressed the solubility and hindered the hydrate to form. At ambient temperature and ratios of 3:2 by mass of methanol and water, no characteristic reflections for the hydrate have been detected by XRPD analysis. In the case of elevated temperatures (353.15 K) ratios of 4:1 became necessary to force the formation of the anhydrous phase.

Provided that no heterochiral interactions are present, the eutectic composition is assumed to remain the same in any solvent (-mixture) at the same temperature. Consequently, the caloric properties of the enantiomer are likely to change for the anhydrous form and the monohydrate. Thus, the relative solubilities of the racemic compound and the single enantiomer (or monohydrate) will vary and cause changes to the eutectic composition in solution. It was found, that the relative solubilities of the single enantiomer rise with respect to the solubilities of the racemic compound leading to even higher eutectic compositions. High alcohol content and low temperatures favour the formation of the anhydrous phase of Serine and also eutectic compositions, which are about 100%.

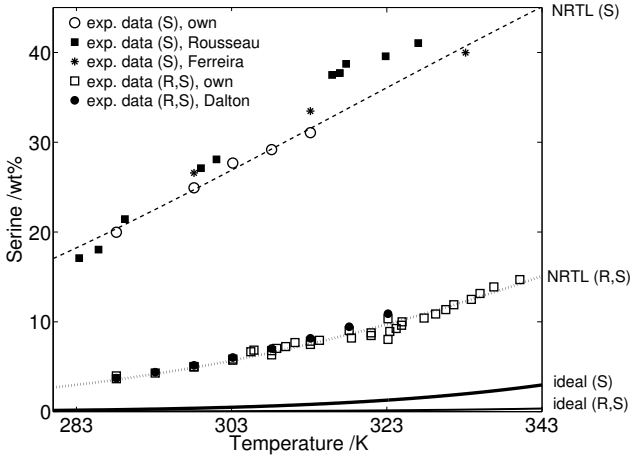

Figure 4.46 *Solubilities of the single enantiomer and the racemic compound of Serine in water-experimental data (open symbols, own; full symbols and stars, [161, 163, 165]) and NRTL model correlations.*

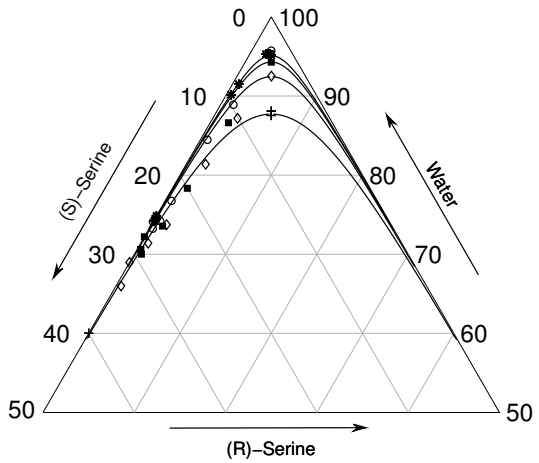

Figure 4.47 *Predicted ternary solubility isotherms and experimental data points at T=298.15 K, 303.15 K, 313.15 K (open symbols, own; Klussmann et al., stars [36]) and at 333.15 K (crosses [163]).*

The initial approach to model the system of Serine/water yielded failed. The insufficiency of the model to parameterise the apparently anhydrous system of serine, indicated erroneous assumptions. The single enantiomer of Serine was found to form a monohydrate between 283.15 K and 353.15 K. Using the known stoichiometry, the revision of the model approach led to a good correlation between the NRTL model and binary as well as ternary experimental data. The hydrate formation was tailored using alcohols in order to investigate changes to the eutectic composition.

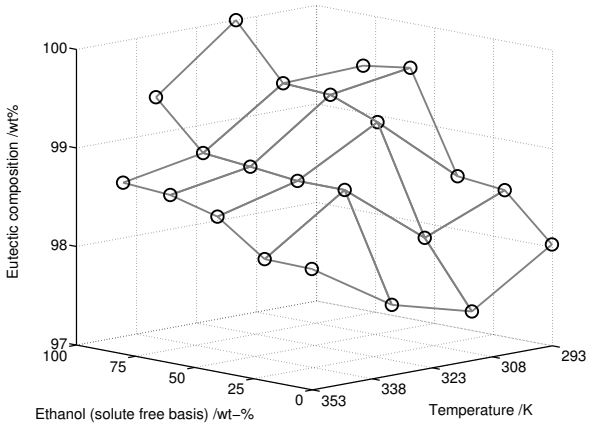

Figure 4.48 *Eutectic compositions within the Serine system in aqueous ethanol solutions (lines are a guide to the eye)*

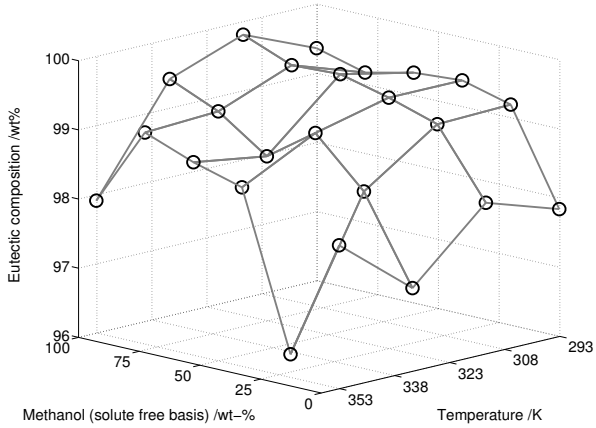

Figure 4.49 *Eutectic compositions within the Serine system in aqueous methanol solutions (lines are a guide to the eye)*

The identification of the correct solid phase helped to overcome the fundamental error in former models approaches. Now, the chemical potential at any composition and temperature within the range of the parameterisation of the model can be derived directly using the presented thermodynamically consistent model.

The estimated model parameters and the heats and temperatures of fusion for the system of serine in water are listed in the appendix in Table A.12 and Table A.13, respectively.

Proline/various solvents

A chiral system, for which the eutectic composition is reported in contradictive manner to be between 57% and 99.6% is the amino acid Proline. It is known from Methionine, that differences of 8% absolute can be attributed to changes in the temperatures. The cause of the significantly larger shifts of the Proline system have been investigated in an own study. The available data sets by Hayashi [166] and Klussmann [36] were extended by own data from isothermal equilibration experiments.

Figure 4.50 *Molecular structures of (S)- and (R)-Proline.*

The large variety of eutectic compositions for the enantiomers of Proline are illustrated by Table 4.1. Among all values two trends can be extracted. Firstly, the solvent applied is decisive. The two alcohols and DMSO reveal similar values around 75%. Within water, the obtained eutectic composition compares to the Propranolol·HCl systems, while chloroform as solvent yields exceptionally high values as in the system of Serine/water. Proline is known to form hydrates, both, the enantiomer and the racemic compound. The well investigated system of Proline/water was not part of this study.

Table 4.1 *Eutectic compositions of the Proline systems as a function of temperature and the solvent used. The table comprises results from own measurements and literature values.*

T/K	Eutectic composition /wt%				
	methanol	dimethyl sulfoxide (DMSO)	chloroform	ethanol	water
273.15	70.5 72		99.2	71.5	57 [166]
293.15	77.7 77.8				
298.15	79.0 [36]	77.7 74.8 [167]	99.6 [36]	77.0 [36]	
313.15	77.6 77.2				
333.15	78.3 77.3		92.6 94.7		

XRPD analysis of the recrystallised solid phases were performed for all other solvent systems. The results are summarised in Figure 4.51.

The pattern of the single enantiomer remained unchanged compared to the reference pattern of the (stable) phase as purchased through Sigma-Aldrich. The pattern of the racemic compound showed additional reflections upon recrystallisation from chloroform only. Klussmann claimed the existence of an air-sensitive hemi-chloroformate, which was not stable enough for XRPD analysis. The crystalline phase obtained in this study was also less stable after drying. Its formation required isothermal equilibration for several days. There is an entity in the CCDC [145] showing a Proline chloroformate. However, its pattern are different and the solid phase obtained

from chloroform here was not assigned to an entity of the database. As for all amino acids studied, neither reliable data were available nor DSC could be used to derive the corresponding heats and temperatures of fusion.

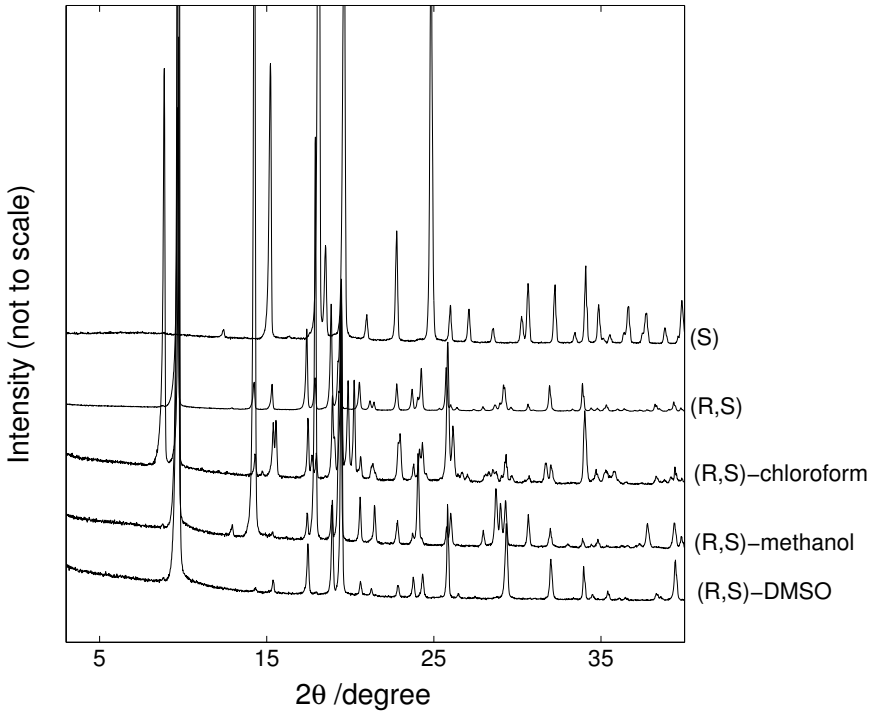

Figure 4.51 *XRPD pattern of the reference solids and the solid phases after recrystallisation from solution. It can be discriminated among the patterns of the (S)-enantiomer and the racemic compound (R,S). The latter patterns are identical when crystallised from DMSO, methanol and water, but deviate in the case of chloroform.*

The data of Proline were obtained as follows. All samples of a series of mixtures of different enantiomeric ratio decomposed shortly above 473 K. Provided, that Proline belongs to the class of compounds, that do not exhibit pronounced heterochiral interactions, the eutectic composition should remain the same in different solvents at comparable temperatures. It was assumed, that the solid phase of the single enantiomer remained unchanged in all solvents. The heat and temperature of fusion of the racemic compound were considered as identical in the alcohols and in DMSO. Thus, a fit of the shortcut model (Eq. (2.43)) to the corresponding determined eutectic compositions should allow the estimation of the missing six values for the heats and temperatures of fusion. Again, initial values for the solvate –free species were derived through the group estimation method by Marrero [149]. The decomposition temperatures were set as lower boundaries for the solver except for the chloroformate. The resulting model correlations are presented by Figure 4.52. The counter trends in both solvents were captured as well as the largely different eutectic compositions. The NRTL model was fitted against ternary solubility data of a single isotherm in DMSO from Klussmann [167]. The binary model parameters were found satisfactory, to describe correctly the given solubility isotherm and the increase in the eutectic compositions with solution temperature. It is interesting to note, that the two different trends of Figure 4.52 can be attributed solely to the heats and temperatures of fusion.

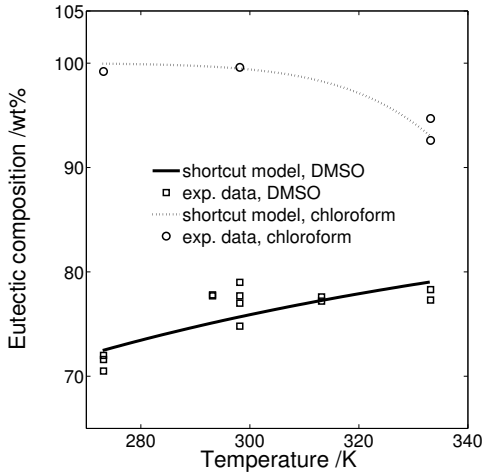

Figure 4.52 *Changes in the eutectic composition of Proline in DMSO and Chloroform. Experimental data and model estimations.*

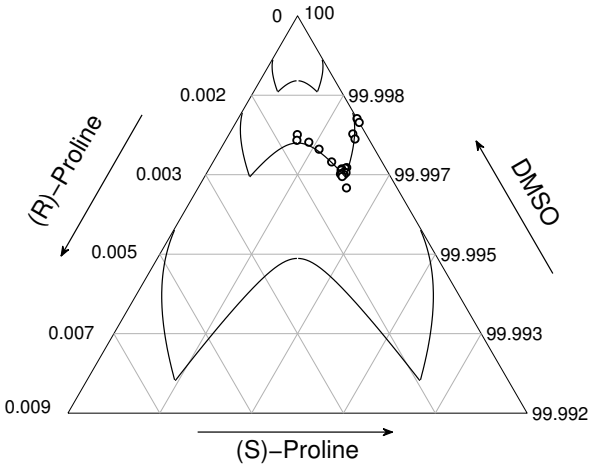

Figure 4.53 *Experimental data at 298 K and predicted solubility isotherms at 273.15 K and 333.15 K for the system of Proline enantiomers in DMSO.*

Due to the absence of heterochiral interactions, a similar trend as in the case of DMSO should be observed in other solvents, provided, no changes to the solid phase occur. Among others, alcohols are suitable to enhance the solubility of Proline, without changing the eutectic composition. In summary, the changes to the system of Proline can be explained through the proposed formation of a hemi-chloroformate and hydrates in water, respectively. The system comprises several degrees of freedom, such that the eutectic composition can be adjusted through the choice of the solvent (-mixture) and temperature.
The estimated model parameters for the system Proline/DMSO and the heats and temperatures of fusion for the enantiomer, the hemi-chloroformate and the racemic compound are listed in the appendix in Table A.14 and Table A.15, respectively.

4.2.4 Quaternary phase diagrams

Different crystallisation applications require the use of more than a single solvent. Mixtures of solvents can simplify the adjustment of a desired solubility strength. Besides evaporative and cooling crystallisation, antisolvents are frequently used to create supersaturation, to initialise nucleation and to foster crystal growth. The system of 3-Chloro-Mandelic acid in mixtures of water and 2-propanol and the system of Bicalutamide in aqueous methanol were studied with the objective to validate the model described above in order to accelerate the estimation of the corresponding quaternary SLE for further process design.

3-Chloro-Mandelic acid/water/2-propanol
SLE data in water and the melting point phase diagram are available *e. g.* from Le Minh *et al.* [168]. Quaternary solubility data of systems of enantiomers are less frequently published. Comprehensive data covering a larger temperature range as well as different solvent ratios has been available for the chiral system of 3-Chloro-Mandelic acid in the solvent system water/2-propanol by Zhang *et al.* [169].

Figure 4.54 *Molecular structures of the (S)- and (R)-enantiomer of 3-chloromandelic acid.*

Two subsequent parameter estimation procedures have been performed, both on binary systems. In this context the term 'binary' means, that solubilities can be determined without any differentiation among the chiral species. Thus, measurements on the basis of density, refractometry or simple gravimetric determination of solubilities are sufficient. Firstly, the binary solubility data of the single enantiomer in pure water was used to parameterise the NRTL model and the parameters α_{23}, Δg_{23} and Δg_{32}. The parameter indices denote the species of the (S)-enantiomer, the (R)-enantiomer, water and 2-propanol in increasing order. Heats and temperatures of fusion of the two solid species were used as published by Zhang [169]. The resulting gap to the ideal solubility curves in Figure 4.55 is significant. Further, the increase in solubility of the single enantiomer at elevated temperature appeares somewhat peculiar. However, the obtained model fit for the enantiomer was considered as satisfying. In addition, the solubilities of the racemic compound were predicted well using the activity coefficients of the enantiomer only. Apparently, heterochiral interactions can be neglected for this compound.
Secondly, solubility data of the racemic compound in isothermal mixtures of 2-propanol and water were available. The values of Figure 4.56 have been used to identify suitable parameters α_{24}, Δg_{24} and Δg_{42}. The agreement between model and experimental data was considered good.

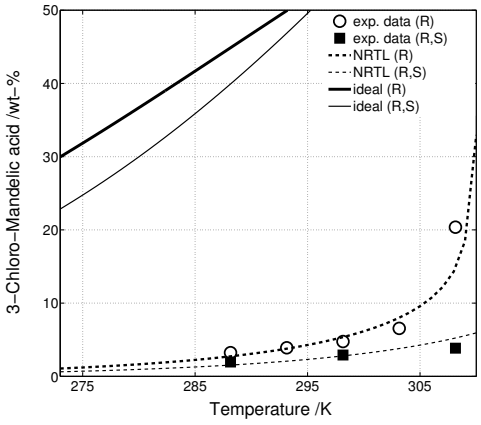

Figure 4.55 *Solubilities of the single enantiomer and the racemic compound of 3-Chloro-Mandelic acid in water-experimental data [169] and model correlations.*

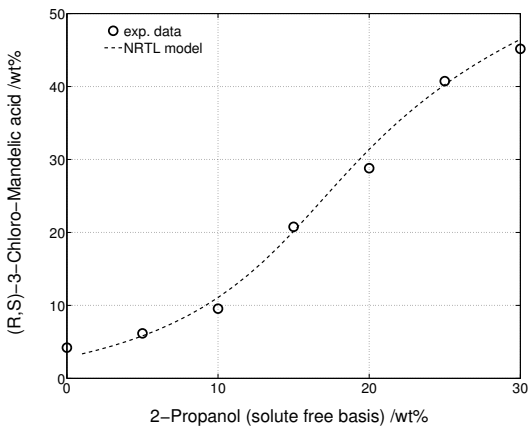

Figure 4.56 *Increase in solubilities upon addition of 2-propanol to water-experimental data from [169] and NRTL model correlation.*

The parameterisation (α34, Δg34 and Δg43) for the third contribution to the quaternary SLE-the solvent/solvent interactions-was taken from the literature. No further measurement data were considered. The predicted quaternary phase diagram is illustrated by Figure 4.57 in the form as described by Figure 2.11b in chapter 2.2.3.

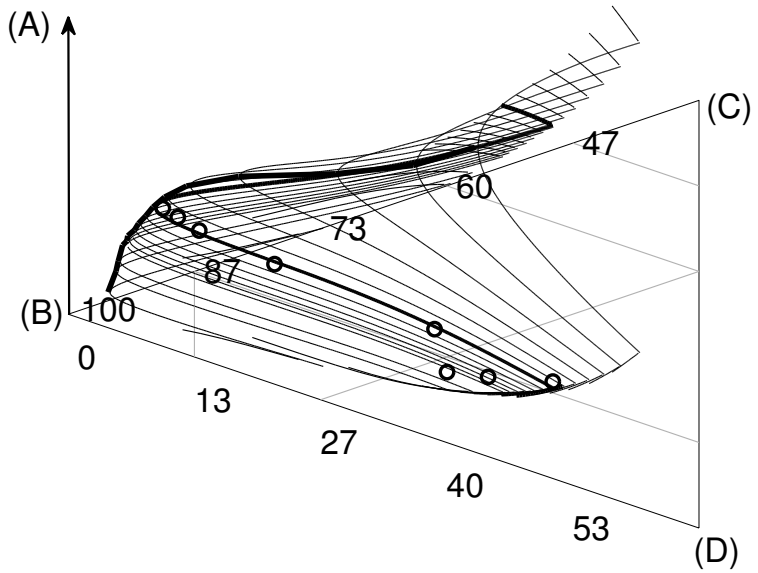

Figure 4.57 *Predicted isothermal quaternary phase diagram (T=298.15 K) of the enantiomers (C/D) of 3-Chloro-Mandelic acid in different water (B)/2-propanol (A) mixtures. The thick solubility isotherm corresponds to the experimental data [169] at a 9/1 ratio of the solvents. Further ratios: 3,4,…,20,25,50/1. All values in percent mass fraction. The second thick line corresponds to Figure 4.56 and links the solubilities of the racemic compound.*

Several solubility isotherms for different solvent ratios at 298.15 K are sketched. The S-shaped solubility increase of the previous Figure 4.56 is highlighted by a solid line. Quaternary experimental data from Zhang *et al.* [169] is accurately predicted by the corresponding solubility isotherm (solid line). The agreement within the domain of the racemic compound is better than for the domain of the enantiomer, probably due to the method of parameterisation. The eutectic composition is estimated rather accurately. Since no heterochiral interactions are present, no shift in the whole figure was determined.

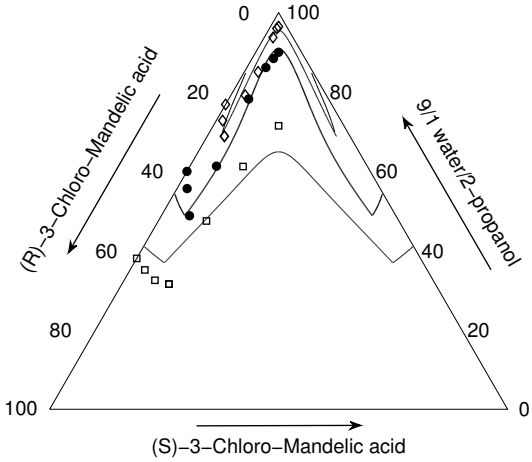

Figure 4.58 *Predicted solubility isotherms and experimental data [169] at a constant solvent ratio of 9/1 and 293.15 K, 303.15 K and 313.15 K.*

Secondly, the model estimation was compared to available experimental data at a constant solvent ratio of 9/1 and for varying temperatures (Figure 4.58). The agreement at 303.15 K is most satisfying, which can be attributed to the temperature of the model parameterisation. Other solubility isotherms exhibit large deviations from experimental data either for the domain of the enantiomer (293.15 K) or for the domain of the racemic compound (313.15 K). These thermodynamic areas are afar of the range of the model parameterisation. The poor fit reveals the limits of the possible extrapolation of modelled data.

In summary, the quaternary phase diagram of the system investigated was derived on the basis of rather limited selected binary data. In total 13 solubility measurements were used to cover the large thermodynamic domain of Figure 4.57. The model predicted thermodynamic data, which would otherwise require cumbersome measurements including analytical chiral HPLC. Its accuracy depends largely on the utilised binary data for parameterisation. Extrapolation into

completely unknown areas should be avoided from the findings of this study. In anticipation of an antisolvent process to design, the provided properties may still be useful to assess in which domain a certain composition is situated and which species will crystallise. The important property of the eutectic composition was estimated correctly within both phase diagrams.
The estimated parameters of the NRTL model for the system 3-Chloro-Mandelic acid/water/2-propanol are listed in the appendix in Table A.16.

Bicalutamide/methanol/water

The chiral active pharmaceutical ingredient Bicalutamide was investigated in collaboration within a joined project embedded in the European Framework Program 7 (*www.INTENANT.eu,* FP7-NMP2-SL2008-214129).
The compound is manufactured at a scale of several metric tons per annum at AstraZeneca and is used as a racemate for the treatment of prostate cancer. The sales value (sales figures are for 2008) is approximately 210 million US dollars. During a development program within AstraZeneca targeting manufacture of the pure (R)-enantiomer of Bicalutamide, the manufacturing method developed utilised SMB-HPLC for essentially full enantioseparation of the racemic material. An alternative separation route based on the selective crystallisation of asymmetric mixtures of Bicalutamide enantiomers required comprehensive SLE data. The separation methodology and a detailed description of the conducted solubility measurements are summarised in chapter 5.1.3.3. Within this paragraph the thermodynamic foundation to the subsequent separation is explained.

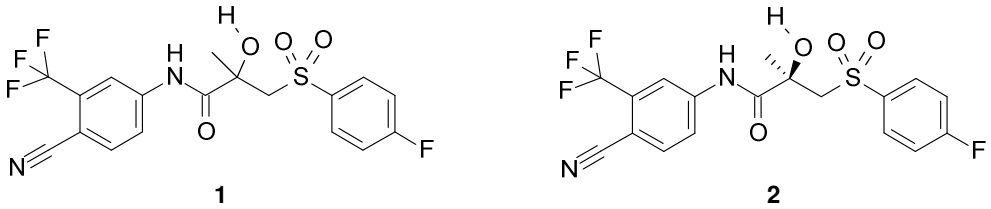

Figure 4.59 *Structures of racemic bicalutamide 1 and the pure (R)-enantiomer 2.*

The results of SLE measurements of Bicalutamide in methanol are plotted in Figure 4.60 for temperatures between 273.15 K and 333.15 K. Open dots represent the solubility of the enantiomer, while open squares indicate the solubility of the racemic compound. Error bars are based on repeated measurements of the same composition. The solubilities of the single enantiomer are almost twice as high as the solubilities of the racemic compound for all temperatures. The NRTL model was fitted to these binary data and the result is given by the solid line. The parameters obtained used to predict the solubility of the racemic compound (dotted line). The agreement with experimental data is excellent. Thus, it is likely that heterochiral interactions, as discussed above, can be neglected for this system. The result obtained here greatly simplifies predictions for other solvents, since solubility data of the single enantiomers is sufficient to derive multiphase equilibria involving several solvents.

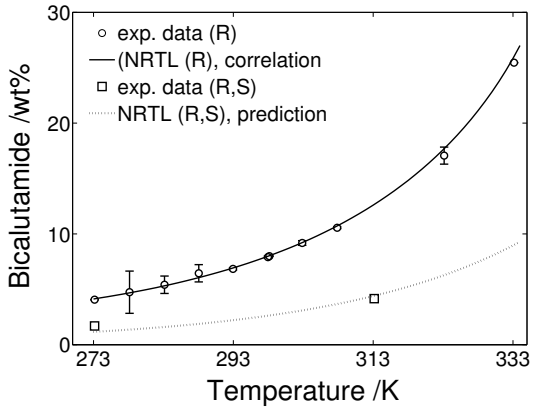

Figure 4.60 *Solubilities of the enantiomers of Bicalutamide in methanol-own experimental data and model correlation.*

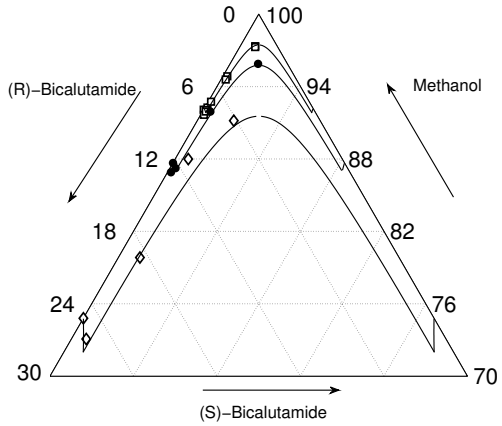

Figure 4.61 *Phase diagram of both enantiomers and methanol for 293.15 K, 313.15 K and 333.15 K. Comparison of solubility measurements and model prediction.*

The ternary SLE determined for mixtures of Bicalutamide enantiomers in methanol are shown in Figure 4.61 for the three temperatures 298.15 K, 303.15 K and 333.15 K, respectively. Solid lines were derived using the NRTL model parameter set as obtained from the solubility data of the (R)-enantiomer (Figure 4.60). The predicted ternary SLE are in good agreement with experimental data for the whole temperature range. The eutectic compositions for all temperatures were captured well.

Selected measurements of quaternary SLE of Bicalutamide enantiomers in methanol/water mixtures were conducted using calibrated ATR FTIR equipment as described in chapter 5.1.3.3.

The obtained isothermal solubility (333.15 K) of Bicalutamide enantiomers of eutectic compositions in methanol/water mixtures (Figure 4.62) were used to identify binary NRTL model parameters for enantiomer/water interactions (α_{14}, Δg_{14} and Δg_{41}). Water acts as an antisolvent to the compound. The solvent/antisolvent model parameters (α_{34}, Δg_{34} and Δg_{43}) were taken from the LLE database of the commercial software package Aspen Plus (Aspentech, USA). Two views onto an identical plot of the estimated quaternary phase diagram of Bicalutamide enantiomers in the two solvents at isothermal conditions are given by the Figure 4.63a/b. All lines represent solubility isotherms at 333.15 K. The pronounced decrease in solubility upon addition of water is clearly visible. As expected, no change in the eutectic composition was observed. The representation of quaternary SLE by the NRTL model (Table 2.1, Eqs. (13-18)) was considered to be sufficiently accurate for process design.

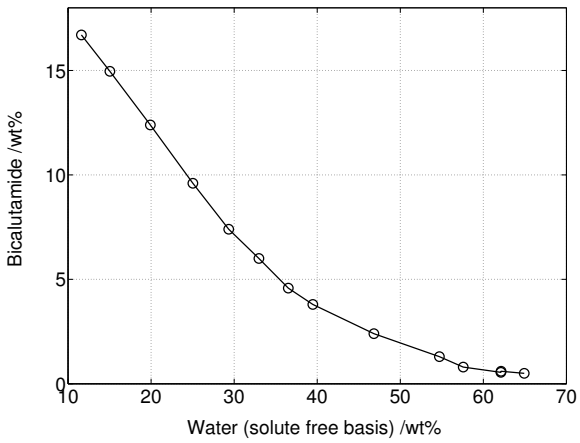

Figure 4.62 *Isothermal solubilities of the enantiomers at the eutectic composition for different methanol/ water ratios (T=333.15 K).*

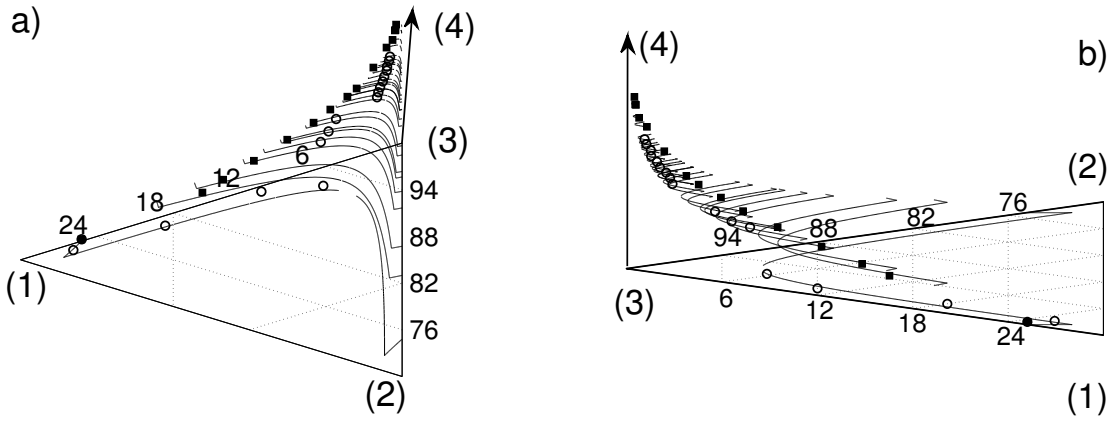

Figure 4.63a/b *Quaternary isothermal (T=333.15 K) phase diagram consisting of [(1)](R)-Bicalutamide, [(2)](S)-Bicalutamide, [(3)]methanol and [(4)]water. Solid symbols were used for model parameterisation, open symbols were not considered for the parameterisation, but for model validation.*

The estimated model parameters and applied heats and temperatures of fusion for the system Bicalutamide/methanol/water are listed in the appendix in Table A.17 and Table A.18.

4.3 Assessment of model parameters for solid/liquid equilibria

The foregoing paragraphs were concerned with methodologies representing chiral SLE by thermodynamic models. The underlying thermodynamic assumptions to the models were summarised in chapter 2. However, the applied parameter estimation methods do not allow to consider individually the contributions from hydrogen-bonds, dipole-dipole interactions and others. The majority of g^E-models incorporate all interactions into a few 'lumped' model parameters. This raises the question, whether both the model parameters obtained through fitting procedures and the applied model itself, can really represent the relevant SLE in such a way that a proper process design is feasible. By the worst scenario an unsuitable model had have been fitted by an effective algorithm to a random ensemble of experimental data points. Those model parameters obtained will not hold any physical relevance and both intrapolations as well as extrapolations by the model were not justified. For this reason and in order to evaluate the impact of typical uncertainties for a given set of experimental data in this work, statistical methods were applied to the NRTL model and the experimental data sets of a selected model compound.

Fisher Information Matrix and Bootstrap Method

The classical method based on the Fisher Information Matrix (FIM) and the bootstrap method (BM, [170]) allow to get a hold on confidence intervals, parameter identifiability and other statistical properties of model parameters [170, 171]. Estimations for confidence intervals of model parameters are usually derived through parameter sensitivities w_i, that describe the change of the state variable x according to a change of the parameter Θ_i. The FIM is calculated by the sum over all sample points with the sensitivity vector $\overline{w} = [w_1 w_2 \ldots w_N]$. In addition, the variance of

the measurements is needed. Parameter confidence intervals are calculated from the variance and from the inverse of the FIM the corresponding correlation coefficients can be gained.

$$w_i = \frac{\partial x}{\partial \Theta_i} \qquad \begin{array}{l} with \\ i: model\ parameter \end{array} \qquad (4.8)$$

For the Bootstrap method a resampling of the experimental data with respect to the observed uncertainties is required. The original data set is replicated and perturbed by a Monte-Carlo method. This results in-typically some thousands of-slightly different data sets and therefore in different sets of estimated parameters. The bootstrap approach allows on this basis to identify and quantify cross-correlations of model parameters. The BM uses parametric histograms, which represent a distribution of the estimated parameter values. From these distributions the confidence limits for the parameters and correlation coefficients can be derived. Here, the statistical methods were applied to analyse the experimental binary and ternary SLE data of the Methionine/water system. A more comprehensive description of the methods and the considered data set is available by Haida and Kaemmerer *et al.* [172].

Parameter identification and cross-correlation

For the study conducted only seven binary data points were available, which turned out to cause problems to the FIM method. Reliable information was obtained through the BM only.

The non-randomness factor α exhibits a physical meaning if set in between zero and unity. It was allowed to vary between these boundaries during the parameter estimation procedure. Its reciprocal value is physically related to the coordination number z of the lattice (s. chapter 2.3.2.1) [49]. In practice, it is often set fixed to 0.1, 0.2, 0.3 or 0.48. However, this rests usually on assumptions similar to the coordination number and equals a 'best guess' [64, 76, 173]. The parameter estimation histograms of Figure 4.64a/b reveal that it cannot be arbitrarily chosen, since it is not compensated by the interaction parameters.

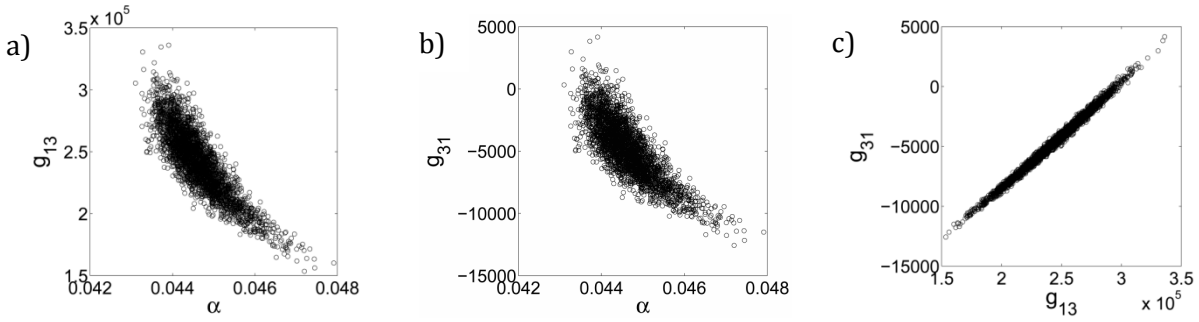

Figure 4.64a/b/c *Results of the estimated parameters plotted against each other. While the randomness parameter is only slightly correlated to both interaction parameters g_{13} and g_{31} (a/b), a slim diagonal data point cloud indicates a pronounced cross-correlation between the interaction parameters themselves (c).*

For the given system, a physically reliable value can be found between 0.043 and 0.048. There is a correlation of the non-randomness parameter and the two solute/solvent interaction parameters g_{13} and g_{31}, which is not pronounced. On the contrary, the parameters g_{13} and g_{31} are heavily correlated irrespective of the applied non-randomness factor. Since numerous combinations of the two parameters allow for a good representation of the given SLE, the physical meaning of the obtained parameters vanishes. It can be followed from the figures, that

another model, which was based on only two parameters might represent the given SLE at similar quality, but with physically more reliable model parameters.

The introduced methodologies allow for a first estimate on the reliability of already identified model parameters and also on the choice for the applied model itself. Since the principles are (within limits) of generic kind, their transfer to other g^E models is possible and might allow for the identification of the most promising model.
Regarding further details it is referred for a more quantitative assessment of the gained statistical data for the case considered to the original publication [172]. The study shows that the physical meaning of parameters of g^E-models must be considered with care and may pose, together with the model applied, uncertainties with respect to process design on the basis of modelled thermodynamic data.

4.4 Utilising estimation models for chiral applications

Estimation models like UNIFAC and COSMO-SAC cannot discriminate among enantiomers. COSMO models suffer the inherent limitation, that the 3-dimensional information of the molecular structure is broken down into a 2-dimensional representation. Within this step, any information regarding chirality is lost. While this procedure simplifies tremendously the derivation of thermodynamic data for most molecules, the predictive power of COSMO models appears limited with respect to chiral systems. It is aimed within this paragraph to elucidate how estimations from the COSMO-SAC model can be utilised despite the named restrictions for the design of selective crystallisation processes for chiral compounds.

4.4.1 Methods and tools

The performed predictive calculations on activity coefficients for chiral substances in solution rest on the procedures published by Lin and Sandler [76] and Mullins *et al.* [75, 173]. For consistency, the corresponding parameterisations and sigma profile databanks were utilised. The following procedure was adopted to estimate activity coefficients in solution:

I. Charge profiles of solutes and solvents were either taken from databases or generated with the commercial software package Materials studio (V4.3, Accelrys, USA) and the implementation of COSMO within the module *DMol3.*

II. Numerous procedures are suggested in the literature on how to proceed in terms of geometry structure optimisation [45, 75, 174]. In general, DFT geometry optimisations were performed beginning with up to 10 initial conformations, selected from I.) and from additional molecular sketches, that were generated manually. Pre-optimisations were performed with the module *VAMP.* The relevant parameters are listed in the appendix in Table C.1. The general procedure was kept identical to the conditions used for the model parameterisations. The resulting locally optimised structures were compared to identify the conformation lowest in energy, which was used for the next steps. The output file generated for this conformation contains a list of surface charge segments assigned to corresponding atoms. Furthermore, the

location of each segment, its assumed charge and the cavity volume in the dielectric continuum necessary to immerse the molecule, is provided.

III. The obtained charge profiles were processed further using the Segment Activity Coefficient (SAC) approach. The required segment averaging procedure and the iterative algorithm for the generation of segment activity coefficients were performed in analogy to the Fortran code available online at the Virginia Tech from Oldland *et al.* [175, 176]. The published scripts yield activity coefficients for binary mixtures. The code was implemented in the Matlab (Mathworks, USA) environment and extended for multicomponent systems and chiral applications.

The surface-charge densities need to be averaged to 'smooth' the charge distribution according to the COSMO-RS/SAC theory. Firstly, the averaging algorithm as proposed by Mullins *et al.* was considered.

$$\sigma_m = \frac{\sum_{m,n=1}^{n\_\cos mo} \sigma_n^* \frac{r_n^2 r_{av}^2}{r_n^2 + r_{av}^2} \exp\left(-\frac{d_{mn}^2}{r_n^2 + r_{av}^2}\right)}{\sum_{m,n=1}^{n\_\cos mo} \frac{r_n^2 r_{av}^2}{r_n^2 + r_{av}^2} \exp\left(-\frac{d_{mn}^2}{r_n^2 + r_{av}^2}\right)} \qquad \begin{array}{l}\textit{with n\_cosmo:}\\ \textit{number of segments in COSMO file}\end{array} \qquad (4.9)$$

The parameters used are given in Table C.2. r_{av} defines the effective radius of a surface element, r_n denotes the radius of the actual surface segment, σ_m represents the surface segment charge density of segment *m*, d_{mn} equals the distance between segment *m* and *n* (calculated from the coordinates of the segment origins given by the DFT/COSMO calculation) and σ_n^* is the surface segment charge density as derived from the DFT/COSMO calculation.
The sigma profile $p_i(\sigma)$ for a molecule of type i is basically a histogram of the probabilities of finding a segment with a surface charge density σ. The segment number of the latter is given by $n_i(\sigma)$, where n_i is the total number of surface segments covering the molecule i required to build its molecular cavity. The area of the cavity as defined by A_i and $A_i(\sigma)$ respectively, is the total surface area of all segments of a charge density σ. Mullins used the area weighted sigma profiles $p_i'(\sigma)$ of Eq. (4.10). Analogously, mixture sigma profiles $p_S(\sigma)$ for multicomponent mixtures can be obtained from the normalised fraction of each single component sigma profile.

$$p_i'(\sigma) = p_i(\sigma) A_i = A_i(\sigma) \qquad (4.10)$$

$$p_s(\sigma) = \frac{\sum_{i=1}^{C} x_i A_i p_i(\sigma)}{\sum_{i=1}^{C} x_i A_i} = \frac{\sum_{i=1}^{C} x_i p_i'(\sigma)}{\sum_{i=1}^{C} x_i A_i} \qquad (4.11)$$

In the course of the averaging process a discretisation and re-assigment of charge densities is performed such, that n_i equals 51 segments now and throughout further computations.

IV. The activity coefficient $\gamma_{i/S}$ of a molecule of type i in a solution S is related to the difference in the Gibbs energies $\Delta G_{i/S}^{res}$ of restoring the charges around a pure species i in a solution of S and the Gibbs energies $\Delta G_{i/i}^{res}$ of restoring the charges around a pure species i in a solution of i. The Gibbs energies are derived by the assumption of individual and independent

charged segments. To each segment of the screening procedure another segment is added with opposite charge. The paired segments are assumed to have no interaction with each other. Combinations of segments of the same charge vanish, while others show a certain 'misfit', which is summed up. Segment pairs with charge differences above an empirical threshold gain hereby additional attention, since they might be prone to form hydrogen bonds. The concept of independent segments allows the simple compilation of charge histograms for binary (and multicomponent) mixtures of desired composition. The difference in the mixture $\Delta G_{i/S}^{res}$ for a solute in the solvent and the reference case for $\Delta G_{i/i}^{res}$, the solute *i* in a solution of *i* yields the activity coefficient of the solute in solution.

$$\ln(\gamma_{i/S}) = \frac{\Delta G_{i/S}^{res} - \Delta G_{i/i}^{res}}{RT} + \ln(\gamma_{i/S}^{SG}) \tag{2.62}$$

According to Lin and Sandler the difference can be expressed by the sum of the products of the (area weighted) sigma profiles and the natural logarithm of the segment activity coefficients over all surface segments n_i.

$$\frac{\Delta G_{i/S}^{res} - \Delta G_{i/i}^{res}}{RT} = \frac{1}{a_{eff}} \sum_{m=1}^{51} p_i'(\sigma_m)\left[\ln\left(\Gamma_{i/S}(\sigma_m)\right) - \ln\left(\Gamma_{i/i}(\sigma_m)\right)\right] \tag{4.12}$$

The respective segment activity coefficients $\Gamma_{i/S}$ and $\Gamma_{i/i}$ for each segment in solution and in a pure liquid can be derived using statistical mechanics.

$$\ln\left(\Gamma_{i/S}(\sigma_m)\right) = -\ln\left\{\sum_{m,n=1}^{51} p_s(\sigma_n)\Gamma_{i/S}(\sigma_n)\exp\left[\frac{-\Delta W(\sigma_m,\sigma_n)}{RT}\right]\right\} \tag{4.13}$$

$$\ln\left(\Gamma_{i/i}(\sigma_m)\right) = -\ln\left\{\sum_{m,n=1}^{51} p_s(\sigma_n)\Gamma_{i/i}(\sigma_n)\exp\left[\frac{-\Delta W(\sigma_m,\sigma_n)}{RT}\right]\right\} \tag{4.14}$$

$$\Delta W(\sigma_m,\sigma_n) = \left(\frac{\alpha'}{2}\right)(\sigma_m + \sigma_n)^2 + c_{hb}\max[0,\sigma_{acc} - \sigma_{hb}]\min[0,\sigma_{don} + \sigma_{hb}] \tag{4.15}$$

The exchange energy $\Delta W(\sigma_m,\sigma_n)$ consists of the three contributions, namely the misfit energy E_{mf}, hydrogen-bonding interaction energy E_{hb} and energy for nonelectrostatic interactions E_{ne} for the segment pairs. ΔW accounts for the difference between a neutral and realistic pair of segments. E_{ne} is assumed constant and removed from Eq. (4.15). The decision whether a segment can contribute to the formation of hydrogen bonds is based on a charge threshold c_{hb}, which must be exceeded in order to form hydrogen bonds. The misfit energy constant α', the hydrogen bonding constant c_{hb}, and the hydrogen bonding threshold value σ_{hb} were fitted by various authors according to the model variation applied to experimental data sets. Lin and Sandler as well as Klamt calculated the polarisability factor according to Eqs. (4.16)/(4.17).

$$\alpha = \frac{0.3a_{eff}^{3/2}}{\varepsilon_0} \tag{4.16}$$

$$\alpha' = f_{pol}\alpha \tag{4.17}$$

The parameter sets considered within this thesis are summarised in the appendix in Table C.2. A Matlab script developed solves Eqs. (4.12) and (4.14) iteratively and yields the activity coefficients of each species in a mixture for a given composition and temperature.

4.4.2 Screening of solid/liquid equilibria with respect to an antisolvent

The adjustment of solvent strength for a given solute by a combination of solvents is far from being a trivial task. Known cases are rare, where stoichiometric mixtures of solvents and antisolvents led to exactly averaged solubilities. On the contrary, solubility values in solvent mixtures above or below the solubilities of both individual solvents are frequently found [42, 177-179]. An illustrative example has been determined by Romero *et al.* [180] and describes the increase in solubility of Paracetamol in mixtures of ethanol/water mixtures. A pronounced solubility maximum was observed at about ~15% water at 298.15 K (Figure 4.66). Here, an attempt was made to derive the same ternary system from the predictive COSMO-SAC model without referring back to experimental solubility data. A similar approach was publishes by Hsieh *et al.* and Shu *et al.* [181, 182]. The only inputs to the model have been the molecular structures of all constituents and the heats and temperatures of fusion of Paracetamol as given by Rüther *et al.* [42]. A pre-optimised molecular structure of Paracetamol was obtained from a free database [152]. Using the *DMol3* module *a* conformation of lower energy was identified and used for further computations. The ethanol molecule was taken from the NIST database [183] and geometrically optimised. A readily optimised water molecule from the same database was used as obtained. The corresponding charge density profiles of the three molecules are plotted in Figure 4.65. For the water molecule, all charge densities between -0.015 e/Å^2 and 0.015 e/Å^2 are present with similar frequency, resulting in an even distribution. On the contrary, most segments of ethanol exhibit a charge density close to zero, which is, as a rough interpretation, more similar to the profile of Paracetamol. The solubilities for different solvent ratios at constant temperature were obtained from consistent solutions of Eqs.(2.16),(2.62) and (4.11) using the nonlinear solver 'lsqnonlin' within the Matlab environment.

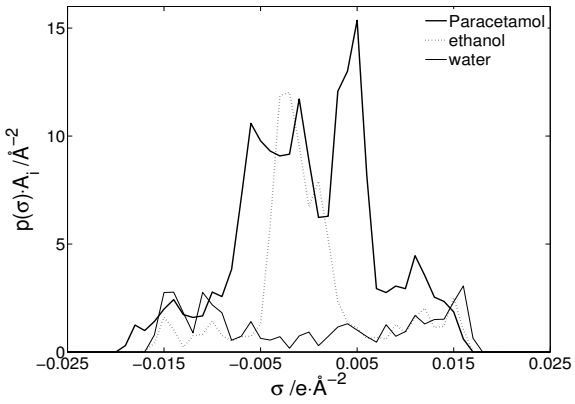

Figure 4.65 *Charge distribution profiles of Paracetamol and two solvents.*

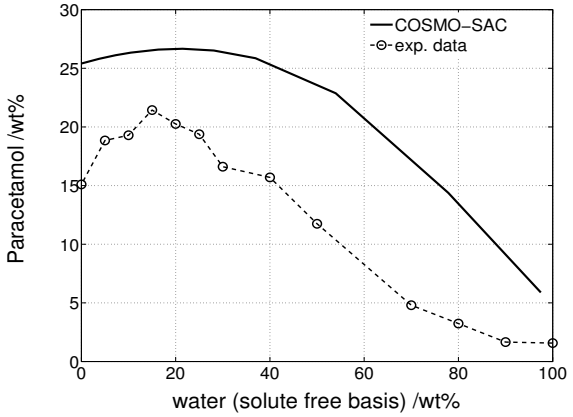

Figure 4.66 *Solubility of Paracetamol in water/ethanol mixtures at 298.15 K- experimental data [42] and 'a priori' COSMO-SAC prediction.*

The prediction reflects the complex solution behaviour qualitatively. The locus of the solubility maximum was estimated well. However, the overall solubility is largely overestimated in the

mixture and also for the individual solvents. The measurement-free prediction is appropriate to exclude water as an antisolvent candidate for Paracetamol, even if the solubility in pure water is rather low.

Motivated by the rather positive results of the Paracetamol/water/ethanol system an antisolvent screening on the basis of the COSMO-SAC model for another compound of pharmaceutical interest was performed. Prior to the collaborative study, a continuous chromatographic process for the separation of enantiomers of the compound Bicalutamide was established at the pharmaceutical company AstraZeneca. Herein, pure methanol was used for the eluent. In order to enhance the yield of the chiral separation process, two subsequent crystallisation steps were designed, which are explained in more detail in chapter 5. Within the second crystallisation step, an antisolvent was sought, which lowers significantly the solubility of Bicalutamide in methanol at isothermal conditions. The developed screening procedure was based on the four steps introduced above. Initial molecular structures of Bicalutamide were obtained from databases and literature [152, 183, 184]. The most promising geometry was found by the *DMol3* module. Solvent sigma profiles were taken from a free database [75]. The database used covers in total 1432 compounds, of which 1268 have boiling points above 323.15 K. Only the latter entities were considered, since only elevated initial temperatures allowed two crystallisation steps with a maximal gap in temperature, which enhances the specific process yield. The heat and temperature of fusion of Bicalutamide were determined by differential scanning calorimetry (Table A.18). The solubilities of the single enantiomer of Bicalutamide were computed for an antisolvent content of 0, 17, 33, 41, 50, 60, 75, 90 and 99 mol-% and for the three temperatures 273.15 K, 303.15 K and 333.15 K, respectively. This sums up to 34‘236 mixtures. Three criteria were applied to identify suitable antisolvents. Only the subset of antisolvents, which passed the criteria at all three temperatures, was investigated further.

a) First, the solubility in the antisolvent was required to be lower than that in methanol. This was not the case for 344 compounds, which exhibited higher solubilities for Bicalutamide.

b) In general, the amount of antisolvent to be added to a solution should be small, since it also dilutes the solution and this effect must be overcompensated. Thus, the slope of the isothermal solubility curve upon antisolvent addition should be negative and exhibit the steepest decline right at the beginning. No inflection points should be present. These aspects were addressed as secondary criteria. Selected results out of 762 antisolvents with other shapes of solubility curves are shown in Figures 4.67b). These were removed from further consideration.

c) Finally, as an empirical constraint, a solubility of <0.01 mol-% of Bicalutamide in the antisolvent, was applied and another 159 antisolvents were removed from the screening ensemble.

d) In total three out of 1268 solvents were found ‘suitable’ based on the results of the COSMO-SAC computations.

The remaining antisolvent candidate ensemble consisted of water, formamide and N-tetradecylcyclopentane. It is likely that some candidates are not fully miscible with methanol and may undergo a liquid–liquid phase split, which is undesired. This aspect was not addressed by this study, though some approaches are known from the literature, which consider this aspect within the framework of the COSMO-RS model and with some success. Formamide is

known to be miscible with lower alcohols [185], but its toxicity is high. N-tetradecylcyclopentane can be considered as non-standard in a pharmaceutical environment and requires additional data acquisition. Fortunately, water was among the candidates, and the advantages of this solvent are manifold. Amongst others it poses no health hazard, has a low price, high availability and is fully miscible with methanol. Thus, water was chosen for further crystallisation studies. It is evident, that a higher empirical threshold would increase the candidate ensemble and uncover other solvents with only slightly higher solubilities, but favourable physical properties in other regards. This matrix was not investigated further.

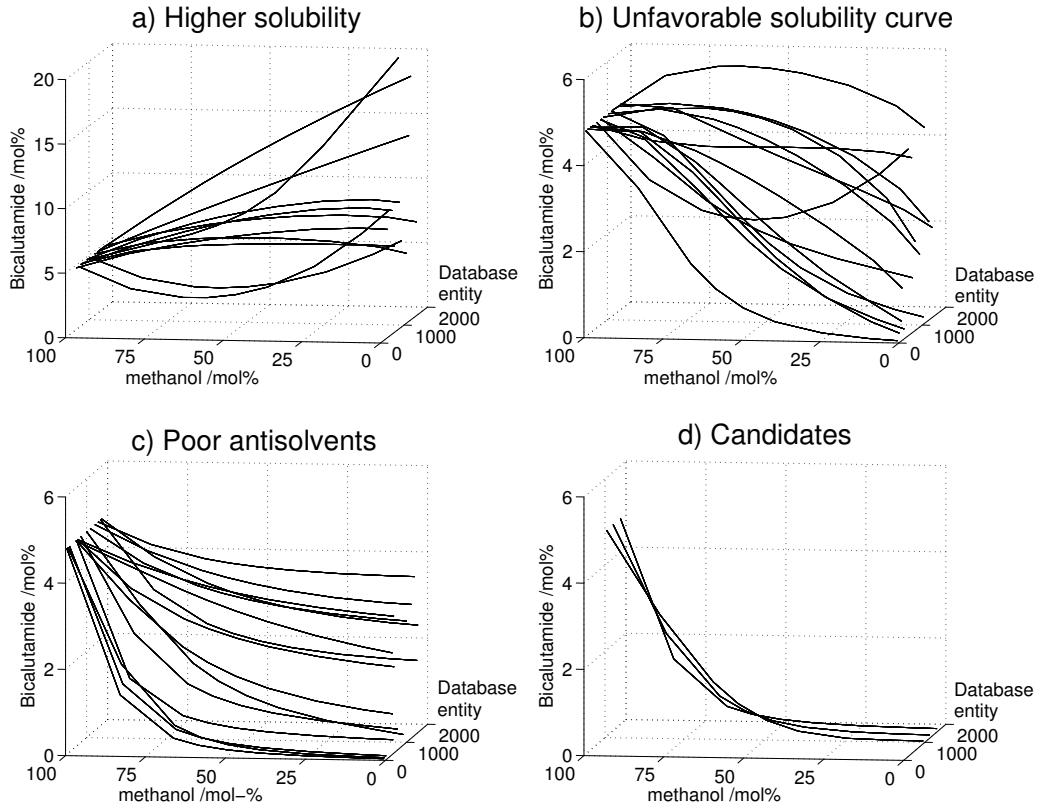

Figures 4.67a)-d) *Predicted solubilities of Bicalutamide in methanol/antisolvent mixtures. 1268 solvent database entities were considered and classified according to the criteria described. Only approximately every tens database entity is plotted for improved visibility.*

Two solvent systems were chosen to evaluate the reliability of the qualitative prediction. The quaternary phase diagram of Bicalutamide enantiomers in different methanol/water systems has been introduced already in chapter 4.2.4. Indeed, water acts as a strong antisolvent to Bicalutamide/methanol solutions. In addition, an assessment was made on the basis of toluene, since it represents very low solubilities on the one hand, but the predicted isothermal solubility curve exhibited a maximum solubility for a 3:1 methanol/toluene mixture and belonged to the candidate group of Figures 4.67b) according to the criteria introduced above (steepest decline of solubility not right at the antisolvent addition).

Solid/liquid equilibria determined for (R)-Bicalutamide in methanol/toluene mixtures were plotted for a temperature range of 280 K to 330 K. A simple two-dimensional polynomial fit of fourth order was used to interpolate among the experimental data points using the Matlab function 'polyfitn'. The surface spans over a solubility range starting at the side of pure methanol between 0.5 and 1.7 mol-%, passes through a maximum with solubilities between 0.74 and

3.8 mol-% and ends at the pure toluene side, where the solubility was lower than the detection limit. The solid lines represent the solubility predicted by the COSMO-SAC model for the 6 temperatures 280 K, 290 K, 300 K, 310 K, 320 K and 330 K. The shape of the solubility isotherms agrees well and the solubility maxima are captured correctly with a peak at a 3:1 ratio of methanol and toluene. However, the prediction can only be used on a qualitative basis for process design, since the computed absolute values overestimate the measured solubility. This is pronounced in particular on the methanol side at elevated temperatures.

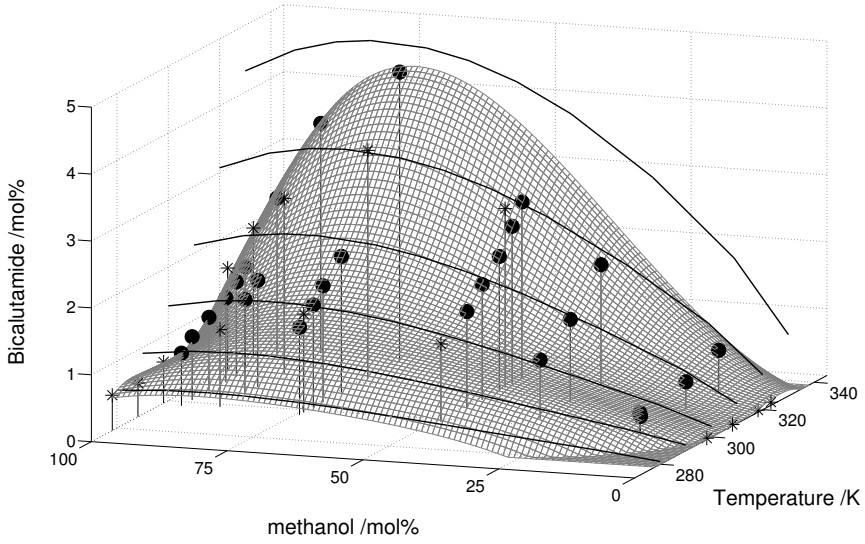

Figure 4.68 *Predicted solubilities of (R)-Bicalutamide in methanol/toluene mixtures (solid lines) and comparison with experimental data (symbols and grid); full dots, polythermal solubility measurements; stars, gravimetric solubility measurements. The polynomial of the grid is given in the appendix (chapter B).*

Summarising this paragraph, the screening of 1432 compounds resulted in the identification of three antisolvent candidates, which are supposed to exhibit favourable properties in combination with methanol, which was fixed earlier as an eluent. Two solvent/antisolvent combinations were evaluated on an experimental basis, covering a wide temperature and solvent ratio field. The measurement data were compared to predicted solubilities in solvent mixtures and a good qualitative agreement was found. The methodology cannot substitute correlative g^E-models, since the design of crystallisation processes requires a much larger accuracy. However, it is believed, that laboratory time can be saved using the introduced methodology. The most promising approach is considered to be a two step process using both, firstly an estimation model followed by a correlative g^E-model.

4.4.3 *A priori* estimation of chiral solid/liquid equilibria

The introduced methodology aimed to achieve a ranking of solvents or solvent mixtures disregarding the absolute solubility values. Although this is a major class of applications for this type of models, it is tempting to evaluate how closely chiral equilibria can be estimated from a fully ‘a priori’ concept. Thus, the solubilities of the enantiomers and the racemic compound of Bicalutamide in methanol were considered for a second time. The term ‘a priori’ is not entirely rigorous, since the model itself has been parameterised once to a larger dataset of atoms and molecules and further, both, the heat and the temperature of fusion of the enantiomer and the

racemic compound are required. The introduced COSMO-SAC and a later re-implementation, the so-called 'refined COSMO-SAC' model by Wang [77] were evaluated in this study. The refined model varies by three theoretical considerations and applied a largely different parameter set with respect to the hydrogen bonding cutoff, the averaging radius and other values of Table C.2 (in the appendix).

Firstly, the averaging procedure was performed by an altered expression introducing an empirical factor f_{decay}. The meaning of the averaging radius r_{av} remains the same as in the original model formulation, though its value is different in the new model parameter set. The combination of a new averaging value and f_{decay} resulted in very similar sigma profiles for the compounds investigated.

$$\sigma_m = \frac{\sum_{m,n=1}^{n\_cosmo} \sigma_n^* \frac{r_n^2 r_{av}^2}{r_n^2 + r_{av}^2} \exp\left(-f_{decay} \frac{d_{mn}^2}{r_n^2 + r_{av}^2}\right)}{\sum_{m,n=1}^{n\_cosmo} \frac{r_n^2 r_{av}^2}{r_n^2 + r_{av}^2} \exp\left(-f_{decay} \frac{d_{mn}^2}{r_n^2 + r_{av}^2}\right)} \qquad \begin{array}{l}\textit{with}\\ \textit{n\_cosmo: number of segments in}\\ \textit{COSMO file}\end{array} \tag{4.18}$$

Secondly, the decision whether a segment can contribute to the formation of hydrogen bonds was treated differently as by Mullins and Wang. For both models a certain charge threshold must be exceeded in order to form hydrogen bonds. Mullins treated all atoms in the same manner, while Wang allows only the formation of hydrogen bonds from N/O/F atoms and attached hydrogen atoms. Thus, two separate sigma profiles for N/O/F atoms (*hb*) and others (*nhb*) need to be considered. This also involves the separate summation of segment activity coefficients $\Gamma_{i/S}^s$ and $\Gamma_{i/i}^s$, respectively, with *s* and *t* designating either *hb* or *nhb* type hydrogen bonds in Eqs. (4.19) and (4.20). The difference in restoring Gibbs energy is derived from the double summation of contributions arising from hydrogen-bonding and non-hydrogen-bonding segments.

$$\frac{\Delta G_{i/S}^{res} - \Delta G_{i/i}^{res}}{RT} = n_{eff} \sum_{seg=1}^{hb,nhb} \sum_{m=1}^{51} p(\sigma_m^s)\left[\ln\left(\Gamma_{i/S}^s(\sigma_m^s)\right) - \ln\left(\Gamma_{i/i}^s(\sigma_m^s)\right)\right] \tag{4.19}$$

with i: component; S: solvent; n_{eff}: effective segments; seg: 1…either hb or nhb; s: hb or nhb segments

The individual terms, the segment activity coefficients in solution and in pure liquid, are also double summations over *hb* and *nhb* segments.

$$\ln\left(\Gamma_{i/S}^t(\sigma_m^t)\right) = -\ln\left\{\sum_{seg}^{nhb.hb} \sum_{m,n=1}^{51} p_S^s(\sigma_n^s)\Gamma_{i/S}^s(\sigma_n^s) \exp\left[\frac{-\Delta W(\sigma_m^t, \sigma_n^s)}{RT}\right]\right\} \tag{4.20}$$

$$\ln\left(\Gamma_{i/i}^t(\sigma_m^t)\right) = -\ln\left\{\sum_{seg}^{nhb.hb} \sum_{m,n=1}^{51} p_i^s(\sigma_n^s)\Gamma_{i/i}^s(\sigma_n^s) \exp\left[\frac{-\Delta W(\sigma_m^t, \sigma_n^s)}{RT}\right]\right\} \tag{4.21}$$

with i: component; S: solvent; seg: 1…either hb or nhb; t,s: hb or nhb segments

The exchange energy term $\Delta W(\sigma_m^t, \sigma_n^s)$ is modified such, that the hydrogen bonding part contributes only to segment combinations of *hb–hb* type and then only if their product is negative. The fitted parameters of hydrogen bonding constant c_{hb}, misfit energy constant α' and the hydrogen bonding threshold value σ_{hb} vary from the values of the COSMO-SAC model.

$$\Delta W(\sigma_m^t, \sigma_n^s) = \left(\frac{\alpha'}{2}\right)\left(\sigma_m^t + \sigma_n^s\right)^2 + c_{hb}(\sigma_m^t, \sigma_n^s)(\sigma_m^t - \sigma_n^s) \qquad (4.22)$$

with
n,m: 1...51;
t,s: hb or nhb segments

Thirdly, a redistribution of charges is performed in the model by Wang. Contributions arising from small charges are damped in the *hb*-profiles and added to the *nhb*-profiles. This is realised by the Gaussian-type function of Eq. (4.21), which weights the *hb*-sigma profile. Differences between the weighted and the unweighted profile are added to the *nhb*-profile.

$$p^{hb}(\sigma) = 1 - \exp\left(-\frac{\sigma^2}{2\sigma_0^2}\right) \qquad (4.23)$$

with
$\sigma_0^2 = 0.007\ e/Å^2$

The algorithm for the refined COSMO-SAC model was implemented in the Matlab environment. In addition to the file generated by Materials Studio, which contains the segment charge information ('*.cosmo'), the compound structure file ('*.xsd') was needed in order to assign the segment charges to either N/O/F atoms or others. The files for Bicalutamide and methanol were generated by the *DMol3* module. Unfortunately, those files are not available from the 'VT2005 Sigma Profile database' for other solvents and the refined model cannot be used with the database entries.

The obtained averaged sigma profiles for the *hb*- and the *nhb*-contributions of the Bicalutamide and the methanol molecule are displayed in Figure 4.69a/b.

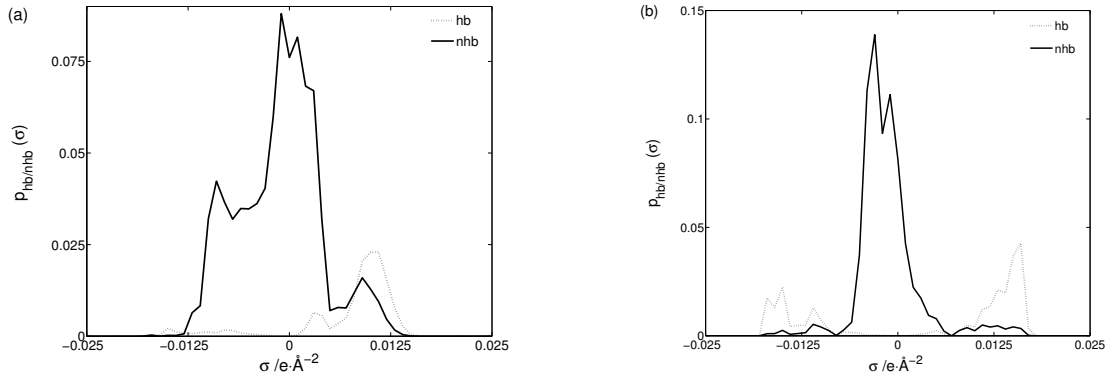

Figure 4.69a/b *Sigma profile of Bicalutamide (a) and methanol (b) according to the refined COSMO-SAC model. Dashed line, contributions by 'hydrogen bond' atoms; solid line, contributions by 'non-hydrogen bond' atoms.*

The solubilities of Bicalutamide in methanol were obtained from consistent solutions of Eqs. (2.16), (2.62), (4.11) and (4.19). The nonlinear solver 'lsqnonlin' within the Matlab environment was used to identify the corresponding SLE compositions within the temperature range of 273-333 K. Figure 4.70 compares the obtained results from the two COSMO-SAC model implementations. The thin solid line represents the best fit by the NRTL model as derived in chapter 4.2.4. The original COSMO-SAC model overestimates the experimental solubility values throughout the entire temperature range, while the prediction by the refined model overestimates the experimental values in the worst case by 5.6 wt% absolute, which is a remarkably good estimation for an 'a priori' model.

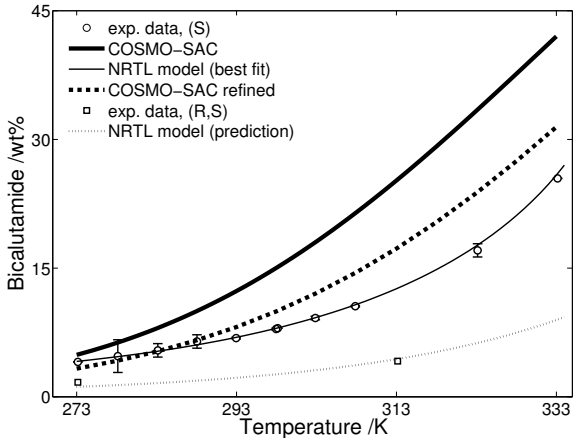

Figure 4.70 *Solubility of (R)-Bicalutamide in methanol and comparison with two 'a priori' models. The refined COSMO-SAC model reveals a better agreement over the COSMO-SAC model.*

It was shown earlier, that heterochiral interactions are negligible in the Bicalutamide/methanol system. Thus, the binary system contains the entire information necessary to sketch the ternary phase diagram of both enantiomers in solution. However, the refined COSMO-SAC model has not yet been adapted to racemic compounds, while the NRTL model [49] has already successfully been applied to compound-forming systems [33, 186, 187]. A simple approach comprises the generation of a set of activity coefficients for the relevant temperature (273.15 K to 333.15 K) and composition (0 to 2 mol-%) ranges by the refined COSMO-SAC model. A set of 260 activity coefficients covering 20 compositions and 13 temperatures was used. Thereafter, suitable NRTL model parameters were estimated for this set. The model estimates by the refined COSMO-SAC model are compared to experimental data and the best fit of the NRTL model as presented in chapter 4.2.4. The relevant SLE are split into two figures for improved visibility. The 'a priori' model overestimates the solubility of the single enantiomer, in agreement to the binary SLE. This is pronounced at higher temperatures. The solubility isotherms of the two models coincide over a large domain at 283.15 K (Figure 4.71a)).

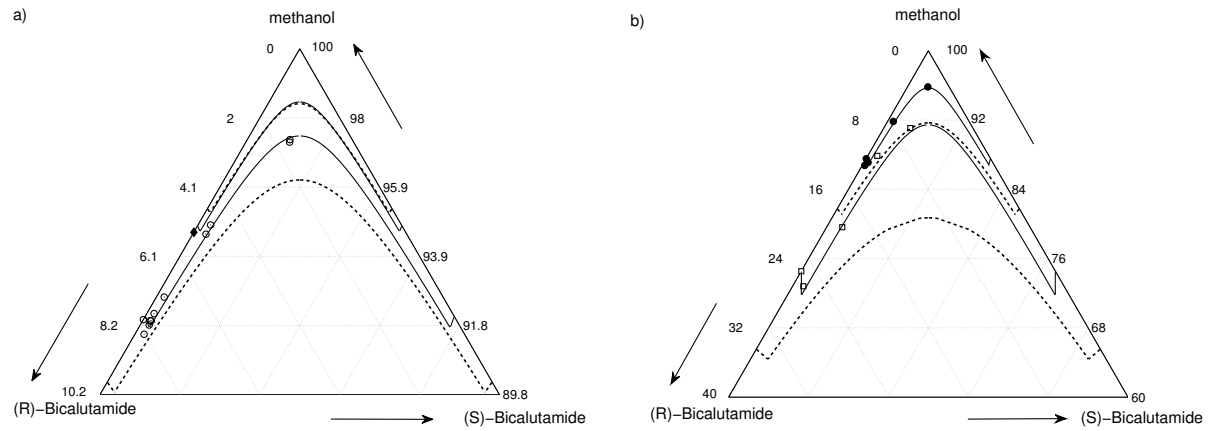

Figure 4.71 a/b *Ternary SLE of Bicalutamide enantiomers in methanol at two different scales for 283.15 K (full diamond, a)), 298.15 K (open dots, a)), 313.15 K (full dots, b)) and 333.15 K (open squares, b)). Solid lines are drawn according to the NRTL model, dashed lines represent the estimated solubilities by the refined COSMO-SAC model.*

The errors caused by the too low activity coefficients are exactly doubled in the region of the racemic compound. This is self-explaining in view of Eq. (4.6). The composition of the eutectic composition is reflected correctly by all models due to the absence of heterochiral interactions.

In summary, the estimation of ternary solid-liquid equilibria of the given system by the 'a priori' model yielded a phase diagram, which reflects correctly the general shape and certain SLE characteristics. Its accuracy at low temperatures is sufficient for process design. At higher temperatures, the SLE information is of limited use. It depends strongly on the application and the crystallisation domain whether the provided accuracy will be sufficient. On the basis of the conducted ternary SLE estimation, the additional (experimental) determination of SLE data appears recommended.

4.4.4 Screening with respect to the eutectic composition

As studies on a number of compound-forming systems revealed, minor changes to the eutectic composition due to temperature or the choice of solvents are not exceptional cases and is found more frequently than it might be expected. It was elaborated within the previous paragraphs how the magnitude of these shifts can be estimated for a given system on the basis of limited data. Here, an attempt is made to go one step further. As shown for the mandelic acid system (chapter 4.2.2), heterochiral interactions can remain unchanged in different solvents. It should therefore be possible to apply an available parameter set to a solvent (system), from which no data are available. The proposed procedure assumes, that heterochiral interactions are not solvent specific. For those cases, the different temperature and composition at the corresponding solubility isotherm will effect the magnitude of heterochiral interactions. Consequently, the eutectic composition can deviate from the system of parameterisation.
In this study, the system of Methionine in water was considered for a second time. The contribution of heterochiral interactions on the shape of the solubility isotherms was illustrated in chapter 4.2.2. It is assumed, that heterochiral interactions pose a larger effect at higher concentrations, *i. e.* if the solute fraction is high. Thus, solvents, that allow to dissolve larger amounts of the same solute (small activity coefficients) at a constant temperature, should exhibit a smaller eutectic composition. The following paragraph addresses the aspect by a conceptional study.
Methionine is hardly soluble in alcohols. Isothermal equilibration experiments yielded a strong dependency of solubility on temperature and on the amount of ethanol and methanol, respectively. Thus, saturated solutions are rather dilute and only weak heterochiral interactions are expected.

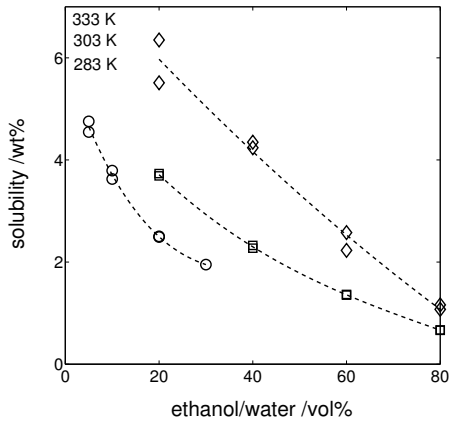

Figure 4.72 *Determined solubilities of eutectic Methionine in aqueous ethanol.*

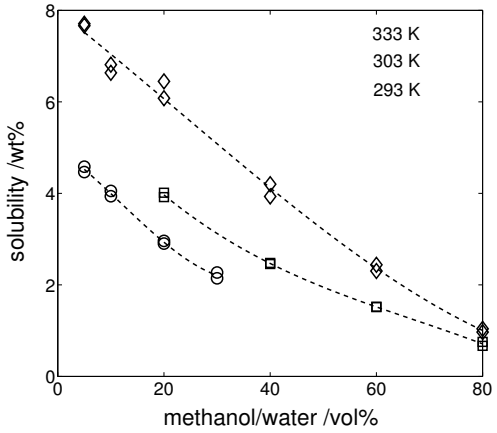

Figure 4.73 *Determined solubilities of eutectic Methionine in aqueous methanol.*

Although, the 6-parameters NRTL model yielded a good estimation of changes in the eutectic composition of Methionine in water, a gap to experimental data remained. It can generally be assumed, that, either the model is not appropriately chosen or its parameterisation was not optimal. In order to estimate the possibility of transferring heterochiral interactions, a better agreement in particular with respect to the experimental eutectic compositions is sought.

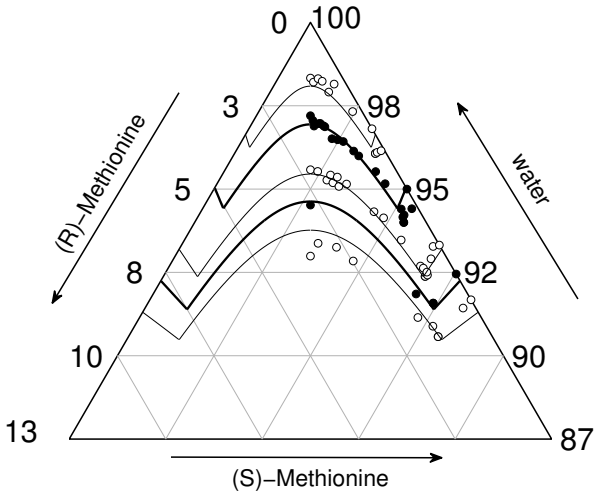

Figure 4.74 *Best model fit to ternary data of Methionine in water.*

Here, a practical approach is proposed, which relaxes the physical link between the dissociated enantiomers of the racemic compound and mixtures of the enantiomers in the domains beside the racemic compound. If a single parameter set does not cover both domains, a successful identification of three parameters for the heterochiral interactions is not possible.

Thus, a separate parameterisation of the domain of the enantiomer until the eutectic composition and a second parameterisation of the domain of the racemic compound was performed using all available ternary data. The new parameter set is given in the appendix (Table A.6), the achieved improved fit to ternary data can be seen in Figure 4.74.

The new parameter set was applied for a concept validation using solvents with different solvent strength for Methionine. 5 successive steps were performed:

I. Sketch and computational optimisation of the molecular geometry of (S)-Methionine. The applied COSMO-SAC model is parameterised for a real space cutoff of 5.5 Å for the charge density profile generation [173]. However, solubilities of (S)-Methionine in arbitrary solvents are highly overestimated in this case. Choosing a smaller value of 4.0 Å as proposed by other authors resulted in better results and was used with all solvents.

II. The COSMO-SAC model was used to identify common and frequently used solvents, for which Methionine exhibits very large or very small activity coefficients. The required sigma profiles were taken from a solvent database [75]. Besides methanol and ethanol, the sigma profiles from ethyl acetate (ET) (large activity coefficients) and dimethyl sulfoxide (DMSO) (small activity coefficients) were chosen from the screening ensemble for a more detailed investigation.

III. Activity coefficients for Methionine in the considered solvents at relevant compositions and temperatures were plotted using the COSMO-SAC model. The grid allowed for the parameterisation of the NRTL model instead of using experimental data. This step might be substituted, since the profiles by the COSMO-SAC model are only estimates. Correlative models or experimental data are always favoured, if available.

IV. The binary NRTL parameters for heterochiral interaction and the binary NRTL parameters for solvent/solute interactions were combined to derive the corresponding ternary SLE.

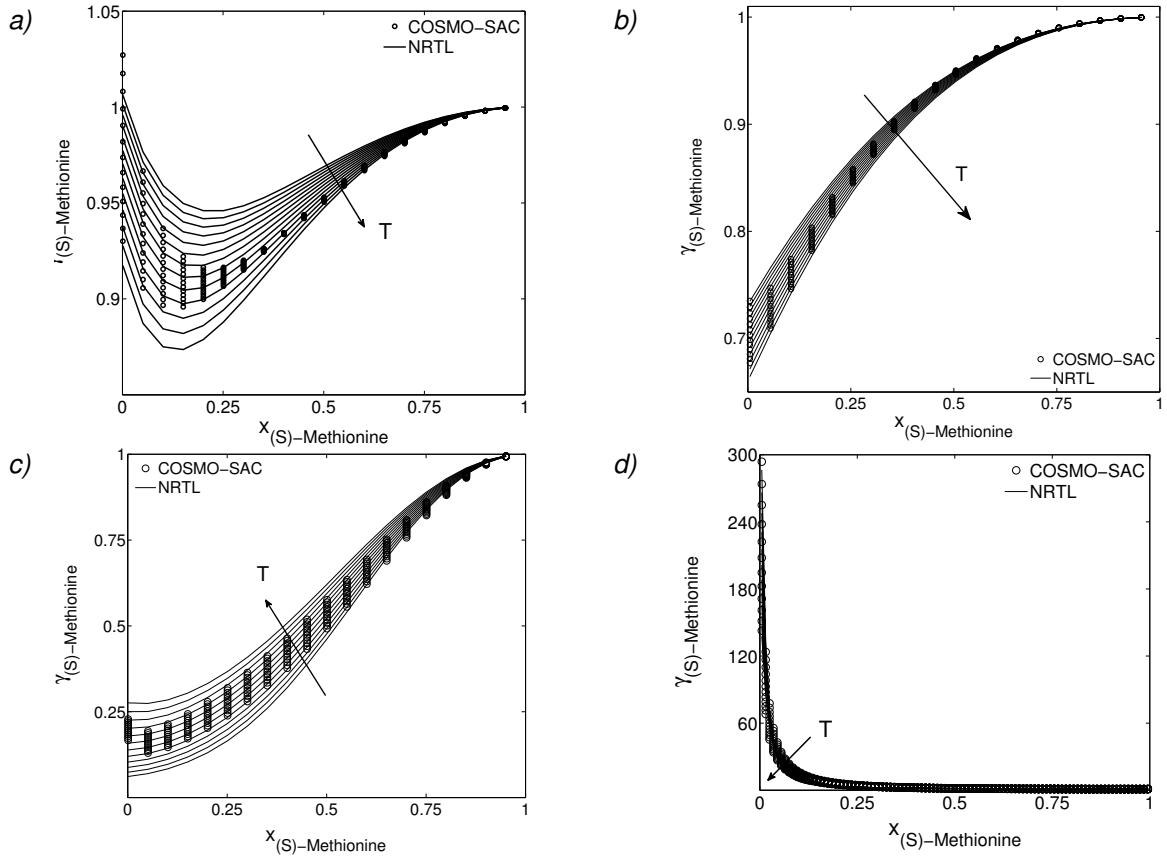

Figure 4.75 *Activity coefficient profiles (symbols) of (S)-Methionine between 273-333 K as obtained through the COSMO-SAC model for a) ethanol, b) methanol, c) DMSO and d) ethyl acetate. Lines: correlation by the NRTL model.*

Within Figure 4.76 the estimated corresponding shifts of the eutectic composition of Methionine in the solvents ethanol, methanol and ethyl acetate are summarised. The thick bold line corresponds to the shift in water as given by Figure 4.74.

The solubility of (S)-Methionine in water at low temperatures is much higher as the corresponding ideal values up to 330 K. Activity coefficients above this temperature become greater than unity (compare Figure 4.19). The activity coefficients of Methionine in both alcohols

are lower than in water up to 298 K, the order is switched for higher temperatures. Accordingly, the curves of the proposed eutectic compositions of the alcohols intersect at 298 K in Figure 4.76 with the eutectic composition in water. The performed equilibrium experiments with ethanol and methanol (dashed lines, symbols) reveal an intersection, too. The experimental intersection is situated at temperatures 15 K higher. It is tempting to suggest, that the activity coefficients of Methionine in ethanol and methanol are not accurately represented by the COSMO-SAC model for higher temperatures. This could explain the deviation from experimental data at higher temperatures. Nevertheless, the plot provides an indication, that larger shifts of the eutectic compositions in alcohols compared to water might be possible. An extreme case is given by the system of Methionine in ethyl acetate. The very high activity coefficients disallow for high solubilities. This aspect is reflected by high eutectic compositions at all temperatures and the corresponding upper dashed line in Figure 4.76. The second extreme case- low activity coefficients- is given for the solvent DMSO. The shape of the resulting solubility isotherm is rather steep, leading to very low eutectic compositions. The NRTL model was not capable to predict these values accurately over a larger temperature range. Thus, the eutectic compositions are not drawn in Figure 4.76, but indicated for a single isotherm in Figure 4.77. Eutectic compositions are estimated to 70-80 %. Further the shapes of the solubility isotherms of the enantiomer and the racemic compound in DMSO and in water are plotted in the same figure for comparison.

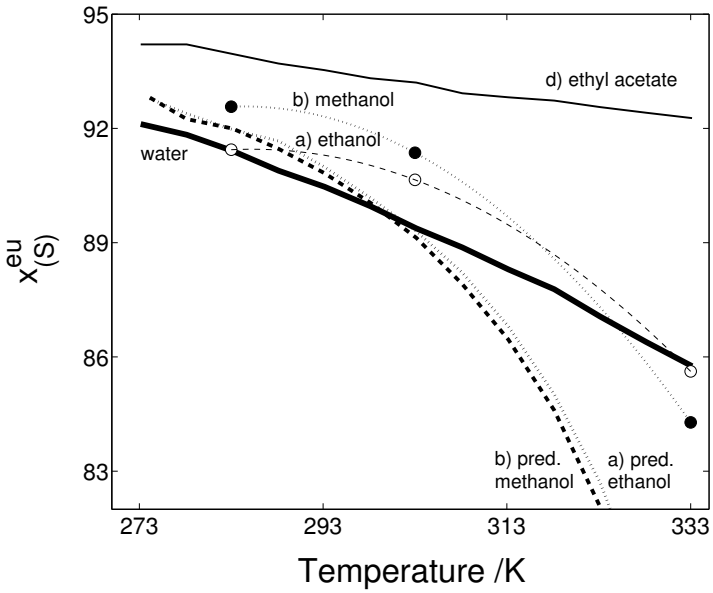

Figure 4.76 *Experimental and predicted eutectic compositions for ethanol (a), dashed lines, open symbols), methanol (b), dotted lines, full symbols) and ethyl acetate (d)). The eutectic composition in water according the NRTL model is given by the bold solid line.*

Both, DMSO and ethyl acetate reveal largely different isotherms with respect to water. Here, a correlation of low eutectic compositions and low activity coefficients is found. This trend can be explained by reference to the equation by Prigogine and Defay (Eq. (4.6)). Low activity coefficients account for a larger fraction of dissolved solute, since the left side of the equation remains constant for isothermal conditions. Compared to the equation by Schröder and van-Laar (Eq. (2.16)), the activity coefficients are multiplied, thus that the increase in solubility is higher for the racemate than for the enantiomer and the eutectic compositions shifts to lower values.

However, these considerations must be more subtle. It is possible that the contribution by pronounced homochiral interactions prevails and correlations different from the presented ones are obtained. The (artificial) two systems presented in chapter 4.1.2 are one example, where high activity coefficients led to steep solubility isotherms in the absence of heterochiral interactions. Thus, both contributions can be relevant for proper estimations.

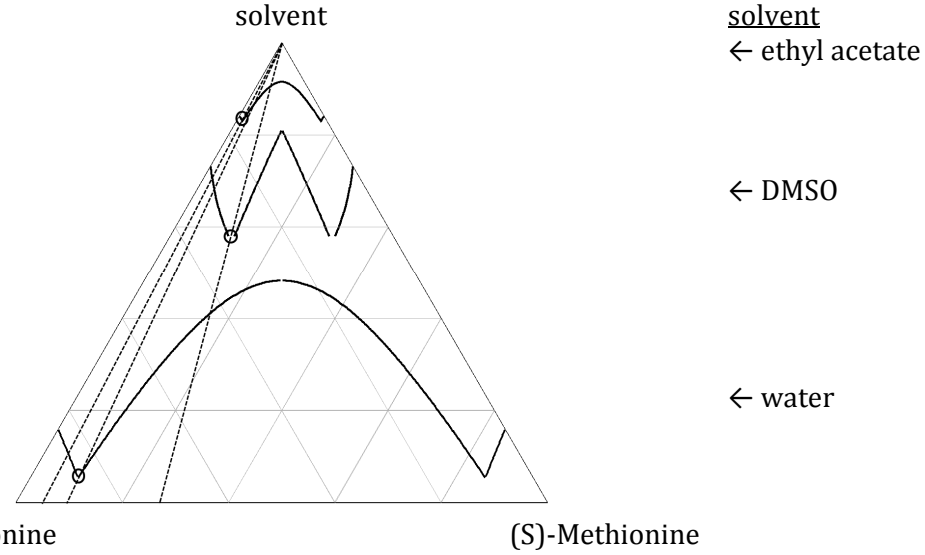

Figure 4.77 *Comparison of shapes of solubility isotherms at 293 K (scaled) of Methionine in water (lower line), DMSO (middle line) and ethyl acetate (upper line).*

The conducted conceptual approach appears attractive, although the quantitative estimates of shifts in the solvents ethanol and methanol lack accuracy. Provided, that more reliable data on the solubility of a compound of interest are available (through experiments or group contribution methods), a higher quality of estimates is expected. The identification of solvents with low activity coefficients and presumably large changes in the eutectic composition is in demand for high process yields of crystallisation process. This aspect is addressed again in more depth in chapter 5.1.3.

4.4.5 Solid state properties from the analysis of solid/liquid equilibria

The phase behaviour of Malic acid (chapter 3) outlines the general obstacle, that the knowledge of solubility isotherms is not sufficient to assign phase domains to solid species aiming to crystallise the latter selectively. SLE models can be suitable to derive the slope of solubility isotherms, provided, that the corresponding solid phases are known. The reverse direction-solid state properties from SLE analysis-is usually plurivalent and may lead to miss-interpretations as explained more comprehensively in chapter 3. In fortunate cases, model parameterisation from solubility isotherms will fail vigorously as described for the case of the Serine anhydrate. Those cases underline the need for in-depth solid state analysis. A complete description of SLE appears ill-posed until an appropriate (theoretical) description of the solid phase is found.
An illustrative example is given by the system of Escitalopram. Hereby, the (S)-enantiomer of the compound Citalopram is the pharmaceutically active species.

It is sold as Escitalopram oxalate, which is a molecular salt of the N-protonated Escitalopram cation. The molecular weight of Escitalopram (324.39 g/mol) and the oxalic acid molecule (90.04 g/mol) sum up to M=414.43 g/mol. Binary solubility data of the Escitalopram oxalate/ethanol system are available from a master thesis by Ewelina Płoszaj [188]. The thesis comprises an attempt for the chiral separation by crystallisation. It is shown, that the system belongs the class of solid solutions (compare Figure 4.23c)), which can be less suitable for chiral separation by crystallisation (see chapter 3). Thus, understanding of the solid phase (formation) might be the first step to tailor more suitable SLE for this compound.

Determination of the heat and temperature of fusion of Escitalopram oxalate by DSC yielded a temperature of fusion of 425.4 K and a heat of fusion of 39.8 kJ/mol. The refined COSMO-SAC model was used to estimate the activities of the oxalate salt in ethanol. In a first step, a proposed molecular structure of the neutral salt of Escitalopram oxalate ((Figure 4.78a), denoted 'Mono') was geometrically optimised.

Further, sigma profiles were generated and allowed the estimation of solubilities of the undissociated salt in ethanol. The results revealed a large gap with respect to the experimental values (dashed line, Figure 4.79). Such a large error of prediction was considered very unusual. Harrison *et al.* [189] offered an explanation proposing a larger molecular complex as previously assumed. Herein, two N-protonated Escitalopram cations and a double negatively charged oxalate anion are accompanied by a neutral oxalic acid molecule and a partially occupied water molecule (not shown) in the crystalline state. The complex, denoted herein 'Dimer', was obtained from crystallisation from ethanol. Consequently, the molecular mass of the 'Dimer 'complex doubles to M=828.86 g/mol (with disregard of the water molecule) and the specific heat of fusion changes to 78.8 kJ/mol. The latter is due to the conducted mass based DSC measurement, which yields the molar heat of fusion from the information of the molar mass only. Geometrical optimisation of the published molecular structure and re-calculation of the solubility in solution revealed a much better agreement between the estimates and the experimental data (Figure 4.79, solid line).

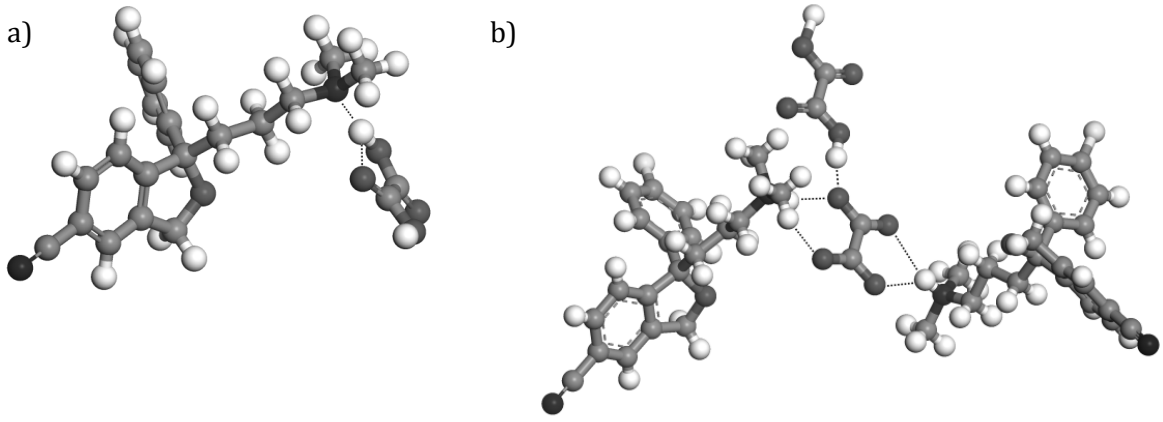

Figure 4.78 *Complexes of Escitalopram oxalate involving 2 molecules ('Mono', a)) and 4 molecules ('Dimer', b)).*

It is an open discussion, if and where organisation of molecules in solution takes place. It may happen prior to the incorporation into a restricted unit cell and again while entering into the crystalline lattice. In the limiting case, there are molecularly organised structures surrounded by solvent molecules, which are identical to the structures in the crystal. In the opposite case, the molecular structure and conformation of the molecules involved is not related to the structure

within the corresponding crystals and the crystalline structure forms right at the solid/liquid interface. The latter implies for the case of Escitalopram oxalate, that either the whole 'Mono'-complex or alternatively Escitalopram and oxalic acid molecules are placed alternately into a growth unit forming a 'Dimer'.

Both cases were considered for the solubility estimates. The solid line of Figure 4.79, denoted 'Dimer/Dimer', represents the estimate for the large complex both in the solid and in the liquid state, whilst 'Mono/Dimer' is the estimate for the proposed case of a small complex in the liquid phase and the large complex in the solid phase. The results support the case of different structures in the crystal and in the liquid phase due to the better agreement with experimental data. However, the difference to the estimate of the 'Dimer/Dimer' case is within the accuracy of the COSMO-SAC model estimate. Thus, rather an indication than a concluding remark can be stated here. In contrast, the existence of the proposed large complex in the crystalline phase is strongly favoured over the simple salt structure, since the differences in the estimates are surprisingly large and far beyond the typical error of the model. In summary, the citalopram oxalate system investigated poses a selected example, for which indications regarding the correct solid state can be derived through SLE models. Since the considered model rests on the determination of the heats and temperatures of fusion only, a decision between two theories can be supported from limited experimental data.

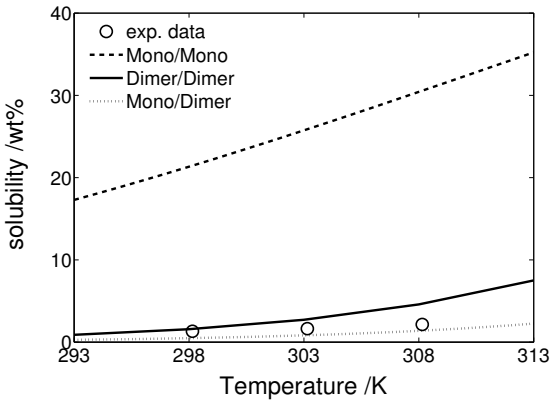

Figure 4.79 *Solubility of Escitalopram oxalate in ethanol. Experimental data [188] and estimates by the refined COSMO-SAC model. 'Mono' denotes the small complex made of a single Escitalopram cation and 'Dimer' denotes the large complex in the liquid/solid phase.*

4.5 Summary

The preceding chapter 4 relates to the description of characteristic properties of SLE, which are in demand for successful chiral separations. The most relevant types, conglomerate- and compound-forming phase diagrams, were derived for a number of compounds. The NRTL model was capable of predicting ternary and quaternary phase diagrams from binary data, if systems appeared more simple and heterochiral interactions were less pronounced. The model was found suitable for the estimation of changes to the eutectic composition, which is relevant for chiral separations. It was shown, that heterochiral interactions can be, once determined, transferred from one solvent to another. Since changes to the eutectic composition alter with a specific solvent strength, the approach opens up possibilities for a targeted screening of solvents with suitable properties for chiral crystallisations.

Parameters of thermodynamic g^E-models can be highly correlated and their physical meaning might vanish. A studies involving the NRTL model and Methionine in water quantified typical uncertainties and parameters sensitivities providing a more general framework how to assess the quality of a models and their parameters.

Recent SLE estimation models cannot discriminate among enantiomers. This is no hurdle in the identification of suitable antisolvents. Tools like the COSMO-SAC model appeared appropriate here. Provided, simple systems without pronounced heterochiral interactions are present, the quantitative estimation of the relevant SLE for process design is possible for chiral systems. The limited accuracy of estimation models entails generally larger errors in the prediction of solubilities of the racemic compound compared to the single enantiomer, since the estimated activity coefficients are multiplied. This aspect necessitates particular attention in the use of group contribution and COSMO-type model for chiral systems. On the other hand, the use of estimation models might serve as an powerful tool in the first identification of solvents, which allow for larger shifts in the eutectic composition, if pronounced heterochiral interactions can be expected. On a less accurate level, which can be appropriate for selected cases, predictions of estimation model can assist in judging whether a certain solid state can exist or not and may allow the accelerated system description.

More comprehensive information on the aspects introduced in this chapter were published in the Journal of Chemical Engineering Data [150, 187], in the Journal of Fluid Phase Equilibria [190] and in the Journal of Chemical Engineering and Technology [172].

5 Separation of enantiomers

Being aware of fundamental properties for a given chiral system, the most promising strategies for its separation can be identified. Selected theoretical approaches for the crystallisation-based and chromatography-based chiral separations together with coupled processes were corroborated by experiments, validated and assessed in this chapter. The scale-up of a coupled process aimed to prove its practical relevance.

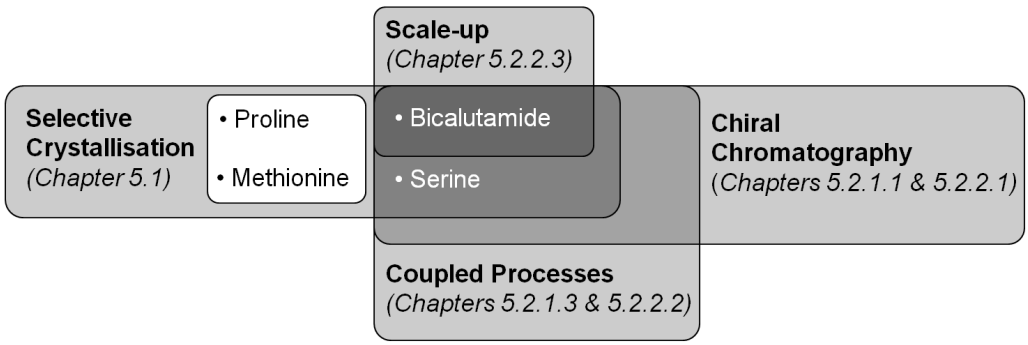

Figure 5.1 *Structure of chapter 5. The most comprehensive study was performed for the pharmaceutical compound Bicalutamide, other compounds were analysed according to the mapping chapters only.*

5.1 Selective crystallisation of enantiomers

Within the previous chapter a number of phase diagrams have been presented. Methodologies affecting the eutectic composition and the slope of solubility isotherms were presented. Facing the design process of a thermodynamic separation, the spatial distribution of the different domains is of importance in the first place. However, there are more aspects to be considered, of which selected examples will be explained in this paragraph.

5.1.1 Solubility ratios

The ratio of the solubilities of a racemic mixture and the solubilities of the single enantiomer have a large influence on the possible productivity of preferential crystallisation strategies due to the change in the slope of the metastable solubility isotherms. Metastable solubility isotherms are prolonged isothermal solubility lines into the supersaturated area. They denote the driving force for crystallisation, *i. e.* the species-specific supersaturation and can be used to estimate the theoretical yield. A comprehensive discussion of this aspect is reported by Collet *et. al.,* Levilain *et al.* and Polenske *et al.* [16, 99, 191, 192]. In theory, the crystallisation trajectories of a seeded preferential crystallisation process are extended for small ratios and more target enantiomer

can be crystallised and harvested, provided that no nucleation of the undesired counter enantiomer takes place. Within Figure 5.2 a racemic supersaturated solution is seeded with crystals of the (R)-enantiomer. The lengths of the crystallisation trajectories equal the maximal thermodynamic potential, that can be used for a directed selective crystallisation process. The area of possible entrainment, *i .e.* the possible enrichment before the metastable solubility isotherm is approached, is larger in the case (bold lines), where flat solubility isotherms are present. The upper dashed arrow is prolonged in comparison to the lower dashed arrow as a result of the different slope of the solubility isotherms. Attention is invited to the fact, that the solubility of the single enantiomer in both solvents is assumed identical. The resulting change of the compositions of the mother liquors after selective crystallisations (denoted by solid arrows) is large and consequently different crystallisation process yields can be expected.

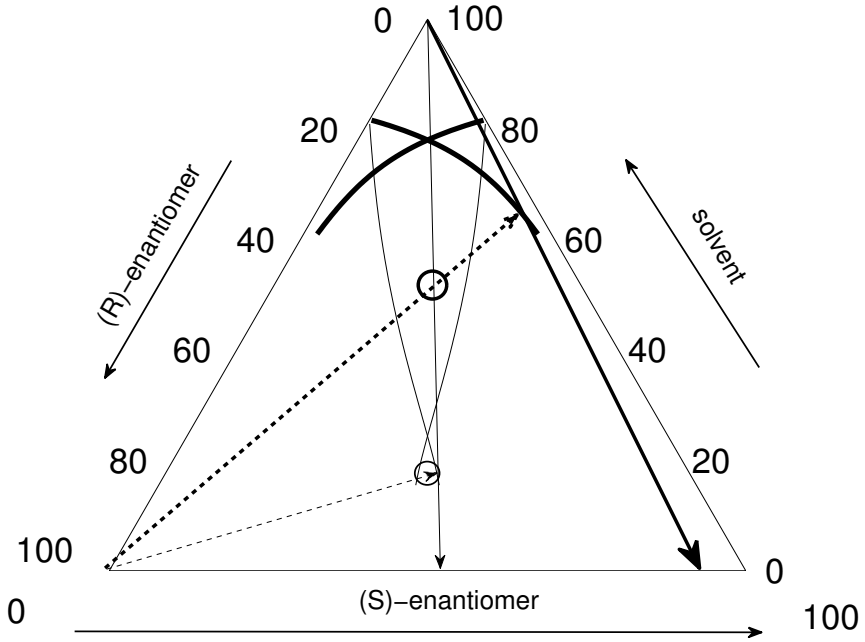

Figure 5.2 *Two cases of seeded crystallisations for a compound exhibiting the same solubility in a solvent but largely different slopes of solubility isotherms (thin and bold lines, respectively). Flat solubility isotherms (bold) allow the efficient purification of a racemic mixture (initial composition, open bold symbol). The remaining mother liquor holds mainly the (S)-enantiomer (bold arrow). Seeded crystallisation witin a system with steep solubility isotherms (thin steep lines) allows only for very minor yields, the process trajectory (thin dotted arrow) hits the solubility isotherm in the vicinity of the racemic composition an the initial composition (open thin symbol). The remaining mother liquor is only slightly enriched by the (S)-enantiomer.*

Within chapter 4.1.2, the slope of solubility isotherms was related to values of activity coefficients. From this findings, it is simple to follow, that well chosen solvents will yield more flat solubility isotherms and therefore larger areas for entrainment. Estimation models as the COSMO-SAC approach can provide activity coefficients and may assist in identifying suitable solvents. If heterochiral interactions are known to be present, a parameterisation of the latter and re-use of the obtained parameters in the solvent screening procedure (as described in chapter 4.4.4) might allow the identification of promising solvent (systems).

5.1.2 Preferential enrichment in the liquid phase

Though, originally introduced by Tamura and co-workers for enantioseparation by a polymorphic transition process [193], the term 'preferential enrichment' describes well a simple process variation for systems exhibiting an eutectic composition close to unity. In analogy to Tamura's process, the target enantiomer is not crystallised, but dissolved selectively in the liquid phase. Another reference to this concept is given by Chen *et al.* [92]. The process allows the purification of any asymmetric initial mixture, provided suitable ternary SLE are present.
The corresponding mass balances, necessary for process design, and a generic expression for process yield are derived in the following. An initial feed mixture can consist either of solvent-free solids or, as the result of a pre-enrichment step, be fed as solution. Adjustment of this mixture by addition of a specific amount of solvent or removal of the surplus of solvent by *e. g.* partial evaporation, respectively, places the overall composition onto the phase boundary between the 3-phase and the inner 2-phase region as illustrated in Figure 5.3.

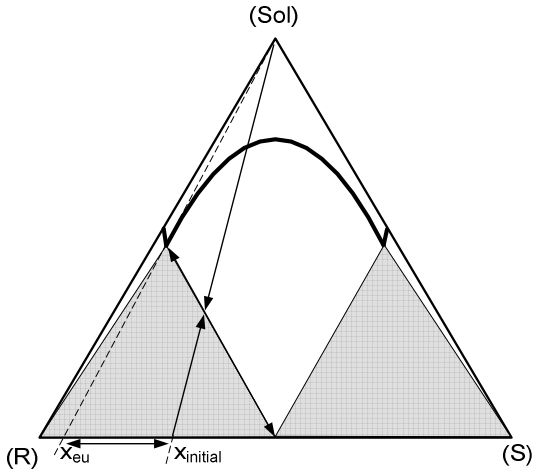

Figure 5.3 *Concept of 'preferential enrichment' via the liquid phase.*

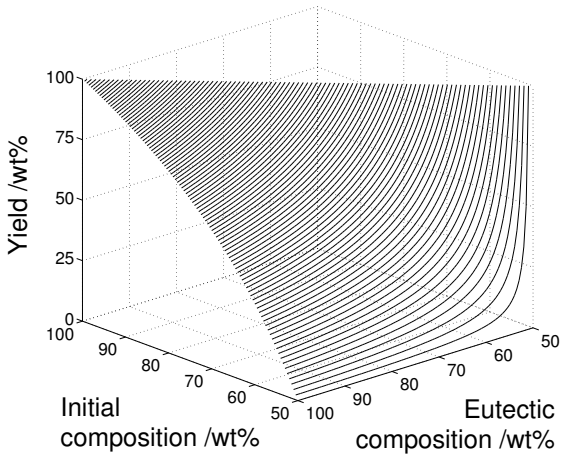

Figure 5.4 *Theoretical yield of the process introduced for various initial feed compositions and eutectic compositions for given systems.*

The theoretical yield of this process is derived from a mass balance considering the enantiomer in the racemic solid phase m^s, in the liquid phase m^{eu} and in the initial composition $m^{initial}$. The balance for a racemic compound and the (R)-enantiomer reads

$$m^{initial} = m^{eu} + m^s \qquad (5.1)$$

$$m^{initial}\, x_{(R)}^{initial} = m^{eu}\, x_{(R)}^{eu} + 0.5\ m^s \qquad (5.2)$$

with $x_{(R)}^k$ being the ratio of the enantiomers defined as

$$x_{(R)}^k = \frac{m_{(R)}^k}{m_{(R)}^k + m_{(S)}^k} \qquad k: \textit{initial, eu.} \qquad (5.3)$$

Algebraic reformulation leads to an expression, that relates the dissolved amount of the compound to the initial amount of substance to be separated. Provided, that the solubility at the eutectic composition w^{eu} is known, the amount of solvent to be added to a dry mixture of solids

can be derived. Analogously, $m^{solvent}$ can be used to derive the amount of solvent to be removed from a diluted initial solution.

$$\frac{m^{eu}}{m^{initial}} = \frac{(x_{(R)}^{initial} - 0.5)}{(x_{(R)}^{eu} - 0.5)} \quad (5.4) \qquad m^{solvent} = m^{initial} \frac{(x_{(R)}^{eu} - 0.5)}{(x_{(R)}^{initial} - 0.5)} \frac{(1 - w^{eu})}{w^{eu}} \quad (5.5)$$

Introducing expressions for the mass of the target component (here, the (R)-enantiomer) and the amount of the target component in the initial mixture, the yield $Y_{(R)}^{PE}$ can be defined as

$$m_{(R)}^{eu} = m^{eu} x_{(R)}^{eu} \quad (5.6) \qquad m_{(R)}^{initial} = m^{initial} x_{(R)}^{initial} \quad (5.7)$$

$$Y_{(R)}^{PE} = \frac{m_{(R)}^{eu}}{m_{(R)}^{initial}} = \frac{x_{(R)}^{eu}(x_{(R)}^{initial} - 0.5)}{x_{(R)}^{initial}(x_{(R)}^{eu} - 0.5)}. \quad (5.8)$$

It is illustrated in Figure 5.4, that virtually every asymmetric mixture can be enriched in the liquid phase, provided that the eutectic composition exceeds the initial composition. It should be noted, that the elevated theoretical yields according to Eq. (5.8) refer always to the purity at the corresponding eutectic composition.

In case of Serine, the eutectic composition is quite close to unity and highest purities at elevated yields are possible using this enrichment procedure. This concept has been evaluated experimentally in combination with a pre-enrichment step based on chiral chromatography within chapter 5.2.1.

Example: Separation of Proline enantiomers

The eutectic composition of the system of the Proline hemi-chloroformate yields an almost enantiopure eutectic composition in chloroform (chapter 4.2.3). The drawback of the solvent is the very low solubility of 0.05 wt%. Klussmann showed, that the solubility can be increased by the addition of methanol. The co-solvent leads to a subsequent disappearance of the solvate and therefore to lower eutectic compositions. In summary, a typical optimisation problem is found here, which depends on cost factors for solvents and the purity requirements. An alternative separation process for Proline is introduced in the next paragraph.

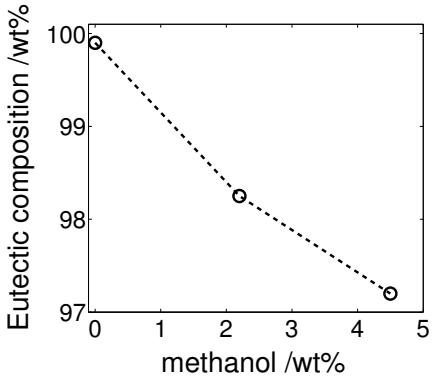

Figure 5.5 *Change in the eutectic composition through co-solvent addition. Data from Klussmann [36].*

5.1.3 Exploitation of shifts in the eutectic composition

5.1.3.1 Theoretical concept and process yield

The concept above is limited to substances, whose eutectic compositions exceed already the purity requirements. Another, more general, concept is introduced in the following. It shares the first step with the preferential enrichment process. The new concept is independent on the

eutectic composition, it rather exploits a shift of this property between two thermodynamic states. The process can be compared to the among chemical engineers probably better known concept of pressure-swing-rectification. Two thermodynamic states are used here to alter the position of an azeotrope for more difficult separation problems. Firstly, a (pseudo-) binary mixture is equilibrated such, that the distillate composition equals the composition of the azeotrope, which is closer to the target component. In a second step, the azeotrope is shifted by a pressure and temperature change towards lower values. Now, the target component can be withdrawn as the bottom product, while the distillate composition equals the lower azeotrope and can be fed back to the first column. The separation of chloroform/methanol is such an example.

Analogously, it can be attempted to exploit changes to the eutectic composition in solution for separation purposes. Starting from any asymmetric mixture of enantiomers (Figure 5.6, point 1, $x_{(R)}^{initial}$), preferential enrichment can be achieved through solvent removal and equilibration at a low temperature T_{low}. The composition will approach point 2 at the phase boundary between the inner two-phase region and the three-phase region (shaded) and will separate into a solid phase (point 3) and a liquid phase of eutectic composition (point 4). The latter composition $x_{(R)}^{eu,1}$ is enriched by the target enantiomer compared to the initial composition $x_{(R)}^{initial}$ at point 1.

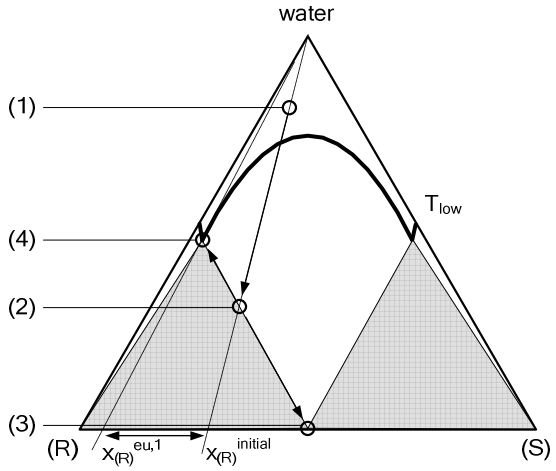

Figure 5.6 *1st step: Preferential enrichment of the liquid phase until the high eutectic composition.*

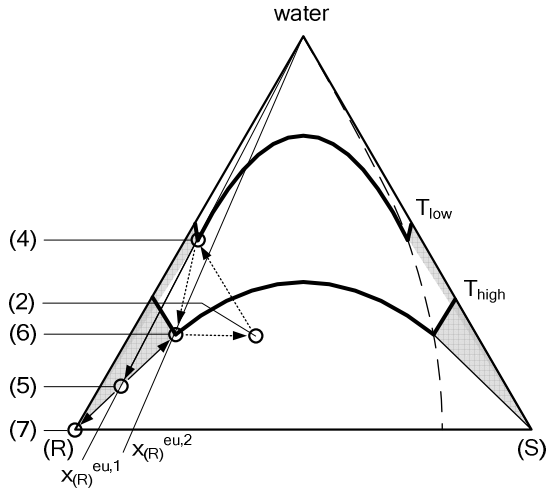

Figure 5.7 *2nd step: Solvent removal and selective crystallisation of the (S)-enantiomer.*

The change in the eutectic compositions $x_{(R)}^{eu,1}$ and $x_{(R)}^{eu,2}$ between two temperatures is illustrated by a bent dashed line within Figure 5.7. The corresponding variation in the shape of the outer 2-phase areas is visible. The enriched liquid phase of Figure 5.6 is separated from the (racemic) solid phase and re-used at a higher temperature T_{high} (Figure 5.7). Point 4 represents the initial state for a 2nd process step. There are two options for shifting point 4 into the outer two-phase region (shaded), in which selective crystallisation of the target enantiomer can take place. Either more solvent is evaporated in order to concentrate the solution up to the phase boundary towards the three-phase region, or, alternatively, the solubility isotherm can be shifted upwards by controlled injection of an antisolvent. The optimal yield is obtained at the phase boundary between the outer 2-phase and the 3-phase region (point 5). Its composition splits into a liquid phase with the lower eutectic composition $x_{(R)}^{eu,2}$ (point 6) and a pure solid phase consisting solely of the target enantiomer (point 7). The composition of interest, *i. e.* point 5 on the phase

boundary can be found from a mass balance. Herein, the optimal amount of solvent is given by Eq. (5.13), with $w^{eu,2}$ being the sum of the solubilities of the enantiomers at the lower eutectic composition, defined as

$$w^{eu,i} = \frac{m^{eu}_{(R)} + m^{eu}_{(S)}}{m^{eu}_{(R)} + m^{eu}_{(S)} + m_{solvent}}. \tag{5.9}$$

$$m^{eu,1} = m^{s,2} + m^{eu,2} \tag{5.10}$$

$$m^{s,2} + m^{eu,2} x^{eu,2}_{(S)} = m^{eu,1} x^{eu,1}_{(S)} \tag{5.11}$$

$$\frac{m^{eu,2}}{m^{eu,1}} = \frac{(x^{eu,1}_{(R)} - 1)}{(x^{eu,2}_{(R)} - 1)} \tag{5.12}$$

$$m^{solvent,2} = m^{eu,1} \frac{(x^{eu,1}_{(R)} - 1)}{(x^{eu,2}_{(R)} - 1)} \frac{(1 - w^{eu,2})}{w^{eu,2}} \tag{5.13}$$

A principle drawback of the process using the introduced tie lines becomes visible. The liquid phase with $x^{eu,2}_{(R)}$ remains largely enriched by the target enantiomer, even after a successful crystallisation run. Thus, it appears favourable to merge this fraction with feed material of point (1) and a fraction of the already crystallised racemic compound of point (3). Hereby, a composition identical to the initial composition prior to the 1st crystallisation step can be obtained and hence, the same amount of product can be crystallised from less feed material. In summary, the 2-step process circulates alongside the three thermodynamic states (2), (4) and (6) as depicted in Figure 5.6.

The fact, that the proposed 2-step process is defined through thermodynamically stable states, allows applying a simple balance. Since the change of $\Delta x^{eu}_{(R)} = x^{eu,1}_{(R)} - x^{eu,2}_{(R)}$ for different temperatures can be relatively large (methionine/water: 8% [89, 186]; less for other systems [33, 35, 169]), the theoretical outcome and the optimal conditions (temperature, solvent/antisolvent) for maximum yield are of interest. Therefore, it is convenient to define the yield as the mass of the crystallised target enantiomer relative to the mass of the excess of the more abundant enantiomer in the feed, since it ranges in this manner between zero and unity. A simple mass balance for the more abundant (enriched) enantiomer, in this case the (R)-enantiomer, can be written as follows. It will result in an expression for the theoretical process yield. The initial total amount of solute to be separated $m^{initial}$ is based on the contributions by the mass of the (R)-enantiomer and the mass of the racemic compound (R,S). In the 1st process step, $m^{initial}$ is distributed amongst the liquid and the solid phase according to the equilibrium isotherms at T_{low}. The purities and the amounts obtained are independent of the initial composition $x^{initial}$ and depend on the composition and solubility at point 4 in Figure 5.6 at T_{low} only. Further, the dissolved amount $m^{eu,1}$ depends neither on $m^{initial}$ nor on $x^{initial}$, but only on the size of the system, *i. e.* the volume of the liquid phase.

$$m^{initial} = \left(m^{l}_{(R)} + m^{l}_{(R,S)}\right) + m^{s,1}_{(R,S)} = m^{eu,1} + m^{s,1}_{(R,S)} \tag{5.14}$$

The 2nd process step is balanced by the amount of the crystallised target enantiomer using the composition at point 5 shown in Figure 5.7 at the temperature T_{high}. The mass of solutes $m^{eu,1}$, dissolved in the 1st process step at the temperature T_{low}, is transferred to the 2nd process step. This mass is reduced after equilibration by the amount of the target enantiomer crystallised in the 2nd process step $m^{s,2}_{(R)}$:

$$m^{eu,2} = m^{eu,1} - m^{s,2}_{(R)} \tag{5.15}$$

A corresponding balance of the (R)-enantiomer only yields a description of the 2nd process step after equilibration:

$$x^{eu,2}_{(R)}\ m^{eu,2} = x^{eu,1}_{(R)} \cdot m^{eu,1} - x^{s,2}_{(R)}\ m^{s,2}_{(R)} \tag{5.16}$$

Hereby, the composition of the solid phase is defined by pure (R)-enantiomer:

$$x^{s,2}_{(R)} = 1 \tag{5.17}$$

and the equations above can be rewritten as:

$$x^{eu,2}_{(R)}\ \left(m^{l}_{(R)} + m^{l}_{(R,S)} - m^{s,2}_{(R)}\right) = x^{eu,1}_{(R)} \cdot \left(m^{l}_{(R)} + m^{l}_{(R,S)}\right) - m^{s,2}_{(R)} \tag{5.18}$$

With the yield $Y_{(R)}$, defined as the excess of the target (R)-enantiomer in the initial, enriched solution in relation to the crystallised target enantiomer, division of Eq. (5.18) by $m^{l}_{(R)}$ and consideration of the definition of the eutectic composition (Eqs. (5.20) and (5.21)) the following set of expressions can be followed.

$$Y_{(R)} = \frac{m^{s,2}_{(R)}}{m^{l}_{(R)}} \tag{5.19}$$

$$x^{eu,1}_{(R)} = \frac{m^{l}_{(R)} + 0.5 \cdot m^{l}_{(R,S)}}{m^{l}_{(R)} + m^{l}_{(R,S)}} \tag{5.20}$$

$$\frac{m^{l}_{(R,S)}}{m^{l}_{(R)}} = \frac{1 - x^{eu,1}_{(R)}}{x^{eu,1}_{(R)} - 0.5} \tag{5.21}$$

$$x^{eu,2}_{(R)}\left(1 + \frac{m^{l}_{(R,S)}}{m^{l}_{(R)}} - Y_{(R)}\right) = x^{eu,1}_{(R)} \cdot \left(1 + \frac{m^{l}_{(R,S)}}{m^{l}_{(R)}}\right) - Y_{(R)} \tag{5.22}$$

$$x^{eu,2}_{(R)}\left(1 + \frac{1 - x^{eu,1}_{(R)}}{x^{eu,1}_{(R)} - 0.5} - Y_{(R)}\right) = x^{eu,1}_{(R)} \cdot \left(1 + \frac{1 - x^{eu,1}_{(R)}}{x^{eu,1}_{(R)} - 0.5}\right) - Y_{(R)} \tag{5.23}$$

$$Y_{(R)} = \frac{1}{(2 \cdot x^{eu,1}_{(R)} - 1)} \frac{x^{eu,1}_{(R)} - x^{eu,2}_{(R)}}{(1 - x^{eu,2}_{(R)})} \tag{5.24}$$

The theoretical process yield depends herein on the eutectic compositions only. A generic plot of the theoretical yield of the 2-step process for a given eutectic composition $x^{eu,1}_{(R)}$ in the 1st step and a difference $\Delta x^{eu}_{(R)} = x^{eu,1}_{(R)} - x^{eu,2}_{(R)}$ between both steps is presented by Figure 5.8. Certainly, the value of $\Delta x^{eu}_{(R)}$ is decisive, but also the eutectic composition itself. Elevated yields can be expected from either high eutectic compositions or from low compositions.

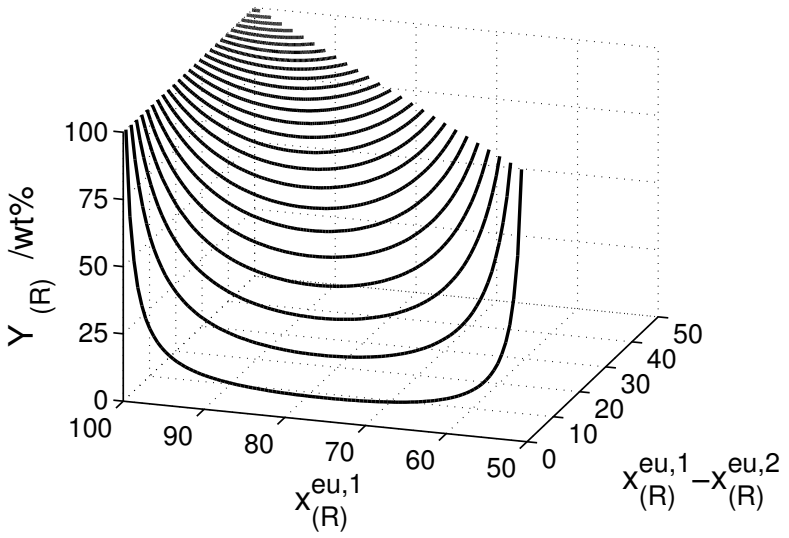

Figure 5.8 *Generic plot of theoretical process yields according to the eutectic composition in the first step and the difference between both eutectic compositions.*

Application of this concept to Proline results in a yield above 84 % according to the data from Figure 5.5 and Eq. (5.24).

5.1.3.2 Validation experiments based on a model system (Methionine)

The 2-step concept was exemplarily validated on the amino acid Methionine, which represents a system with a temperature-depending eutectic composition between 94% and 86% (chapter 4.2.2). Thus, a yield of 68 wt% was expected. Though, the locus of the tie line to be met in the 1st process step is known in theory, three aspects were considered to simplify validation experiments. A too diluted solution led to a drop in the eutectic composition. Thus, a surplus of solids is recommended to be added to the solution, leading to a solid phase of 52% (S)-enantiomer. 5 wt% loss of solid phase was assumed to happen during filtration in between the two steps and again during the final product filtration process. Finally, the reduction of the amount of solvent to be removed in the 2nd step by 10% appeared appropriate to assure, that the overall composition remained in the outer 2-phase region. Otherwise, nucleation of the racemic compound would be possible. The resulting drop in the expected yields is sketched in Figure 5.9. The largest difference to the theoretical yield (68 wt%) is observed from only slightly enriched solutions. Within other areas, the gap to the ideal yield is not significant. It is interesting to note, that initial enrichments above 70 wt% do not lead to a further improvement of the yield. A simple stirred vessel and a fully equipped

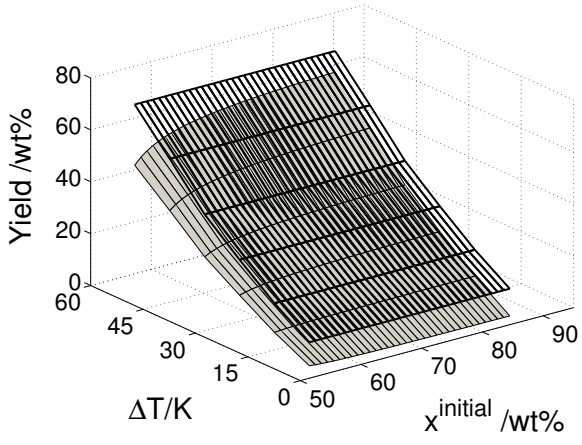

Figure 5.9 *Ideal yield (upper mesh) and more realistic yield (lower plane) of the proposed process for different initial conditions and temperature differences between the two process steps.*

(Pt-100 element, turbidity probe, vacuum gauge) and automised crystallisation reactor (2-pot automate, HEL ,UK) have been used for process validation experiments.

In a first step, a double-walled flask was tempered to 274 K and a supersaturated solution (1 l water, 55 g racemic Methionine, 37 g (S)-Methionine, $x_{(S)}^{initial} = 0.7$) was added and agitated by a magnetic stirrer bar for 24 hours. The supernatant was filtered of by vacuum filtration and the solid phase was washed with methanol. Both phases were analysed by chiral HPLC (Chirobiotic T, 250x4.6 mm, 5 µm; mobile phase: methanol/water 60/40 v/v, 1 mL/min, 298 K; UV: 210 nm). The liquid phase was concentrated up at 333 K and ~190 mbar in subsequent batches of 300 mL each. The batches were recombined to the concentration needed for the 1st crystallisation step. The start of the crystallisation and the thermodynamic equilibrium was estimated by the turbidity probe. The target component was separated from the liquid phase by vacuum filtration. Again, the purities of both phases were analysed by chiral HPLC.

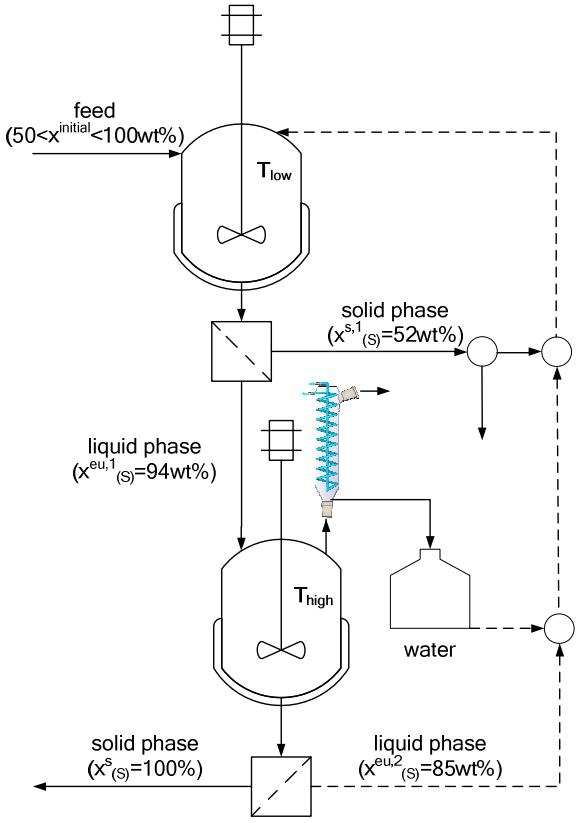

Figure 5.10 *Schematic representation of two subsequent crystallisations of Methionine enantiomers. Arbitrary asymmetric mixtures are enriched up to 100% purity.*

Internal recycling

The introduced crystallisation concept suffers from a general disadvantage in comparison to pressure-swing-distillation. The final product is crystallised within the outer 2-phase area leaving a mother liquor, which is still highly enriched by the target enantiomer ($x_{(S)}^{eu,2}$). In distillation processes, this fraction is continuously fed back and remixed with the feed. Analogously, the recycling of fractions within subsequent crystallisation batches will lead to superior mass of product per mass of feed ratios. The whole amount of the solute in the liquid phase in the second step and also a fraction of the solid phase crystallised from the first step can be recycled internally as illustrated by Figure 5.10. In addition, the solvent can be re-used. The corresponding trajectory of the liquid phase compositions upon recycling is presented by the points *i)-iii)* in Figure 5.7. Provided, that the establishment of thermodynamic equilibria is fast, a continuous crystallisation process involving this three states might be feasible. The purity of the initial feed stream determines the grade of recycling of the solid phase from the first step and also the gain in productivity. It is visible, that already a second batch increases the overall productivity significantly. The value approaches unity for an infinite number of subsequent batches, if the considered losses due to filtration, etc. are neglected. Recycling processes bear the inherent difficulty, that impurities accumulate. On order to evaluate this aspect and the whole concept, three subsequent batches were crystallised. Hereby, the mother liquor after the 2nd

process step was reused and combined with a fraction of dry solids from the first crystallisation step and fresh feed material. The composition of this mixture was adjusted to maintain the same initial composition $x_{(S)}^{initial} = 0.7$ in all batches.

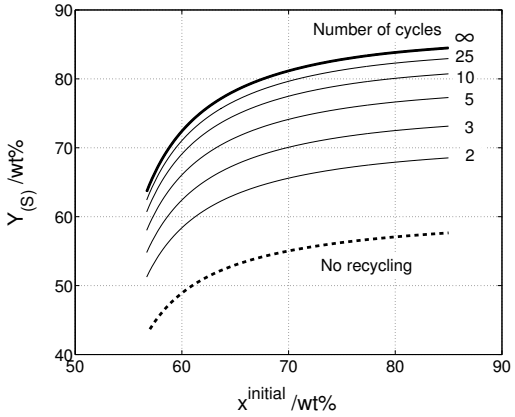

Figure 5.11 *Realistic productivities for a single batch and a number of subsequent batches.*

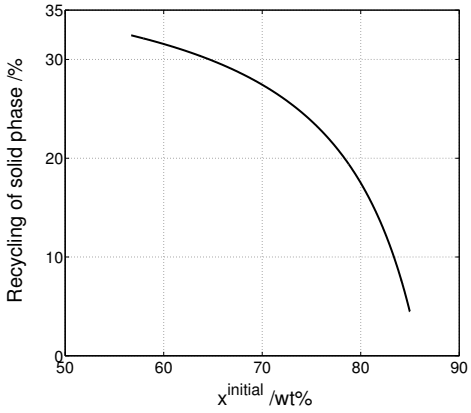

Figure 5.12 *Fraction of the solid phase to be recycled from the 1st step.*

Results of crystallisation runs

Three successful separations of Methionine enantiomers have been performed. Due to internal recycling, reduced amounts of feed became necessary to achieve to same product mass. This applied from the 2nd batch on. The product purities have been close to 100% throughout the series of experiments. No contamination by impurities or degradation products was determined. The solvent consumption became negligible after the first batch, since the solvent was recovered directly from distillation. The practical considerations on product losses appeared reasonable, since the obtained yields followed the theoretical values quite closely (5.14).

Table 5.1 *Feed, yield and purity figures of three subsequent crystallisation runs for the separation of Methionine enantiomers.*

	Methionine /g		water	product	purity
run	(R,S)	(S)	/g	/g	/%
I	55	37	1000	21	>99
II	37	27	76	21	99
III	37	27	57	21	>99

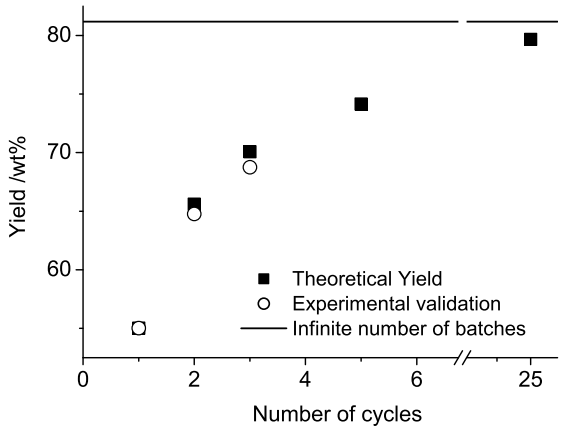

Figure 5.13 *Increase in process yield for subsequent batches-model estimation and experimental validation (three runs).*

Variables as dissolution kinetics and the duration until the thermodynamic equilibrium is established, can pose limiting factors, but have not been considered quantitatively. No delay between the end of the partial solvent evaporation in the 2nd step and the equilibration was determined. The evaporation rate was considered as the main bottleneck and therefore the heating of the reactor. Cost factors for more a powerful heating may help to assess this issue in the context of a whole process framework. Dissolution kinetics have been the limiting factor in the 1st process step. However, it is known, that crystal sizes, crystal surface properties, crystal habitus and fluid dynamics have a large influence on these kinetics. It was found, that ground crystals dissolve within a few minutes and no further

optimisation was undertaken in this regard. Obviously, there is room for improvement, which is beyond the focus of this study.
In summary, a new process variation was proposed for the crystallisation-based enantioseparation of Methionine. The process was balanced and validated exemplarily for one amino acid. The fact, that the process is not requiring any substance-specific enrichment, allowed the purification of a feed stream of 70 %, which was below the eutectic composition of this compound. Feeds streams of much lower initial enrichment can be purified also. In theory, no drop in the process yield has to be accepted. However, validation experiments have shown, that for slightly enriched feed streams, a reduction in the process yield occurs. One option for compensation is given by a series of subsequent crystallisation batches.

5.1.3.3 Validation experiments based on an API (Bicalutamide)

One key result of this thesis comprises the application of the developed separation scheme to an API of pharmaceutical and economic relevance in order to prove the generic applicability of the new concept. Bicalutamide was selected for evaluation in the course of a collaborative project between the MPI Magdeburg and AstraZeneca. The joint work was embedded in a 3-years project under the umbrella of the European Framework Program 7 (FP7-NMP2-SL2008-214129, www.INTENANT.eu). The compound is manufactured at a scale of several metric tons per annum at AstraZeneca and is used as a racemate for the treatment of prostate cancer. It is the active pharmaceutical ingredient of the drug Casodex™. The sales value (sales figures are for 2008) is approximately 210 million US dollars. During a development program within AstraZeneca targeting manufacture of the pure (R)-enantiomer of Bicalutamide, the manufacturing method developed utilised SMB-HPLC for essentially full enantioseparation of the racemic material. It was aimed to benchmark the developed 2-step separation scheme with respect to the actual production routine performed at AstraZeneca.
Therefore, the introduced 2-step crystallisation scheme was modified, adapted and evaluated on AstraZeneca's API Bicalutamide. Firstly, binary, ternary and quaternary SLE were derived and parameterised using the methodologies described in chapter 4. Secondly, the introduced 2-step process was modified and applied and the compound was separated. Further, a scale-up of the developed process was performed (scale factor: 600) aiming to elucidate, whether such a process can be conducted succesfully at a pharmaceutically relevant scale (s. chapter 5.2.2). The transfer of bench-scale experiments to pilot and even production scale is considered as a non-trivial task. Crystallisation kinetics and MSZW can differ significantly [87]. Thus, it was believed that the practical process realisation provides the best insight in the process applicability.

Experimental section 1
a) Solid phase analysis
(R)-and (S)-Bicalutamide were obtained from AstraZeneca via a collaborative project. The purities were given as >99%. The heats and temperatures of fusion of (R)-Bicalutamide and the racemic compound were determined using differential scanning calorimetry (DSC). A sufficient amount of methanol was added (typically 5 mL) to Bicalutamide and the sample was gently stirred until complete dissolution occurred. The solid samples were dried in an oven at 323 K under vacuum and subsequently crushed and ground in a mortar. The samples prepared were

divided for DSC (DSC 131, SETARAM, France; closed aluminium crucibles, ~12 mg substance, 1 K/min, 20 mL/min helium purge gas flow) and XRPD (X'Pert Pro Diffractometer (PANalytical GmbH, Germany; X'Celerator detector, Cu Kα radiation, 2θ range of 3-40°, step size of 0.017°, counting time of 50 s or 100 s per step) analysis respectively.

b) Measurement of multiphase equilibria

The results of the preceding solvent screening were provided in chapter 4.4.2. For validation experiments a promising candidate (methanol/water) and a less favourable combination (methanol/toluene) were chosen. The ternary solid-liquid phase equilibria (SLE) of Bicalutamide in both solvent systems were determined by means of in-situ ATR-FTIR spectroscopy, gravimetric off-line measurements and a polythermal, in-line measurement device. In addition, the binary and the quaternary solid-liquid phase equilibria (SLE) of Bicalutamide in methanol/water were determined.

The determination of the solubility of (R)-Bicalutamide in both methanol/water and methanol/toluene mixtures was initially carried out by means of an isothermal equilibration method. Sealed flasks with a volume of 5 mL were filled with a predefined amount of solvent (mixture) and (R)-Bicalutamide with a large excess of the solid phase. The mixtures were agitated by a magnetic stirrer for at least 48 hours and kept at a controlled temperature between 273 and 333 K using a thermostat (RC6 CP, Lauda edition 2000, Germany). Subsequently, the liquid phase was withdrawn quickly with a syringe and filtered (45 µm pore size). The solvent was evaporated and the differences in weight were recorded. Ternary SLE were derived analogously using predefined slurries of (R)- and (S)-Bicalutamide in solvent (mixtures). Here, both the liquid and the solid phase were analysed after solvent evaporation by means of chiral HPLC (methanol, 298 K, 1 mL/min, Chiralpak AD, 250 x 4.6 mm, V_{inj}=1 mL). In addition, the solid phase was investigated using XRPD analysis to ensure, that the same solid phase was present for all measurements.

Further to this, solubility measurements were conducted in the system (R)-Bicalutamide in methanol/toluene, where applicable, by means of a polythermal dissolution method using a Crystal16™ device (Avantium Tec. BV, NL). Predefined amounts of mixtures of the enantiomers were dissolved in a solvent (mixture) at high temperature, then cooled and recrystallised and then completely dissolved again by applying a heating ramp of 3 K/hr and sufficient agitation at 700 rpm. The cloud- and the clear-points were determined by a turbidity probe and the corresponding temperatures were recorded. The application of this device is restricted to temperature ranges far above the crystallisation point of the solvent, since recrystallisation can require substantial subcooling of the solution. It is generally impossible to assign a crystal structure to the solid phase investigated and thus, no information on polymorphism can be derived. The advantage of this method is the rather quick acquisition of solubility data. It is believed that the two techniques described above should be used in combination for best reliability and performance.

c) In-Situ Concentration Measurements

The experimental setup used was based on a jacketed 50 mL vessel equipped with a Pt-100 element, which was connected to a thermostat (RC6 CP, Lauda edition 2000, Germany). A simple magnetic stirrer bar was used for agitation. Changes in absorption in the liquid phase were

determined from Fourier Transform Infrared Spectroscopy (FTIR) data acquired using an in situ probe for attenuated total reflection (ATR). The probe (DiComp) was equipped with a diamond ATR crystal, immersed at a slight angle against the flow direction of the solution and connected to a ReactIR45m device (Mettler Toledo, Switzerland). Spectra were recorded continuously in the region 2800-650 cm^{-1} and averaged over 90 s (256 scans) with a resolution of 4 cm-1. Three different measurements were performed using ATR FTIR.

The solubility of Bicalutamide enantiomers at the eutectic composition was measured for different methanol/water ratios and under isothermal conditions (333 K). A slurry consisting of methanol and both enantiomers with a composition in the three-phase region was agitated and the spectra were recorded until thermodynamic equilibrium was assumed (20 min after the last change in the spectra). The concentration was determined from a calibration model and a defined amount of water was added to obtain the next data point.

A number of SLE points in the quaternary phase diagram consisting of both enantiomers in methanol/water mixtures were then measured for model evaluation. Within the domain of the racemic compound and the inner two-phase region, all tie lines end at the same composition (Figure 2.22a)). Starting with any composition of the enantiomers in this region, the composition separates into a solid phase consisting of the racemic compound only and a liquid phase corresponding to the solubility isotherm. The liquid phase concentration was measured by ATR-FTIR and the ratio of the enantiomers was computed from simple mass balances. The initial composition of the slurry consisted of 43 g methanol, 16 g water, 1.6 g (R)-Bicalutamide and 2.4 g (S)- Bicalutamide. The solutions were allowed to attain thermodynamic equilibration after injection of a defined amount of water by waiting for at least 20 minutes after the recorded spectrum remained constant. The procedure was repeated for 12 data points, which are plotted in Figure 4.63.

d) Multivariate Data Analysis

Reliable and accurate tracking of changes in the liquid phase composition is a crucial requirement for crystallisation processes in general and in particular if more than two components are involved. Measurement techniques such as refractometry or the determination of density fail if the solvent mixture composition cannot be kept constant due to effects such as partial evaporation of solvents or if a second solvent is dosed. In these cases, models based on IR absorbance measurements can serve as useful tools to overcome this limitation [158, 194-198]. The spectrum of the compound Bicalutamide and the spectra of the solvents water, methanol and toluene overlap almost in the entire spectral range considered, providing very little hope for a successful univariant calibration. Since the content of the solute in the liquid phase was expected to change with the ratio of the solvents, no simple subtraction of any background or reference state is possible. Consequently, multivariate calibration models were set up, validated and used in this study.

e) Calibration Sets

(R)-Bicalutamide was used exclusively for all calibrations, since the (S)-enantiomer and also the (solid) racemic compound should not affect any changes to the recorded spectra of the liquid phase, *i. e.* it is sufficient to measure spectra involving the (R)-enantiomer. Although this assumption is often found in the recent literature; there are examples to the contrary, where the

solid phase can indeed influence the measurements. Kee *et al.* [199] and Alatalo *et al.* [198] reported, that crystals can lead to interferences, if they are comparable in size to the penetration depth of the IR energy field. Fortunately, none of these phenomena have been encountered in this study.
Three different calibration methods were used aiming to achieve a broad range of model applicability. First, controlled amounts of a defined solvent mixture were added to a concentrated (R)-Bicalutamide solution under isothermal conditions. The resulting spectra were recorded and thermodynamic equilibrium was assumed, when the spectrum remained constant for at least 20 minutes. The spectrum was added to the calibration set and, again, a controlled amount of defined solvent mixture was added.
Then, just a single solvent was added to the mixture and the samples were allowed to equilibrate. In the case of nucleation occurring due to antisolvent addition, the sample was rejected from the calibration data set.
Finally, the temperature was changed in 10 K steps at constant solution composition in order to identify temperature dependent peak shifts in the spectra. Again, if nucleation occurred, no measurements were carried out.
Calibration sets were generated for the systems (R)-Bicalutamide/methanol/toluene and (R)-Bicalutamide/methanol/water. The first set consisted of 122 spectra, from which 112 were used for model description and 10 spectra were rejected as outliers. For the second system a set of 86 spectra was recorded, from which 5 spectra were removed as outliers. Two different calibration models were derived from the remaining data set; a model with lower accuracy covering a broader range of compositions and a second, high-accuracy model, which covers a range of compositions of particular interest. The latter calibration model is based on 49 spectra only and is restricted to solutions containing less than 6 wt% Bicalutamide. The spectra recorded were found to vary significantly with temperature, which in general requires a very comprehensive data set. However, the available data set is based on a narrow temperature range 328 K to 343 K, which guarantees high accuracy, but is limited to almost isothermal applications.

f) Calibration Models

Since the compound specific information is stored in the whole characteristic spectrum and can be extracted to a different extend from a multitude of wave numbers, the problem can considered to be ill-posed. Most wave numbers are highly correlated and for this reason a number of different methods such as principal component analysis (PCA) and partial least squares regression (PLSR) are often used in order to obtain a quantitative description of the specific IR absorbance. The calibration models developed in this study are based on the information contained in the absorbance at wave numbers in the region 1784-655 cm^{-1} and on 283 variables. PLS regression and model building was carried out with the software ICIR Quant (Metter Toledo, Switzerland). Initially, factors (also called latent variables) were identified, which are linear combinations of the measured spectra (dependent variables) and are suitable for regression of the given concentrations (independent data). The most promising number of factors for a given problem can be derived through a cross validation procedure. In this procedure, the number of factors is increased stepwise while searching for the lowest ratio of the error with respect to the number of factors or, if present, for a minimum error region. Therefore, the 'leave-one-out' method was applied. The models were built based on subsets (whole set reduced by one) and the missing data were estimated based on the model derived.

Every spectrum was removed once, leading to 112 repetitions for the first system. The decision criterion was the root-mean-square-error of cross validation (RMSECV). Prior to the model building step, different pre-processing procedures were applied to the measured spectra.

Results and model parameterisation

Quaternary SLE measurements of Bicalutamide enantiomers in methanol/water mixtures were conducted using calibrated ATR-FTIR equipment. In addition, a FTIR calibration for Bicalutamide in methanol/toluene mixtures was carried out. Although, the latter was not applied in this particular study, both calibrations are summarised here. The optimum model performance for the system Bicalutamide/methanol/toluene was obtained with 19 latent factors for all components independently (appendix, Figure D.1a)). This rather high number can be reduced by introducing temperature as additional independent data. However, for the system considered, the RMSECV then increased significantly. It is likely, that temperature effects can be compensated better by introducing more factors, as was also found by Profir *et al.* [158].

The impact of pre-processing procedures was different for the calibration models. Autoscaling by means of a combination of mean centring (subtraction of the mean value of the dataset from each variable) and variance scaling (dividing each variable by its variance over the whole dataset) did result in significant improvements for the system Bicalutamide/methanol/toluene, while normalisation, baseline correction and the use of derivatives of the dependent variables did not contribute to a lower RMSECV. The second and the third calibration models for the system Bicalutamide/methanol/water both benefited from each of the pre-processing procedures, specifically mean centring, variance scaling, baseline correction and normalisation. The second and the first derivative of the spectral information resulted in the lowest RMSECV at 9 and 6 factors, respectively (appendix, Figure D.1b/c). The corresponding model agreements for both systems are plotted in Figure D.1d/e and provided in the appendix. The average error of solubility measurements using the calibration models derived is expected to be <0.4, <0.5 and <0.2 wt%, respectively, within the ranges of compositions and temperatures considered. Thermodynamic equilibration and solubility measurements were controlled using the most accurate FTIR calibration model.

Process Design

The shortcut model was used to estimate the eutectic composition by assuming negligible heterochiral interactions. The solubility of the racemic compound was estimated correctly on the basis of activity coefficients derived from the single enantiomer. This finding and experimental data of the eutectic compositions in methanol/water solutions confirmed, that the simple estimation methods is suitable. The solvent independent shift of the eutectic composition x^{eu} ranges from 97.7 wt% to 95 wt% for a temperature range of 273.15 K to 333.15 K. Thus, the maximum theoretical yield of this separation process is 55.3% (Eq. (5.24)), provided that the 2nd process step is conducted at 333.15 K and the 1st process step is performed at 273.15 K (compare Figure 5.14 and Figure 5.15). Again, the yield is defined by the ratio of the crystallised target enantiomer with respect to the excess of the target enantiomer in the initial mixture.

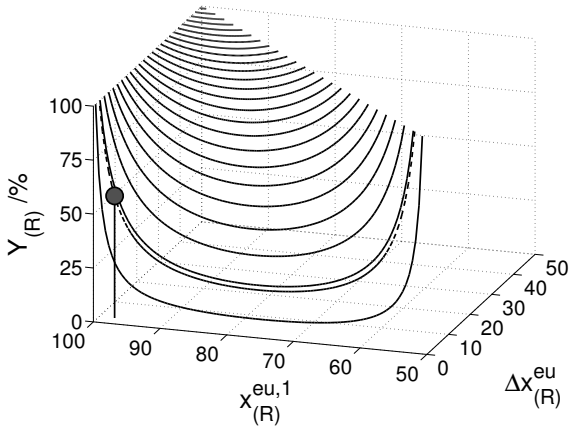

Figure 5.14 *Expected yield of the separation of Bicalutamide enantiomers from mass balances.*

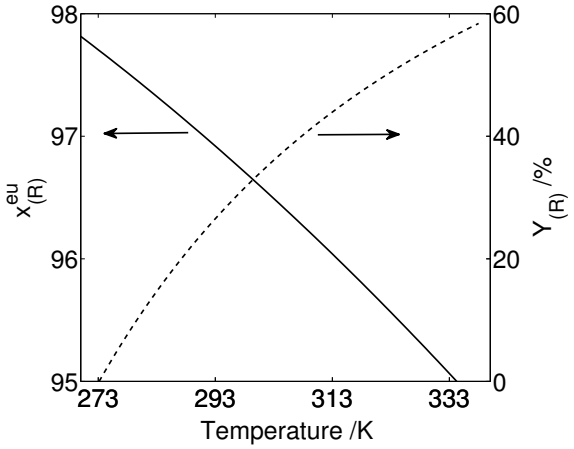

Figure 5.15 *Estimated eutectic composition for various temperatures (solid line) and corresponding process yield according to the given temperatures of the 2nd process step (dashed line) and a temperature in the 1st process step of 273.15 K.*

The 1st process step was applied analogously to the case of Methionine. An antisolvent was used in the 2nd crystallisation step, since solvent evaporation was found feasible in principle, but less efficient. The applicability of solvent evaporation depends strongly on the solubility of the compound considered. It is possible, that almost the complete solvent needs to be evaporated to achieve the maximum yield.

Heavy slurries are generally undesired, since SLE can hardly be controlled. The situation is illustrated in Figure 5.16 and Figure 5.17. The enriched mother liquor at point 4 is filtered off and transferred to the second batch and heated to T_{high}. Upon solvent evaporation, the outer two-phase region is reached and the solution will separate into a solid phase containing the crystalline target enantiomer (point 7) and the corresponding equilibrated liquid phase (point 6').

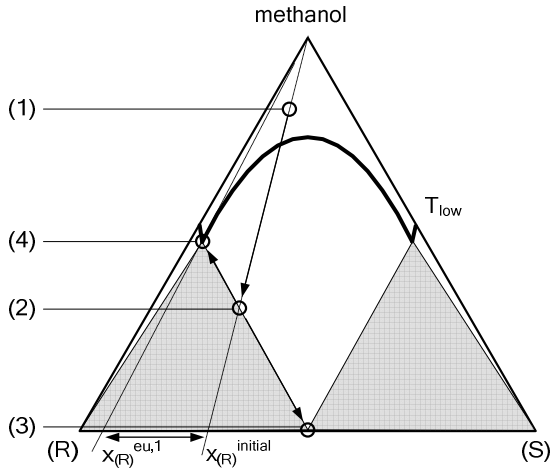

Figure 5.16 *1st process step at low temperature, preferential enrichment.*

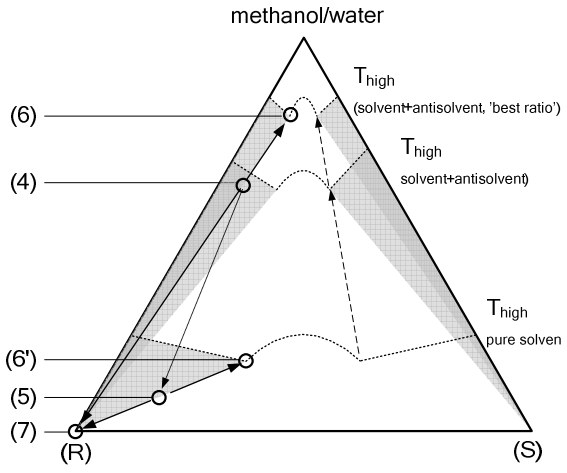

Figure 5.17 *2na process step at higher temperature, addition of an antisolvent or evaporation of solvent, respectively.*

According to the 'lever-rule' the proportion between the liquid phase and the solid phase illustrated is 1:1. The figure is not drawn to scale. In the case of Bicalutamide in methanol the

proportion is even more unfavourable. For this reason, water was used to suppress the solubility. Its addition at isothermal conditions shifts the solubility isotherm upwards. Hereby, the liquid phase will contain less substance (point 6), which is beneficial for the overall process.

Additional amounts of antisolvent shift the overall composition into the three-phase region, which is the domain of the solid racemic compound, the solid pure enantiomer and the liquid phase, which will contain both enantiomers at the eutectic composition. Within this undesired region the racemic compound may also crystallise and will become an impurity in the final product. Thus, the amount of antisolvent needs to be chosen well.

Experimental section 2
a) Chiral separation

After evaluation of ternary and quaternary SLE, the proposed 2-step separation process was designed. An experimental crystallisation run was conducted to evaluate the introduced balances. The theoretical and the determined compositions of the liquid and the solid phase at all process states are given by Table 5.2.

Therefore, a solution of enantiomers (point 1) was considered as an adequate output of a SMB-HPLC run with reduced purity requirements and was used as a reference mixture for separation. The solvent was partially evaporated according to the definition of the 1st process step and balances provided. 12 g of methanol remained after the concentration step. The ratio of the enantiomers in the liquid phase obtained was determined by HPLC as 97.7 % (R)-Bicalutamide and the solubility was measured by ATR-FTIR to 4.17 wt%. Solid-liquid separation was carried out by means of vacuum filtration and the liquid phase was reused.

Point 5 in Figure 5.17 and Table 5.2 show the results of a theoretical process variation, which was applied earlier for the separation of Methionine enantiomers [186].

Table 5.2 *Evaluated process states of a conducted chiral separation run (in brackets: theoretical values)*

Point in Figure 5.16, Figure 5.17	Process step	Temperature /K	$\frac{(R)}{(R)+(S)}$ /wt-%	solute concentration /wt%	$\frac{m_{methanol}}{m_{methanol}+m_{water}}$ /wt%, solute free basis
1	1st	273.15 (T_{low})	70 (70)	2.2 (2.2)	100 (pure)
2	1st	273.15	70 (70)	(9.4)	100
3	1st	273.15	50 (50)	100.0 (100)	-
4	1st	273.15	97.7 (97.7)	4.2 (4.2)	100
5 (not conducted)	2nd	333.15 (T_{high})	(97.7)	(43)	(100)
4	2nd	333.15	97.7 (97.7)	(1.7)	40 (60 wt% water)
6	2nd	333.15	95.1 (95.0)	1.0 (0.8)	40
7	2nd	333.15	99.2/98.4 (100.0)	100.0 (100)	-

Partial solvent evaporation led to supersaturation and selective crystallisation of the target enantiomer. In the case of Bicalutamide 11.3 g of solvent would become necessary to evaporate in order to crystallise the (R)-enantiomer with maximum yield. The remaining slurry would consist of 43 wt% Bicalutamide and a solid-liquid separation would become practically impossible. Thus, for the 2nd process step an antisolvent was used instead. The run was designed to stop directly at the computed phase boundary in the 2nd process step (Figure 5.17, point 4). Figure 4.63 provides the necessary information to derive the more practical Figure 5.18 and Figure 5.19, which allow for the quantification of the antisolvent to be added at constant

temperature. The operating window for a successful crystallisation process is obtained. The threshold 'Δsolubility' in this diagram is defined by the difference in solubility of point 4 (Figure 5.17) and the solubility at the intersection with the phase boundary to the three-phase region. A supersaturated solution was generated at a water content of about 41 wt%. The possible addition of antisolvent is limited. The maximum water content must not exceed 57 wt%, which corresponds to a yield of 50.5 wt%. The deviation from the above mentioned theoretical yield originates from the NRTL model accuracy. The same experimental setup as described in the experimental section 1 (4.2.2) was used for the 2nd process step. The solution was kept isothermal at 333.15 K and water was added in 4 discrete steps. The ATR FTIR probe was used to track changes in solution composition during the chiral separation run. The process trajectories obtained can be seen in Figure 5.20.

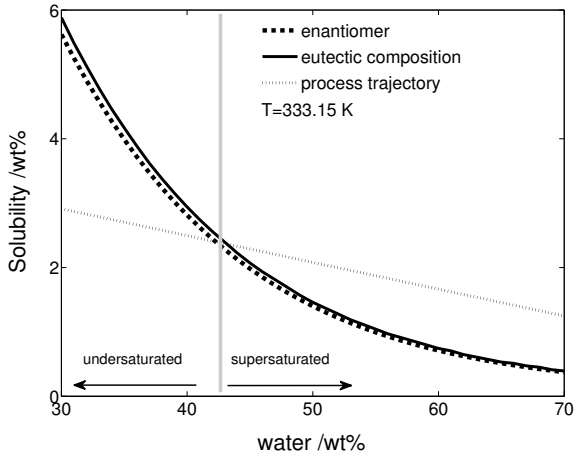

Figure 5.18 *Solubilities of the mixture of eutectic composition and the enantiomer. The intersection with the process trajectory marks the crossing of the liquidus line and the beginning of supersaturation.*

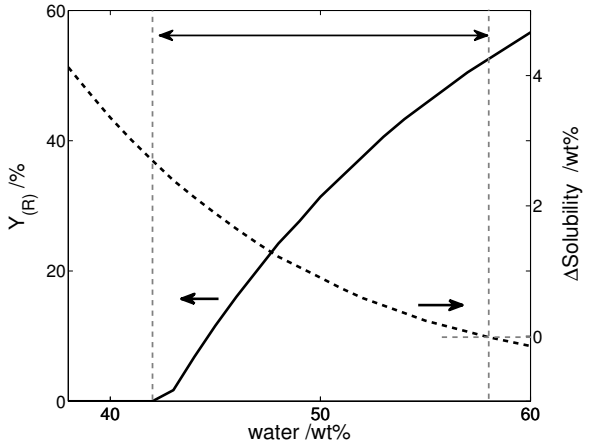

Figure 5.19 *Beginning of supersaturation and maximal amount of antisolvent to be added for the 2nd process step of a separation of Bicalutamide enantiomers.*

Upon water addition, nucleation was observed to occur at every injection step, followed by dissolution of crystals. Apparently, strong supersaturation is generated locally, due to the inability of Bicalutamide to dissolve in water, which, in addition, was not preheated and fed at ambient temperature. Nucleation is considered favourable here, since even at rather high supersaturation nucleation events do not necessarily occur due to large metastable zone widths and seeding was not planned for the process. Thus, in this case nuclei or small crystals were always present after antisolvent injections and helped to establish the required corresponding thermodynamic equilibrium. Starting from a concentration of approximately 4.2 wt% Bicalutamide, the value dropped to ca. 2.2 wt% upon antisolvent additions. Crystals did not dissolve again from here on and supersaturation was depleted by crystal growth until an equilibrium value of 1 wt% solubility was achieved. A sample of the first crystals to remain was taken and the ratio of the enantiomers was determined as 99.2 % (R)-Bicalutamide by HPLC. After two hours the ratio of the enantiomers in the liquid phase was determined by HPLC and was found to be 95.0 % (R)-Bicalutamide. The solid phase was separated from the mother liquor by vacuum filtration and washed with pure methanol. Its purity was determined (98.4 %) and found to be higher than the purity prior to this step (97.7 %). problems. However, the counter enantiomer was still present. It has to be taken into account that small amounts of adhering or

included mother liquor can always remain and there is room for improvement using more intensive downstream processing. Furthermore, the experimental run did in fact slightly exceed the phase boundary, as can be seen from the water content (60 wt%) in Figure 5.20, which is too high. Crystallisation of the racemic compound might already have occurred. The crystallisation kinetics have been rather fast in view of the establishment of the thermodynamic equilibrium. The crystal sizes were, due to locally large supersaturations, initially very small. Le *et al.* reported, that the addition of ethanol acts as an antisolvent to a DMSO solution and produces Bicalutamide crystals of 450 nm sizes. Crystals, produced through the addition of water to methanol were much larger when removed from the vessel and did not cause any filtration issues.

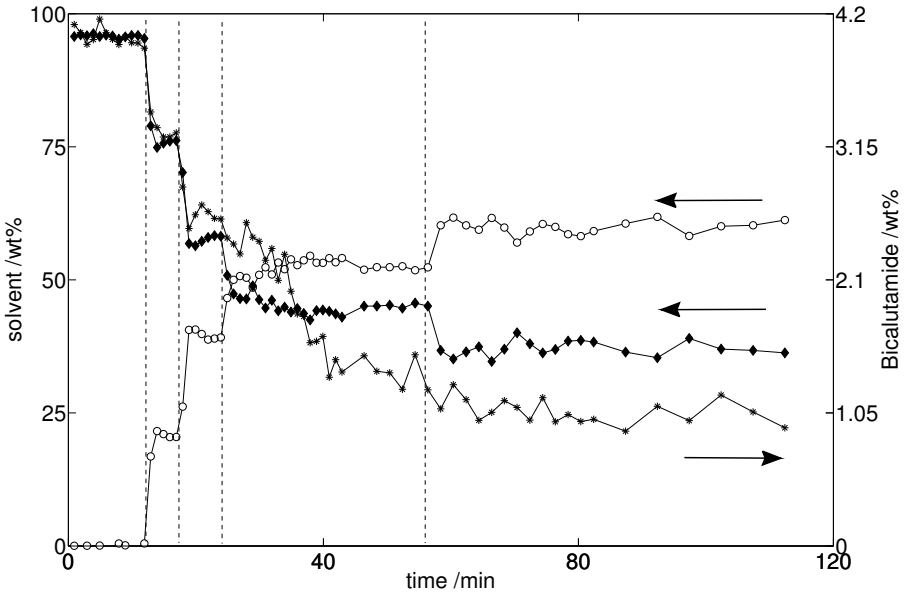

Figure 5.20 *Transient of the separation process progress of Bicalutamide. The vertical dashed lines highlight discrete water injections. Open symbols: water content. Full symbols: methanol content. Stars: Bicalutamide content. All data were recorded by ATR FTIR.*

Summary

A new 2-step process for enantioseparation was evaluated on the chiral compound Bicalutamide. The process was balanced and the theoretical yield was estimated based on the heats and temperatures of fusion of the enantiomer and the racemic compound. The concept of defined antisolvent dosing for selective crystallisation was explained.

In total three ATR FTIR calibration sets were generated for in situ process control. The calibrations derived helped to target suitable compositions for multicomponent SLE determination, thus improving the efficiency of process development. In addition, the calibrations were useful in tracking process progress.

The study yielded the purified (R)-enantiomer of Bicalutamide from an asymmetric mixture of 70 % purity. In the first step, the initial purity was increased from 70 % to 97.7 %. In the 2nd process step this was increased even further to 98.4 % (99.2 %). The design of both process steps was based on the SLE models derived. Process control was provided by the calibrated in situ ATR FTIR probe. The experimental crystallisation run proved the concept to be feasible and accurate.

The methodology described can serve as a general guideline for the separation of enantiomers with compound formation, provided either a pronounced shift of the eutectic composition or a eutectic composition close to unity is identified. A quick quantification of the theoretical process yield of the proposed two-step process is easily possible with knowledge of the corresponding heats and temperatures of fusion. The tools applied here for the first time in this comprehensive manner are rather generic and are not restricted to certain substance specific properties.

5.2 Chiral separation by coupled processes

The majority of the introduced selective crystallisation schemes demand an (at least slightly) asymmetric initial mixture. Those mixtures can originate from asymmetric synthesis with low yields in terms of enantioselectivity. Another source will be described in the following.
The throughput of chiral separation methods, that exploit chiral selectors (compare Figure 2.3), is limited by the capacity and often the price of the corresponding selector. Lowered purity requirements can allow the increase in productivity for a given enantiomer. Since process throughput can only be assessed by a holistic approach, the individual productivities of processes capable of breaking racemates and to feed selective crystallisation processes with asymmetric mixtures are of interest. *E. g.* chromatographic separation processes exhibits the common drawback, that an increase in purity does not come along with an increase in productivity. Often, compromises are required. A number of publications have considered this aspect on a theoretical basis. Wibowo [128] and Kaspereit [123, 127], as well as Ammanullah [126, 200] presented solutions for the identification of suitable interfaces between the two unit operations of chromatography and selective crystallisation. Within this chapter the specific interfaces for two systems with different characteristics were derived on the basis of dynamic models and mass balances. Both systems have been separated experimentally to allow the concept validation. The processes were compared to other hybrid methodologies state of the art.

5.2.1 Separation of Serine enantiomers

The large number of available efficient stationary phases for chiral separation tasks render chromatographic separation techniques almost universal. Often, the transfer of efficient preparative-scale processes from analytical methods is challenging. Preparative chromatography and in particular its optimisation requires in general more comprehensive knowledge of firstly the corresponding adsorption equilibria (s. chapter 2.4.2), secondly of the characteristics of the available columns and chromatographic equipment and finally on the mode of operation. In addition, the identification of suitable or even optimal operating points can be a tough task. The following paragraphs provide guidance to a comparison of standalone chromatography and the coupling of chromatographic pre-enrichment and selective crystallisation for the case study of Serine enantiomers.
The chiral separation of the amino acid serine depicts a scenario, where an analytical chiral HPLC method is available, but the capacities of the chiral columns are limited such, that a large scale production of the single enantiomer by chromatographic methods required tremendous volumes of suitable stationary phase. Within a case study, the coupling of a highly selective

commercial column and a subsequent crystallisation scheme was investigated. The proposed separation scheme is depicted in Figure 5.21.

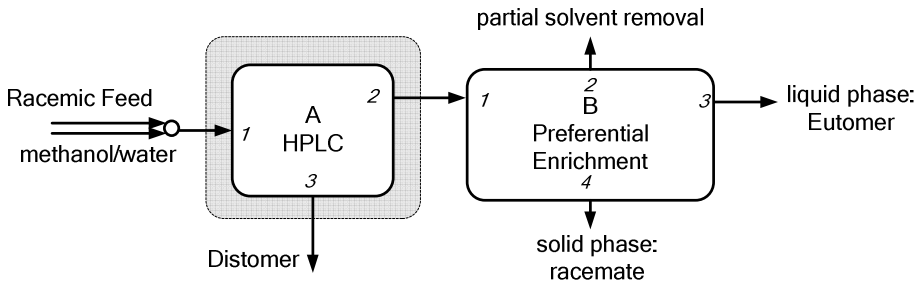

Figure 5.21 *Partial separation of racemic Serine followed by a crystallisation-based preferential enrichment step.*

A systematic study of different mobile phases and operating conditions was conducted in a first step. Selective adsorption of the enantiomers was quantified and a functional relation of productivity and product purity was obtained through a model approach. Secondly, the knowledge, gained in chapter 4.2.3 on the SLE of Serine in aqueous alcohols, was exploited to design an efficient selective crystallisation process for the purification of asymmetric mixtures. Its optimisation and outcome is illustrated in chapter 5.2.1.3.

5.2.1.1 Inducing asymmetry by chiral chromatography

Determination of adsorption isotherms

The column characterisation and the determination of adsorption isotherms was performed using a fully equipped HPLC device (HP1100). Flow rates were limited to 0.5 mL/min due to pressure drop constraints of the Chirobiotic T column (Astec, ICZ Chemietechnik GmbH, 250 mm x 4,6 mm, 5 µm). The stationary phase consists of silica beads functionalised by the macrocyclic glycopeptide Teicoplanin, which offers by more than 20 chiral centres a high chiral selectivity. Supplier-recommended HPLC grade solvents methanol, ethanol and deionised water were used. Injections were performed with 1-5 µL volume at different temperatures (293.15 K, 298.15 K, 303.15 K, 308.15 K), elution profiles were recorded at a wavelength of 205 nm. The alcohol content in the mobile phase was varied between 0-40 % by volume. A comprehensive summary of all conditions is given by Vorster as part of a diploma thesis conducted at the MPI Magdeburg [201].

Results

A number of trends in the chromatographic separations were observed from the screening procedure, which are summarised here in brief. The capacity as well as the resolution of the stationary phase increased slightly for higher alcohol contents for both enantiomers. A counter-trend was found for the separation factors and the NTP values. While the separation factor was not affected by temperature, much lower capacities were obtained from elevated temperatures. As reported in a several publications, a cyclic shift of retention times can take place using this column. This might be attributed to a folding of functional groups, but the predominant cause is not found up to now. For the experiments conducted, a shift was observed from aqueous ethanol

solutions, but not in case of methanol. In summary, a mobile phase composition of 20/80 methanol/water at 298.15 K (separation factor of 1.5) was chosen as the most promising separation condition.

Selected elution profiles were used to identify suitable adsorption model parameters. Overloading of the column happened already from injection amounts of 0.25 mg Serine on (Figure 5.22 left). Characteristic peak shapes of (Bi-) Langmuir-type were obtained.

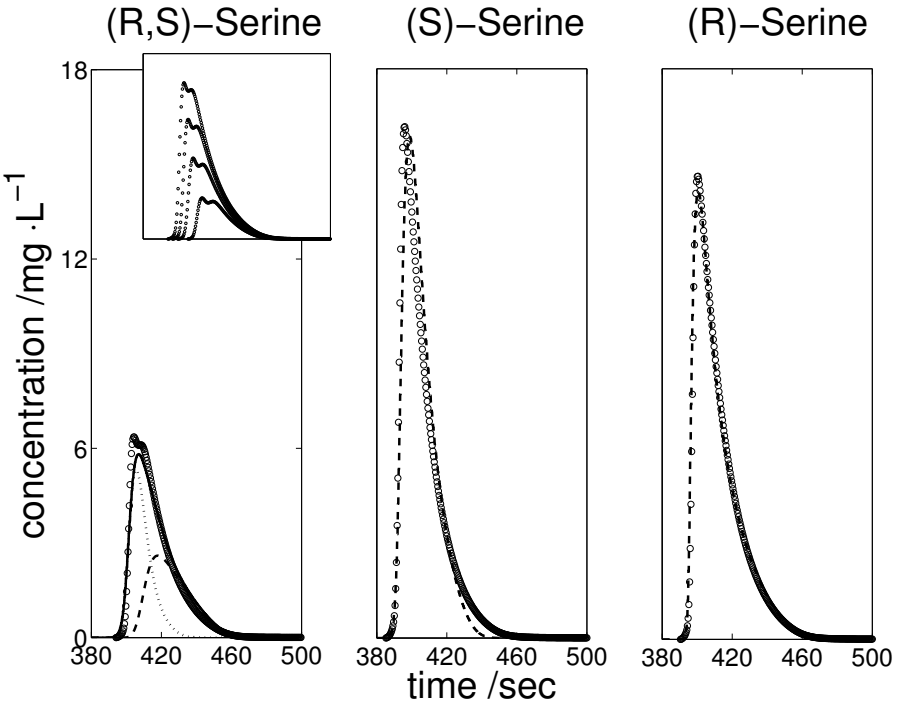

Figure 5.22 *Serine elution profiles of racemic mixtures (solid line), the (S)-enantiomer (dotted lines) and the (R)-enantiomer (dashed lines). Symbols denote measurements, lines indicate simulation results. (injection volumes: 50 µL; injection concentrations: (R,S), 25, 20,…,5 g/L; (S)/(R), 50 g/L).*

Thus, the Bi-Langmuir model for multi-component-systems (Eq. (2.86) and Eq. (2.87)) was chosen to reflect the competitive adsorption behaviour of the two enantiomers. The loading at saturation was assumed equal for both components as well as the adsorption onto the silica matrix. Thus, a single parameter only describes the difference in adsorption onto the chiral sites, while in total 5 parameters need to be identified. Their estimation was conducted using the peak-fitting method. Migration of the solutes through the column was modelled using the equilibrium-dispersive model (Eq. (2.93)). The Matlab solver 'patternsearch' was found suitable for fitting theoretical chromatograms based on the chosen adsorption isotherm model to experimental chromatograms. The NTP (Eq. (2.77) to Eq. (2.81)) were not identical for both enantiomers- an assumption, the equilibrium-dispersive model rests on- but here the differences were less pronounced. However, since the tailing of the (R)-enantiomer profiles (less plates) was found more pronounced than for the (S)-enantiomer, a compromise had to be made during the parameter estimation procedure and minor discrepancies between the model and the experimental data set remained.

The model parameters obtained through the simultaneous fit of the three profiles of Figure 5.22 are listed in Table E.2 in the appendix.

5.2.1.2 Design of a continuous counter-current chromatographic separation process

Identification of process parameters

External constraints as *e. g.* flow limits on pumps and limits on switching times can have a large impact on the choice for an optimal set of operating parameters. For the case study of the model compound Serine, no constraints of such kind were considered, except for the maximal flow rate (here: 0.5 mL/min), which is limited intrinsically by the kind and size of packing material and the related pressure drop. Further, the minimal solubility of Serine, given by the racemic compound, is relevant. Methanol lowers the solubility down to 25 g/l at 298.15 K and a 20/80 volumetric Methanol/water ratio. Though, the market values of (R)-Serine is significantly higher, it was chosen to evaluate the maximal productivity with respect to the (S)-enantiomer for the simple reason, that a crystallisation process for this enantiomer was evaluated beforehand already. Due to the mirror symmetry of phase equilibria, no hurdle is expected in the analogue crystallisation, the purification the (R)-enantiomer. However, the specific productivity of a SMB separation will vary, since the (R)-enantiomer-rich fraction leaves at the extract port, while the (S)-enantiomer-rich fraction can be withdrawn at the raffinate port and no symmetry applies.

In summary, maximal productivity with respect to the amount of Serine in the raffinate fraction was chosen as the objective function. Constraints on the optimisation have been, the inequalities on the dimensionless flow rates (m_i: $m_{II} \leq m_{III}$; $m_{IV} \leq m_I$; $m_{II} \leq m_I$; $m_{IV} \leq m_{III}$) and high purities (>99%) at the opposite port in order to avoid (S)-Serine losses. The minimal purities at the raffinate port were varied between 70 to 100 % (S)-enantiomer. Serine was not allowed to migrate between zone I and IV (compare Figure 2.28). The maximal flow rate is critical to the process productivity and the flow in zone I was set to 0.5 mL/min. Thus, only the four m_i values were optimised. Four columns, each identical to the one used, compiled in a 1-1-1-1 arrangement were considered as a suitable model setup.

The number of transport plates derived from the adsorption quantification procedure is in the order of 4.000-13.000 for this column. The optimisation of separation tasks based on the introduced model for very high NTP requires either enormous patience or computing power or both. Since this case study shall rather provide a profound indication than most accurate data, it was attempted to estimate characteristic productivity-purity curves from optimisations involving a series of individual optimisations with increasing NTP.

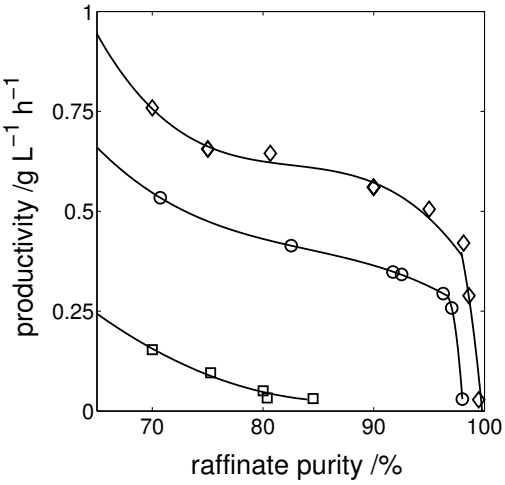

Figure 5.23 *Optimised productivities with respect to the raffinate port and (S)-Serine for different product purities and NTP (100, squares; 200, dots; 300, diamonds).*

Results of the parameter estimation procedure

For the optimisation problem, a pronounced drop in productivity was observed between 95 and 100 % purity. The estimated productivities for the chiral separation of Serine enantiomers are highly depending on the number of transport plates, *i. e.* the quality of the packing and also the

length of the column. Both, productivities and achievable raffinate purity increases significantly for the range of NTP considered. The main aspect relevant for a process coupling is given by the S-shape of the productivity curve, which is present beginning with from 200 NTP on. Simple extrapolation of productivities towards the effective NTP is not recommended- however, the S-shape is expected to remain unchanged also for higher NTP. The productivity/ purity correlation is very relevant for process design and for process synthesis in view of process coupling as proposed in chapter 5.2.1.

5.2.1.3 Performance of a coupled separation process

The case study on continues chiral chromatography revealed largely different productivities for slightly asymmetric mixtures compared to a fraction containing only the single enantiomer as product. The ternary phase diagram of Serine/water was introduced in chapter 4.2.3. The key property, to be exploited here, is the hydrate-/anhydrate relation. Depending on the amount of alcohol, very high eutectic compositions (up to 99.5 %) and therefore product purities can be achieved. The corresponding SLE favour a selective crystallisation process based on preferential enrichment. The combination of the information on chiral chromatography and preferential enrichment allows the estimation of the productivities of a coupled process. Herein, the yield of a crystallisation process is given by the Eqs. (5.4) and (5.35) with $x_{(S)}^{initial}$ being the raffinate purity and $x_{(S)}^{eu} = 99.5\%$.

$$Y_{(S)}^{PE,tot} = \frac{m^{eu}}{m^{initial}} = \frac{(x_{(S)}^{initial} - 0.5)}{(x_{(S)}^{eu} - 0.5)} \qquad (5.4)$$

Provides, the same assumptions hold as in the case of the Bicalutamide separation, *i. e.* no additional time losses due to the crystallisation step, the overall productivity can be estimated by

$$P_{(S)}^{tot} = Y_{(S)}^{PE,tot} \cdot P^{chrom}. \qquad (5.25)$$

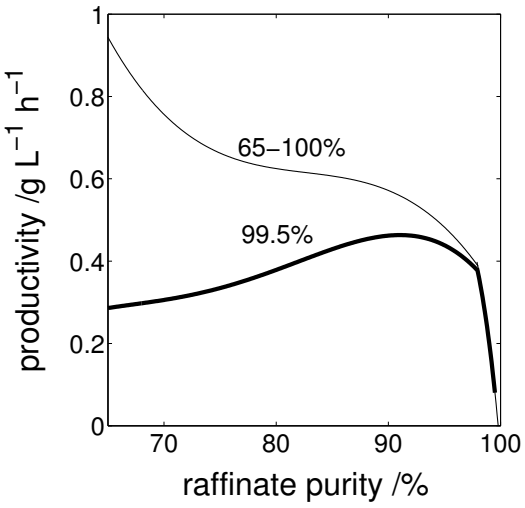

Figure 5.24 *Comparison of productivities the standalone chromatographic process for (S)-Serine (thin line, 300 NTP) and for a coupled process (bold line). Points on the upper curve correspond to the abscissa, while all points on the lower curve are of 99.5 % purity.*

The productivities of a coupled process for the Serine separation by continuous chromatography followed by the crystallisation process of preferential enrichment are illustrated by Figure 5.24. A significant increase is found, compared to the productivities of a standalone chromatography and 99.5% raffinate purity. The curves reflect a coupled process, wherein the pre-enrichment step is based on 300 NTP. Thus, the absolute gain in productivity will vary for higher NTP numbers. However, it is expected, that a similar figure will be obtained for other cases as well. The gain in productivity is not limited to certain raffinate purities. Though, there is a pronounced optimum found at ~90 % raffinate purity, basically any other asymmetric feed can be processed successfully by selective crystallisation and will lead to an increase in productivity. This renders

this process coupling robust, since 'off-spec' batches of pre-enrichment processes can be reprocessed also.

5.2.2 Separation of Bicalutamide enantiomers

The successful separation of asymmetric mixtures of Bicalutamide by a 2-step crystallisation (chapter 5.1.3.3) process entailed the optimisation of a method, that provides the asymmetric mixture itself. Secondly, it was attempted to evaluate, whether and how the new processes can be scaled-up from bench-scale to pilot-plant-scale. Thus, 600 g of racemic Bicalutamide were pre-enriched in a validation study using simulated moving bed chromatography. The asymmetric mixture obtained was purified further by selective crystallisation as presented in Figure 5.25.

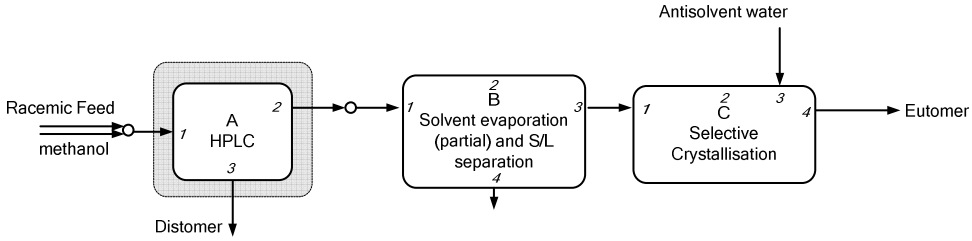

Figure 5.25 *Partial separation of racemic Bicalutamide prior to selective crystallisation.*

5.2.2.1 Inducing asymmetry by chiral chromatography

Determination of adsorption isotherms

A preparative chromatographic method for Bicalutamide was already available through the collaboration with the pharmaceutical company AstraZeneca. It was known, that simulation and experimental results did not agree well due to few data on the adsorption isotherms. For this reason, a re-determination of adsorption isotherms and parameterisation of a suitable model was performed. The type of column has been Chiralpak AD (250x4.6 mm, Daicel Chemical Industries Ltd, Japan) with spherical packing material of 20 µm. The eluent was pure methanol. Very small 'analytical' injections were used to derive the porosity and the Henry constants.

Table 5.3 *Column efficiency measured for the two enantiomers of Bicalutamide for different flow rates Q.*

Q /mL·min^{-1}	u_0 cm·min^{-1}	$NTP_{(S)}$	$NTP_{(R)}$	$HETP_{(S)}$ /cm	$HETP_{(R)}$ /cm
1	6.02	432	288	0.058	0.087
2	12.03	499	213	0.050	0.117
3	18.05	432	126	0.058	0.198
3	18.05	417	122	0.060	0.205
4	24.07	390	88	0.064	0.284
5	30.09	336	89	0.074	0.281

The dead volume caused by tubings and connectors was determined with and without the column in place. The highest possible flow rate according to the determined pressure drop without damage to the column was 5 mL/min. Apparent stage numbers were determined for 1 to 5 mL/min flow rate using 'analytical injections' and the peak width at half-height (Eq. (2.78)).

Remarkable large differences between the adsorption behaviour of the two enantiomers were found. The separation factor was estimated to 7.1. However, the axial dispersion of the more retained (R)-enantiomer (the target compound) was considered to be significant, which caused unfavourably pronounced peak broadening. The van-Deemter plot for both enantiomers highlights the large differences with respect to the height equivalent to the theoretical plate (HETP, s. chapter 2.4.2). This aspect gains more importance during upscaling, when much larger flow rates need to be considered.

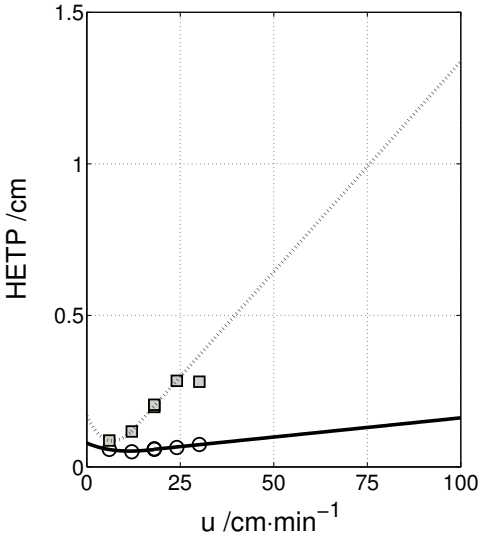

Figure 5.26 *Van-Deemter plot for the less retained (S)-enantiomer (dashed) and the more retained (R)-enantiomer (solid).*

The Bi-Langmuir model for multi-component-systems (Eqs. (2.86) and (2.87)) was chosen to reflect the competitive adsorption behaviour of the two species. Model parameters were estimated using the peak-fitting method. The results are shown in Figure 5.27.

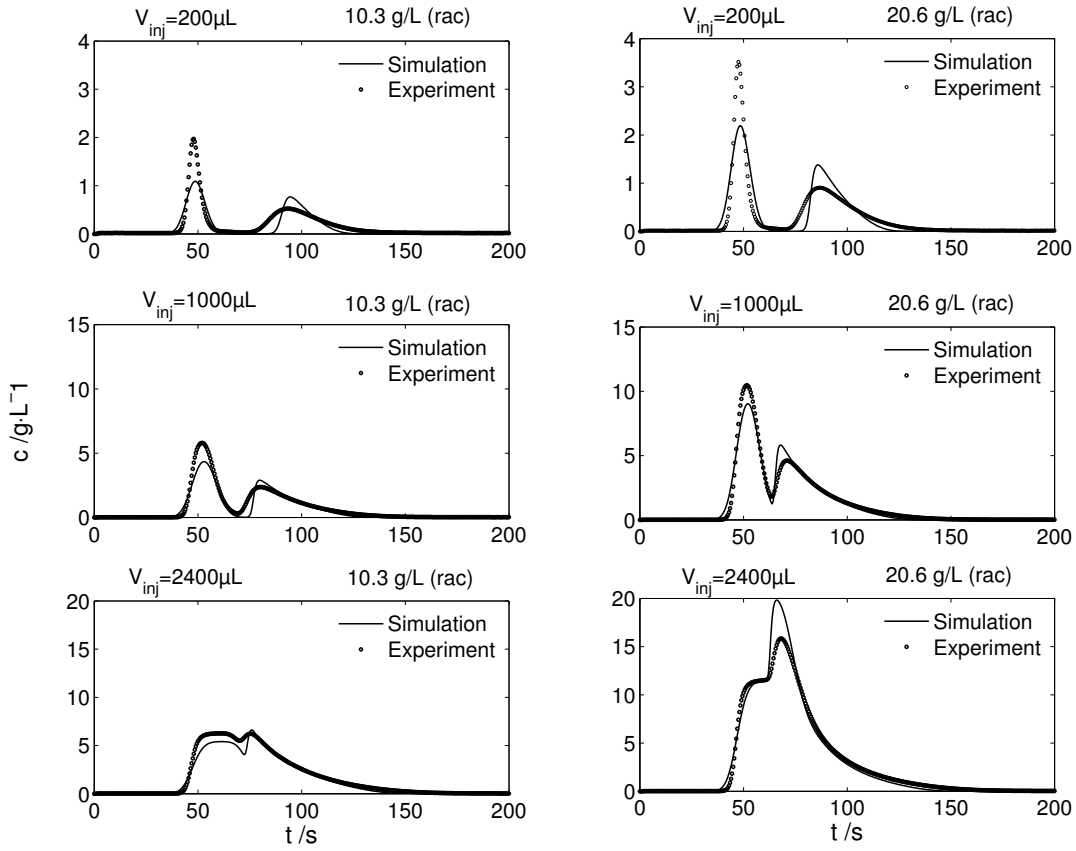

Figure 5.27 *Chromatograms used for peak fitting. Experimental data and modelled elution profiles.*

The column was overloaded using different volumes and concentrations for the injection of racemic mixtures of Bicalutamide in methanol. The highest concentration matched the solubility limit. The eluent flow was set to 5 mL/min. Using the equilibrium-dispersive model and the Matlab solver 'patternsearch', the adsorption isotherm model was fitted to six chromatograms simultaneously. Hereby, the previously obtained Henry constants have been kept constant and the remaining five parameters were estimated only. The applied model assumes similar HETP (Eq. (2.82)) for both components, which did not apply. A rather simple approach makes use of averaging both values and thus, 212 theoretical plates were used during the parameters estimation procedure.

While the model agreement for injections of low volume exhibited large deviations, injections of 1 and 2.4 mL are captured satisfactorily by the model. Higher NTP values (Eq. (2.77)(2.81)) led to a better agreement with respect to the first peak, while lower NTP values captured better the more retained component. The best overall agreement was achieved using the NTP value of the (S)-enantiomer (336). However, this was not theoretically founded and the isotherm parameters obtained from the fit with 212 plates were used for a cross-check with other chromatograms.

Both, the ratio of the enantiomers and the injection volume was changed and the experimentally determined chromatograms were compared to the model prediction. The agreement (Figure 5.28) was assumed to be sufficient for process design, since the retention times of both the peak fronts and the peak tails were reflected with good accuracy. The parameters obtained are listed in the appendix in Table E.1.

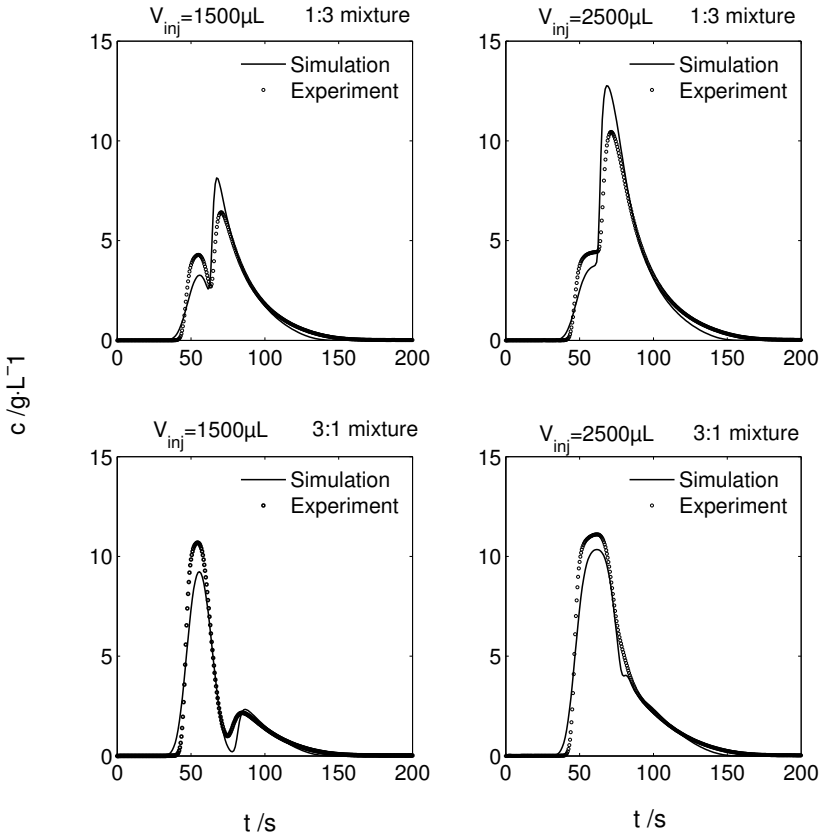

Figure 5.28 *Determined chromatograms from asymmetric mixtures of Bicalutamide enantiomers (symbols) and estimated elution profiles, which were not used for the parameter estimation procedure (lines).*

5.2.2.2 Optimisation of pre-enrichment

Identification of process parameters

Prior to the separation run, a typical optimisation problem had to be solved. A maximal productivity of the stream, rich of the (R)-enantiomer (extract port), was chosen as the objective function. Constraints on the optimisation have been the following inequalities on the dimensionless flow rates m_i: $m_{II} \leq m_{III}$; $m_{IV} \leq m_I$; $m_{II} \leq m_I$; $m_{IV} \leq m_{III}$. Further, the purity at the raffinate port (rich in the (S)-enantiomer) was required to exceed 99%, since losses of the target component through this port should be minimised. The requirements on the purity of the extract port outlet were varied between 70 to 100 % (R)-enantiomer. Due to restrictions of the SMB unit used, the lowest possible shifting time was set to 0.25 min. The maximal flow rate of the feed pump was 90 mL/min and 200 mL/min applied for the eluent pump, respectively. Regeneration of the solvent in zone IV and the stationary phase in zone I was assured by low maximal limits on the terminal concentration profiles. The parameters to be optimised have been the four m_i values and the flow rate within zone I. Only non-negative values were possible. The upper boundary for any flow rate was set to 300 mL/min due to pressure drop constraints on the packing material. The number of transport plates was set to the average value of both enantiomers at the respective flow rate. This is considered a less safe but practical approach, since the estimation requires the extrapolation to interstitial velocities of up to 88 cm/min, which is far above the range of experimental values (compare Figure 5.26).

The modelling of SMB separations was based on a algorithm initially developed by Godunov [202] and transferred later by Rouchon [203] to chromatographic problems. The algorithm makes use of the numerical dispersion, which is generated from the numerical solution of Eq. (2.93). The numerical dispersion and the physical dispersion 'cancel out' mutually, which allows to remove the term of physical dispersion from Eq. (2.93), leaving a first order ordinary differential equation. The chromatographic algorithm was described by Kniep [204] and implemented into a Pascal code. Within this study, the code was edited and compiled to be called by a Matlab routine, which contained the solver for the parameter estimation. Here, a genetic algorithm in combination with the Matlab routine 'fminsearchcon' was used. It is known, that the algorithm can run into parameter areas, where mass balances are not fulfilled. Additional penalties were set for the solver, when mass balance errors exceeded empirical thresholds. The results obtained have never been close to these boundaries.

After feasible start values were obtained from using the genetic algorithm, different scenarios were analysed using the algorithm of Nelder-Mead type. An optimised operating point was obtained herein within an hour or less on a standard notebook (Intel U9400 processor).

Results of the parameter estimation procedure

The maximal productivity with respect to a single enantiomer depends largely on the purity constraints [124]. Kaspereit showed [127], that relaxing the constraints on regeneration within zone I and zone IV can lead to elevated throughputs and so do changes to the purity constraint on the raffinate port. Results of own simulation studies were limited to the purity of the target component and exhibited similar shapes of productivity/purity curves. The productivities given are scaled to 1 l of stationary phase (Figure 5.29).

For the optimisation problem, a pronounced drop in productivity was observed between 95 % and 100 % purity. The function of productivity and feed flow rate are strongly related and

describe a countertrend to the $m_{2/3}$-values. A single operating point was validated on an experimental basis. The obtained purity exceeded slightly the theoretical value after reaching pseudo-steady-state (full symbol in Figure 5.30). The Figures above provide the basis for coupled processes using chiral chromatography as one integrated process step. It is referred back to the given productivity/purity correlation in chapter 5.2.2.

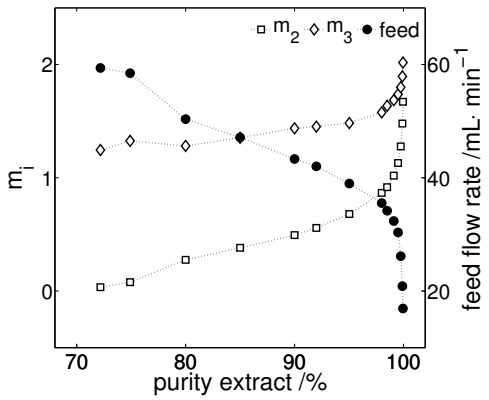

Figure 5.29 *Optimised m-values of the separation zones and corresponding feed flow rates. Lines are drawn to guide the eye.*

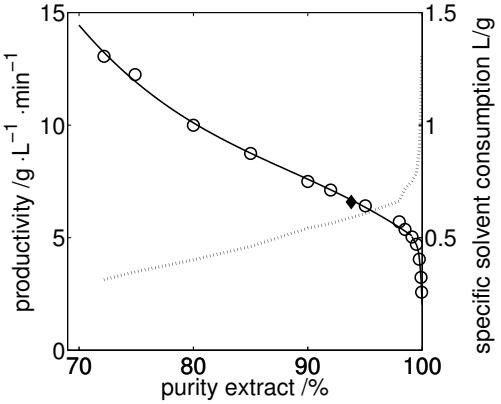

Figure 5.30 *Optimised productivities with respect to the extract port and (R)-Bicalutamide (theoretical values: open symbols; experimental value: full symbol). The specific solvent consumption related to the mass of Bicalutamide in the extract fraction is plotted.*

Performance of the coupled process

The process-relevant SLE of Bicalutamide in solution were summarised within chapter 4.2.4. Herein, the eutectic composition was found to vary between 95-97.7% purity. The identification of the optimal outlet purity of the pre-enrichment step for a coupled process will by illustrated in the following.

Classical coupled processes required the enrichment of a solution above the eutectic composition prior to a selective crystallisation step. The introduced 2-step crystallisation process yields the target enantiomer from any asymmetric solution. It is convenient to alter the definition of process yield as defined by Eq. (5.24) to comply with the definition of other processes for the ease of comparison. The mass of product was related to the excess of the more abundant enantiomer in the initial mixture. This is the definition of the so called- 'enantiomeric excess *ee*'. Multiplication of Eq. (5.26) and Eq. (5.24) leads to the definition of process yield $Y_{(R)}^{tot}$ with respect to the whole initial feed mass.

$$ee_{(R)} = 2 \cdot x_{(R)} - 1 = \frac{m_{(R)}^{initial} - m_{(S)}^{initial}}{m_{(R)}^{initial} + m_{(S)}^{initial}} \tag{5.26}$$

$$Y_{(R)}^{tot} = \frac{m_{(R)}^{s}}{m_{(R)}^{initial} + m_{(S)}^{initial}} = \left(2 \cdot x_{(R)} - 1\right) \cdot Y_{(R)} = \frac{\left(2 \cdot x_{(R)} - 1\right)}{(2 \cdot x_{(R)}^{eu,1} - 1)} \frac{x_{(R)}^{eu,1} - x_{(R)}^{eu,2}}{(1 - x_{(R)}^{eu,2})} \tag{5.27}$$

$$Y_{(R)}^{tot,classical} = \frac{m_{(R)}^{s}}{m_{(R)}^{initial} + m_{(S)}^{initial}} = \frac{1}{x_{(R)}^{feed}} \frac{x_{(R)}^{feed} - x_{(R)}^{eu}}{1 - x_{(R)}^{eu}} \tag{5.28}$$

The equation shares similarities to the process yield of the classical process (Eq. (5.28)). The yields of both processes become very similar, provided that $x_{(R)}^{eu,1}$ coincides with $x_{(R)}^{feed}$. The reason for the deviation of both processes is found in the 1st process step, where racemic

crystals are harvested in order to obtain the enriched liquid phase. In the classical process, the enriched solution is fed directly to the 2nd crystallisation step. Figure 5.31 and Figure 5.32 compare both processes by generic plots.

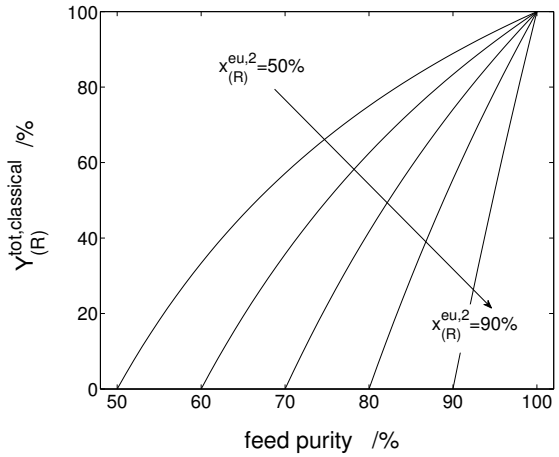

Figure 5.31 *Theoretical yields for the classical process for different feed purities and eutectic compositions.*

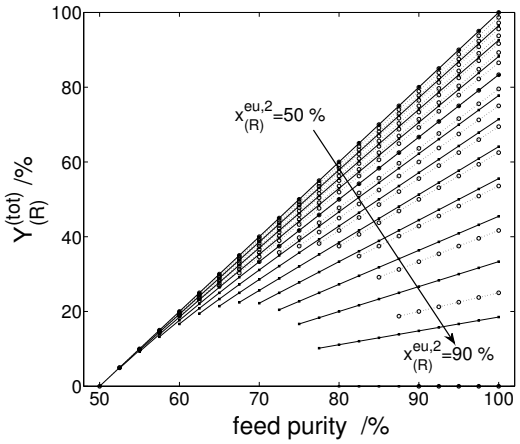

Figure 5.32 *Theoretical yields for the 2-step process (solid lines) for different feed purities and eutectic compositions in the 2nd step and eutectic compositions of 80% (full symbols, solid lines) and 90% (open symbols, dotted lines) in the 1st step.*

It becomes visible, that each process shows superior performance with respect to limited areas. However, the 2-step process can be conducted from any pre-enrichment, which is not possible for the classical case.

The simulation of optimal operating points for the chromatographic separation of Bicalutamide yielded a typical S-shaped productivity curve (P^{chrom}) for different extract purities (Figure 5.29). Combination of this curve and the knowledge of the correlation of crystallisation yield on the initial feed purity (Figure 5.33) allows to draw the productivities for a coupled process. The dashed line of Figure 5.34 represents the productivity of the reference case-entire chromatographic separation- up to 100% purity of the extract fraction. The possible gain in productivity with respect to the pure (R)-enantiomer can be estimated for both the classical process and the 2-step process from Eqs. (5.29) and (5.30).

$$P_{(R)}^{tot,classical} = Y_{(R)}^{tot,classical} \cdot P^{chrom} \tag{5.29}$$

$$P_{(R)}^{tot} = Y_{(R)}^{tot} \cdot P^{chrom} \tag{5.30}$$

Herein, the time needed for the two steps *B/C* (Figure 5.25) is neglected entirely. This is a simplifying assumption and generalisation will fail in particular, if solvents of very low partial pressure need to be evaporated or if a chiral system approaches thermodynamic equilibrium during step *B* or *C* only very slowly. In all cases investigated, step *B* and *C* were not considered to create bottlenecks in comparison to the chromatographic separation (22 hours in the case of Bicalutamide). However, this aspect must be investigated with care for each particular system. Obviously, there is a set-up and cleaning time, which need to be considered for each additional step. In case of pharmaceutical productions, the product formulation requires in most cases the solvent removal and crystallisation of the product anyway. Thus, this aspect vanishes. In any case, cost factors are needed to balance and assess different process variations. It should be

noted, that the comparison introduced here rests exclusively on purification and productivity and aspects of product formulation were not taken into account.

The gain in productivity for coupled processes is illustrated exemplarily for the system of Bicalutamide by Figure 5.34. All points at the dashed line, the bold line and the dotted line correspond to 100 % extract purity, whilst only the thin solid line (Figure 5.30) corresponds to the abscissa.

The intersection of the dotted line with the dashed horizontal line denotes the beginning of an increase in productivity for the classical process. The productivity curve peaks at 99.4% purity and doubles the productivity compared to the standalone chromatographic process. The rather narrow area can be attributed both to the steep decline in productivity for this particular system and its high eutectic composition. Elevated productivities can be expected only, if the pre-enrichment exceeds the eutectic composition, which is >95 % in the case of Bicalutamide.

The bold line represents the productivities of the coupled process involving the 2-step process. It intersects with the classical process at the high eutectic composition. The process shows superior performance up to the higher eutectic composition. The curve exhibits hereby rather a plateau, than a productivity maximum. The maximal gain in productivity is estimated to 73 %. Apparently, the optimal interface between both process units is not limited by a specific extract purity for this particular separation problem. The curve reveals a quite robust process combination, since any output of a pre-enrichment step can be advantageously processed. Taking into account, that the solvent consumption is lowered at reduced purity requirements (compare Figure 5.30), the curve suggests to operate at 70 % purity as the most promising interface. However, solvent consumption was not issued for the separation of Bicalutamide and thus, the extract purity requirement was lowered to the beginning of the productivity plateau to 90 %.

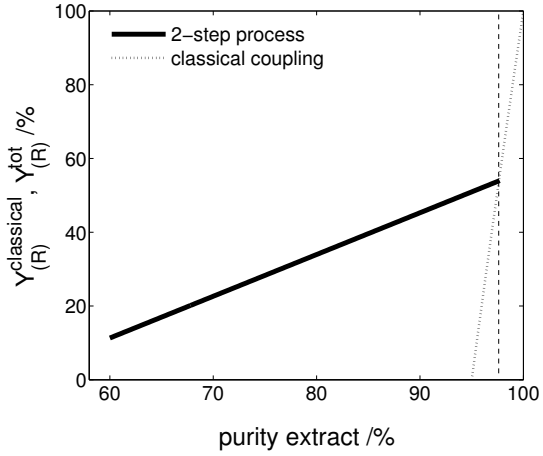

Figure 5.33 *Correlation of crystallisation process yields and purity at the extract port for the classical process and the 2-step process. The vertical dashed line denotes the higher eutectic composition at 273 K. The classical process can be applied beginning at the lower eutectic composition of 95 %, while the 2-step process can be applied from negligible enrichment up to the higher eutectic composition.*

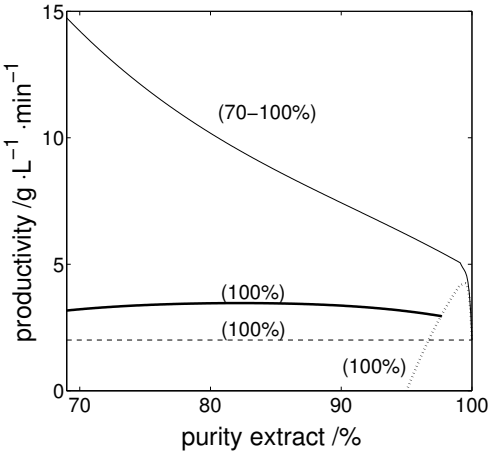

Figure 5.34 *Estimated productivities for the separation of Bicalutamide enantiomers by entire chromatographic separation (thin solid line, dashed line), the classical coupling scheme (dotted line) and coupling using the 2-step crystallisation process (bold line). The numbers in brackets denote the final product purities to be obtained by the corresponding process.*

In summary, the performance of the stand-alone chromatographic process can be improved in combination with each of the crystallisation methods. The characteristics of the coupled

processes complement each other. The classical process shows higher yields, while the 2-step process does not require the rather high pre-enrichment and improves the coupled process from basically every degree of pre-enrichment.

5.2.2.3 Chiral separation by preparative scale chromatography and crystallisation

Continuous counter-current chiral chromatography

Experimental setup

Through the FP7 project INTENANT and the collaboration with AstraZeneca, 150 g of stationary phase (Chiralpak AD) and 4 preparative scale columns (100x25 mm) were obtained for process validation. The columns were packed with ~30 g of stationary phase each (97.5 mm bed length) and arranged in a classical 1-1-1-1 mode. The columns were characterised in terms of pressure drop, porosity and in addition by 'analytical injections' to assess their homogeneity. All packings were of similar quality with a porosity slightly above the value of the analytical column. The simulated moving bed chromatographic unit was a CSEP 912 system (Knauer, Berlin), which consists of 4 preparative pumps (K-1800, Knauer, Germany) and 2 UV detectors (K-2501, Knauer, Germany) located at the extract and the raffinate lines, respectively. A multi-port valve allowed for the connection of up to 12 columns. Since only 1 column per zone was used and switching over two positions was not successful in practise, a rearrangement of the connecting lines became necessary. The setup is described in more detail in the annex of a publication [205].

Figure 5.35 *Preparative scale multi column chromatographic separation unit. Four identical columns are installed (centre of figure) and connected to a multiport valve, which operates from top. The pumps for feed, extract, raffinate and eluent are placed on the left side.*

Step A-process parameters

The pre-enrichment step, denoted *A* (Figure 5.25) was conducted with the parameters as given by Table 5.4. Extract purities to be achieved by chromatography were 90% from considerations

on process coupling (Figure 5.34). In total 600 g of racemic Bicalutamide was dissolved as feed in 30.33 l methanol. The mixture was separated in two chromatography runs of similar duration.

Table 5.4 *Process parameters and results of the chromatographic separation of Bicalutamide enantiomers.*

Internal dimensionless flow rates m_I,...m_{IV}	6.713, 0.665, 1.426, 0.203	
External flow rates		
Feed	23.70	mL/min
Eluent	200.00	mL/min
Raffinate	36.50	mL/min
Extract	179.70	mL/min
Volumes		
Eluent	255.96	l
Feed	30.33	l
Raffinate	47.53	l
Extract	233.94	l
Purity raffinate	99.54	%
Mass Bicalutamide in raffinate	274.00	g
Purity extract	92.38	%
Mass Bicalutamide in extract	322.00	g
Mass lost on column, etc.	7.43	g
Overall separation time	21:27	hh:mm
Switching time	29	s

Step B-preferential enrichment and solvent removal

(first step of 2-step selective crystallisation process)

The outlet stream of unit *A* was transferred batch-wise into unit *B*, a 20 l crystallisation vessel. The setup used consisted of a double-walled and temperature-controlled vessel, equipped with a draft tube for agitation and Pt-elements for temperature control. The crystalliser was extended by a reflux cooler, a distillate collecting vessel positioned on a balance and a vaccum pump.

In total 237 l of extract with a purity of 92.38% (R)-enantiomer was concentrated up by solvent evaporation at ~300 mbar and ~313 K. The remaining amount of 8.2 l solvent contained 322 g of Bicalutamide. The double-walled vessel was cooled down by a thermostat to 273.15 K to force the crystallisation of the racemic compound and to perform preferential enrichment in the liquid phase up to 97.7 wt% of the (R)-enantiomer. Even after 12 hours no crystals became visible. Apparently, the MSZW of Bicalutamide was much larger in this vessel compared to the bench-scale experiments. Addition of 1 g of ground racemic Bicalutamide caused immediately a nucleation event and the solution

Figure 5.36 *Batch-crystalliser equipped with solvent reflux and distillate balance. The draft tube inside the vessel is visible.*

equilibrated within minutes. The integration of the crystallisation process in the coupled scheme is depicted in Figure 5.37.

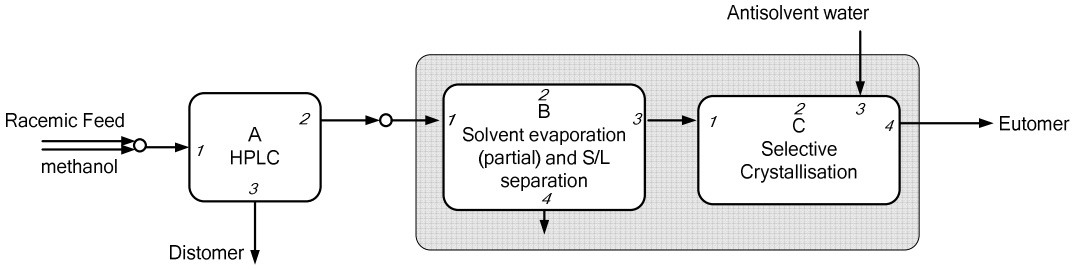

Figure 5.37 *Schematic figure of connected single units and process streams.*

The whole process was initially scaled such, that in the 2nd step after addition of the antisolvent, the whole volume of the crystalliser (20 l) was used. Thus, 8.2 l in this intermediate step were rather suboptimal and caused stirring issues. The vessel was equipped with a draft tube for typical loop-like agitation. Unfortunately, the baffle plate was not covered due to a too low liquid level disallowing for proper stirring. The poor agitation led to splashes of mother liquor onto the freeboard, where crystallisation took place and significant losses of the solute were recognised. The solid phase generated, exhibited the desired racemic composition, while the overall composition of the crystallised material deviated largely and was summed up to 70 % purity (stream *B4*). Hereby, the amount of target enantiomer in the liquid phase (stream *B3*) was diminished and additional material crystallised. The obtained purity was only slightly below the theoretical value. The stirrer was shut off allowing the solids to settle. Afterwards the liquid phase was pumped off the vessel through a filter and stored.

Step C-selective crystallisation of the target enantiomer using antisolvent
(second step of the 2-step selective crystallisation process)
After removal of remaining crystalline material, the vessels was filled with the previously stored mother liquor and heated up to 333.15 K. About 8 kg of water was added; the amount was controlled by mass. Nucleation of the target enantiomer happened instantly and the thermodynamic equilibrium was approached again within minutes. The stirrer was switched off and crystals of the target compound settled down. The liquid phase was removed by a pump and the solid phase was filtered off and washed firstly with the mother liquor and secondly with cooled methanol. The solids were dried in a drying cupboard under vacuum. The mother liquor was fed back into the crystalliser and cooled down to 283 K to force crystallisation of the dissolved material of eutectic composition. No solubility could be determined at these conditions and virtually all Bicalutamide was recovered. The purities of all phases were analysed by chiral chromatography. The overall mass balance and the yield of the individual steps is depicted in Figure 5.38 on the next page.

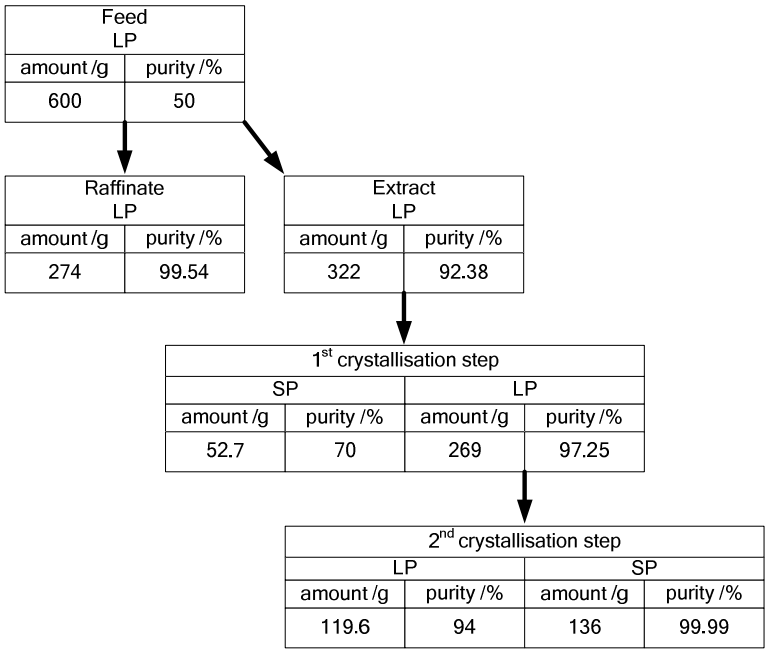

Figure 5.38 *Development of product purity and yield for the conducted separation of Bicalutamide enantiomers at a larger scale. LP and SP denote liquid and solid phase, respectively.*

Summary

The purification of a pre-enriched mixture of Bicalutamide enantiomers was transferred successfully from a 'less than a gram' scale to 600 g of racemic substance. In contrast to bench-scale experiments, nucleation of the racemic compound did not happen and seeding with the racemic compound became necessary. Further, experimental stirring issues prevented from obtaining the theoretical yield of 56%. For the single batch conducted a yield of 45% was measured. The crystal purity was excellent and exceeded the purities of bench-scale experiments by far.

5.2.2.4 Considerations on internal recycling-comparison of processes

A concept of recycling of side streams for yield improvements was illustrated and validated for the separation of Methionine in chapter 5.1.3.2 and will be applied for Bicalutamide as well. Its relevancy for productivities of coupled processes will be discussed in this chapter.

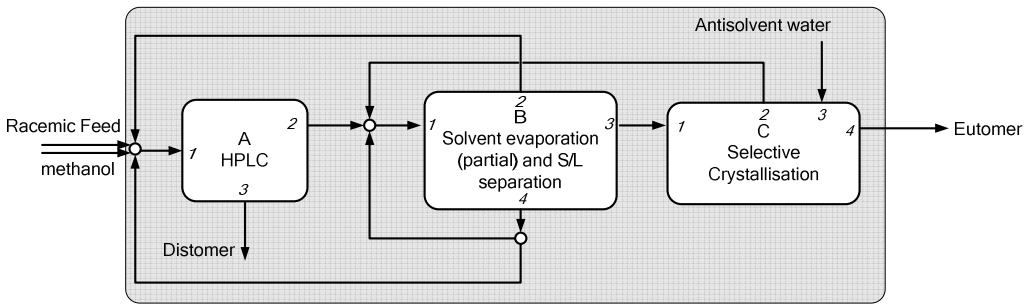

Figure 5.39 *Recycle streams within the proposed process scheme.*

There are two streams, that evolve from the crystallisations *B* and *C*, which contain Bicalutamide below the required purities. *C2* represents the eutectic mother liquor after selective

crystallisation and *B4* contains the racemic Bicalutamide. For the setup of *B*, a certain amount of pre-enriched material *B1* is fed to a vessel. Its composition is always below the composition of *C2*. Thus, the stream *A2*, the stream *C2* and a fraction of the stream *B4* can be pooled. It yields the same amount of product at the cost of less feed material.
This applies to all subsequent batches, except for the first batch. While *C2* can be recovered entirely, the fraction of *B4* varies. In case of Bicalutamide the lower eutectic composition (95%) allows *a*-values of up to 40 % depending on the purity of the extract. Further, the solvent removed (*B2*) in the concentration step *B* can be fed back to the chromatography unit *A*. The balance around the node prior to *B* allows the quantification of the recycling flow of *B4*.

$$m^{B1} = m^{A2,reduced} + m^{C2} + a \cdot m^{B4} \qquad \text{with} \qquad 0 \le a \le 1 \tag{5.31}$$

It is suitable to introduce the overall yield $Y_{(S)}^{recycle}$, which applies beginning with the second batch. Provided the whole excess of the more abundant enantiomer is harvested and only a fraction of the racemic stream *B4* is fed back to the pre-enrichment step, the yield can be defined according to the 'enantiomeric excess'.

$$Y_{(R)}^{recycle} = 2 \cdot x_{(R)}^{initial} - 1 = \frac{m_{(R)}^{A2,reduced} - m_{(S)}^{A2,reduced}}{m_{(R)}^{A2,reduced} + m_{(S)}^{A2,reduced}} = \frac{m^{C4}}{m^{A2,reduced}} \tag{5.32}$$

The quotient of the yield of the first and the subsequent batches defines the ratio of the feed mass needed to produce the same amount of product, with and without recycling.

$$\frac{Y_{(R)}^{tot}}{Y_{(R)}^{recycle}} = \frac{m^{C4}}{m_{(R)}^{B1} + m_{(S)}^{B1}} \cdot \frac{m_{(R)}^{A2,reduced} + m_{(S)}^{A2,reduced}}{m^{C4}} = \frac{m^{A2,reduced}}{m^{B1}} \tag{5.33}$$

An expression for the amount of dissolved material in *B3* with respect to the initial amount *B1* was introduced by Eq. (5.4) and is re-used here. It is denoted the total yield $Y_{(R)}^{PE,tot}$ of preferential enrichment.

$$m^{C2} = m^{B3} - m^{C4} \tag{5.34}$$

$$Y_{(R)}^{PE,tot} = \frac{m^{B3}}{m^{B1}} = \frac{(x^{B1} - 0.5)}{(x^{B3} - 0.5)} \tag{5.35}$$

$$\frac{m^{C2}}{m^{B1}} = Y_{(R)}^{PE,tot} - Y_{(R)}^{tot} \tag{5.36}$$

Compilation of Eqs.(5.31) to (5.36) reads

$$\frac{a \cdot m^{B4}}{m^{B1}} = 1 - \frac{Y_{(R)}^{tot}}{Y_{(R)}^{recycle}} - Y_{(R)}^{PE,tot} + Y_{(R)}^{tot} \tag{5.37}$$

and finally

$$a = \frac{1 - \frac{Y_{(R)}^{tot}}{Y_{(R)}^{recycle}} - Y_{(R)}^{PE,tot} + Y_{(R)}^{tot}}{1 - Y_{(R)}^{PE,tot}}. \tag{5.38}$$

The corresponding fraction of racemic Bicalutamide to be recycled and its dependency on the purity of pre-enriched feed stream are plotted in Figure 5.40. The aspect of internal recycling is beneficial compared to the classical coupling process, where the remaining mother liquor exhibits a lower composition than the feed and needs to be withdrawn. The comparison of the process variations highlights the pronounced increase in yield and productivity, respectively (Figure 5.41 and Figure 5.42). In theory, the chromatographic productivity can be more than tripled neglecting the first batch. Further, improvements can be achieved over the whole range of extract purities provided.

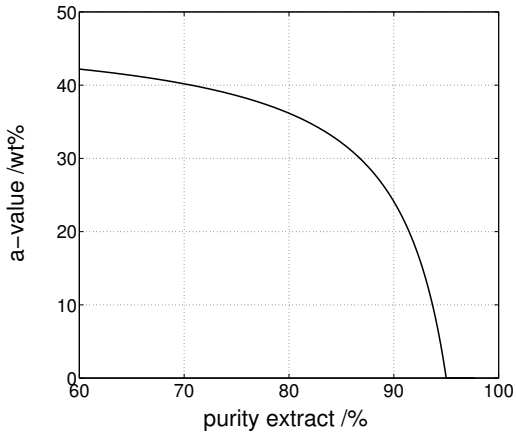

Figure 5.40 *Internal recycling rate for racemic Bicalutamide (B4).*

From the internal recycling between B and C a fraction of racemic material is not recovered, but send back to A instead. At this point, a clear differentiation among two objectives needs to be made. The coupled process introduced here was optimised for the production of a single enantiomer from a racemic mixture. Another objective would be the separation of a given amount of substance with the highest yield in the shortest time.

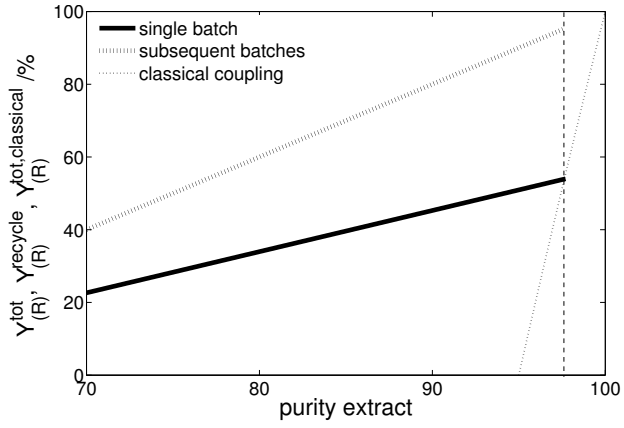

Figure 5.41 *Comparison of process yields for the classical case, the 2-step process and the 2-step process with internal recycling. The dashed vertical line denotes the upper application limit of the 2-step process.*

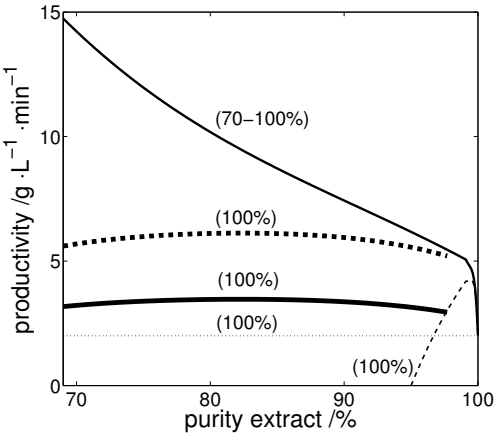

Figure 5.42 *Comparison of productivities for the classical case (thin dashed line), the 2-step process (thick solid line) and the 2-step process with internal recycling (thick dashed line). The latter process shows superior performance over the whole figure.*

Within the classical schema, eutectic material is recycled, which can be considered as a severe drawback, since the already highly enriched stream is mixed with fresh racemic feed. The two objectives can lead to different optimal operating parameters. For the 2-step crystallisation process, both variations coincide, since the recycled material is of racemic composition, too.

Process robustness

Referring back to the conducted crystallisation process, the theoretical mass balances were not entirely fulfilled. Losses in the first crystallisation step due to the low liquid level led to a fraction of crystallised product. Results of imperfect crystallisations as in the conducted 1st batch can be recovered in subsequent batches improving the overall yield. Considering mass balances and the experimental results as given in Figure 5.38, it is possible to feed back the entire stream *C2* and 22 % of the stream *B4* to the unit *B*. Within Figure 5.42 a series of imperfect crystallisations based on the results of the single conducted crystallisation run are plotted. The overall yield will never approach 100 %, but the increase in yield even for small numbers of subsequent batches is significant.

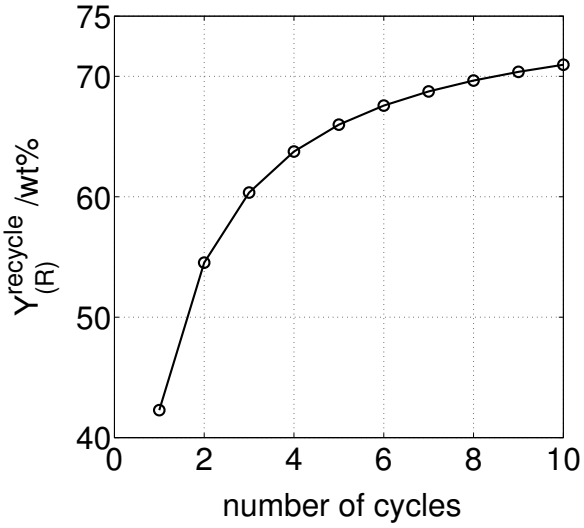

Figure 5.43 *Increase in process yield for subsequent batches considering a series of batches identical to the one conducted.*

5.3 Summary

Within the fifth chapter selected options for chiral pre-enrichment and resolution, which are linked to the underlying SLE, were presented. Two of these, a preferential enrichment process and a new 2-step crystallisation process were balanced and evaluated for different compounds.

The experimental validation work was performed both at lab-scale and also using a 20 l pharmaceutical pilot-plant-scale crystalliser and a preparative-scale SMB unit. Crystallisation processes were monitored by in situ ATR-FTIR and offline analytics as density meter and chiral HPLC.

The potential of preferential enrichment in combination with tailored SLE through the choice of solvents was illustrated for the amino acids Proline and Serine. It was shown for the systems of Methionine and Bicalutamide, how shifts in the eutectic composition in solution can be tailored and exploited for enantioseparation using a 2-step process.

The crystallisation processes were modelled based on general mass balances, which allowed the rapid assessment of theoretical yields and process trajectories for the compounds considered and others. The experimental experiments validated the theoretical considerations to a very large extend. Further, losses due to experimental issues were corroborated into the models leading to more precise predictions of *e. g.* a series of batches. Hereby, rather realistic estimations of process yields were possible and the robustness of the introduced processes with respect to typical disturbences could be rated.

The single process units of chiral continuous chromatography and selective crystallisation were optimised individually and again based on a proposed coupled mode. The optimal operating points of the pre-enrichment steps were altered for the coupled processes considered. Hereby, the overal productivities for all coupled processes were found to be largely above the corresponding values for the individual units. It was shown theoretically and on an experimental basis that a framework of recycling streams led to large increases in the overal process yields and productivities. Further, the degree of process robustness was increased, when streams were recycled in subsequent batches. The introduced 2-step process conducted in a coupled mode was compared to similar coupled process state-of-the-art. The comparison revealed significant advantages for the majority of applications.

More details on the studies conducted can be found published in the German Journal of *Chemie, Ingenieur, Technik* [186], the Journal of *Fluid Phase Equilibria* [190] and the Journal of *Organic Process Research and Development* [205].

6 Conclusions and outlook

The availability of chiral selectors allowing for the effective and efficient separation of enantiomers remains limited. In contrast to the large datasets available from liquid/liquid and liquid/vapour equilibria, the amount of fundamental comprehensive data of solid/liquid equilibria and in particular of chiral systems is scarce. However, crystals of chiral compounds pose highly specific chiral selectors themselves, whose potential appears far from being exploited. The eminent lack of generic tools and fundamental knowledge in the field of solid/liquid equilibria and related multiphase correlation of chiral systems leaves the potential of selective crystallisation untouched.
Within the course of this work in total 24 chiral systems were analysed theoretically and practically attempting to identify a minima of characteristics necessary to assess the feasibility of the corresponding chiral separation. Besides others, a thermodynamic property was identified, whose purposeful variation opened up the way for a new crystallisation-based separation scheme. This property and corresponding schemes were evaluated together with descriptive thermodynamic tools on an experimental basis. The thesis in hand aims to assist in the identification of suitable separation modes involving enantioselective crystallisation for a given chiral system.

The experimental techniques included primarily the determination of relevant SLE by gravimetry, ATR-FTIR and HPLC and the measurement of the heats and temperatures of fusion by DSC. Solid phase transformations were analysed by XRPD.
Modifications of the Non Random Two Liquid g^E model (NRTL) and the COSMO-SAC models (Conductor-like Screening MOdel with the Segment Activity Coefficient approach) were implemented into scripts in order to describe and predict binary/ternary and quaternary SLE of chiral systems in solutions. For the latter model a non-commercial solvent database was used.

The thesis is divided into three main chapters according to three coherent aspects of the crystallisation-based separation of enantiomers.

Firstly, emphasis was spent on analysis techniques to follow the thermodynamic and kinetic development of chiral phase formations upon crystallisation from different SLE phase domains. Within a detailed case study the chiral compound Malic acid was investigated. The systematic study of the identified partial solid solutions allowed for the assessment of chiral separation procedures for this and related systems. An accompanying thermodynamic model for the description of partial solid solutions was proposed.

The consecutive chapter comprised the determination, analysis and model-based description of 12 chiral model and pharmaceutical compounds in solvents and solvent systems. The comprehensive studies revealed, that the composition of the eutectic composition of chiral systems can be shifted in solution in advantageous manner. Controlled shifts through purposeful variations in temperature and/or solvent (mixtures) disclosed new powerful strategies for the

chiral separation of enantiomers. A shortcut model approach allowed the prediction of shifts of the characteristic property for systems exhibiting no heterochiral interactions. Further, an extended model and an '*a priori*' approach for the description and estimation of shifts in the eutectic composition in various solvents were proposed and validated to some extend. Particular focus was set on the assessment of SLE models for chiral separation applications. The fourth chapter explained identified feasible tasks of recent correlative g^E and estimation models and summarised the conducted attempts to widen the field of applications of thermodynamic SLE models to chiral applications. The limits of the individual approaches considered are named and the developed model extensions beyond the state-of-the-art are discussed and compared to experimental data.

The preceding chapters provided the basis for conceptual studies on new crystallisation schemes and coupled modes of chiral separations, which were summarised in the fifth chapter. Quantitative relations between the shape of solubility isotherms, thermodynamic domains for successful selective crystallisations and the underlying activity coefficients of chiral solutes in solution supported the identification of the most promising crystallisation scheme to conduct.
A newly developed 2-step separation scheme, which exploits shifts in the eutectic composition, allows the purification of any asymmetric mixture of enantiomers irrespectively of the eutectic composition of the system. The scheme was evaluated first for the amino acid Methionine and further for the active pharmaceutical ingredient (API) Bicalutamide. The most promising separation for the API consisted of a hybrid process based on a pre-enrichment step using continuous counter-current chromatography (SMB) and a 2-step separation scheme using an antisolvent in the 2nd process step. The separation of the API at lab-scale was repeated successfully at pilot-plant scale providing even higher product purities.
The chromatographic step was optimised beforehand using a dynamic model. Selective adsorption of the two enantiomers was quantified through a peak fitting method. Optimal operating points of the SMB unit were derived using an equilibrium-dispersive model and nonlinear solvers. The coupling of the two processes revealed rather a plateau than a maximum with respect to the purity at the optimal interface between both processes. The conducted process validation was compared to a standalone chromatographic separation and further coupled processes. The proposed coupling mode exhibited clearly enhanced productivity and improved robustness. If the 2-step crystallisation process would be operated in a cyclic mode, even superior productivities with respect to all considered coupled processes are expected.
Specific characteristics of the quaternary SLE of Serine in aqueous methanol solution motivated a second coupled process of continuous chromatography and selective crystallisation. An enantioselective chromatographic separation method for Serine was identified, quantified and a case study involving the corresponding SMB was set up and optimised. Again, enhanced productivities and improved robustness can be expected for this process compared to a standard standalone batch chromatographic separation.

Outlook

The conducted studies leave space for follow-up research in various directions. Though, numerous poor crystallisation results reported can be assigned to the unknown presence of mixed crystals, the thermodynamic data of systems exhibiting solid solutions is scarce. Further,

in depth studies for *e. g.* Malic acid might assist in the identification of a common pattern for solid state formations of similar kind.

The fact, that the eutectic composition is invariant for a given thermodynamic state (constant: p,T,solvent) only, and may be varied by purposeful changes of this state, might motivate further research in this direction. The introduced 2-step process allows the efficient separation of complex chiral systems from any asymmetric mixture. Since slightly enriched mixtures are more frequently found after *e. g*. partial selective asymmetric synthesis, further process combinations involving, enzymes, membranes, partial asymmetric synthesis and others might be of interest to evaluate. The thermodynamic model framework provided might simplify the identification of promising chiral systems and solvents.

There is another unexploited area of preferential crystallisation in the context of the investigated 2-step processes. It is very likely, that kinetically driven crystallisations will enhance the specific yield compared to the thermodynamic separation studies in this work. Provided, sufficient kinetic data becomes available, the investigation of numerous powerful process variantions starting from the 1st or the 2nd process step might be an attractive field.

Another aspect, which was not fully covered in the thesis, consists in the purposeful option to use thermodynamic states and solvents in order to switch the solid state of a given compound back and forth. The resulting SLE and the corresponding shift in the eutectic composition will allow similar 2-step separations as studied in this work.

Bibliography

1. Ault, A., *The Nobel Prize in Chemistry for 2001*, J. Chem. Educ., **2002,** 79, (5), 572.
2. Pasteur, L., *Recherches sur les relation qui peuvent exister entre la forme crystalline e al composition chimique, et le sens de la polarisation rotatoire*, Ann. Chim. Phys., **1848,** (3), 442-459.
3. Fischer, E., *Ueber die Configuration des Traubenzuckers und seiner Isomeren. II*, Berichte der deutschen chemischen Gesellschaft, **1891,** 24, (2), 2683-2687.
4. Cross, L. C.; Klyne, W., *Rules for the nomenclature of organic chemistry*, Pure Appl. Chem., **1974,** 45, 11-30.
5. Moss, G. P., *Basic terminology of stereochemistry*, Pure Appl. Chem., **1996,** 68, (12), 2193-2222.
6. Stinson, S. C., *Chiral pharmaceuticals*, Chem. Eng. News., **2001,** (79), 56-61.
7. Stinson, S. C., *Chiral Drugs*, Chem. Eng. News., **2000,** (78), 55-78.
8. Caner, H.; Groner, E.; Levy, L.; Agranat, I., *Trends in the development of chiral drugs*, Drug Discov. Today, **2004,** 9, (3), 105-110.
9. Rouhi, A. M., *Chiral Chemistry*, Chem. Eng. News, **2004,** 82, (24), 47-62.
10. SDI/Verispan/VONA, *2009 Top 200 branded drugs by retail dollars*, Drug Topics, **2010,** 1-3.
11. *FDA's policy statement for the development of new stereoisomeric drugs*, Chirality, **1992,** 4, (5), 338-340.
12. Nunez, M. C.; Garcia-Rubino, M. E.; Conejo-Garcia, A.; Cruz-Lopez, O.; Kimatrai, M.; Gallo, M. A.; Espinosa, A.; Campos, J. M., *Homochiral Drugs: A Demanding Tendency of the Pharmaceutical Industry*, Curr. Med. Chem., **2009,** 16, 2064-2074.
13. Francotte, E.; Lindner, W.; Manhold, R.; Kubinyi, H.; Folkers, G., *Chirality in Drug research,* Manhold, R., Wiley-VCH, **2006**, Vol. 33.
14. Noorduin, W. L.; Meekes, H.; Bode, A. A. C.; van Enckevort, W. J. P.; Kaptein, B.; Kellogg, R. M.; Vlieg, E., *Explanation for the Emergence of a Single Chiral Solid State during Attrition-Enhanced Ostwald Ripening: Survival of the Fittest*, Cryst. Growth Des., **2008,** 8, (5), 1675-1681.
15. Aubin, E.; Petit, M. N.; Coquerel, G., *Resolution of the ethanolamine salt of (±)mandelic acid by using the AS3PC method: Principle, application and results*, J. Phys. IV France, **2004,** 122, 157-162.
16. Jacques, J.; Collet, A., *Enantiomers, Racemates, and Resolutions,* Krieger Publishing Company, **1994**.
17. McCrone, W., Polymorphism, In *Physics and Chemistry of the Organic Solid State*, ed. Fox, D., John Wiley & Sons Inc, **1965**, Vol. 2, 726-767.
18. Haleblian, J.; McCrone, W., *Pharmaceutical applications of polymorphism*, J. Pharm. Sci., **1969,** 58, (8), 911-929.
19. Bauer, J.; Spanton, S.; Henry, R.; Quick, J.; Dziki, W.; Porter, W.; Morris, J., *Ritonavir: An Extraordinary Example of Conformational Polymorphism*, Pharm. Res., **2001,** 18, (6), 859-866.
20. Jin, Y. S.; Ulrich, J., In proc. of 16th international workshop on industrial crystallization, *New Crystalline Solvates of Atorvastatin Calcim*, Lappenranta, ed. Louhi-Kultanen, M.; Hatakka, H., Lappenranta University of Technology, Lappenranta, **2009,** 45-52.
21. Gu, C.-H.; Jr, V. Y.; Grant, D. J. W., *Polymorph screening: Influence of solvents on the rate of solvent-mediated polymorphic transformation*, J. Pharm. Sci., **2001,** 90, (11), 1878-1890.
22. Burger, A.; Ramberger, R., *On the Polymorphism of Pharmaceuticals and Other Molecular Crystals. I*, Mikrochim. Acta, **1979,** (II), 259-271.
23. Roozeboom, H. W. B., *Löslichkeit und Schmelzpunkt als Kriterien für racemische Verbindungen, pseudoracemische Mischkristalle und inaktive Konglomerate*, Z. Phys. Chem. Stoechiom. Verwandtschafts., **1899,** 28, 494-517.

24. Marchand, P.; Lefebvre, L.; Querniard, F.; Cardinael, P.; Perez, G.; Counioux, J.-J.; Coquerel, G., *Diastereomeric resolution rationalized by phase diagrams under the actual conditions of the experimental process*, Tetrahedron: Asymmetry, **2004,** 15, (16), 2455-2465.
25. Chickos, J. S.; Hesse, D. G., *An experimental test of the double solubility rule*, Struct. Chem., **1991,** V2, (1), 33-40.
26. Meyerhoffer, W., *Stereochemische Notizen*, Ber. Dtsch. Chem. Ges., **1904,** 37, (3), 2604-2610.
27. Prausnitz, J. M.; Lichtenthaler, R. N.; de Azevedo, E. G., *Molecular Thermodynamics of Fluid-Phase Equilibria,* Amundson, N. R., P T R Prentice-Hall inc. , New Jersey, **1986**, 600.
28. Lewis, G. N.; Randall, M., *Thermodynamics,* Pitzer, K. S.; Brewer, L., McGraw-Hill Publications Inc., New York, **1961**.
29. Apelblat, A.; Manzurola, E., *Solubility of oxalic, malonic, succinic, adipic, maleic, malic, citric, and tartaric acids in water from 278.15 to 338.15 K*, J. Chem. Thermodyn., **1987,** 19, (3), 317-320.
30. Cong-Liang, Z.; Bao-Ying, L.; Yan, W., *Solubilities of norfloxacin in ethanol, 1-propanol, acetone, and chloroform from 294.15 to 318.15 K*, Can. J. Chem. Eng., **2009,** 88, (1), 63-66.
31. Prigogine, I.; Defay, R., *Chemical Thermodynamics,* Longmann, London, UK, **1973**.
32. Tabora, J. E.; Corry, J.; Osifchin, R.; Lepore, J. V.; Davidson, O. A.; Thien, M. P., *Identification and characterization of an anomalous racemate*, Fluid Phase Equilibria, **2007,** 258, (2), 140-147.
33. Worlitschek, J.; Bosco, M.; Huber, M.; Gramlich, V.; Mazzotti, M., *Solid-Liquid Equilibrium of Tröger´s Base Enantiomers in Ethanol: Experiments and Modelling*, Helv. Chim. Acta, **2004,** 87, 279-291.
34. Lorenz, H.; Seidel-Morgenstern, A., *Binary and ternary phase diagrams of two enantiomers in solvent systems*, Thermochim. Acta, **2002,** (382), 129-142.
35. Wang, Y.; LoBrutto, R.; Wenslow, R. W.; Santos, I., *Eutectic Composition of a Chiral Mixture Containing a Racemic Compound*, Org. Proc. Res. Dev., **2005,** 9, (5), 670-676.
36. Klussmann, M.; White, A. J. R.; Armstrong, A.; Blackmond, D. G., *Rationalization and prediction of solution enantiomeric excess in ternary phase systems*, Angew. Chem. Int. Ed. , **2006,** 45, (47), 7985-7989.
37. Kaemmerer, H.; Polenske, D.; Lorenz, H.; Seidel-Morgenstern, A., In proc. of 15th international workshop on industrial crystallization, *Selection and application of chiral resolution strategies for compound forming systems on the basis of solubility isotherms*, Magdeburg, ed. Lorenz, H.; Kaemmerer, H., Shaker, Magdeburg, **2008** 42-49.
38. McNaught, A. D.; Wilkinson, A., *IUPAC. Compendium of Chemical Terminology-The 'Gold Book',* Blackwell Scientific Publications, Oxford, **1997**.
39. Nordström, F. L.; Rasmuson, Å. C., *Phase equilibria and thermodynamics of hydroxybenzoic acid*, Journal of Pharmaceutical Sciences, **2006,** 95, (4), 748--760.
40. O'Connell, J. P.; Haile, J. M., *Thermodynamics-Fundamentals for Applications,* Cambridge University Press, Cambridge, **2005**, Vol. 1.
41. Chau-Chyun, C.; Paul, M. M., *Applied thermodynamics for process modeling*, AIChE J., **2002,** 48, (2), 194-200.
42. Feelly, R.; Gabriele, S., *Modeling the solubility of pharmaceuticals in pure solvents and solvent mixtures for drug process design*, J. Pharm. Sc., **2009,** 98, (11), 4205-4215.
43. Onken, U.; Fischer, K.; Rarey, J.; Kleiber, M., *Ullmann's Encyclopedia of Industrial Chemistry-Estimation of Physical Properties,* Wiley VCH, **2008**.
44. Sandler, S. I., *Chemical, Biochemical, and Engineering Thermodynamics,* Sandler, S. I., John Wiley & Sons, Inc, **2006**.
45. Klamt, A., *COSMO-RS From Quantum Chemistry to Fluid Phase Thermodynamics and Drug Design,* Elsevier, Amsterdam, **2005**.
46. Barton, A. F. M., *Solubility parameters*, Chem. Rev., **1975,** 75, (6), 731-753.
47. Sanchez, I. C.; Truskett, T. M., *Configurational Properties and Corresponding States in Simple Fluids and Water*, J. Phys. Chem. B, **1999,** 103, (24), 5106-5116.
48. Wilson, G. M.; Deal, C. H., *Activity Coefficients and Molecular Structure. Activity Coefficients in Changing Environments-Solutions of Groups*, Ind. Eng. Chem. Fundam., **1962,** 1, (1), 20-23.
49. Renon, H.; Prausnitz, J. M., *Local compositions in thermodynamic excess functions for liquid mixtures*, AIChE Journal, **1968,** 14, (1), 135-144.

50. Wu, D.-W.; Cui, Y.; Donohue, M. D., *Local Composition Models for Lattice Mixtures*, Ind. Eng. Chem. Res., **1998,** 37, (8), 2936-2946.
51. Stavermann, A. J., Rec. Trac. Chim. Pays-Bas, **1950,** 69, (163).
52. Guggenheim, E. A., *Mixtures,* Oxford University Press, Oxford, **1952**.
53. Fredenslund, A.; Jones, R. L.; Prausnitz, J. M., *Group-contribution estimation of activity coefficients in nonideal liquid mixtures*, AIChE J., **1975,** 21, (6), 1086-1099.
54. Chen, C.-C., *A segment-based local composition model for the gibbs energy of polymer solutions*, Fluid Phase Equilib., **1993,** 83, 301-312.
55. Chen, C. C.; Crafts, P. A., *Correlation and Prediction of Drug Molecule Solubility in Mixed Solvent Systems with the Nonrandom Two-Liquid Segment Activity Coefficient (NRTL–SAC) Model*, Ind. Eng. Chem. Res., **2006,** 45, (13), 4816-4824.
56. Chen, C. C.; Song, Y., *Solubility Modeling with a Nonrandom Two-Liquid Segment Activity Coefficient Model*, Ind. Eng. Chem. Res., **2004,** 43, (26), 8354-8362.
57. Chau-Chyun Chen, Y. S., *Generalized electrolyte-NRTL model for mixed-solvent electrolyte systems*, AIChE Journal, **2004,** 50, (8), 1928-1941.
58. Wang, S.; Song, Y.; Chen, C.-C., *Extension of COSMO-SAC Solvation Model for Electrolytes*, Ind. Eng. Chem. Res., **2011,** 50, (1), 176-187.
59. Simoni, L. D.; Lin, Y.; Brennecke, J. F.; Stadtherr, M. A., *Modeling Liquid-Liquid Equilibrium of Ionic Liquid Systems with NRTL, Electrolyte-NRTL, and UNIQUAC*, Ind. Eng. Chem. Res., **2008,** 47, (1), 256-272.
60. Gross, J.; Sadowski, G., *Perturbed-chain SAFT: An equation of state based on a perturbation theory for chain molecules*, Ind. Eng. Chem. Res., **2001,** 40, (4), 1244-1260.
61. Tumakaka, F.; Prikhod'ko, I. V.; Sadowski, G., *Modeling of solid-liquid equilibria for systems with solid complex phase formation*, Fluid phase equilibria, **2007,** 260, 98-104.
62. Prikhod'ko, I. V.; F., T., *Application of the PC-SAFT Equation of State to Modeling of Solid-Liquid Equilibria in Systems with Organic Components Forming Chemical Compounds*, Russian Journal of Applied Chemistry, **2007,** 80, (4), 542-548.
63. Scatchard, G., *Equilibria in Non-electrolyte Solutions in Relation to the Vapor Pressures and Densities of the Components*, Chem. Rev., **1931,** 8, (2), 321-333.
64. Poling, B. E.; Prausnitz, J. M.; O'Connell, J. P., *The Properties of Gases and Liquids* Mcgraw-Hill Professional, **2000**, 768.
65. Abbott, S.; Hansen, C. M., *Hansen Solubility Parameters in Practice - Complete with software, data, and examples,* Hansen, C. M., CRC Press, **2010**.
66. Lucas, K., *Molecular Models for Fluids,* Cambridge University Press, Aachen, **2007**, Vol. 1, 838.
67. Hinchliffe, A., *Molecular Modelling for Beginners,* Wiley, Manchester, **2008**, Vol. 1, 405.
68. Born, M.; Oppenheimer, R., *Zur Quantentheorie der Molekeln*, Ann. Phys., **1927,** 389, (20), 457-484.
69. Koch, W.; Holthausen, M. C., *A Chemist's Guide to Density Functional Theory,* Wiley-VCH, Weinheim/Germany, **2002**.
70. Klamt, A., *Conductor-like Screening Model for Real Solvents: A New Approach to the Quantitative Calculation of Solvation Phenomena*, J. Phys. Chem., **1995,** 99, (7), 2224-2235.
71. Spuhl, O., Doctoral thesis: *Anwendung quantenchemischer Methoden in der Thermodynamik der Stofftrennung,* Friedrich Alexander University of Erlangen-Nürnberg, Erlangen-Nürnberg, **2006**.
72. Mu, T.; Rarey, J.; Gmehling, J., *Group contribution prediction of surface charge density distribution of molecules for COSMO-SAC*, AIChE J., **2009,** 55, (12), 3298-3300.
73. Mu, T.; Rarey, J.; Gmehling, J., *Group contribution prediction of surface charge density profiles for COSMO-RS(Ol)*, AIChE J., **2007,** 53, (12), 3231-3240.
74. Wang, S.; Lin, S.-T.; Watanasiri, S.; Chen, C.-C., *Use of GAMESS/COSMO program in support of COSMO-SAC model applications in phase equilibrium prediction calculations*, Fluid Phase Equilib., **2009,** 276, (1), 37-45.
75. Mullins, E.; Liu, Y. A.; Ghaderi, A.; Fast, S. D., *Sigma Profile Database for Predicting Solid Solubility in Pure and Mixed Solvent Mixtures for Organic Pharmacological Compounds with COSMO-Based Thermodynamic Methods*, Ind. Eng. Chem. Res., **2008,** 47, (5), 1707-1725.
76. Lin, S. T.; Sandler, S. I., *A Priori Phase Equilibrium Prediction from a Segment Contribution Solvation Model*, Ind. Eng. Chem. Res., **2002,** 41, (5), 899-913.
77. Wang, S.; Sandler, S. I.; Chen, C. C., *Refinement of COSMO-SAC and the Applications*, Ind. Eng. Chem. Res., **2007,** 46, (22), 7275-7288.

78. Lin, S. T.; Chang, J.; Wang, S.; Goddard, W. A.; Sandler, S. I., *Prediction of Vapor Pressures and Enthalpies of Vaporization Using a COSMO Solvation Model*, J. Phys. Chem. A, **2004,** 108, (36), 7429-7439.
79. Wang, S.; Lin, S.-T.; Chang, J.; Goddard, W. A.; Sandler, S. I., *Application of the COSMO-SAC-BP Solvation Model to Predictions of Normal Boiling Temperatures for Environmentally Significant Substances*, Ind. Eng. Chem. Res., **2006,** 45, (16), 5426-5434.
80. Banerjee, T.; Sahoo, R. K.; Rath, S. S.; Kumar, R.; Khanna, A., *Multicomponent Liquid-Liquid Equilibria Prediction for Aromatic Extraction Systems Using COSMO-RS*, Ind. Eng. Chem. Res., **2007,** 46, (4), 1292-1304.
81. Zhao, L.; Yalkowsky, S. H., *A Combined Group Contribution and Molecular Geometry Approach for Predicting Melting Points of Aliphatic Compounds*, Ind. Eng. Chem. Res., **1999,** 38, (9), 3581-3584.
82. Joback, K. G.; Reid, R. C., *Estimation of pure component properties from group-contributions*, Chem. Eng. Commun., **1987,** 57, (1), 233-243.
83. Fuchs, D.; Fischer, J.; Tumakaka, F.; Sadowski, G., *Solubility of amino acids: Influence of the pH value and the addition of alcoholic cosolvents on aqueous solubility*, Ind. Eng. Chem. Res., **2006,** 45, (19), 6578-6584.
84. Mullin, J. W., *Crystallization,* 3rd, Butterworth-Heinemann, Oxford, **1997**.
85. Kashchiev, D., *Nucleation: Basic Theory with Applications,* Butterworth Heinemann, **2000**.
86. Roth, K., *Polymorphie: Fast ein kristallographisches Wintermärchen*, Chem. unserer Zeit, **2006,** 40, (6), 398-406.
87. Nyvlt, J.; Söhnel, O.; Matuchova, M.; Broul, M., *The Kinetics of Industrial Crystallizations,* Elsevier, Amsterdam, **1985**, 68, 284.
88. Perlberg, A.; Lorenz, H.; Seidel-Morgenstern, A., *Crystal Growth Kinetics via Isothermal Seeded Batch Crystallization: Evaluation of Measurement Techniques and Application to Mandelic Acid in Water*, Ind. Eng. Chem. Res., **2005,** 44, (4), 1012-1020.
89. Polenske, D.; Lorenz, H., *Solubility and Metastable Zone Width of the Methionine Enantiomers and Their Mixtures in Water*, J. Chem. Eng. Data, **2009,** 54, (8), 2277-2280.
90. Kaemmerer, H.; Lorenz, H.; Black, S. N.; Seidel-Morgenstern, A., *Study of System Thermodynamics and the Feasibility of Chiral Resolution of the Polymorphic System of Malic Acid Enantiomers and Its Partial Solid Solutions*, Cryst. Growth Des. , **2009,** 9, (4), 1851-1862
91. Wang, X.; Yang, X.; Liu, Y.; Ching, C. B., *Intrinsic MSZW characteristics of racemic species: Implication for chiral crystallization*, AlChE J., **2008,** 54, (9), 2281-2292.
92. Chen, A. M.; Wang, Y.; Wenslow, R. M., *Purification of Partially Resolved Enantiomeric Mixtures with the Guidance of Ternary Phase Diagram*, Org. Process Res. Dev., **2008,** 12, (2), 271-281.
93. Wang, Y.; Chen, A. M., *Enantioenrichment by Crystallization*, Org. Proc. Res. Dev., **2008,** 12, (2), 282-290.
94. Lin, S. W.; Ng, K. M.; Wibowo, C., *Synthesis of crystallization processes for systems involving solid solutions*, Comput. Chem. Eng., **2008,** 32, (4-5), 956-970.
95. Harada, K., *Optical resolution of monoammonium DL-Malate by preferential crystallisation*, Chem and Ind Com., **1986,** 68+69.
96. Beilles, S.; Cardinael, P.; Ndzié, E.; Petit, S.; Coquerel, G., *Preferential crystallisation and comparative crystal growth study between pure enantiomer and racemic mixture of a chiral molecule: 5-ethyl-5-methylhydantoin*, Chem. Eng. Sci., **2001,** (56), 2281-2294.
97. Elsner, M. P.; Menéndez, D. F.; Muslera, E. A.; Seidel-Morgenstern, A., *Experimental study and simplified mathematical description of preferential chrystallization*, Chirality, **2005,** (17), 183-195.
98. Rodrigo, A. A.; Lorenz, H.; Seidel-Morgenstern, A., *Online monitoring of preferential crystallization of enantiomers*, Chirality, **2004,** (16), 499-508.
99. Polenske, D.; Lorenz, H.; Seidel-Morgenstern, A., *Separation of Propranolol Hydrochloride Enantiomers by Preferential Crystallization: Thermodynamic Basis and Experimental Verification*, Cryst. Growth Des., **2007,** 7, (9), 1628-1634.
100. Czapla, F.; Lorenz, H.; Seidel-Morgenstern, A., *Modellierung und Vergleich von polythermen autoseeded Prozessvarianten der Bevorzugten Kristallisation*, Chem. Ing. Tech., **2009,** 81, (6), 1-11.

101. Yamanari, K.; Akira, F., *Temperature-dependent conglomerate crystallization of carbonatobis(ethylenediamine)cobalt(III) bromide and its application to kinetic optical resolution*, J. Chem. Soc., Dalton Trans, **1991,** 2903-2905.
102. Levkin, P. A.; Schweda, E.; Kolb, H.-J.; Schurig, V.; Kostyanovsky, R. G., *Solid-phase racemic compound-conglomerate transformation of 2,3:6,7-dibenzobicyclo[3.3.1]nona-2,6-diene-4,8-dione*, Tetrahedron: Asymmetry, **2004,** 15, (9), 1445-1450.
103. Kuhnert-Brandstätter, M.; Ulmer, R.; Langhammer, L., *Thermoanalytische Untersuchungen an Mentholen*, Arch. Pharm., **1974,** 307, (7), 497-503.
104. Beckmann, W.; Lorenz, H., *Partial miscibility of organic compounds in the solid state- the case of two epimers of a diastereoisomer*, Chem. Eng. Technol., **2006,** (29), 226-232.
105. Wermester, N.; Aubin, E.; Pauchet, M.; Coste, S.; Coquerel, G., *Preferential crystallization in an unusual case of conglomerate with partial solid solutions*, Tetrahedron-Asymmetry, **2007,** 18, (7), 821-831.
106. Huang, J.; Chen, S.; Guzei, I. A.; Yu, L., *Discovery of a solid solution of enantiomers in a racemate-forming system by seeding*, Journal of the American Chemical Society, **2006,** 128, (36), 11985-11992.
107. Guiochon, G.; Felinger, A.; Shirazi, D. G.; Katti, A. M., *Fundamentals of Preparative and Nonlinear Chromatography,* Academic Press, Boston, **2006**.
108. Guiochon, G., *Modeling for Preparative Chromatography*, Elsevier, Amsterdam, **2003**.
109. Snyder, L. R.; Kirkland, J. J., *Introduction to Modern Liquid Chromatography,* Wiley VCH, **1979**, 896.
110. van Deemter, J. J.; Zuiderweg, F. J.; Klinkenberg, A., *Longitudinal diffusion and resistance to mass transfer as causes of nonideality in chromatography*, Chem. Eng. Sc., **1956,** 5, (6), 271-289.
111. Schmidt-Traub, H., *Preparative Chromatography of Fine Chemicals and Pharmaceutical Agents,* WILEY VCH, Weinheim, **2005**.
112. Pais, L. S.; Loureiro, J. M.; Rodrigues, A. E., *Separation of enantiomers of a chiral epoxide by simulated moving bed chromatography*, J. Chromatogr. A, **1998,** 827, (2), 215-233.
113. Mihlbachler, K.; Kaczmarski, K.; Seidel-Morgenstern, A.; Guiochon, G., *Measurement and modeling of the equilibrium behavior of the Tröger's base enantiomers on an amylose-based chiral stationary phase*, J. Chrom. A, **2002,** 955, (1), 35-52.
114. Petrusevska, K.; Kuznetsov, M. A.; Gedicke, K.; Meshko, V.; Staroverov, S. M.; Seidel-Morgenstern, A., *Chromatographic enantioseparation of amino acids using a new chiral stationary phase based on a macrocyclic glycopeptide antibiotic*, J. Sep. Sc., **2006,** 29, (10), 1447-1457.
115. Seidel-Morgenstern, A., *Experimental determination of single solute and competitive adsorption isotherms*, J. Chromatogr. A, **2004,** 1037, (1-2), 255-272.
116. Sainio, T.; Kaspereit, M., *Analysis of steady state recycling chromatography using equilibrium theory*, Sep. Purif. Technol., **2009,** 66, (1), 9-18.
117. Grill, C. M.; Miller, L., *Separation of a racemic pharmaceutical intermediate using closed-loop steady state recycling*, J. Chromatogr. A, **1998,** 827, (2), 359-371.
118. Siitonen, J.; Sainio, T.; Kaspereit, M., *Theoretical analysis of steady state recycling chromatography with solvent removal*, Sep. Purif. Technol., **2011,** 78, (1), 21-32.
119. Zhang, L.; Gedicke, K.; Kuznetsov, M. A.; Staroverov, S. M.; Seidel-Morgenstern, A., *Application of an eremomycin-chiral stationary phase for the separation of dl-methionine using simulated moving bed technology*, J. Chromatogr. A, **2007,** 1162, (1), 90-96.
120. Keßler, L. C., Doctoral thesis: *Enhancing the Potential of Simulated Moving Bed Chromatography,* Otto-von-Guericke-University Magdeburg, Magdeburg/Germany, **2009**.
121. Mazzotti, M.; Storti, G.; Morbidelli, M., *Optimal operation of simulated moving bed units for nonlinear chromatographic separations*, J. Chromatogr. A, **1997,** 769, (1), 3-24.
122. Storti, G.; Mazzotti, M.; Morbidelli, M.; Carra, S., *Robust design of binary countercurrent adsorption separation processes*, AIChE J., **1993,** 39, 471-492.
123. Kaspereit, M.; Gedicke, K.; Zahn, V.; Mahoney, A. W.; Seidel-Morgenstern, A., *Shortcut method for evaluation and design of a hybrid process for enantioseparations*, J. of Chrom. A, **2005,** 1092, (1), 43-54.
124. Kaspereit, M.; Seidel-Morgenstern, A.; Kienle, A., *Design of simulated moving bed processes under reduced purity requirements*, Journal of Chromatography A, **2007,** 1162, (1), 2-13.

125. Gedicke, K.; Kaspereit, M.; Beckmann, W.; Budde, U.; Lorenz, H.; Seidel-Morgenstern, A., *Conceptual Design and Feasibility Study of Combining Continuous Chromatography and Crystallization for Stereoisomer Separations*, Chem. Eng. Res. Des., **2007,** 85, (7), 928-936.
126. Amanullah, M.; Mazzotti, M., *Optimization of a hybrid chromatography-crystallization process for the separation of Tröger's base enantiomers*, Journal of Chromatography A, **2006,** 1107, (1-2), 36-45.
127. Kaspereit, M., Doctoral thesis: *Separation of Enantiomers by a Process Combination of Chromatography and Crystallisation,* Otto-von-Guericke-University, Magdeburg, **2006**.
128. Wibowo, C.; O'Young, L., *A hybrid route to chiral pure products*, Chem. Eng. Prog., **2005,** 11, 22-27.
129. Francotte, E. R., *Application of simulated moving-bed chromatography to the separation of the enantiomers of chiral drugs*, J. Chromatogr. A, **1997,** (769), 101--107.
130. Takahashi, H.; Tamura, R.; Fujimoto, D.; Lepp, Z.; Kobayashi, R.; Ushio, T., *Preferential Enrichment: Full Crystallographiy Analysis of the unusual Phenomenon in the mixed Crystal' Version*, Chirality, **2002,** 14, 541--547.
131. Anandamanoharan, P. R.; Cains, P. W.; Jones, A. G., *Separability of diastereomer salt pairs of 1-phenylethylamine with enantiomeric 2-substituted phenylacetic acids by fractional crystallization, and its relation to physical and phase properties*, Tetrahedron: Asymmetry, **2006,** 17, (12), 1867-1874.
132. Coquerel, G., *Thermodynamic Predictions of Physical Properties - Prediction of Solid Solutions in Molecular Solutes Exhibiting Polymorphism*, Chem. Eng. Technol., **2006,** 29, (2), 182-186.
133. Renou, L.; Morelli, T.; Coste, S.; Petit, M. N.; Berton, B.; Malandain, J. J.; Coquerel, G., *Chiral Discrimination at the Solid State of Methyl 2-(Diphenylmethylsulfinyl)acetate*, Cryst. Growth Des., **2007,** 7, (9), 1599-1607.
134. Kuhnert-Brandstätter, M.; Friedl, L., *Zur Frage der Existenz anomaler Racemate*, Mikrochim. Acta, **1977,** (II), 507-516.
135. Ceolin, R.; Szwarc, H.; Lepage, F., *On the Dimorphism of DL-malic acid*, Thermochim. Acta, **1990,** (158), 347-352.
136. Andersson, M.; Fredga, A., *Anomalous Racemates of malic acid*, Acta Chem. Scand., **1966,** 20, 1060-1063.
137. Kaemmerer, H.; Lorenz, H.; Seidel-Morgenstern, A., In proc. of 13th International Workshop on Industrial Crystallization, *Study of solubility equilibria in the chiral malic acid system*, Delft, ed. IOS Press, Delft, **2006,**
138. Giron, D., *Investigations of Polymorphism and Pseudo-polymorphism in Pharmaceuticals by Combined Thermoanalytical Techniques*, J, Therm. Anal. Calorim., **2001,** 64, (1), 37-60.
139. Tôke, L.; Âcs, M.; Fogassy, E.; Faigl, F.; Gâl, S.; Sztatisz, J., *A new Anomalous Racemate*, Acta Chimica Academiae Scientiarum Hungaricae, **1979,** 102, (1), 59-65.
140. Slaughter, D. W.; Doherty, M. F., *Calculation of solid-liquid equilibrium and crystallization paths for melt crystallization processes*, Chem. Eng. Sc., **1995,** 50, (11), 1679-1694.
141. Etter, M. C., *Encoding and decoding hydrogen-bond patterns of organic compounds*, Acc. Chem. Res., **1990,** 23, (4), 120-126.
142. Clair, S.; Pons, S.; Seitsonen, A. P.; Brune, H.; Kern, K.; Barth, J. V., *STM Study of Terephthalic Acid Self-Assembly on Au(111): Hydrogen-Bonded Sheets on an Inhomogeneous Substrate*, J. Phys. Chem. B, **2004,** 108, (38), 14585-14590.
143. Fjaer, H.; Samuelsen, E. J., *Order-disorder in the linear chain structure of terephthalic acid, studied by Raman scattering*, Journal of Physics C: Solid State Physics, **1986,** 19, (30), 5945-5956.
144. Srinivasa Gopalan, R.; Kumaradhas, P.; Kulkarni, G. U.; Rao, C. N. R., *An experimental charge density study of aliphatic dicarboxylic acids*, J. Mol. Struct., **2000,** 521, (1-3), 97-106.
145. Allen, F., *The Cambridge Structural Database: a quarter of a million crystal structures and rising*, Acta Crystallogr. Sect. B: Struc. Sci., **2002,** 58, (3 Part 1), 380-388.
146. Lorenz, H.; Polenske, D.; Seidel-Morgenstern, A., *Application of preferential crystallization to resolve racemic compounds in a hybrid process*, Chirality, **2006,** 18, (10), 828-840.
147. Sapoundjiev, D.; Lorenz, H.; Seidel-Morgenstern, A., *Solubility of Chiral Threonine Species in Water/Ethanol Mixtures*, J. Chem. Eng. Data, **2006,** 51, (5), 1562-1566.
148. Held, C.; Cameretti, L. F.; Sadowski, G., *Measuring and Modeling Activity Coefficients in Aqueous Amino-Acid Solutions*, Ind. Eng. Chem. Res., **2010**.

149. Marrero, J.; Gani, R., *Group-contribution based estimation of pure component properties*, Fluid Phase Equilib. , **2001,** 183, 183-208.
150. Kaemmerer, H.; Tulashie, S. K.; Lorenz, H.; Seidel-Morgenstern, A., *Solid Liquid Phase Equilibria of N-Methylephedrine Enantiomers in Two Chiral Solvents*, J. Chem. Eng. Data, **2010,** 55, (3), 1131-1136.
151. Held, C.; Cameretti, L. F.; Sadowski, G., *Measuring and Modeling Activity Coefficients in Aqueous Amino-Acid Solutions*, Ind. Eng. Chem. Res., **2011,** 50, (1), 131-141.
152. Wishart, D. S.; Knox, C.; Guo, A. C.; Cheng, D.; Shrivastava, S.; Tzur, D.; Gautam, B.; Hassanali, M., *DrugBank: a knowledge base for drugs, drug actions and drug targets*, Nucl. Acids Res., **2008,** 36, (suppl_1), D901-906.
153. Weast, R. C., *CRC Handbook of Chemistry and Physics,* Weast, R. C., CRC Press, Boca Raton, USA, **1981**.
154. Lorenz, H.; Sapoundjiev, D.; Seidel-Morgenstern, A., *Enantiomeric Mandelic Acid System Melting Point Phase Diagram and Solubility in Water*, J. Chem. Eng. Data, **2002,** 47, (5), 1280-1284.
155. Profir, V. M.; Rasmussen, Å. C., *Influence of Solvent and the operating conditions on the Crystallization of racemic mandelic acid*, Cryst. Growth Des., **2004,** (4,2), 315-323.
156. Tulashie, S. K., Doctoral thesis: *The Potential of Chiral Solvents in Enantioselective Crystallization,* Otto-von-Guericke University, Magdeburg, **2010**.
157. Lorenz, H.; Seidel-Morgenstern, A., *A contribution to the mandelic acid phase diagram*, Thermochim. Acta, **2004,** 415, (1-2), 55-61.
158. Profir, V. M.; Furusjo, E.; Danielsson, L.-G.; Rasmuson, A. C., *Study of the Crystallization of Mandelic Acid in Water Using in Situ ATR-IR Spectroscopy*, Cryst. Growth Des., **2002,** 2, (4), 273-279.
159. Polenske, D.; Lorenz, H.; Seidel-Morgenstern, A., *The binary phase diagram of propranolol hydrochloride and crystallization-based enantioseparation*, J. Pharm. Sc., **2010,** 99, (4), 1762-1773.
160. Wang, X.; Wang, X. J.; Ching, C. B., *Solubility, Metastable Zone Width, and Racemic Characterization of Propranolol Hydrochloride*, Chirality, **2002,** 14, 318-324.
161. Dalton, J. B.; Schmidt, C. L. A., *The solubilities of certain amino acids and related compounds in water, the densities of their solutions at twenty-five degree, and the caluclated heats of solutionand partial molal volumes. II*, J. Biol. Chem., **1935,** 109, (1), 241-248.
162. Seyfi, S.; Pazuki, G.; Aghamiri, S. F.; Beheshti, M., *On the prediction of equilibrium phase behavior of amino acids in aqueous and aqueous-electrolyte solutions using SAFT equation of state*, Fluid Phase Equilib., **2009,** 287, (1), 15-22.
163. Ferreira, L. A.; Breil, M. P.; Pinho, S. P.; Macedo, E. A.; Mollerup, J. M., *Thermodynamic Modeling of Several Aqueous Alkanol Solutions Containing Amino Acids with the Perturbed-Chain Statistical Associated Fluid Theory Equation of State*, Ind. Eng. Chem. Res., **2009,** 48, (11), 5498-5505.
164. Held, C.; Cameretti, L. F.; Sadowski, G., *Measuring and Modeling Activity Coefficients in Aqueous Amino-Acid Solutions*, Ind. Eng. Chem. Res., **2010,** (DOI: 10.1021/ie100088c).
165. Luk, C.-w. J.; Rousseau, R. W., *Solubilities of and Transformations between the Anhydrous and Hydrated Forms of l-Serine in Water-Methanol Solutions*, Cryst. Growth Des., **2006,** 6, (8), 1808-1812.
166. Hayashi, Y.; Matsuzawa, M.; Yamaguchi, J.; Yonehara, S.; Matsumoto, Y.; Shoji, M.; Hashizume, D.; Koshino, H., *Large Nonlinear Effect Observed in the Enantiomeric Excess of Proline in Solution and That in the Solid State*, Angew. Chem., **2006,** 118, (28), 4709-4713.
167. Klussmann, M.; Iwamura, H.; Mathew, S. P.; Wells, D. H.; Pandya, U.; Armstrong, A.; Blackmond, D. G., *Thermodynamic control of asymmetric amplification in amino acid catalysis*, Nature, **2006,** 441, (7093), 621-623.
168. Le Minh, T.; von Langermann, J.; Lorenz, H.; Seidel-Morgenstern, A., *Enantiomeric 3-chloromandelic acid system: Binary melting point phase diagram, ternary solubility phase diagrams and polymorphism*, J. Pharm. Sci., 99, (9), 4084-4095.
169. Zhang, Y.; Ray, A.; Rohani, S., *Measurement and prediction of phase diagrams of the enantiomeric 3-chloromandelic acid system*, Chem. Eng. Sci., **2009,** 64, (2), 192-197.
170. Joshi, M. S.-M., A.; Kremling, A., , *Exploiting the bootstrap method for quantifying parameter confidence intervals in dynamical systems.*, Metab. Eng., **2006,** 8, (5), 447-455.

171. Czapla, F. H., H.; Elsner, M. P.; Lorenz, H.; Seidel-Morgenstern, A., , *Parameterization of population balance models for polythermal auto seeded preferential crystallization of enantiomers.* , Chem. Eng. Sc., **2009,** 64, (4), 753-763.
172. Haida, H.; Kaemmerer, H.; Lorenz, H.; Seidel-Morgenstern, A., *Estimation of Reliable Parameters for Solid-Liquid Equilibrium Description of Chiral Systems*, Chem. Eng. Tech., **2010,** 33, (5), 767-774.
173. Mullins, P. E., Master thesis: *Application of COSMO-SAC to Solid Solubility in pure and Mixed Solvent Mixtures for Organic Pharmacological Compounds,* Virginia State University, Blacksburg, Virginia, **2007**.
174. Wang, S.; Stubbs, J. M.; Siepmann, J. I.; Sandler, S. I., *Effects of Conformational Distributions on Sigma Profiles in COSMO Theories*, J. Phys. Chem. A, **2005,** 109, (49), 11285-11294.
175. Oldland, R. J., Doctoral thesis: *Predicting Phase equilibria using COSMO-based thermodynamic models and the VT-2004-Sigma Profile Database,* Virginia Polytechnic Institute and State University, Blacksburg, **2004**.
176. Oldland, R.; Mullins, E.; Liu, Y. A.; Wang, S.; Sandler, S. I.; Chen, C. C.; Zwolak, M.; Seavey, K., Online ressources http://www.design.che.vt.edu/VT-Databases.html: 'Sigma-average.exe', 'COSMO-SAC-VT-2005.exe', In Virginia Polytechnic Institute and State University: 2005.
177. Bustamante, P.; Ochoa, R.; Reillo, A.; Escalera, J. B., *Chameleonic effect of sulfanilamide and sulfamethazine in solvent mixtures. Solubility curves with two maxima.*, Chem. Pharm. Bull, **1994,** 42, 1129-1133.
178. Jouyban-Gharamaleki, A.; Romero, S.; Bustamante, P.; Clark, B. J., *Multiple Solubility Maxima of Oxolinic Acid in Mixed Solvents and a New Extension of Hildebrand Solubility Approach*, Chem. Pharm. Bull, **2000,** 2, 175-178.
179. Peña, M. A.; Reíllo, A.; Escalera, B.; Bustamante, P., *Solubility parameter of drugs for predicting the solubility profile type within a wide polarity range in solvent mixtures*, Int. J. Pharm., **2006,** 321, (1-2), 155-161.
180. Romero, S.; Reillo, A.; Escalera, B.; Bustamante, P., *The Behavior of Paracetamol in Mixtures of Amphiprotic and Amphiprotic-Aprotic Solvents. Relationship of Solubility Curves to Specific and Nonspecific Interactions*, Chem. Pharm. Bull., **1996,** 44, (5), 1061-1064.
181. Hsieh, C.-M.; Wang, S.; Lin, S.-T.; Sandler, S. I., *A Predictive Model for the Solubility and Octanol-Water Partition Coefficient of Pharmaceuticals*, Chem. Eng. Data, **2011,** 56, (4), 936-945.
182. Shu, C.-C.; Lin, S.-T., *Prediction of Drug Solubility in Mixed Solvent Systems Using the COSMO-SAC Activity Coefficient Model*, Ind. Eng. Chem. Res., **2011,** 50, (1), 142-147.
183. National Institute of Standards and Technology (NIST) Online Database, In U.S. Secretary of Commerce: 2009.
184. Vega, D. R.; Polla, G.; Martinez, A.; Mendioroz, E.; Reinoso, M., *Conformational polymorphism in bicalutamide*, Int. J. Pharm. , **2007,** 328, (2), 112-118.
185. Römpp Thieme Chemistry Online, **2007**
186. Kaemmerer, H.; Lorenz, H.; Seidel-Morgenstern, A., *Alternatives Verfahren zur Racemattrennung verbindungsbildender Systeme mittels Kristallisation*, Chem. Ing. Tech., **2009,** 81, (12), 1955-1965.
187. Tulashie, S. K.; Kaemmerer, H.; Lorenz, H.; Seidel-Morgenstern, A., *Solid Liquid Equilibria of Mandelic Acid Enantiomers in Two Chiral Solvents: Experimental Determination and Model Correlation*, J. Chem. Eng. Data, **2010,** 55, (1), 333-340.
188. Płoszaj, E., Master thesis: *Separation of pharmacologically active substances by means of crystallization,* Rzeszów (Poland), **2008**.
189. Harrison, W. A. T.; Yathirajan, H. S.; Bindya, S.; Anilkumr, H. G.; Devaraju, *Escitalopram oxalate: co-existence of oxalate dianions and oxalic acid molecules in the same crystal*, Acta Cryst. Sect. C: Cryst. Struct. Commun., **2007,** 63, (2), o129-o131.
190. Kaemmerer, H.; Jones, M. J.; Lorenz, H.; Seidel-Morgenstern, A., *Selective crystallisation of a chiral compound-forming system--Solvent screening, SLE determination and process design*, Fluid Phase Equilib., **2010,** 296, (2), 192-205.
191. Levilain, G.; Tauvel, G.; Coquerel, G., In proc. of BIWIC, *How homogenous equilibria between solvated enantiomers can modify the stable and metastable heterogenous equilibria*, Delft (NL), ed. Jansens, J. P.; ter Horst, J. H.; Jiang, S., IOS Press, Delft (NL), **2006,** 244-250.
192. Collet, A.; Brienne, M. J.; Jacques, J., *Optical resolution by direct crystallization of enantiomer mixtures*, Chemical Reviews, **1980,** 80, (3), 215-230.

193. Iwama, S.; Horiguchi, M.; Sato, H.; Uchida, Y.; Takahashi, H.; Tsue, H.; Tamura, R., *Observation of the Preferential Enrichment Phenomenon for Essential alpha-Amino Acids with a Racemic Crystal Structure*, Cryst. Growth Des., 10, (6), 2668-2675.
194. Lindenberg, C.; Krättli, M.; Cornel, J.; Mazzotti, M., *Design and Optimization of a Combined Cooling/Antisolvent Crystallization Process*, Cryst. Growth Des. , **2009,** 9, (2), 1124-1136.
195. Cornel, J.; Lindenberg, C.; Mazzotti, M., *Quantitative Application of in Situ ATR-FTIR and Raman Spectroscopy in Crystallization Processes,* Ind. Eng. Chem. Res., **2008,** 47, (14), 4870-4882.
196. Lewiner, F.; Klein, J. P.; Puel, F.; Févotte, G., *On-line ATR FTIR measurement of supersaturation during solution crystallization processes. Calibration and applications on three solute/solvent systems*, Chem. Eng. Sc., **2001,** 56, (6), 2069-2084.
197. Zhou, G. X.; Fujiwara, M.; Woo, X. Y.; Rusli, E.; Tung, H.-H.; Starbuck, C.; Davidson, O.; Ge, Z.; Braatz, R. D., *Direct Design of Pharmaceutical Antisolvent Crystallization through Concentration Control*, Cryst. Growth Des., **2006,** 6, (4), 892-898.
198. Hannu, A.; Jarno, K.; Haiyan, Q.; Henry, H.; Satu-Pia, R.; Marjatta, L.-K.; Juha, K., *In-line monitoring of reactive crystallization process based on ATR-FTIR and Raman spectroscopy*, J. Chemom., **2008,** 22, (11-12), 644-652.
199. Kee, N. C. S.; Arendt, P. D.; Tan, R. B. H.; Braatz, R. D., *Selective Crystallization of the Metastable Anhydrate Form in the Enantiotropic Pseudo-Dimorph System of l-Phenylalanine using Concentration Feedback Control*, Cryst. Growth Des., **2009,** 9, (7), 3052-3061.
200. Amanullah, M.; Abel, S.; Mazzotti, M., *Separation of Tröger's Base Enantiomers Through a Combination of Simulated Moving Bed Chromatography and Crystallization*, Adsorption, **2005,** 11, (0), 893-897.
201. Vorster, E., Diploma thesis: *Auslegung einer Trennung von Serin-Enantiomeren mittels Verdampfungskristallisation und chiraler Chromatographie,* Max-Planck-Institute for Dynamics of Compex Technical Systems, Magdeburg, **2008**.
202. Godunov, S. K., *A finite difference method for numerical computation and discontinuous solutions of the equations of fluid dynamics*, Math. Sb., **1959,** 47, 271-306.
203. Rouchon, P.; Schonauer, M.; Valentin, P.; Guiochon, G., *Numerical Simulation of Band Propagation in Nonlinear Chromatography*, Sep. Sci. Technol., **1987,** 22, (8), 1793-1833.
204. Kniep, H., Doctoral thesis: *Vergleich verschiedener verfahrenstechnischer Konzepte zur Durchführung der präparativen Flüssigchromatographie,* Otto-von-Guericke University Magdeburg/Germany, **1997**.
205. Kaemmerer, H.; Arnell, R.; Hedberg, M.; Jones, M. J.; Larson, K.; Horvath, Z.; Kaspereit, M.; Lee, J. W.; Lorenz, H.; Seidel-Morgenstern, A., *Separation of racemic bicalutamide by an optimized combination of continuous chromatography and selective crystallization* Org. Process Res. Dev., **2012,** 16, (2), 331-342.

Appendix

A. g^E-model parameters and heats and temperatures of fusion

Table A.1 *Binary interaction parameters of [1](2S,3R)-Threonine, [2](2R,3S)-Threonine and [3]water.*

NRTL model parameters	water
α_{13}	$1.5328 \cdot 10^{-2}$
Δg_{13}	$6.8587 \cdot 10^{1}$ kJ mol^{-1}
Δg_{31}	$-5.3298 \cdot 10^{1}$ kJ mol^{-1}
α_{12}	$2.2371 \cdot 10^{-5}$
Δg_{12}	$2.3781 \cdot 10^{3}$ kJ mol^{-1}
Δg_{21}	$-2.3095 \cdot 10^{3}$ kJ mol^{-1}

Table A.2 *Binary interaction parameters of [1](1S,2R)-N-methylephedrine, [2](1R,2S)-N-methylephedrine and [3](S)-ethyl lactate, [4](2R, 3R)-diethyl tartrate.*

NRTL model parameters	(S)-ethyl lactate, 3)	(2R,3R)- diethyl tartrate, 4)
α_{13}	$2.411 \cdot 10^{-1}$	$7.474 \cdot 10^{1}$
Δg_{13}	$2.118 \cdot 10^{1}$ kJ·mol^{-1}	$1.770 \cdot 10^{3}$ kJ·mol^{-1}
Δg_{31}	-3.728 kJ·mol^{-1}	-2.406 kJ·mol^{-1}
α_{12}	$1.140 \cdot 10^{-12}$	0
Δg_{12}	$1.399 \cdot 10^{6}$ kJ·mol^{-1}	-
Δg_{21}	$-1.399 \cdot 10^{6}$ kJ·mol^{-1}	-

Table A.3 *Heat and temperature of fusion of (1S,2R) N-methylephedrine*

Δh^f	29240 J mol^{-1}
T^f	360.3 K

Table A.4 *Binary interaction parameters of [1](S)-Tröger's Base in [3]ethanol*

NRTL model parameters	ethanol
α_{13}	$1.536e^{-2}$
Δg_{13}	6.521 kJ mol^{-1}
Δg_{31}	$-3.651 \cdot 10^{-3}$ kJ mol^{1}

Table A.5 *Optimised values for the heat and temperature of fusion of the single enantiomer and the racemic compound of Methionine.*

$\Delta h^f_{(R,S)}$	$2 \cdot 30076.1$	J mol^{-1}
$T^f_{(R,S)}$	591.1	K
$\Delta h^f_{(R)}$	28635.36	J mol^{-1}
$T^f_{(R)}$	581.8	K

Table A.6 *Binary interaction parameters of [1](S)-Methionine, [2](R)-Methionine and [3]water.*

NRTL model parameters	water	
α_{13}	$6.6442 \cdot 10^{-2}$	
Δg_{13}	$1.3175 \cdot 10^{2}$	kJ mol^{-1}
Δg_{31}	-5.5268	kJ mol^{-1}
α_{12}	$5.9929 \cdot 10^{-4}$	
Δg_{12}	$1.0977 \cdot 10^{2}$	kJ mol^{-1}
Δg_{21}	$5.7223 \cdot 10^{4}$	kJ mol^{-1}
α_{121}	$4.0740 \cdot 10^{-4}$	
Δg_{121}	$-1.5722 \cdot 10^{3}$	kJ mol^{-1}
Δg_{211}	$3.3842 \cdot 10^{3}$	kJ mol^{-1}
α_{122}	$1.2140 \cdot 10^{-2}$	
Δg_{122}	$1.9878 \cdot 10^{2}$	kJ mol^{-1}
Δg_{212}	$-1.3377 \cdot 10^{2}$	kJ mol^{-1}

Table A.7 *Binary interaction parameters of the undisclosed compound UND: [1](R)-UND, [2](S)-UND and [3]ethyl acetate.*

NRTL model parameters	solution		melt	
α_{13}	$7.4728 \cdot 10^{-5}$			
Δg_{3}	$4.1004 \cdot 10^{3}$	kJ mol^{-1}		
Δg_{31}	$-4.0307 \cdot 10^{3}$	kJ mol^{-1}		
α_{12}	$2.250 \cdot 10^{-14}$		$5.0905 \cdot 10^{-4}$	
Δg_{12}	$-7.680 \cdot 10^{2}\cdot$	kJ mol^{-1}	$-4.6860 \cdot 10^{3}$	kJ mol^{-1}
Δg_{21}	$8.708 \cdot 10^{2}$	kJ mol^{-1}	$5.0819 \cdot 10^{3}$	kJ mol^{-1}

Table A.8 *Binary interaction parameters of [1](S)-Mandelic acid, [2](R)-Mandelic acid and [3]water.*

NRTL model parameters	water	
α_{13}	$8.4021 \cdot 10^{-1}$	
a_{13}	$-7.7452 \cdot 10^{-1}$	kJ mol^{-1}
b_{13}	$7.0767 \cdot 10^{-4}$	kJ mol^{-1} K^{-1}
a_{31}	-8.5421	kJ mol^{-1}
b_{3}	$4.8826 \cdot 10^{-2}$	kJ mol^{-1} K^{-1}
α_{12}	$2.2711 \cdot 10^{-1}$	
Δg_{12}	6.9201	kJ mol^{-1}
Δg_{21}	$1.7507 \cdot 10^{1}$	kJ mol^{-1}

Table A.9 *Binary interaction parameters of [1](S)-Propranolol·HCl and [3]methanol/water.*

NRTL model parameter	ethanol	water
α_{13}	$1.1747 \cdot 10^{-6}$	$3.0001 \cdot 10^{-1}$
Δg_{13}	$5.4058 \cdot 10^{3}$ kJ mol^{-1}	$1.5686 \cdot 10^{1}$ kJ mol^{-1}
Δg_{31}	$-5.3958 \cdot 10^{3}$ kJ mol^{-1}	$1.3985 \cdot 10^{2}$ kJ mol^{-1}

Table A.10 *Binary interaction parameters of [1](S)-Mandelic acid , [2](R)-Mandelic acid and [3](S)-ethyl lactate/(2R, 3R)-diethyl tartrate.*

NRTL model parameters	(S)-ethyl lactate		(2R, 3R)-diethyl tartrate	
α_{13}	$5.7532 \cdot 10^{-1}$		$4.0104e^{-1}$	
Δg_{13}	-2.9341	kJ mol^{-1}	$2.5269e^{4}$	kJ mol^{-1}
Δg_{31}	$3.1028 \cdot 10^{4}$	kJ mol	$3.2357e^{3}$	kJ mol^{-1}
α_{12}	$1.9925 \cdot 10^{-4}$		$1.9388 \cdot 10^{-3}$	
Δg_{12}	$-3.2301 \cdot 10^{2}$	kJ mol^{-1}	$-8.2707 \cdot 10^{1}$	kJ mol^{-1}
Δg_{21}	$3.2897 \cdot 10^{3}$	kJ mol^{-1}	$8.4895 \cdot 10^{1}$	kJ mol^{-1}

Table A.11 *Optimised values for the heat and temperature of fusion of Propranolol·HCl.*

$\Delta h^{f}_{(R,S)}$	2·36800	J mol^{-1}
$T^{f}_{(R,S)}$	436.3	K
$\Delta h^{f}_{(R)}$	35462	J mol^{-1}
$T^{f}_{(R)}$	471.6	K

Table A.12 *Binary interaction parameters of [1](S)-Serine and [3]water.*

NRTL model parameters	water	
α_{13}	$3.0001 \cdot 10^{-1}$	
Δg_{13}	-4.2222	kJ mol^{-1}
Δg_{31}	-5.3578	kJ mol^{-1}

Table A.13 *Optimised values for the heat and temperature of fusion of the single enantiomer and the racemic compound of Serine.*

$\Delta h^{f}_{(R,S)}$	2·41609	J mol^{-1}
$T^{f}_{(R,S)}$	700	K
$\Delta h^{f}_{(R)}$	39611	J mol^{-1}
$T^{f}_{(R)}$	551.9	K

Table A.14 *Binary interaction parameters of [1](S)-Proline and [3]DMSO.*

NRTL model parameters	water	
α_{13}	$1.030 \cdot 10^{-1}$	
Δg_{13}	$6.5570 \cdot 10^{1}$	kJ mol^{-1}
Δg_{31}	$2.2257 \cdot 10^{2}$	kJ mol^{-1}

Table A.15 *Optimised values for the heat and temperature of fusion of Proline and its hemi-chloroformate.*

$\Delta h^{f}_{(R,S)}$	2·26558 J mol^{-1}
$T^{f}_{(R,S)}$	501.8 K
$\Delta h^{f}_{(R,S),hemi-chloroformate}$	2·60275 J mol^{-1}
$T^{f}_{(R,S),hemi-chloroformate}$	404.8 K
$\Delta h^{f}_{(R)}$	28817.6 J mol^{-1}
$T^{f}_{(R)}$	484.6 K

Table A.16 *Binary interaction parameter of [1](S)-3-Chloro-Mandelic acid, [2](R)-3-Chloro-Mandelic acid, [3]water and [4]2-propanol.*

NRTL model parameters	water/2-propanol	
α_{23}	8.7353·10^{-1}	
Δg_{23}	7.468	kJ mol^{-1}
Δg_{32}	8.2266·10^{4}	kJ mol^{-1}
α_{14}	2.1107·10^{-1}	
Δg_{14}	-7.7338	kJ mol^{-1}
Δg_{41}	1.1839·10^{1}	kJ mol^{-1}
α_{34}	2.875·10^{-1}	
Δg_{34}	927.63·R·	K
Δg_{43}	-55.35·R·	K

Table A.17 *Binary interaction parameter of [1](R)-Bicalutamide, [2](S)-Bicalutamide, [3]methanol and [4]water*

NRTL model parameters	methanol/water	
α_{13}	1.1524·10^{-1}	
Δg_{13}	-1.4587·10^{4}	J mol^{-1}
Δg_{31}	2.8845·10^{4}	J mol^{-1}
α_{14}	8.0852·10^{-2}	
Δg_{14}	2.0836·10^{4}	J mol^{-1}
Δg_{41}	7.3571·10^{3}	J mol^{-1}
α_{34}	3.0·10^{-1}	
Δg_{34}	R (2.7312·T-6.1727·10^{2})	J mol^{-1}
Δg_{43}	R (6.93·10^{-1}·T+1.7299·10^{2})	J mol^{-1}

Table A.18 *Determined values for the heat and temperature of fusion of the single enantiomer and the racemic compound of Bicalutamide.*

	own data		Vega *et al.* [184]	
$\Delta h^{f}_{(R,S)}$	2·43185	J mol^{-1}	47771 43037	J mol^{-1} J mol^{-1}
$T^{f}_{(R,S)}$	466.1	K	465.2 462.2	K K
$\Delta h^{f}_{(R)}$	38179	J mol^{-1}		
$T^{f}_{(R)}$	453.7	K		

B. Solubilities of Bicalutamide in methanol/toluene solutions

The solvent composition and temperature dependent solubility was described by Eq. (B.1) with x_m being the methanol fraction in percent on a solute free basis. The R^2 value of the polynomial obtained for the solubility of (R)-Bicalutamide in methanol/toluene mixtures is estimated to 0.9856 and the root mean square error is 0.1166.

$$\begin{aligned} x_{\text{Bicalutamide}}(T, x_m) = \; & -1.1268 \cdot 10^{-6}(\mathrm{T})^4 - 2.2636 \cdot 10^{-7}(T)^3(x_m) + 0.0014077\,(T)^3 \\ & -2.4272 \cdot 10^{-7}(T)^2(x_m)^2 + 0.00024709 \cdot (T)^2(x_m) - 0.65917 \cdot (T)^2 \\ & -4.093 \cdot 10^{-7} \cdot (T)(x_m)^3 + 0.00019923 \cdot (T)(x_m)^2 - 0.088426 \cdot (\mathrm{T})(x_m) \\ & +137.1171(\mathrm{T}) - 6.0618 \cdot 10^{-8}(x_m)^4 + 0.00012865\,(x_m)^3 - 0.038114\,(x_m)^2 \\ & +10.4284\,(x_m) - 10691.0116 \end{aligned} \qquad \textbf{(B.1)}$$

C. Parameters used within COSMO-SAC studies

Table C.1 *Input parameters used within Materials Studio (DMol3) and considered COSMO-SAC parameterisations.*

Task	Settings and Parameters
Geometry optimisation	• DFT Module DMol3 • No solvation scheme • Double Numerical basis with Polarization functions, DNP v4.0.0 • Generalised Gradient Approximation/Becke-Perdew version of the Volsko-Wilk-Nusair functional, GGA/VWN-BP • Real space cutoff: default value • 'fine' tolerances with default values
Energy calculation	• DFT Module DMol3 • COSMO option set 'on', dielectric constant set 'infinity' • Double Numerical basis with Polarisation functions, DNP v4.0.0 • Generalised Gradient Approximation/Becke-Perdew version of the Volsko-Wilk-Nusair functional, GGA/VWN-BP • Real space cutoff: 5.5 Å • 'fine' tolerances with default values

Table C.2 *Parameterisation used within the (refined) COSMO-SAC model.*

	Mullins [75]	Wang [77]	
Cutoff value for hydrogen bonding, σ_{hb}	0.0084	0.0084	e/ Å^2
Hydrogen bonding coefficient, c_{hb}	85580	3484.42	kcal/mol Å^4/e^2
Effective surface area, a_{eff}	7.5	7.25	Å^2
Effective radius, r_{av}	0.81764	$\sqrt{a_{eff}/\pi}$	Å
Empirical correction factor used in the sigma profile averaging process, f_{decay}	[-]	3.57	[-]
Polarisability factor, f_{pol}	0.64	0.6917	[-]
Permittivity of free space, ε_0	2.395e-4		e^2 mol/kcal Å^4/e^2

D. ATR FTIR calibration model

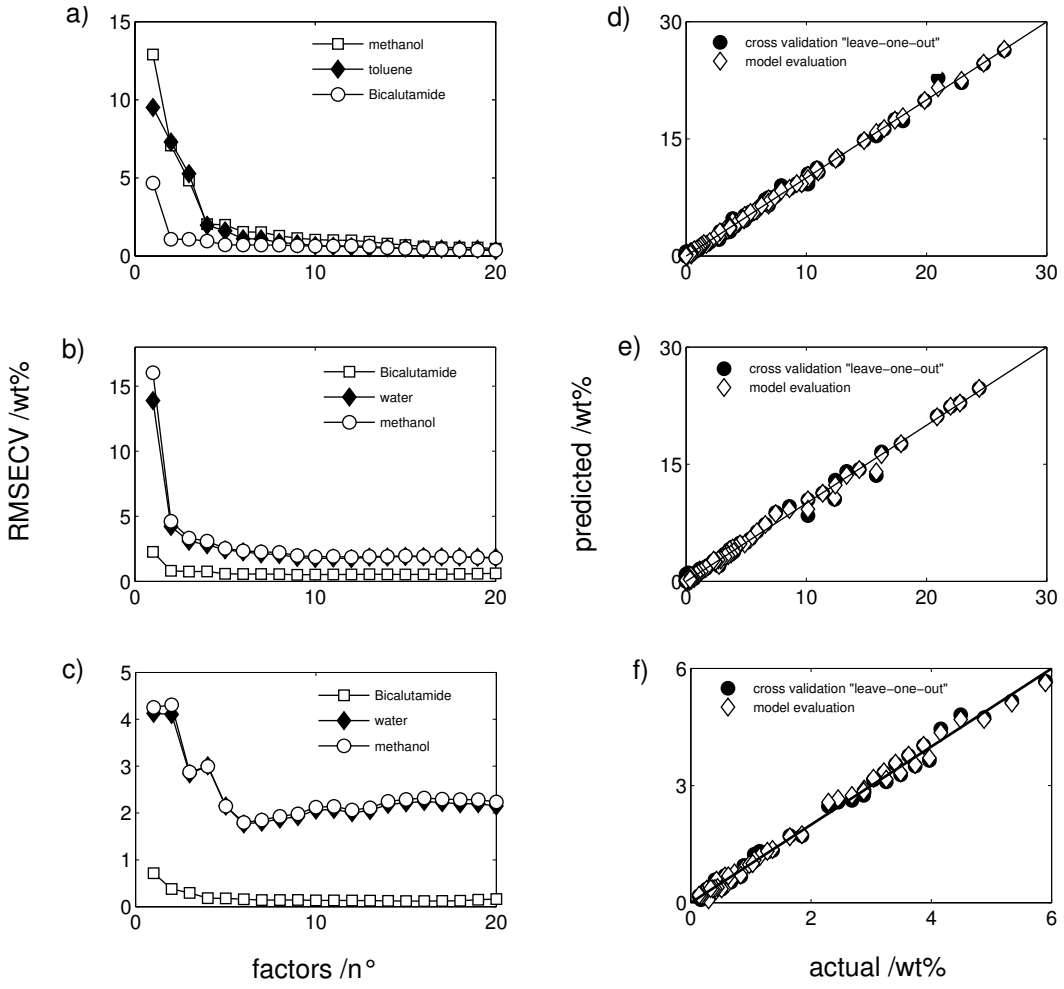

Figure D.1a)-f) *Root-mean-square-error of cross validation (RMSECV) using different numbers of model factors for three calibration models for Bicalutamide in methanol/toluene and methanol/water mixtures (a)-c)). Parity plots of calibration models are given in Figures d)-f).*

Table D.1 *Accuracy of the ATR-FTIR models for Bicalutamide in solution.*

	system 1		system 2 (full data set)		system 2 (small data set)	
	RMSECV[1)]	R^2 cumulative	RMSECV	R^2 cumulative	RMSECV	R^2 cumulative
Bicalutamide	0.37	0.99	0.50	0.996	0.16	0.993
methanol	0.54	1	1.8	0.998	1.77	0.997
toluene	0.43	1	-	-	-	-
water	-	-	2.0	0.998	1.80	0.997

[1)] root mean square error of cross validation

E. Parameters of adsorption isotherm models

Table E.1 *Determined adsorption isotherm model parameters for Bicalutamide enantiomers in methanol (competitive multi-component Bi-Langmuir model, Eq. (2.87)).*

Parameter		(R)-Bicalutamide	(S)-Bicalutamide
$q_{S1,i}$	/g L^{-1}	44.04	44.04
$b_{1,i}$	/L g^{-1}	0.008386	0.008386
$q_{S2,i}$	/g L^{-1}	17.10	17.10
$b_{2,i}$	/L g^{-1}	0.011312	0.199096

Table E.2 *Determined adsorption isotherm model parameters for Serine enantiomers in 20/80 v/v methanol/water (competitive multi-component Bi-Langmuir model, Eq. (2.87)).*

Parameter		(R)-Serine	(S)-Serine
$q_{S1,i}$	/g L^{-1}	93.36	93.36
$b_{1,i}$	/L g^{-1}	6.11E-05	6.11E-05
$q_{S2,i}$	/g L^{-1}	3.87	3.87
$b_{2,i}$	/L g^{-1}	0.0743	0.1291

List of figures

List of tables